Chapter 3

Seismic Sources and Source Parameters

(Version April 2013; draft, under review)

Peter Bormann[1)], Siegfried Wendt[2)], and Domenico DiGiacomo[3)]

[1)] Formerly GFZ German Research Centre for Geosciences, Department 2: Physics of the Earth, Telegrafenberg, 14473 Potsdam, Germany; E-mail: pb65@gmx.net;
[2)] Geophysical Observatory Collm, University of Leipzig, 04779 Wermsdorf, Germany; E-mail: wendt@rz.uni-leipzig.de
[3)] International Seismological Centre (ISC), Pipers Lane, Thatcham, Berkshire, RG19 4NS, United Kingdom; E-mail: domenico@isc.ac.uk

Note 1: This is a preliminary contribution under review and revision. Any comments, criticism and corrections are highly welcome. They should be addressed to the first author and will be acknowledged in the final version.

Note 2: Figure numbers followed by "??" relate to figures in Chapters of NMSOP-1 (2002). They are accessible via this web site too. The numbers will be modified when all revised NMSOP-2 Chapters become available.

3.1 Introduction to seismic sources and source parameters
(P. Bormann)

Seismic waves (Chapter 2), generated by *seismic sources* (Chapter 3), are oscillations due to elastic deformations which propagate through the Earth and can be recorded by *seismic sensors* (Chapter 5) and *data acquisition systems* (Chapter 6) . The *seismic moment* (section 3.1.2.3; IS 3.8, 3.10 and 3.11) and *seismic energy* (section 3.1.2.5; IS 3.6 and 3.9) released by these sources may cover a tremendous range of associated *magnitudes* (see 3.2) and thus can stir up a wide range of shaking *intensities* (Chapter 12) with potentially related damages. These and other source characterizing parameters, their mutual relationships as well as the determination of seismic source mechanisms based on observation of polarity patterns and

amplitude ratios between P and S waves as a function of azimuth are dealt with in detail in this chapter, related Information Sheets (IS) and Exercises (EX).

3.1.1 Types and peculiarities of seismic source processes

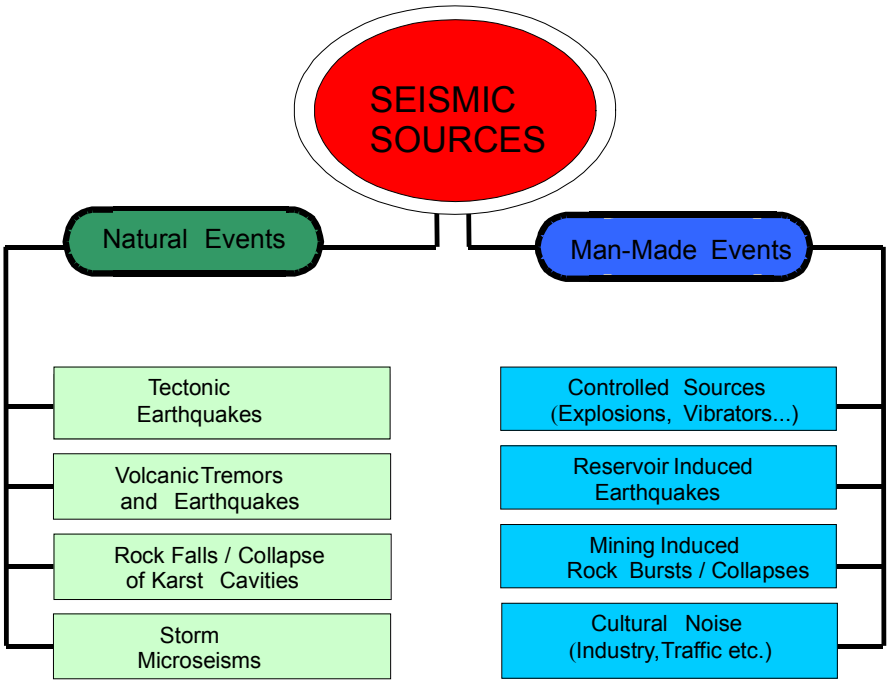

Fig. 3.1 Schematic classification of various kinds of events which generate seismic waves.

3.1.1.1 Tectonic earthquakes

Tectonic earthquakes are caused when the brittle part of the Earth's crust is subjected to stress that exceeds its breaking strength. Sudden rupture will occur, mostly along pre-existing faults or sometimes along newly formed faults. Rocks on each side of the rupture "snap" into a new position. For very large earthquakes, the length of the ruptured zone may be as much as 1000 km and the slip along the fault can reach several meters, sometimes even over a decameter.

Laboratory experiments show that homogeneous consolidated rocks under pressure and temperature conditions at the Earth's surface will fracture at a volume strain on the order of 10^{-2} - 10^{-3} (i.e., about 0.1 % to 1% volume change) depending upon their porosity. Rock strength is generally smaller under tension or shear than under compression. Shear strains on the order of about 10^{-4} or less may already cause fracturing of solid brittle rock. Rock strength is further reduced if the rock is pre-fractured, which is usually the case in continental Earth crust subjected to millions of years of still ongoing or previous phases of increased tectonic activity.

The strength of pre-fractured rock is much less than that of unbroken competent rock and is mainly controlled by the frictional resistance to motion of the two sides of the fault. Frictional resistance, which depends on the orientation of the faults with respect to the stress field and other conditions (see Scholz, 1990 and 2002), can vary over a wide range. Accordingly,

deformations on the order of only 10^{-5} to 10^{-7}, which correspond to bending of a lithospheric plate by about 0.1 mm to 1 cm over a distance of 1 km, may cause shear faulting along pre-existing zones of weakness. But the shear strength depends also on the composition and fabric (anisotropy) of rock, its temperature, the confining pressure, the rate of deformation, etc. as well as the total cumulative strain. More details on the physics of earthquake faulting and related geological and seismotectonic conditions in the real Earth can be found in Scholz (1990 and 2002) and in section 3.1.4. Additional recommended overview articles on the rheology of the stratified lithosphere and its relation to crustal composition, age and heat flow were published by Meissner and Wever (1988), Ranalli and Murphy (1987) and Wever et al. (1987). They also explain the influence of these parameters on the thickness and maximum depth of the seismogenic zone in the Earth crust and lithosphere, i.e., the zone within which brittle fracturing of the rocks is possible when the strains exceed the breaking strength or elastic limit of the rock (see Chapter 2, Fig. 2.1).

The break-up of the lithosphere into plates due to deformation and stress loading is the main cause of tectonic earthquakes. The plates are driven, pushed and pulled by the slow motion of convection currents in the more plastic hot material of the mantle beneath the lithosphere. These relative motions are in the order of several cm per year. Fig. 3.2 shows the global pattern of earthquake belts and the major tectonic plates. There are also numerous small plates called sub- or micro-plates. Shallow earthquakes, within the upper part of the crust, take place mainly at plate boundaries but may also occur inside plates (interplate and intraplate earthquakes, respectively). Intermediate (down to about 300 km) and deep earthquakes (down to a maximum of 700 km depth) occur under ocean trenches and related subduction zones where the lithosphere plates are thrusted or pulled down into the upper mantle. The major trenches are found around the Circum-Pacific earthquake and volcanic belt (see Fig. 3.2). However, intermediate and deep earthquakes may occur also in some other marine or continental collision zones (e.g., the Tyrrhenian and Aegean Sea or the Carpathians and Hindu Kush, respectively).

Most earthquakes occur along the main plate boundaries. These boundaries constitute either zones of extension (e.g., in the up-welling zones of the mid-oceanic ridges or intra-plate rifts), transcurrent shear zones (e.g., the San Andreas fault in the west coast of North America or the North Anatolian fault in Turkey), or zones of plate collision (e.g., the Himalayan thrust front) or zones of subduction (mostly along deep sea trenches). Accordingly, tectonic earthquakes may be associated with many different faulting types (strike-slip, normal, reverse, thrust faulting or mixed; see text and Figures in 3.4.2).

The largest strain rates are observed near active plate boundaries (about 10^{-8} to 3×10^{-10} per year). Strain rates are significantly less in active plate interiors (about 5×10^{-10} to 3×10^{-11} per year) or within stable continental platforms (about 5×10^{-11} to 10^{-12} per year) (personal communication by Giardini, 1994). Consequently, the critical cumulative strain for the pre-fractured/faulted seismogenic zone of lithosphere, which is on the order of about 10^{-6} to 10^{-7}, is reached roughly after some 100, 1000 to 10,000 or 10,000 to 100,000 years of loading, respectively. This agrees well with estimates of the mean return period of the largest possible events (seismic cycles) in different plate environments (Muir-Wood, 1993; Scholz, 1990).

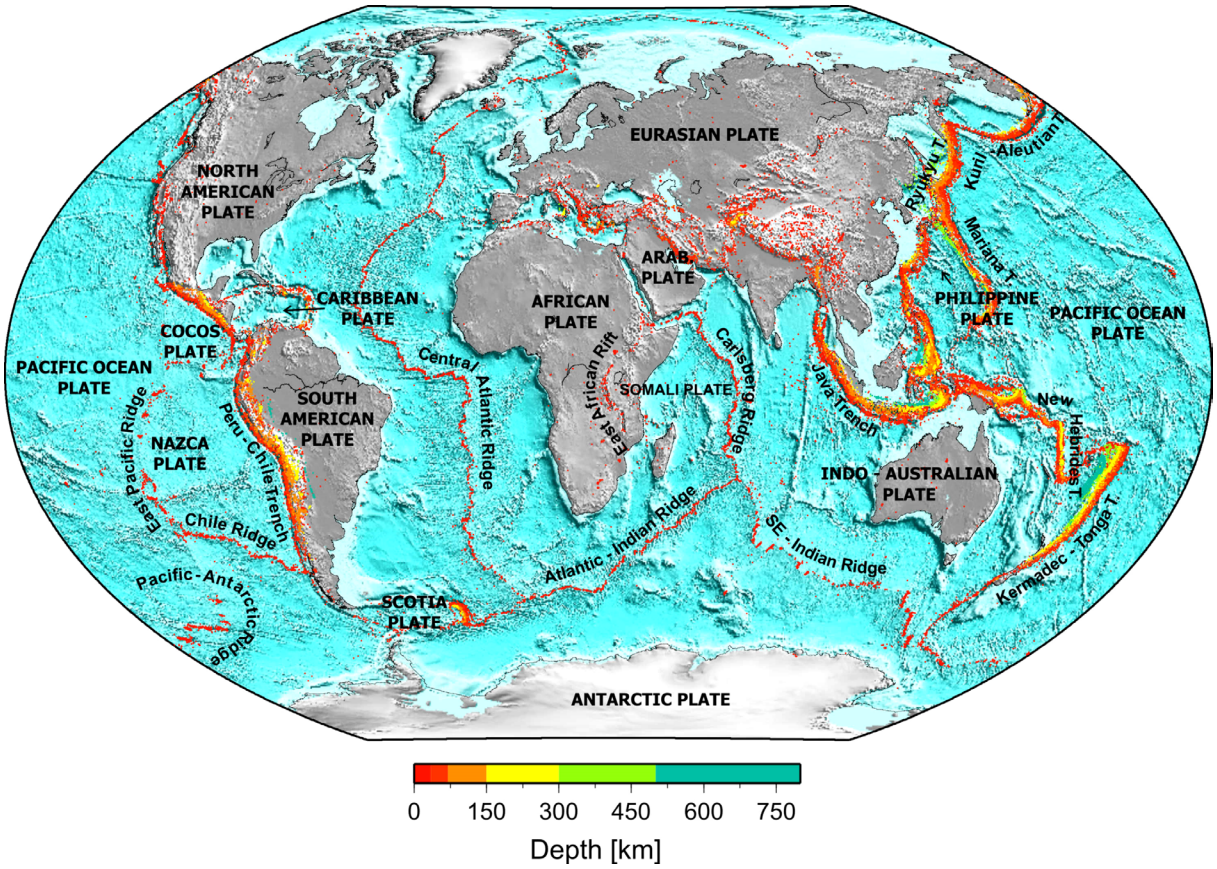

Fig. 3.2 Global distribution of earthquake epicenters according to the data catalog of the United States National Earthquake Information Center (NEIC), January 1960 to November 2011, and the related major lithosphere plates. (Figure by courtesy of Regina Milkereit, GFZ German Research Centre for Geosciences),

Although there are hundreds of thousands of weak tectonic earthquakes globally every year, most of them can only be recorded by sensitive nearby instruments. But in the long-term global statistical average about 100,000 earthquakes are strong enough (magnitude M ≥ 3) to be potentially perceptible by humans in the near-source area. A few thousand are strong enough (M ≥ 5) to cause slight damage and some 100 with magnitude M > 6 can cause heavy damage, if there are nearby settlements and built-up areas; while about 1 to 4 (in 2007) events every year (with M ≥ 8) may result in wide-spread devastation and disaster. During the 20th century the 1995 Great Hanshin/Kobe earthquake caused the greatest economic loss (about 100 billion US$), the 1976 Tangshan earthquake inflicted the most terrible human loss (about 243,000 people killed) while the Chile earthquake of 1960 released the largest amount of *seismic energy* E_S of about $5 \cdot 10^{18}$ to 10^{19} Joule. The latter corresponds to about 25 to 100 years of the long-term annual average of global seismic energy release which is about $1 - 2 \times 10^{17}$ J (Lay and Wallace, 1995) and to about half a year of the total kinetic energy contained in the global lithosphere plate motion. The total *seismic moment* (see 3.1.2.3. below) of the Chile earthquake was about 3×10^{23} Nm. It ruptured about 800 - 1000 km of the subduction zone interface at the Peru-Chile trench in a width of about 200 km (Boore, 1977; Scholz, 1990). Yet, according to Cifuentes and Silver (1989) this great Valdivia May 22nd 1960 Chile earthquake was in fact a multiple rupture, consisting of three events with a combined seismic moment of at least $M_0 = 5.5 \times 10^{23}$ Nm and a duration of about 1500 s. The faster rupturing

main shock was preceded by a large scale slip with a rise time of 300 s and observable only at low frequencies, starting some 1150 s before the more high-frequency main shock initiated and another event that followed the main shock about 350 s later. The combined seismic moment would correspond to Mw = 9.76, and might even have been larger (about Mw ~ 9.9; personal communication by W. H. K. Lee, 2012) when fully accounting for the probable very long-period energy release, associated with the long lasting slow rupture, which was not yet properly measurable with the 1960 available instrumentation. If this is correct, then about 4 times more seismic energy than discussed above was released in this huge seismotectonic event.

In summary: about 85 % of the total world-wide seismic moment release by earthquakes occurs in subduction zones and more than 95 % by shallow earthquakes along plate boundaries. The other 5 % are distributed between intraplate events and deep and intermediate focus earthquakes. The single 1960 Chile earthquake accounts for about 25 % of the total seismic moment release between 1904 and 1986. And some of the devastating great earthquakes of the early 21st century were almost comparably large, such as the Mw9.3 Sumatra-Andaman earthquake of December 26, 2004 with a rupture duration of about 9 min, a rupture length of about 1300 km and with some 15 to 20 m fault slip, causing a tsunami with maximum run-up heights on land of almost 30 m locally, killing in total more than 230,000 people (Wikipedia).

It should be noted that most of the total energy release, $E_{T,}$ is required to power the growth of the earthquake fracture and the production of heat. Only a small fraction of $E_T = E_S + E_f$ (with E_f - friction energy) goes into producing seismic waves. The seismic efficiency, i.e., the ratio of E_S/E_T , is perhaps only about 0.01 to 0.1. It depends both on the *stress drop* during the rupture as well as on the total stress in the source region (Spence, 1977; Scholz, 1990).

3.1.1.2 Volcanic earthquakes

Although the total energy released by the strongest historically known volcanic eruptions was even larger than E_T of the Chile earthquake, the seismic efficiency of volcanic eruptions is generally much smaller, due to their long duration. Nevertheless, in some cases, volcanic earthquakes may locally reach the shaking strength of destructive earthquakes (e.g., *magnitudes* of about 6). Most of the seismic oscillations produced in conjunction with sub-surface magma flows are of the tremor type, i.e., long-lasting and more or less monochromatic oscillations which come from a two- or three-phase (liquid- and/or gas-solid) source process which is not narrowly localized in space and time. They can not be analyzed in the traditional way of seismic recordings from tectonic earthquakes or explosions nor be described with traditional source parameters (see Chapter 13). Volcanic earthquakes contribute only an insignificant amount to the global seismic moment release (see Scholz, 1990).

3.1.1.3 Explosions, implosions and other seismic events

Explosions are mostly anthropogenic, i.e., “man-made”, and controlled, i.e., with known location and source time. However, strong natural explosions in conjunction with volcanic eruptions or meteorite impacts, such as the Tunguska meteorite of 30 June 1908 in Siberia or

the Chelyabinsk/Ural meteorite impact on 15 February 2013 (see seismic records in Fig. 3.3a), may also occur.

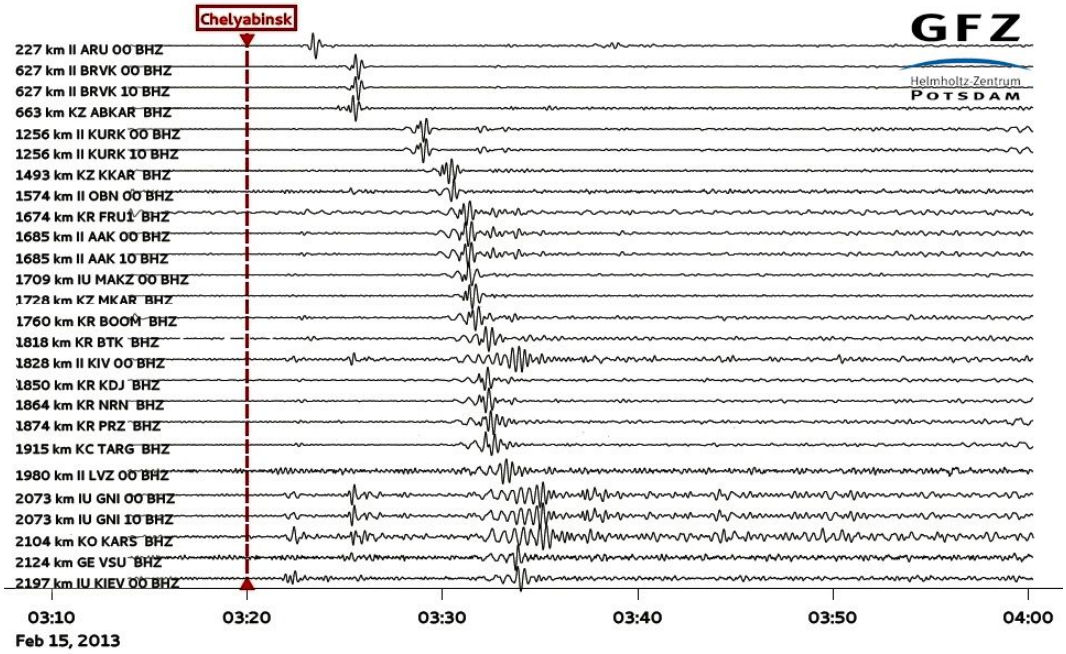

Fig. 3.3a Seismic records of the Chelyabinsk/Ural meteorite impact of February 15, 2013, compiled at the GFZ German Research Centre for Geosciences (GFZ).

Explosions used in exploration seismology for the investigation of the crust have yields, Y, of a few kg to tons of TNT (Trinitrotoluol; 1 kt TNT = 4.2 x 10^{12} J). This is sufficient to produce seismic waves which can be recorded from several km to hundreds of km distance. Underground nuclear explosions (UNE) of kt up to Mt of equivalent TNT may be seismically recorded even world-wide. Nevertheless, the strongest of all UNE, with an equivalent yield of about 5 Mt TNT, produced only a body-wave magnitude mb ≈ 7. This corresponds to roughly 0.1% of the seismic energy released by the Chile earthquake of 1960. After 1974, underground tests with only Y ≤ 150 kt were carried out. Only well contained underground chemical or nuclear explosions have a sufficiently good seismic coupling factor ε (ε ≈ 10^{-2} to 10^{-3}, i.e., only 1 % to 0.1 % of the total released explosion energy is transformed into seismic energy). By means of decoupling techniques ε may be reduced by 2 to 5 orders (Adams and Allen, 1961; Adams and Swift, 1961; Latter et al., 1961a and b; Willies and Wilson, 1962). The coupling factor of explosions on the surface or in the atmosphere is much less (ε ≈ 10^{-3} to 10^{-6} depending on the altitude) and in the hydrosphere much larger (ε ≈ 10^{-1}) (see compilation of ε values in Bormann, 1966; or Båth, 1962; Griggs and Press, 1961; Pasečnik et al., 1960; Pomeroy and Oliver, 1960;, 1960; Willies, 1963).

Explosions are expected to produce an outward directed compressional first motion in all directions while tectonic earthquakes produce first motions of different amplitude and polarity in different directions (Fig. 3.3b). These characteristics can be used to identify the type of source process (see 3.4) and to discriminate between explosions and tectonic earthquakes.

Compared to tectonic earthquakes, the *duration* of the source process of explosions and the *rise time* to the maximum level of displacement is much shorter (milliseconds as compared to

seconds up to a few minutes) and more impulsive (Fig. 3.4). Accordingly, explosions of comparable body-wave magnitude excite more high-frequent oscillations and source spectra with about one order higher corner frequencies for equal plateau level of displacement amplitudes than average earthquakes (see Fig. 3.5).

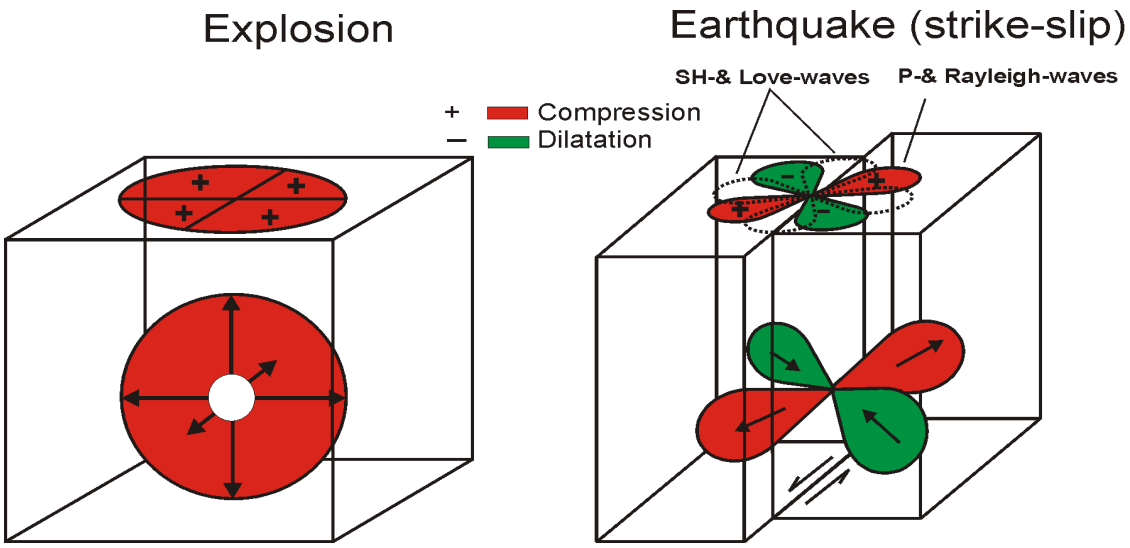

Fig. 3.3b Schematic sketches of an idealized underground explosion and of a strike-slip earthquake along a vertically dipping fault. The fault motion is "left-lateral", i.e., counter-clockwise. The arrows show the directions of compressional (outward, polarity +, red shaded) and dilatational (inward, polarity -, green shaded) motions. The patterns shown on the surface, termed amplitude or polarity patterns, indicate the azimuthal variation of observed amplitudes or of the direction of first motions in seismic records (UP = + or DOWN = –), respectively. While point-like explosions in an isotropic medium should show no azimuth-dependent amplitudes and compressional first motions only, amplitudes and polarities vary for a tectonic earthquake. The dotted amplitude lobes in Fig. 3.3, right side, indicate qualitatively the different azimuth dependence of shear (S) waves as compared to longitudinal (P) waves (rotated by 45°) but their absolute displacement amplitudes are – on average – about 5 times larger than those of P waves.

Rock falls may last for several minutes and cause seismic waves but generally with less distinct onsets and less separation of wave groups. The collapse of karst caves, mining-induced rock bursts or collapses of mining galleries are generally of an *implosion* type. Accordingly, their first motion patterns should show dilatations in all azimuths if a secondary tectonic event has not been triggered by the collapse. The strongest events may reach magnitudes up to about M = 5.5 and be recorded world-wide (e.g., Bormann et al., 1992). *Reservoir induced* earthquakes have been frequently observed in conjunction with the impoundment of water or rapid water level changes behind large dams. Since these events are triggered along pre-existing and pre-stressed tectonic faults they show the typical polarity patterns of tectonic earthquakes. The strongest events reported so far have reached magnitudes up to 6.5 (e.g., Koyna earthquake in 1967).

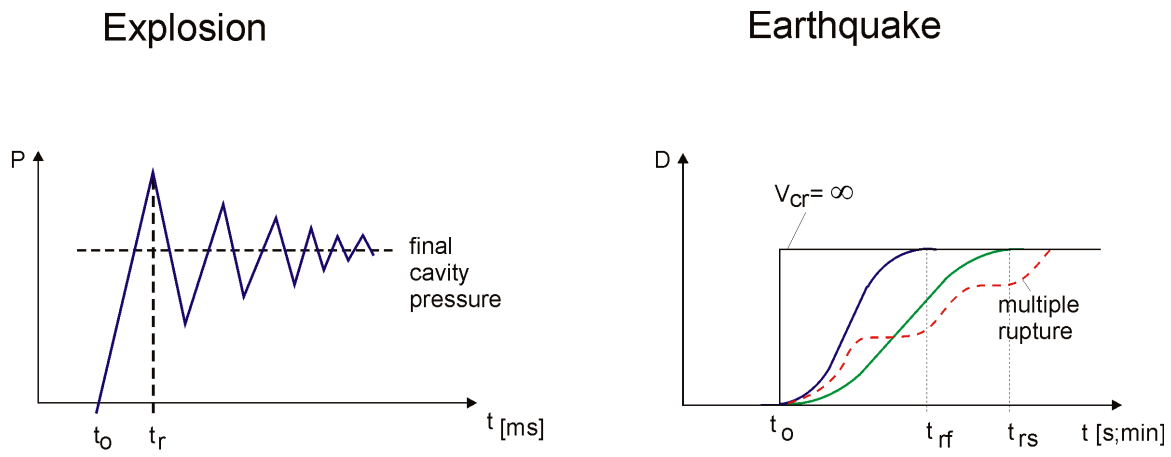

Fig. 3.4 Schematic diagrams of the different source functions of explosions (left) and earthquakes (right). P - pressure in the explosion cavity, D - fault displacement, t - time, t_0 - origin time of the event, t_r - rise time of P or D to its maximum values, t_{rf} - rise time of fast rupture, t_{rs} - rise time of slow rupture; the step function in the right diagram would correspond to an earthquake with infinite velocity of crack propagation v_{cr}. Common rupture models assume v_{cr} to be about 0.6 to 0.9 times of the velocity of shear-wave propagation, v_s (e.g., Madariaga, 1976), yet for very slow *tsunami earthquakes* it may be as slow as about 0.2 v_s (Kanamori and Brodsky, 2004; Venkataraman and Kanamori, 2004b).

3.1.1.4 Microseisms and seismic noise

Seismic signals produced by storms over oceans or large water basins (seas, lakes, reservoirs) as well as by wind action on topography, vegetation or built-up surface cover are called *microseisms*. In contrast, seismic signals due to human activities such as rotating or hammering machinery, traffic etc., are *cultural seismic noise.* Rushing waters or gas/steam (in rivers, water falls, dams, pipelines, geysers) may be additional sources of natural or anthropogenic *seismic noise*. They are neither well localized in space nor fixed to a defined *origin time*. Accordingly, they produce more or less permanent on-going non-coherent interfering signals of more or less random amplitude fluctuations in a very wide frequency range of about 16 octaves (from about 50 Hz to 1 mHz) which are often controlled in their intensity by the season (natural noise) or time of day (anthropogenic noise). Despite the large range of ambient noise displacement amplitudes (about 6 to 10 orders of magnitude; see Chapter 4, Fig. 4.7"??") they are generally much smaller than those of earthquakes and not felt by people.

Differences between signals from coherent seismic sources on the one hand and microseisms/seismic noise on the other hand are dealt with in more detail in Chapter 4, filter, processing and installation procedures for the improvement of the signal-to-noise ratio (SNR) in seismic records in Chapters 4 and 7 and the use of ambient noise for microzonation in Chapter 14.

3.1.2 Parameters which characterize size, strength and mechanism of seismic sources

3.1.2.1 Macroseismic intensity

The effect of a seismic source may be characterized by its *macroseismic intensity,* **I**. Intensity describes the strength of shaking in terms of human perception, damage to buildings and other structures, as well as changes in the surrounding environment. **I** depends on the distance from the source and the soil conditions and is mostly classified according to macroseismic scales of 12 degrees (e.g., Wood and Newman, 1931; Medvedev, 1962; Stover and Coffman, 1993; Grünthal, 1998). Exceptions are, e.g., the 7 degrees scales of Japan (see Chapter 12) and of Taiwan (Wu et al., 2003). From an analysis of the areal distribution of felt reports and damage one can estimate the epicentral intensity $\mathbf{I_0}$ in the source area as well as the source depth, h (e.g., Sponheuer, 1960). There exist empirical relationships between $\mathbf{I_0}$ and other instrumentally determined measures of the earthquake size such as the *magnitude*.peak ground velocity (PGV) and peak ground acceleration (PGA). Although these relationships are rather noisy it has been found that the earthquake damage statistics is much closer correlated with the PGV than with PGA (Wu et al., 2003). And magnitude-wise **I** is best correlated with local magnitude Ml and energy magnitude Me. For more details see Chapter 12 and for a comprehensive summary Grünthal (2011).

3.1.2.2 Magnitude and early relationships to seismic energy

Magnitude is a logarithmic measure of the size of an earthquake or explosion based on instrumental measurements. The magnitude concept was first proposed by Richter (1935). Magnitudes are commonly derived from ground motion amplitudes and periods or from *signal duration* measured on instrumental records. There is no *a priori* scale limitation to magnitudes as it exists for macroseismic intensity scales. Magnitudes are often misleadingly referred to in the press as "... according to the open-ended RICHTER scale...". In fact, the maximum size of tectonic earthquakes is limited by nature, i.e., by the maximum size of a brittle fracture in a finite and heterogeneous lithospheric plate. The largest moment magnitude, Mw, observed so far, was that of the Chile earthquake in 1960 (Mw ≈ 9.5; Kanamori, 1977). On the other hand, the magnitude scale is open at the lower end. Nowadays, highly sensitive instrumentation close to the sources may record events with magnitude smaller than zero. According to Richter´s original definition these magnitude values become negative. With empirical *energy-magnitude-relationships* the *seismic energy,* E_S, radiated by the seismic source as seismic waves can be estimated. Common relationships are those given by Gutenberg and Richter (1954, 1956a, b, c; Richter, 1958) between E_S and the surface-wave magnitude M_S and the body-wave magnitude mB: $\log E_S = 11.8 + 1.5$ Ms and $\log E_S = 5.8 + 2.4$ mB, respectively (when E_S is given in erg; 1 erg = 10^{-7} Joule). According to the first relationship, a change of Ms or mB by one unit corresponds to a change in E_S by a factor of about 32 times or 250 times, respectively.

Based on the analysis of digital recordings, there exist also direct procedures to estimate E_S (e.g., Purcaru and Berckhemer, 1978; Seidl and Berckhemer, 1982; Boatwright and Choy, 1986; Kanamori et al., 1993; Choy and Boatwright, 1995) and to define an "energy magnitude" Me (see section 3.2.7.2). Because most of the seismic energy is concentrated in

the higher frequencies around the *corner frequency* fc of the radiated spectrum (see next section), Me is a very suitable measure of the earthquakes' potential for damage. In contrast, the seismic moment, which is estimated from the displacement amplitude plateau at frequencies f >> fc, M_0 is related to the final static displacement after an earthquake and consequently, the moment magnitude, Mw, is more closely related to the tectonic effects of an earthquake (see Choy and Kirby, 2004; Di Giacomo et al., 2010; Bormann and Di Giacomo, 2011; IS 3.5).

3.1.2.3 Scalar seismic and geometric moment, source spectrum, source dimension and stress drop in relation to magnitude

Another quantitative measure of the size and strength of a seismic shear source is the *scalar seismic moment* M_0 (for its derivation see IS 3.1):

$$M_0 = \mu \, \bar{D} \, A \qquad (3.1)$$

with μ - rigidity or shear modulus of the source medium, $\bar{D}$ - average final displacement after the rupture, A - the surface area of the rupture. M_0 is a measure of the irreversible inelastic deformation in the rupture area. This inelastic strain is described in (3.1) by the product $\bar{D}$ A. On the basis of reasonable average assumptions about μ and the stress drop $\Delta\sigma$ its determination is now standard in the routine analysis of strong earthquakes by means of waveform inversion of long-period digital records (see Dziewonski et al., 1981 and IS 3.8).

Although the scalar seismic moment provides a better physical quantification of the earthquake source than magnitude it is not directly measurable, since according to Ben-Zion (1989 and 2001) linear elastic waves generated by a slip source have no information on material properties at the source region itself. Only the product P = $\bar{D}$ A, termed "geometric moment" by King (1978) or "potency P" by Ben.Menahem and Singh (1981), can be determined directly from the zero spectral asymptote of the source in a seismogram, respectively by integrating over the area underneath the restituted broadband displacement P and/or S waveforms recorded in the far-field of the source (e.g., Seidl and Berckhemer, 1982; Seidl and Hellweg (1988; see, e.g., Figs. 3.9, 3.63, 3.65a). The values for the rigidity μ, however, has to be *assumed*. And different authors may assume in their moment calculations different values, e.g., when estimating M_0 for earthquakes in very different seismotectonic environments and at very different source depths in the crust or upper mantle, in continental or oceanic areas. Then earthquakes of volumetrically equal size or potency have different seismic moment. Therefore, Ben-Zion (2001) recommends to convert reported moments to potencies by removing the assumed rigidities in order to make earthquakes sizes geometrically, respectively volumetrically comparable. In practice, however this often meets the difficulty that the rigidities assumed in the calculation of M_0 are often not formally recorded. However, for southern California earthquakes with 1.0 < Ml < 7.0, Ben-Zion and Zhu (2002) demonstrated a proper potency-magnitude scaling.

In a homogeneous half-space M_0 can be determined from the spectra of seismic waves observed at the Earth's surface by using the relationship:

$$M_0 = 4\pi \, d \, \rho \, v^3_{p,s} \, u_0 / R^{p,s}_{\theta,\varphi} \qquad (3.2)$$

with: d - hypocentral distance between the event and the seismic station; ρ - average density of the rock and $v_{p,s}$ - velocity of the P or S waves around the source; $R^{p,s}_{\theta,\varphi}$ - a factor correcting the observed seismic amplitudes for the influence of the radiation pattern of the seismic source, which is different for P and S waves (see Figs. 3.3 and 3.100-3.103), u_0 - the low-frequency level of displacement amplitudes as derived from the seismic spectrum of P or S waves, corrected for the instrument response, wave attenuation and surface amplification. For details see EX 3.4.

According to Aki (1967) a simple seismic shear source with linear rupture propagation shows in the far-field smooth displacement and velocity spectra. When corrected for the effects of geometrical spreading and attenuation we get "source spectra" similar to the generalized ones shown in Fig. 3.5. There the displacement spectral amplitudes have been scaled to the scalar seismic moment M_0 (left) and the related velocity amplitudes to moment rate dM_0/dt (right), respectively. Additionally shown are the bandwidth ranges for measuring the IASPEI standard body wave magnitudes mb and mB(BB) as well as the standard surface-wave magnitudes Ms(20) and Ms(BB) (see IS 3.3). The spectral curves (solid lines) have been calculated on the basis of an ω^{-2} source model (Aki, 1967) in which the moment rate function can be expressed as $\hat{\dot{M}}(f) = (M_o f_c^2)/(f^2 + f_c^2)$ (Houston and Kanamori, 1986; Polet and Kanamori, 2000) with the corner frequency $f_c = c\beta(\Delta\sigma/M_0)^{1/3}$ (Brune, 1970), β the shear-wave velocity near the source (assumed to be 3.75 km/s), c = 0.49 and $\Delta\sigma$ the stress drop in the source. $\Delta\sigma$ has been assumed to be 3 MPa in agreement with Kanamori´s (1977) condition $E_S/M_0 = 5\times10^{-5}$, on which the derivation of the Mw-logM_0 relationship (Hanks and Kanamori, 1979) is based. According to this model, the amplitudes decay is $\sim f^{-2}$ for $f >> f_c$. In real data, however, many kinds of departure from the f^{-2} decay law have been observed. Further, for earthquakes of a given seismic moment, $\Delta\sigma$ may differ by about 3 orders of magnitude (e.g., Choy and Boatwright, 1995) and thus f_c according to the Brune relation by about a factor of 10. Finally, f_c is for P-wave source spectra about $\sqrt{3}$ times larger than for S-wave spectra.

Before discussing the inferences one can draw from *seismic scaling laws*, respectively *source spectra* corrected for propagation effects (geometric spreading and attenuation), such as the ones in Fig. 3.5, we should make clear that details of theoretical "source spectra" depend on the model assumptions of the rupture process. E.g., when the rupture is bilateral, the displacement spectrum of the source-time function drops for $f >> f_c$ proportional to f^{-2}, as in Fig. 3.5. In contrast, for an unilateral rupture, the high-frequency decay is proportional to f^{-3}. The high-frequency drop-off of real spectra typically ranges between about -1 and -3 (e.g., Hartzel and Heaton, 1985; Boatwright and Choy, 1989; Polet and Kanamori, 2000; IS 3.4), depending also on the specific source-time function. But even steeper decays have been observed. On the other hand, when the linear dimensions of the fault rupture differ in length and width then two corner frequencies will occur. Whether the two or three corner frequencies are resolvable will depend on their separation along the spectral axis and the spectral signal-to-noise ratio. In contrast to the smooth theoretical spectral curves in Fig. 3.5 real spectra calculated from noisy records of limited duration and bandwidth from earthquakes with different source-time functions and fault geometries will show fluctuating spectral amplitudes, sometime more than one corner frequency or – more likely - a rather broad range of transition with different slopes from the displacement plateau to the final drop-off. Therefore, real source spectra may not be well matched by such a smooth "average" ω^{-2} source model and not allow to discriminate between different types of rupture propagation and source geometry. Nevertheless, Fig. 3.5 allows us to discus essential differences and

required bandwidth ranges for reasonably reliable measurements of M_0 and E_S, of the related magnitudes Mw and Me or complementary ones, as well as of the derivation of other source parameters of interest.

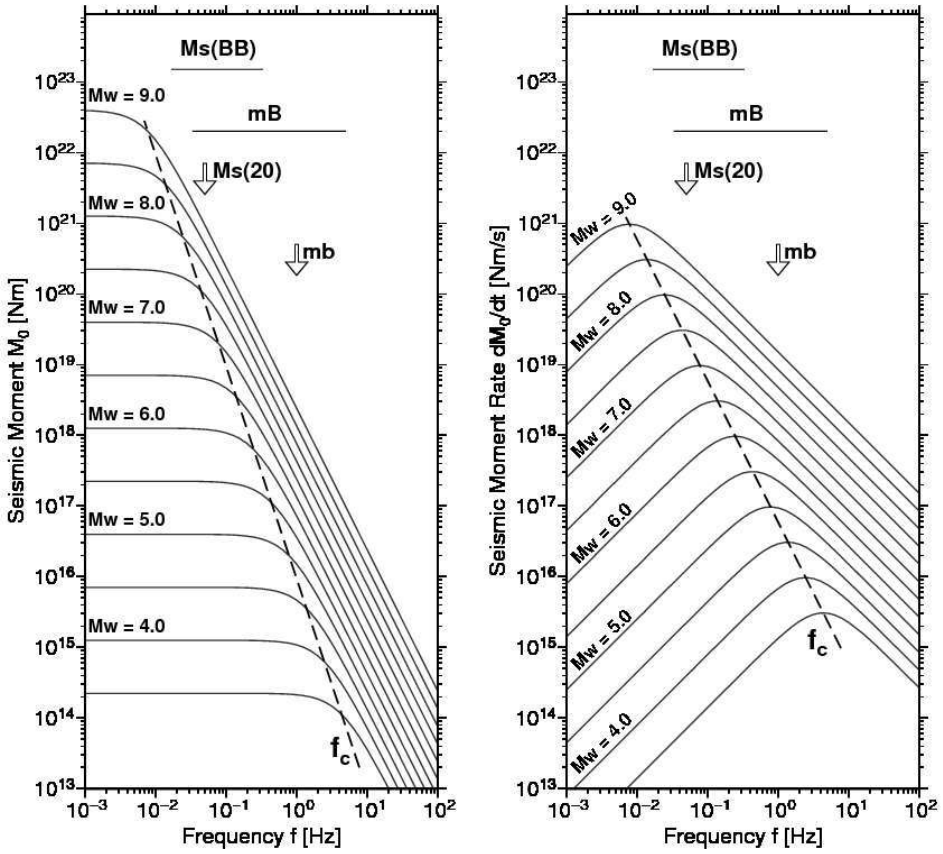

Fig. 3.5 Left: "Source spectra" of ground displacement amplitudes A for an "average" seismic shear source as a function of frequency *f*, scaled to seismic moment M_0 and the equivalent moment magnitude Mw. **Right:** The same as left, but for ground motion velocity amplitudes V, scaled to seismic moment rate and Mw. Note that the maximum of seismic energy $E_S \sim V^2$ is radiated around f_c. The open arrows point to the center frequencies on the abscissa at which the 1 Hz body-wave magnitude m_b and the 20 sec surface-wave magnitude Ms(20), respectively, are determined. The horizontal interval bars mark the range of frequencies within which the maximum P-wave and Rayleigh-wave amplitudes for mB(BB) and Ms(BB) should be measured. For procedure of calculation see text (courtesy of Domenico Di Giacomo, 2008). Copy of Fig. 1 in Bormann et al. (2009, BSSA, Vol. 99, No. 3, p. 1870); © granted by the Seismological Society of America.

With reference to Fig. 3.5, we ask and answer now the following questions:

- What does the shape of the spectra in Fig. 3.5 tell us about the source process?
- Which parameters should accordingly be measured?
- How do they relate to the size, shape, slip and stress drop in the seismic source?
- How do these parameter influence the measurement of magnitudes in different spectral ranges?

The following general features are obvious from Fig. 3.5:

- "Source spectra" are characterized by a "plateau" of constant displacement for frequencies smaller than the "corner frequency" f_c which is inversely proportional to the source dimension, i.e., $f_c \sim 1/L$.
- The decay of spectral displacement amplitude beyond $f > f_c$ is on average approximately proportional to f^{-2}.
- The plateau amplitude increases with seismic moment M_0 and magnitude, while at the same time f_c decreases in the case of the validity of the ω^{-2} model proportional to M_0^{-3} (see Aki, 1967).
- Magnitude estimates of earthquake size are closely related to seismic moment M_0, if the displacement amplitudes are sampled at frequencies smaller than the corner frequency f_c of the source spectrum, i.e., on or near to the low-frequency asymptote plateau of the source spectrum. This can be expected for mb only at moment magnitudes Mw < 5.5 and for $M_S(20)$ at Mw < 8. For larger earthquakes, however, these magnitudes are likely to underestimate moment-related earthquake size, mb much more than Ms(20). In contrast, one can expect that mB(BB) and Ms(BB) cover rather well the range up to Mw ≈ 8. These general rough estimates are supported by empirical data of the average differences between mb, mB, Ms and Mw (see section 3.2.5).
- Since wave energy is proportional to the square of ground motion particle velocity, i.e., $E_S \sim (2\pi f\, u)^2 = (\omega\, u(\omega))^2$, its maximum occurs at f_c. Therefore, for magnitudes to be a good measure of the amount of released seismic energy and thus of the earthquake strength in terms of ground-shaking and damage potential, V_{max} and the related period have to be measured at or near to f_c.
- This is in agreement with the $\log(A/T)_{max}$ input into the classical teleseismic magnitude formulas (see DS 3.1 and sections 3.2.5.11 and 3.2.5.2), provided that no a priori limits for the period range are imposed. The latter, however, is the case for mb and Ms(20), which sample Vmax only in very limited ranges of frequency, not, however, mB(BB) and Ms(BB), which cover the average maxima of the released velocity spectra reasonably well in the magnitude ranges 4 to 8 and 5.5 to 8.5, respectively.
- Good estimates of energy magnitude Me require to integrate squared velocity source spectra sufficiently wide towards both sides of the spectral velocity peak (see Fig. 3.5, section 3.2.7.2 and Bormann and Di Giacomo, 2011).
- measuring displacement amplitudes at f > fc or velocity amplitudes at f < or > fc results in systematic underestimation of either moment or energy related magnitudes, the more the larger the frequencies differ from fc.

The effect of underestimating the magnitude and thus the (dimensional) *size* or (potential shaking) *strength* of the earthquake is often misleadingly termed *magnitude saturation*. More correct would be to speak of a systematic underestimation of a magnitude with respect to a true non-saturating moment or energy related reference magnitude which grows linearly and everywhere with the same slope proportional with $\log M_0$ or $\log E_S$, respectively. The underestimation of a non-reference magnitude is then due to the slower increase of its related measurement amplitudes with growing Mw or Me when they are measured at frequencies outside the displacement plateau or the velocity maximum, respectively. In fact, any conventional magnitude that is measured at a constant period or in a narrow period range, such as Ml, mb, mb(Lg) or Ms_20, features “saturation” as soon as the measured periods fall

below the corner period of the radiated source spectrum or are much smaller than the rupture duration. Yet, for short, we continue to term this effect in the following as the *spectral component of magnitude "saturation"*.

The general shape of the displacement source spectrum in Fig. 3.5 can be understood as follows:

We know from optics that under a microscope no objects can be resolved which are smaller than the wavelength λ of the light with which it is observed. In this case the objects appear as a blurred point or dot. In order to resolve more details, electron microscopes are used which operate with much smaller wavelengths. The same holds in seismology. When observing a seismic source of radius r with wavelengths $\lambda >> r$ at a great distance, one can not derive any information about the details of the source process but only of its overall (integral) features, i.e., one "sees" a *point source*. Accordingly, spectral amplitudes with wavelengths $\lambda >> r$ are constant and form a spectral plateau (if source duration is neglected). On the other hand, wavelengths that have $\lambda << r$ can resolve internal details of the rupture process. In the case of an earthquake they correspond to smaller and smaller elements of the rupture processes or of the fault roughness *(asperities* and *barriers*). Therefore, their spectral amplitude contributions decay rapidly with size and thus related higher frequencies.

Accordingly, the corner frequency, f_c, marks a critical position in the spectrum which is obviously related to the size of the source. According to Brune (1970) and Madariaga (1976), both of whom modeled a circular fault, the corner frequency in the P- or S-wave spectrum, respectively, is $f_{c\ p/s} = c_m\ v_{p,s} / \pi\ r$. In contrast, assuming a rectangular fault, Haskell (1964) gives the relationship $f_{c\ p/s} = c_m\ v_{p,s} / (L \times W)^{1/2}$ with L the length and W the width of the fault. The values c_m are model-dependent constants. Accordingly, the critical wavelength $\lambda_c = v/f_c$, beyond which the source can be realized as a point source only, is $\lambda_c = c_m\ \pi\ r$ or $\lambda_c = c_m\ (L \times W)^{1/2}$, respectively, with different c_m for circular or rectangular faults.

But real fault ruptures may have any other shape which can only be approximated roughly by either a circular fault (more likely for small earthquakes within the brittle fracturing seismogenic zone of the Earth crust) or by a rectangular fault of different *aspect ratio* L/W, which is growing with the magnitude of great earthquakes that rupture the whole width (depth range) of the seismogenic zone and may, therefore, grow further only in L direction. This has consequences for seismic scaling laws for small and large earthquakes [see related discussions and controversies, e.g., Scholz (1982, 1994, 1997) and Wang and Ou (1998) with further related references].

Nevertheless, being aware of the model dependence and inherent uncertainties of seismic scaling laws such as the ones in Fig. 3.5, related rupture models and formulas as given, e.g. by Brune (1970) and Madariaga (1976) allows to roughly estimate the following source parameters by reading the following parameters from seismic source spectra that have been corrected for propagation effects (geometric spreading and attenuation):

- M_0 via Eq. (3.2) when measuring the displacement plateau amplitude u^0 and accounting for the other parameters in that formula;
- Source radius $R \sim 1 / 2\pi\ f_{cp/s}$;
- Area of the assumed circular rupture plane: $A = \pi\ R^2$;

- Average dislocation $\bar{D} = M_0/(\mu A)$ by assuming a reasonable value for rigidity $\mu = v_s^2 \rho$ in the source volume;
- Stress drop $\Delta\sigma = (7/3)M_0/16R^3$ according to Keilis-Borok (1959).

Stress drop means the difference in acting stress at the source region before and after the earthquake. For more details see Figure 10 in IS 3.1. Note, however, that $\Delta\sigma \sim R^{-3}$ and estimates of R not very reliable. Reasons are the relatively large reading errors in f_c plus the model-dependence of R (or other geometric parameter) estimates, which also depend on the assumed *rupture velocity* v_R. Therefore, stress-drop estimates maybe rather uncertain within about an order of magnitude. For more details see EX 3.4 with discussions.

3.1.2.4 The influence of rupture velocity and duration on magnitude estimates

For reducing saturation, *rupture duration*, depending on rupture length and speed, has additionally to be taken into account, especially, when the largest amplitudes of non-dispersive of P-wave trains have to measured. The average rupture duration T_{Rav} increases according to Bormann and Saul (2009a) with magnitude M according to

$$\log T_{Rav} \text{ (in s)} \approx 0.6\ M - 2.8. \qquad (3.3)$$

M means in this relationship the largest measured magnitude, which is for Mw < 6 usually the local magnitude Ml or mb and for larger events Ms or Mw. Relationship (3.3) has been derived by using data published in Olson and Allen (2005) that are based on rupture velocity estimates in Somerville et al. (1999) and scaling relations between rupture length and magnitude published by Wells and Coppersmith (1994), complementing them by some direct rupture duration estimates of recent great earthquakes. This simple average relationship is easy to recall and yields with 0.5 magnitude units increase a doubling of T_{Rav}, e.g., for M = 6 about 6 s, for M = 7 about 25 s, for M = 8 about 100 s, for M = 9 about 400 s, and for M = 10 about 1600 s. The last but one duration figure is close to respective estimates for the somewhat greater Mw9.3 Sumatra-Andaman earthquake of December 26, 2004 by Bormann and Wylegalla (2005), Gusev et al. (2007), Hara (2007), Bormann and Saul (2009b), and Lomax and Michelini (2009a and b, 2011). All these authors,ll with the exception of Gusev et al., describe procedures of non-saturating magnitude estimates in near real-time based on broadband P-wave data and take explicitely rupture duration into account. And the last duration figure of 1600 s agrees well with rupture durations given in Cifuentes and Silver (1989) for the "revised" Mw ≈ 9.9 of the great 1960 Chile earthquake (see discussion in 3.1.1.1).

Average estimates of T_{Rav} according to relationship (3.3) agree within a factor less than two with those that could be estimated from the corner frequencies f_c of the source spectra in Fig. 3.5 as a function of Mw when one assumes an average rupture velocity of about 2.5 km/s. For a given event magnitude, however, depending mainly on variations in stress drop (e.g., Choy and Boatwright, 1995) and rigidity in the source region (for *tsunami earthquakes* see., e.g., Houston, 1999; Polet and Kanamori, 2000), but other factors as well (see 3.1.2.5), true T_R may be a factor of 2 to 3 smaller or larger then T_{Rav} because of related differences in rupture velocity, v_R. v_R may range between about 0.2 and 0.9 times of the shear-wave velocity v_s (Venkataraman and Kanamori, 2004b), or even more than v_s if the hypothesis and still

debated observations of supershear slip pulses with rupture velocities up to 5 km/s holds (e.g., Bouchon and Vallée, 2003). Fig. 3.6 shows an example of very large differences in rupture duration and thus duration of the P-wave trains radiated from events with equal Mw.

If the largest amplitude for magnitude determination is measured only within an a priori fixed limited measurement-time windows after the first body-wave onset that is shorter than the rupture duration, then the required **maximum** amplitude in the whole P-wave train may have been missed and thus mb or mB been underestimated. Since $T_{Rav} > 6$ s for earthquakes with $M > 6$, it is likely that this is indeed the case for such earthquakes when Amax is measured within a time window < 6 s, as it is is common practice at the International Data Center (IDC) of the CTBTO (Comprehensive Test Ban Treaty Organization; see Chapter 17). We term this the *measurement time-window component* of saturation, which adds to the pronounced spectral saturation component of mb. In combination, both component may indeed result in true saturation, as shown in Fig. 3.7 for mb(test). In contrast, the new IASPEI standard mb, which measures always the maximum amplitude within the whole P-wave train, including the range of depth phases, and ending (preferably) before the onset of PP is only reduced by the spectral component of saturation. Yet, standard mb keeps growing up to values of about 7.6 for the largest earthquakes with Mw around 9.

Compared with an earthquake of the same seismic moment or magnitude, the corner frequency f_c of a well contained underground nuclear explosion (UNE) in hard rock is about ten times larger. Accordingly, an UNE produces more high-frequent energy and thus has a larger E_S as compared with an earthquake of comparable mb. Accordingly, mb(IDC) does not underestimate mb even for the largest UNE but only for earthquakes with comparable seismic moment but much smaller corner frequency. Main cause of this difference in E_S and high-frequency content between UNE and earthquakes is that the source *duration* and thus the *rise time,* t_r, to the final level of static displacement is much shorter for explosions (see Fig. 3.4).

Moreover, the shock-wave front of an explosion, which causes the deformation and fracturing of the surrounding rocks and thus the generation of seismic waves, propagates with approximately the P-wave velocity v_p while the velocity of crack propagation along a shear fracture/fault is only about 0.5 to 0.9 of the S-wave velocity, i.e., about 0.3 to 0.5 times that of v_p. Additionally, the equivalent wave radiating surface area in the case of an explosion is a sphere with $A = 4\pi r^2$ and not a plane with $A = \pi r^2$. Accordingly, for equal A the source radius R in the case of an explosion is smaller and thus the related corner frequency larger.

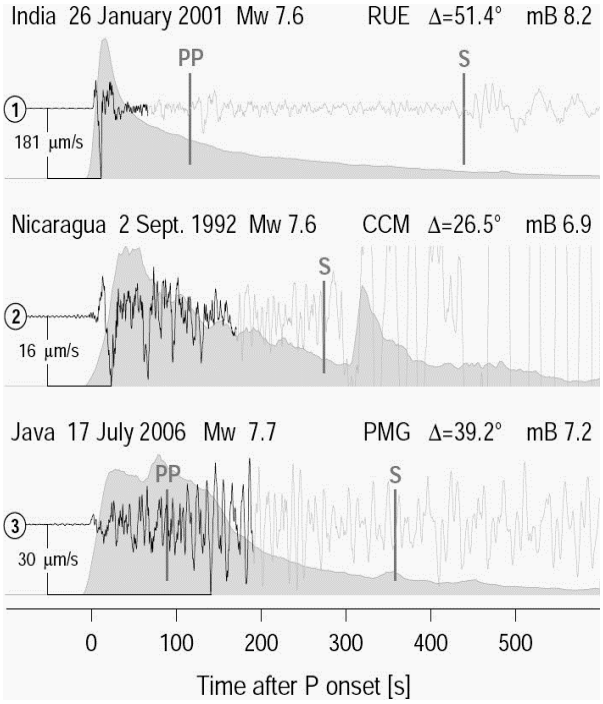

Fig. 3.6 Velocity broadband records of earthquakes with practically identical Mw but very different rupture durations and therefore length of the P-wave trains. Record 2 and 3 are slow tsunami earthquakes. Grey shaded areas: Envelopes of high-frequency (1-3 Hz) filtered BB records. Estimated rupture durations range from about 25 s (record 1) to 190 s (record 3). The average TRav according to Eq. (3.3) for Mw = 7.7 would be 66 s. Figure copied from Figure 2 of Bormann and Saul Bormann et al. (2009, p. 700) with © granted by the Seismological Society of America.

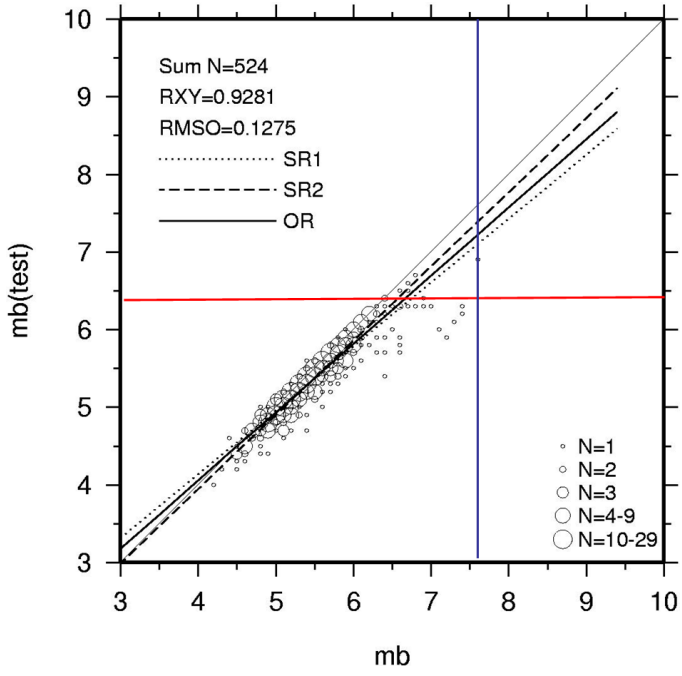

Fig. 3.7 Comparison of mb measured on WWSSN-SP filtered records a) within the first 6 s after the P-wave onset (mb test) and b) within the whole P-wave train according to the new IASPEI standard rules for mb measurement. For instrument response function and measurement rules see IS 3.3. While mb(test) saturates at about 6.4 (**red line**), with early underestimations beginning already at mb > 6, mb itself may grow up to about 7.6 for the greatest earthquakes (**blue line**).RXY = correlation coefficient, RMSO = orthogonal rms error. Figure compiled according to data in Bormann et al. (2009).

3.1.2.5 Factors which influence energy radiation and seismic efficiency

The ratio between radiated seismic energy and seismic moment, E_S/M_0, i.e., the seismic energy radiated per unit of moment release and termed "scaled energy" by Kanamori and Brodsky (2004), would remain constant if a seismic scaling law such as the one in Fig. 3.5, calculated for a specific rupture model with fixed stress drop and rupture velocity, would hold for all earthquakes. In fact, this was assumed by Kanamori (1977) and Hanks and Kanamori (1979) when they developed the moment magnitude scale Mw under the condition of

$$E_S/M_0 = 5 \times 10^{-5} = \text{constant.} \qquad (3.4)$$

This, however, is not the case. According to Wyss and Brune (1968) holds

$$E_S/M_0 = \Delta\sigma/2\mu = \tau_a/\mu \qquad (3.5)$$

with τ_a = *apparent stress*, which can – with Eq. (3.1) - also be written as $\tau_a = E_S/(D \cdot A)$. Thus, τ_a is equivalent to the seismic energy release per unit area of the ruptured surface A and per unit of slip. Since both $\Delta\sigma$ and μ may vary E_S/M_0 is a useful parameter to characterize the dynamic properties of an earthquake (Aki, 1966; Wyss and Brune, 1968).

$\Delta\sigma$ and thus τ_a may vary by about 3 to 4 orders of magnitude (e.g., Abercrombie, 1995; Choy and Boatwright, 1995). Accordingly, the difference between energy magnitude Me and moment magnitude Mw may reach 1 m.u. and even more (e.g., Kirby and Choy, 2004; Di Giacomo et al., 2010a and b; Bormann and Di Giacomo, 2011; Figure 5 in IS 3.5).

In the case of tsunami earthquakes unusually low rigidity values μ in the rupturing source volume, i.e., along near surface faults in shallow dipping subduction zones with water saturated ocean sediments (Houston, 1999; Polet and Kanamori, 2002) may be the reason for their exceptionally slow ($v_R \approx 0.2\ v_s$) and unusually long lasting ruptures. The ratio E_S/M_0 of *tsunami earthquakes* ranges between about 2×10^{-6} and almost 10^{-7} and the related values of $\Theta = \log E_S/M_0$ – termed "slowness parameter" by Okal and Talandier (1989) - between -5.7 and -7 (Lomax and Michelini, 2007). Note that observed global average values of Θ for earthquakes with magnitudes larger than 5.5 range between -4.7 and -4.9 (Choy and Boatwright, 1995; Choy et al., 2006; Weinstein and Okal, 2005), whereas the Kanamori (1977) condition in Eq. (3.4) corresponds to $\Theta_K = -4.3$.

According to Kanamori (1972) tsunami earthquakes are characterized by generating a much larger tsunami than it would be expected from their seismic moment. The reason is that according to Eq. (3.1) for a measured M_0 the product $\bar{D} \times A$ is strongly underestimated when instead of the much smaller real rigidity in the rupture area the much larger Kanamori (1977) value for average crust-upper mantle condition is assumed (Hirshorn and Weinstein, 2009). The latter, however, is routine in M_0 calculations.

In this context we have to clarify that Kanamori (1977), when introducing the relationship

$$W = W_0\ (= E_S) = (\Delta\sigma/2\mu)\ M_0 \qquad (3.5)$$

based it on a simplified assumptions of the rupture process which did not account for the total energy balance. According to Kanamori and Brodsky (2004) the total change in potential energy W due to the rupture process has to be written as

$$\Delta W = E_S + E_G + E_H \tag{3.6}$$

with E_G = fracture energy and E_H = energy dissipated as heat due to kinematic friction on the fault and generated sound. Eq. (3.5), however, holds only when both $E_G = E_H = 0$, i.e., when neglecting both the fracture energy and the dissipated energy in the total energy budget. Yet, the radiated energy is less, at least (in the case with no dissipation)

$$E_S = (\Delta\sigma/2\mu)\, M_0 - E_G. \tag{3.7}$$

Husseini (1977) introduced the term of *radiation efficiency*, which for radiated seismic energy would read:

$$\eta_R = E_S/(E_S + E_G) \tag{3.8}$$

According to Kanamori (2006) this can also be written as

$$\eta_R = (2\mu/\Delta\sigma)\, (E_S/M_0). \tag{3.9}$$

Yet, then it becomes clear that $E_S = (\Delta\sigma/2\mu)\, M_0$ holds only for $\eta_R = 1$, i.e., when all energy available for strain release is converted into seismic wave energy, and no energy E_G is dissipated during fracturing. This, however, is not the case. η_R ranges between about 0,02 and (by definition) <1. For some earthquakes, however, $\eta_{R\eta}$ >1 were computed, either due to incorrect data correction, model inaccuracies or even real supershear slip-pulses (Bouchon and Vallée, 2003; Venkataraman and Kanamori, 2004b).

Moreover, it has to be made clear that radiation efficiency according to Eq. (3.8) should not be mistaken as the better known seismic efficiency, which additionally accounts for energy dissipation losses due to frictional heat and sound, E_H, i.e.,

$$\eta = E_S/(E_S + E_G + E_H). \tag{3.10}$$

Thus, seismic efficiency is significantly smaller than η_R, being in the order of 1 % or less [see compilation in Bormann (1966), or Griggs (1961) and Pasečnik et al. (1960)].

In the above discussion we have focussed on the influence of variations in stress drop, respectively of $\Delta\sigma/\mu$ on the ratio E_S/M_0, although we mentioned already related velocity variations. According to Newman and Okal (1998), even in the case of a kinematically simple rupture model this ratio is controlled by five dimensionless factors, namely the ratios (with different exponent) between (1) S- versus P-wave velocity with exp5, (2) rupture length versus rupture duration and Rayleigh-wave speed with exp3, (3) rupture velocity v_R versus shear-wave velocity v_s with exp 3, (4) the aspect ratio rupture width versus rupture length with exp 2, and (5) fault slip versus rupture width. Yet, the first factor is, for most rise and fall times of the source time function and for a Poissonian solid about 0.5. The second factor, however, depends on the *directivity* of the rupture which will be 1 for unilateral rupture but may increase up to 8 for a symmetric bilateral rupture. However, Venkataraman and Kanamori (2004a) showed for a suite of earthquakes that the directivity corrections were less than a factor three and for dip-slip earthquakes with rupture propagation along strike even less

than two at teleseismic distances. The third facture expresses the slowness of rupture, which may vary between about 0.5 for a "regular" ratio $v_R/v_s \approx 0.8$ and about 0.01 and 0.03 for very slow earthquake ruptures with $v_R/v_s \approx 0.2$-0.3 and $v_R \approx 1$ km/s, slowed down by subducted sedimentary material along the fault zone (Kikuchi and Kanamori, 1995). The fourth factor, the squared aspect ratio, might be around ¼ for most rupture geometries, but could be significantly smaller for ribbon-like ruptures on strike-slip faults and in the case of great earthquakes which brake the whole brittle-fracturing seismogenic zone of the lithosphere and can then grow further only in strike direction. And the last factor depends on the geometry model of the source. Thus we see that a great many of factors, most of them not directly measurable, may influence the "scaled energy" or slowness parameter Θ of individual earthquakes.

In an effort to reduce this complexity down to the most important factors one finds that according to Kostrov (1966) and Eshelby (1969) the radiation efficiency of transverse shear cracks is

$$\eta_R \approx (v_R/v_s)^2. \tag{3.11}$$

When inserting (3.11) into (3.9) and resolves it for the ratio E_S/M_0 one gets according to Bormann and Di Giacomo (2011):

$$E_S/M_0 = \eta_R \cdot (\Delta\sigma/2\mu) \approx (v_R/v_s)^2 \cdot (\Delta\sigma/2\mu). \tag{3.12}$$

Although being model-dependent (and other models are likely to produce other relationships), Eq. (3.12) illustrates a trade-off between variations in stress drop, rigidity, rupture velocity and shear-wave velocity in controlling the ratio E_S/M_0 and thus, the relationship between Mw and Me. Since, however, stress-drop estimates, despite their principle uncertainty, show the largest variability with 3 to 4 orders of magnitude, most of the observed differences in scaled seismic energy released by individual earthquakes may be attributable to differences in stress drop, the more so, since $\Delta\sigma/2\mu$ in the source volume seem to set the stage for v_R/v_s, i.e., the two terms in (3.12) are not fully independent.

Finally, on should note in this context that a thorough investigation by Oth et al. (2010) of 1,826 earthquakes with M(JMA) magnitudes (see Eq. 3.34) between 2.7 and 8 throughout Japan led to the conclusions that:

- the calculated source spectra can be well characterized by the omega-square model (i.e., as in Fig. 3.5);
- on average self-similar scaling over the entire magnitude range holds, with median stress drops of 1.1 and 9.2 MPa for crustal and subcrustal events, respectively;
- the **ratio E_S/M_0**, as theoretically expected if the omega-square model is valid, does not depend on magnitude and that the observed large scatter is mainly related to the scatter in stress drop.

3.1.2.6 Parameters which describe and control the source mechanism

Assuming that the earthquake rupture occurs along a planar fault surface the orientation of this plane in space can be described by three angles: *strike* ϕ (0° to 360° clockwise from north), *dip* δ (0° to 90° against the horizontal) and the direction of slip on the fault by the *rake*

angle λ (- 180° to + 180° against the horizontal). Figures 5 and 6 in exercise EX 3.2 define these angles and Figures 3 as well as the solution figures show how to determine them from a stereographic (Wulff) net or equal area (Lambert-Schmidt) projection using observations of first motion polarities. It can be shown that a rupture along a plane perpendicular to the fault plane and with a slip vector perpendicular to the slip on the first plane causes an identical angular distribution of first motions. Therefore, on the basis of first motion analysis alone one can not decide which of the two planes is the truly acting one. For more detailed discussion on this see section 2.4 in IS 1.1.

Note that in the case of a shear model the fault-plane solution (i.e., the information about the orientation of the fault plane and of the fault slip in space) forms, together with the information about the static seismic moment M_0 (see 3.1.2.3), the seismic moment tensor M_{ij} (see Equation (25) in IS 3.1). Its principal axes coincide with the direction of the pressure axis, P, and the tension axis, T, associated with fault-plane solutions. However, they should not be mistaken for the principal axes σ_1, σ_2 and σ_3 (with $\sigma_1 > \sigma_2 > \sigma_3$) of the acting stress field in the Earth which is described by the stress tensor. Only in the case of a fresh crack in a homogeneous isotropic medium in a whole space with no pre-existing faults or zones of weakness and vanishing internal friction is P in the direction of σ_1 while T has the opposite sense of σ_3. P and T are perpendicular to each other and each one forms, under the above conditions, an angle of 45° with the two possible conjugate fault planes (*45°-hypothesis*) which are in this case perpendicular to each other (see Figs. 3.99-3.101, 3.106 and 3.111 in sections 3.4.1 and 3.4.2). The orientation of P and T is also described by two angles each: the *azimuth* and the *plunge*. They can be determined by knowing the respective angles of the fault plane (see EX 3.2). If the above model assumptions hold true, one can, knowing the orientation of P and T in space, roughly estimate the orientations of σ_1 and σ_3. Most of the data used for compiling the global stress map (Zoback, 1992; Zoback and Zoback, 2002) come from earthquake fault-plane solutions calculated under these assumptions.

In reality, the internal friction of rocks is not zero. For most rocks this results, according to Andersons´s (1951) theory of faulting in the formation of conjugate pairs of faults which are oriented at about ± 30° to σ_1. In this case, the directions of P and T, as derived from fault-plane solutions, will not coincide with the principal stress directions. Moreover, near the surface of the Earth one of the principal stresses is almost always vertical. In the case of a horizontal compressive regime, the minimum stress σ_3 is vertical while σ_1 is horizontal. This results, when fresh faults are formed in unbroken rock, in thrust faults dipping about 30° and striking parallel or anti-parallel to σ_2. In an extensional environment, σ_1 is vertical and the resulting dip of fresh normal faults is about 60°. When both σ_1 and σ_3 are horizontal, vertical strike-slip faults will develop, striking with ± 30° to σ_1. But most earthquakes are associated with the reactivation of pre-existing faults rather than occurring on fresh faults.

Since the frictional strength of faults is generally less than that of unbroken rock, faults may be reactivated at angles between σ_1 and fault strike that are different from 30°. In a pre-faulted medium this tends to prevent breaking of a new fault. Accordingly, there is no straightforward way to infer from the P and T directions determined for an individual earthquake the directions of the acting principal stress. On the other hand, it is possible to infer the regional stress based on the analysis of many earthquakes in that region since the possible suite of rupture mechanisms activated by a given stress regime is constrained. This method aims at finding an orientation for σ_1 and σ_3 which is consistent with as many as possible of the

actually observed fault-plane solutions (e.g., Gephart and Forsyth, 1984; Reches, 1987; Rivera, 1989).

3.1.3 Mathematical, physical and geological representation of earthquakes

It is beyond the scope of the NMSOP to dwell on the physical and geological models of seismic sources and their mathematical representation. There exists quite a number of good text books on these issues (e.g., Aki and Richards, 1980 and 2002; Ben-Menahem and Singh, 1981 and 2000; Das and Kostrov, 1988; Scholz, 1990 and 2002; Lay and Wallace, 1995; Udías, 1999) as well as review papers on the physics and dynamics of earthquakes (e.g., Madariaga and Olsen, 2002; Teisseyre and Majewski, 2002; Kanamori and Brodsky, 2004; Madariaga, 2011), on earthquakes as a complex system (Turcotte and Malamud, 2002) and quite many on earthquake geology and mechanics in Lee et al. (2002).

However, many of these texts are rather elaborate and more research oriented. Therefore, we have added to this Manual a more concise introduction into the theory of source representation in IS 3.1. It outlines how the basic relationships used in practical applications of source parameter determinations have been derived, on what assumptions they are based and what their limitations are. We have also added some exercises (EX 3.2-3.4) based on very simplified model assumptions and try to give with the following short section at least some idea of earthquakes as complex activated fault systems in real Earth.

3.1.4 Empirical analysis of rupture geometry, kinematics and dynamics in space and time

So far we have mainly considered simple earthquake models applied routinely in seismological practice to derive suitable parameters for describing the size and behavior of faulting of earthquakes and to some extent also of explosions. In actuality, earthquakes do not rupture along perfect planes, nor are their rupture areas truly circular or rectangular. They do not occur in homogeneous rock, nor do they slip just unilaterally or bilaterally. All these features are at best first order approximations or simplifications to the truth in order to make the problem mathematically and with limited data tractable. Real faults show jogs, steps, branching, splays, etc., both in their horizontal and vertical extent (Fig. 3.8). Such jogs and steps, depending on their severity, are impediments to smooth or ideal rupture, as are bumps or rough features along the contacting fault surfaces. More examples can be found in Scholz (1990 and 2002). Since these features exist at all scales, which implies the self-similarity of fracture and faulting processes and their fractal nature (Turcotte,1997; Turcotte and Malamud, 2002), this will necessarily result in heterogeneous dynamic rupturing and finally also in rupture termi nation.

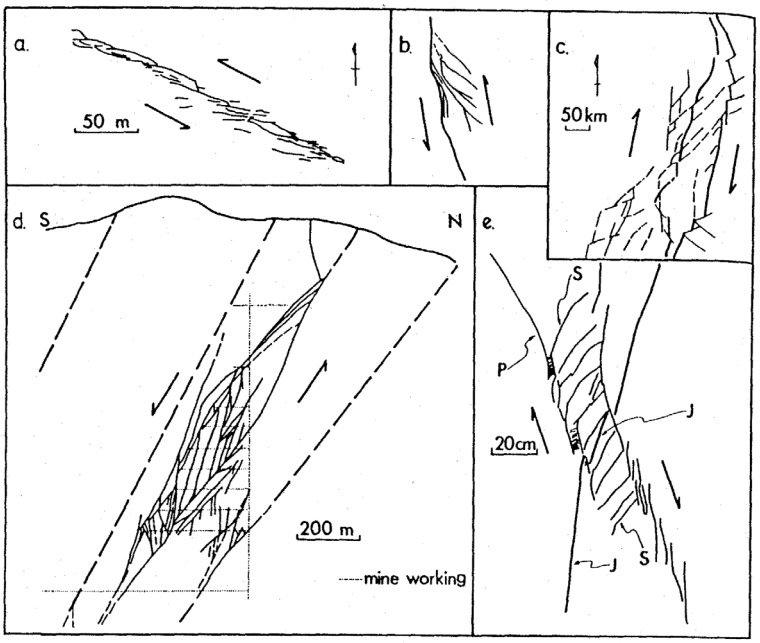

Fig. 3.8 Several fault zones mapped at different scales and viewed approximately normal to slip (from Scholz, The mechanics of earthquakes and faulting, 1990, Fig. 3.6, p. 106; with permission of Cambridge University Press).

Fig. 3.9 illustrates the complexity of earthquake ruptures over time as a common feature. Each event, often occurring as a multiple rupture process, seems to have its own "moment-rate fingerprint". Only in recent decades dense strong-motion networks been fortuitously deployed in the very source region of a strong earthquake. Strong-motion records enable a detailed analysis of the rupture history in space and time using the moment-rate density.

As an early example, Fig. 3.10 depicts an inversion of data by Mendez and Anderson (1991) for the rupture process of the 1985 Michoacán, Mexico earthquake. Shown are snapshots, 4 s apart from each other, of the dip-slip velocity field. The contours represent dip-slip velocity at 5 cm/s interval, the cross denotes the NEIC hypocenter. Three consecutively darker shadings are used to depict areas with dip-slip velocities in the range: 12 to 22, 22 to 32, and greater than 32 cm/s, respectively. Abbreviations used: t - snapshot time after the origin time of the event, h - depth, D - distance in strike direction of the fault. One recognizes two main clusters of maximum slip velocity being about 120 km and 30 s apart from each other. The related maximum cumulative displacement was more than 3 m in the first cluster and more than 4 m in the second cluster at about 55 km and 40 km depth, respectively. About 90 % of the total seismic moment was released within these two main clusters which had a rupture duration each of only 8 s while the total rupture lasted for about 56 s (Mendez and Anderson, 1991). Although the overall rupture of the 1985 Michoacán, Mexico, earthquake was unilateral, both segments of main moment release expanded also bilaterally both in strike and vertical direction.

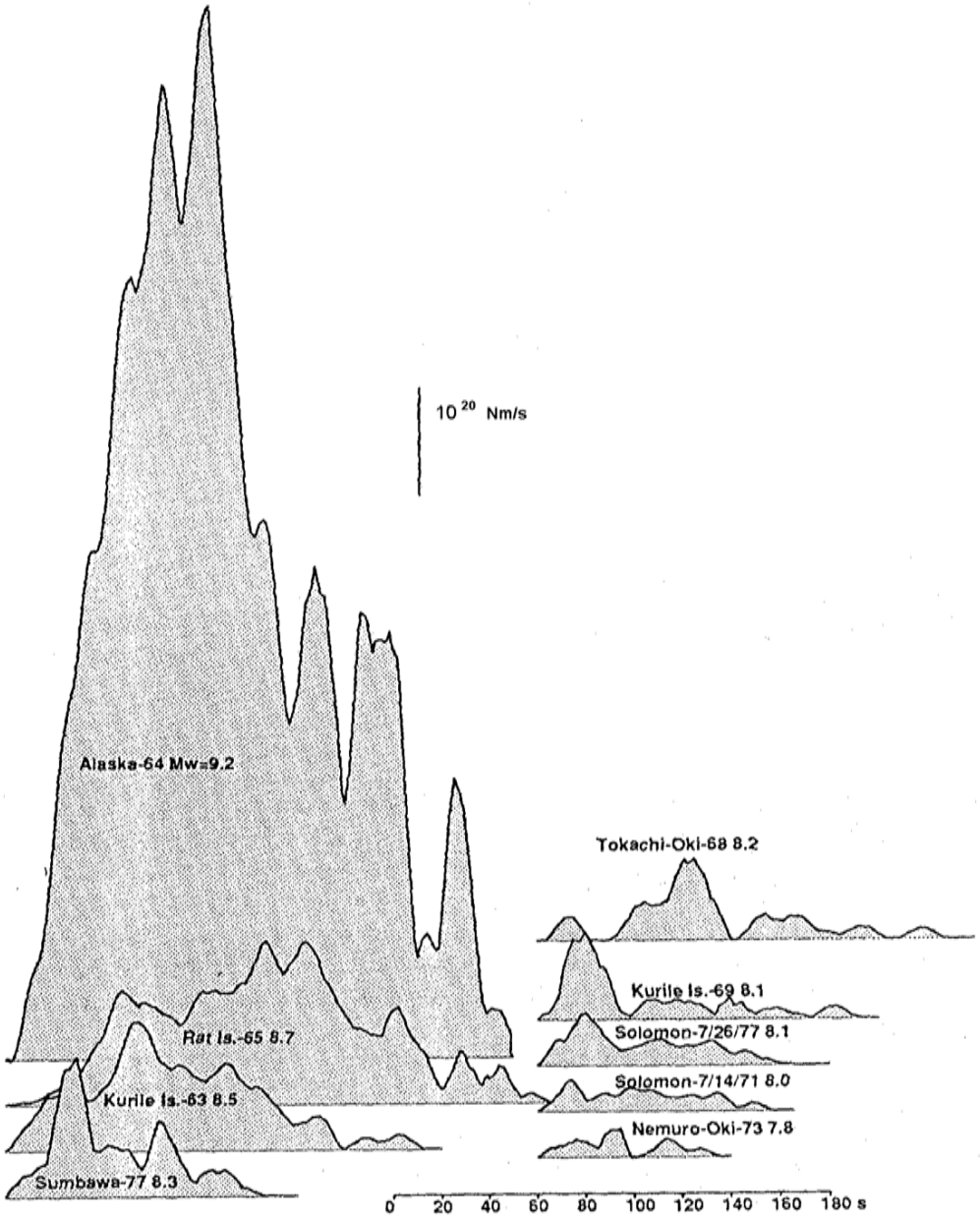

Fig. 3.9 Moment-rate (source time) functions for the largest earthquakes in the1960s and 1970s as obtained by Kikuchi and Fukao (1987) (modified from Fig. 9 in Kikuchi and Ishida, Source retrieval for deep local earthquakes with broadband records, *Bull. Seism. Soc. Am.*., Vol. 83, No. 6, p. 1868, 1993, © Seismological Society of America).

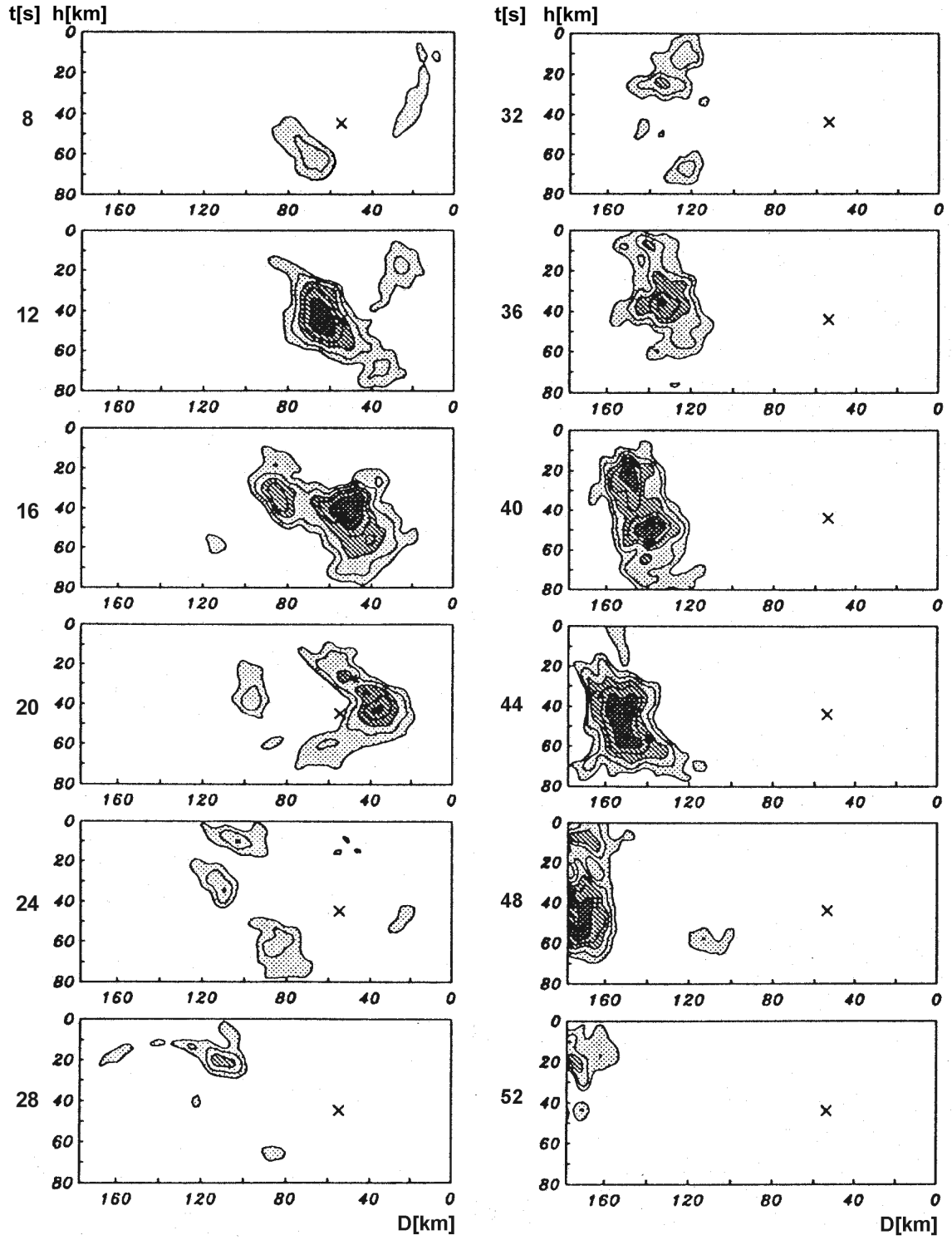

Fig. 3.10 Snapshots of the development in space and time of the inferred rupture process of the 1985 Michoacán, Mexico, earthquake. See text for discussion (redrawn and modified from Mendez and Anderson, The temporal and spatial evolution of the 19 September 1985 Michoacán earthquake as inferred from near-source ground-motion records, *Bull. Seism. Soc. Am.,* Vol. 81, No. 3, Fig. 6, p. 857-858, 1991; © Seismological Society of America).

Realizing in Fig. 3.10 the very large differences in moment release over the total rupture area one really has to question the relevance for seismic hazard assessment of the average point source displacement in relationship (3.1) for the scalar seismic moment, but also of the concept of the low resolution overall "centroid" time (usually calculated at half-time of the source-time function) and of the related centroid epi- and hypocenter. Calculating the rupture velocity from the ratio of total rupture length L / total rupture duration T_R , average slip and/or stress drop would yield a misleading picture which by no means reflects the kinematic and dynamic complexity of such complex earthquakes. Gross (1996) referred to the fact that inversions of waveforms in large earthquakes have consistently shown that the spatial distribution of moment release in real earthquakes is very irregular and not at all like the smooth distribution that one would expect if the classical theory of homogeneous elastic solids according to Kanamori and Anderson (1975) would hold for all earthquakes. This led Koyama (1985) to develop a theory of incoherent fracture of random fault heterogeneities and to discuss from this perspective the physical basis of earthquake magnitudes and the relationships of Ms on the one hand and of the maximum short-period P-wave magnitude mb* on the other hand (Koyama and Zheng, 1985) with ruptured fault area.

Gross (1996) proposed other heterogeneous slip models. They have the advantage of not only accounting for heterogeneous slip of large earthquakes due to the breaking of major asperities but also of predicting complex sources for small events, i.e., earthquake ruptures with dimensions less than the thickness of the seismogenic zone of brittle fracturing. On the other hand, for small earthquakes, the Gross models resemble classical crack theory by yielding also the well established area scaling relationship between average slip S and rupture area A, which is $S \propto \sqrt{A}$.

The rupturing of local asperities produces most of the high-frequency content of earthquakes. Accordingly, they contribute more to the cumulative seismic energy release than to the moment release. This is particularly important for engineering seismological assessments of expected earthquake effects. Damage to (predominately low-rise) structures is mainly due to frequencies > 2 Hz. They are grossly underestimated when analyzing strong earthquakes only on the basis of medium and long-period teleseismic records or when calculating model spectra assuming smooth (average point source) rupturing along big faults of large earthquakes.

First results of a detailed investigation of rupture propagation by means of a close-by linear accelerometer line to the 1979 Ms = 6.9 Imperial Valley, California, earthquake were published by Spudich and Cranswick (1984). They showed that the observed high-frequency ground motions (accelerations up to 1.9 g were measured during this earthquake!) originate at irregularly distributed regions on the fault surface or are due to variable rupture velocity or both.

Two years later, Goldstein and Archuleta (published 1991) made first direct measurements of 2-D earthquake rupture propagation using the SMART 1 array in Taiwan. They showed that the Jan. 29, 1981 Ml = 6.3 Taiwan earthquake ruptured unilaterally up-dip and towards the west on a 60° dipping and 109° striking reverse fault. They calculated a fault length of 25 ± 18 km and a rupture duration of $T_R = 9.4 \pm 3.6$ s. The latter is in perfect agreement with formula (3.3) for average magnitude-dependent rupture duration. In contrast, the overall rupture duration of the Nov. 14, 1986, the Ml = 7.0 Hualien, Taiwan, earthquake, has been about 35 s, about 10 s longer than expected according to formula (3.3), however, the source-time function showed two distinct sub-events with the by far dominating first one breaking

within some 12 s only (see Fig. 3.11 above). These strong-motion data highlighted that realistic strong-motion modeling requires much more detailed information about the source process than long-period moment tensor point source solutions can provide. Moreover, a detailed analysis of teleseismic data allowed to prove for the Hualien earthquake a clear migration in both horizontal and vertical directions of the patches of main seismic moment release (Hwang and Kanamori, 1989; Fig. 3.11 below), thus confirming the complexity of the source process both in space and time.

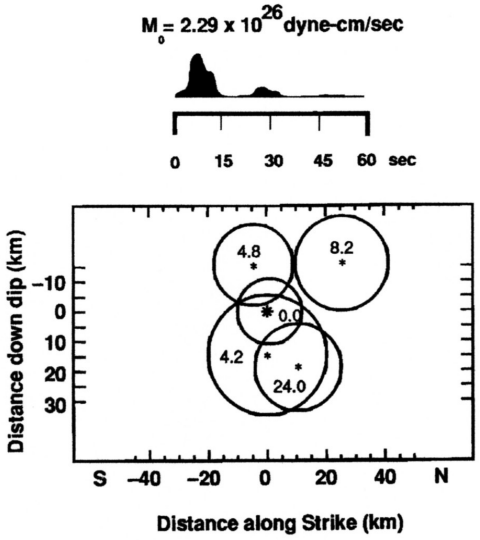

Fig. 3.11 Source-time function (top) and spatial and time migration of areas of main moment release (bottom) of the 1986 Ml = 7.0 Hualien earthquake, Taiwan according to Hwang and Kanamori (1989), derived from teleseismic observations. Circle radii are proportional to the released seismic moment, numbers in the middle of the circles give the time after origin time in seconds. (Copy of Fig. 12 in Goldstein and Archuleta, J. (1991), Geophys. Res., 96, p. 6197; © with kind permission of American Geophysical Society).

After the devastating great 2004 Mw9.3 Sumatra-Andaman earthquake Krüger and Ohrnberger (2005) used the large aperture (500 km by 700 km) German Regional Seismic Network (GRSN) as a broadband array to track the propagation of this some 1200 km long rupture from a distance of about 9000 km (Fig. 3.12). An animation or the rupture tracking can be viewed and downloaded from section 2.5 in IS 1.1.

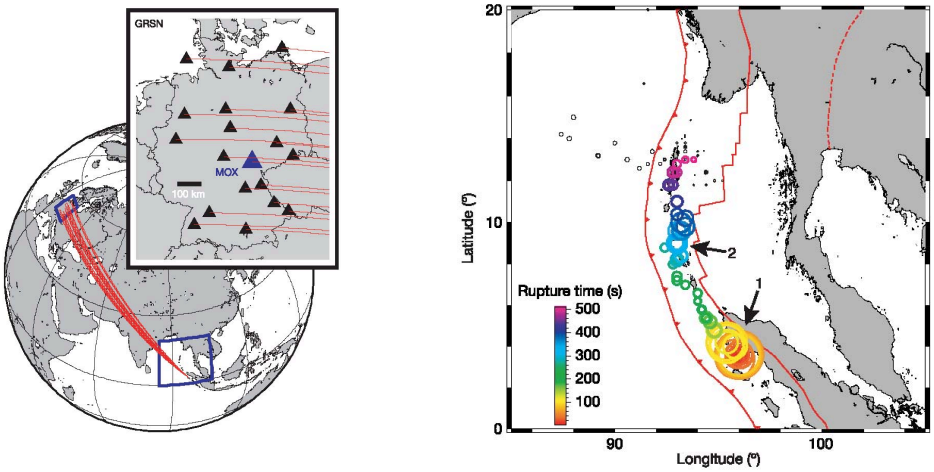

Fig. 3.12 Left: Source area of the great 2004 Sumatra-Andaman earthquake and great circle paths of from the epicenter location to the German Regional Seismic Network. **Right**: Map of maxima of seismic energy released during the earthquake in space and time from below upward. Circle radii are proportional to released seismic energy, circle colors are coded to rupture time. (Compiled from Figures 1 and 3 of Krüger and Ohrnberger (2005), Nature, 435, p. 937 and 938; © granted with kind permission by Nature Publishing Group).

The following conclusions could be drawn from this teleseismic array rupture tracking:

- The propagating rupture front could be tracked over a total length of 1,150 km;
- The average rupture speed was estimated to be 2.3 – 2.7 km/s but with slightly higher velocity on the southern segment (2.4-2.8 km/s) as compared to the northern branch of the rupture (2.1-2.4 km/s);
- The total rupture duration was at least 430, probably between 480 and 500 s;
- During the first 60 s, the position of the energy maximum did not move, which hints to a phase of bilateral growth of the rupture surface, whereas the remaining rupture was unilateral towards the north, with a second center of major energy release about 600 km NNW of the epicenter, which developed some 300 s after rupture initiation;
- The rupture did not progress farther to the south-southeast at the beginning of the rupture. This may indicate that the rupture front hit a barrier in this direction, which broke, in fact three months later during the March 28, 2005, Mw = 8.5 earthquake;
- The complete estimate of source extension by means of rupture tracking of such a great event could be made available within about 30 min when using teleseismic station networks or large aperture arrays.

It should be noted, however, that first rough estimates of several of these aspects of the rupture process as a function of time, such as rupture duration, rise time and identifying time segments of increased energy radiation could already be derived within about 10 to 15 min. after origin time by processing and plotting single station records according to the procedure described by Bormann and Saul (2009b) for a fully automatic determination of the cumulative body-wave magnitude mBc (for details see section 3.2.8.1). Applied to a record of the great Sumatra-Andaman earthquake at epicentral distance of 52.7° (Fig. 3.13) one realizes that

- initial rupture episodes around 30 s and 100 s after rupture initiation correspond already to sub-event broadband body-wave magnitudes mB around 8;
- the second episode released by far most of the energy of the whole rupture process;
- other, although less pronounced, episodes around 300s and 400 s after rupture initiation resulted in similarly large sub-event mB values (up to 8.3);
- thus the source-time function of the earthquake was rather asymmetric and therefore could not be approximated well by a symmetric triangular moment-rate function as prescribed by the routine Harvard/GCMT moment tensor procedure;
- the latter point explains the initial underestimation of Mw(GCMT) = 8.9 and 9.0, respectively, for this earthquake. This could only be corrected by a later offline multiple CMT source analysis, which approximated the source-time function by trapezoid source-time functions of 5 individual sources, yielding then an overall Mw = 9.3 (Tsai et al., 2005);
- cumulative mBc may yield the same value straight away as the asymptotic "saturation" value of the real-time development of mBc as a function of time;
- the rupture duration can be estimated reasonably well from the average amplitude envelops of several high-frequency (1-3Hz) filtered records, when they fall below 40% of their maximum amplitudes (corresponding to 16% of the maximum energy release), even after the arrival of stronger but in high-frequency content depleted secondary arrivals after P (see also Kanamori and Helmberger, 2005);
- thus estimated rupture duration of 540 s for the Sumatra-Andaman earthquake estimate agrees well (within about 10%) with similar independent estimates (e.g., Lomax, 2005; Kanamori and Helmberger, 2005).

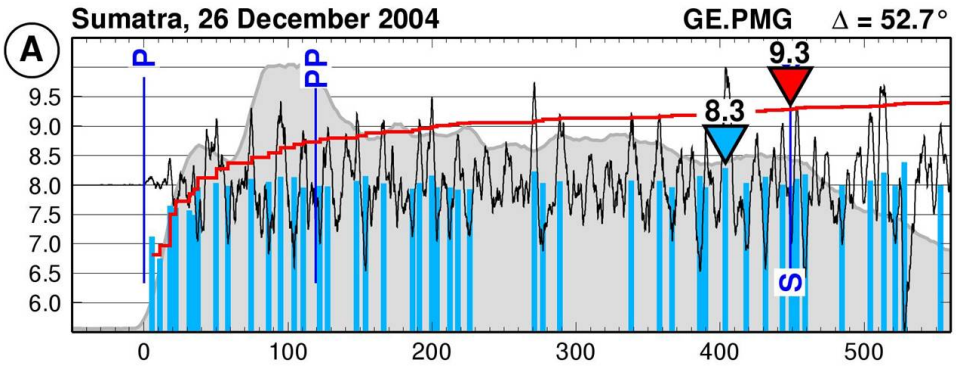

Fig. 3.13 Velocity-proportional recording of the great Sumatra-Andaman earthquake at station PMG, processed with the mBc procedure originally proposed by Bormann and Khalturin (1975) and developed as a fully automated procedure by Bormann and Saul (2009b). Blue bars correspond to mB values of major amplitude onsets according to the condition $V_i \geq 0.6V_{max,t}$ with $V_{max,t}$ being the maximum velocity amplitude up to the time t, with the largest single amplitude mB marked by a blue triangle. The red curve shows the development of mBc with time and the red triangle the mBc values reached prior to the onset of S. The grey shaded area marks the high-frequency P-wave envelop (courtesy of J. Saul, 2009)

With respect to source complexity and related energy radiation of this gigantic earthquake Kanamori (2006) added, that the ratio $E_S/M_0 = 4.6\times10^{-6}$ was slightly smaller than that for other large subduction-zone earthquakes and that the average radiation efficiency was only 0.16, which ranges between regular earthquakes and tsunami earthquakes. Yet this values changed with time during the rupture process, being initially 0.21 for the southern Sumatra segment and dropping down to 0.053 for the Nicobar segment in the North. The very low value hints to large amounts of energy dissipation associated with water-filled thick sediments.

For another very interesting example of rupture tracking (with animation) of the rather complex Mw8.8 Chile earthquake of 2010 see section 2.6 or IS 1.1. The tracking was made by using records of US Array and permanent California network stations. The rupture was neither unilateral nor bilateteral but “jumped” several times forth and back in several sub-events covering the whole subsequent aftershock area, which extended over some 600 km.

Nowadays, modern geodetic data may provide very useful independent information on seismic moment tensor, rupture mechanism and magnitude, even in the early warning context, e.g., for real-time predictions of the amplitudes of local tsunami, which strongly depend on the rupture model and source-time function. Sobolev et al. (2006 and 2007) demonstrated how reliable input data for the simulation process, which are for local tsunami mainly the mean and maximum fault slip rather than seismic moment, could be acquired by GPS-Shield arrays that are strategically deployed on off-shore islands in front of the mainland coasts at risk. But a GPS-Shield array or even a single GPS station can also resolve seismic moment and thus moment magnitude of the rupture with very high accuracy, even if it is located several 100 km away from the trench. As a minimum, the GPS-Shield arrays placed along the trench will allow to estimate M_0 and Mw for the corresponding sections of a rupture zone (partial magnitude) within just a few minutes of an earthquake.

Additionally, imaging synthetic aperture satellite radar interferometry (INSAR) (nowadays allows to derive reliable information about the areal distribution of surface deformation patterns that have been produced by earthquakes, even if the faults did not rupture through the surface. The interferometric fringe patterns are particularly well developed in vegetation-less arid areas (see Fig. 3.14).

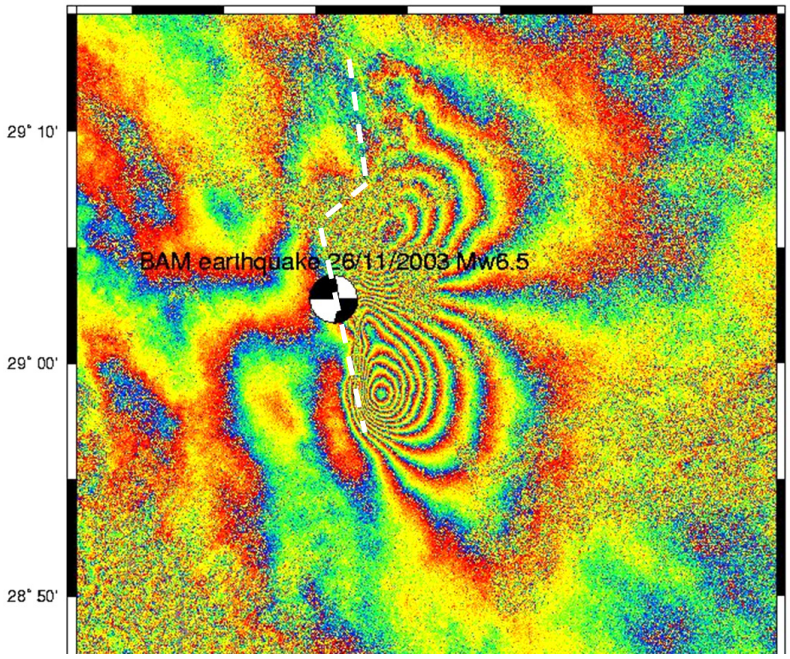

Fig. 3.14 INSAR Fresnell-zone patterns from the 26 December 2003, Mw 6.5 Bam earthquake, Iran, together with the teleseismic point-source fault-plane solution and the more detailed approximate fault trend (broken white line) with a step-over towards NE as inferred from the Fresnell-zone patterns. The maximum surface uplift and subsidence (in the line of sight to satellite) are 30 cm and 18 cm, respectively, the largest inferred fault slip 270 cm and the estimated total rupture length about 24 km. More than 80% of the seismic moment was released from the southern 13 km long fault segment. This preliminary figure has kindly be made available by R. Wang, GFZ German Research Centre for Geosciences. For more detailed final results and interpretation see Wang et al. (2004).

3.1.5 Summary and conclusions

The detailed understanding and quantification of the physical processes and geometry of seismic sources is one of the ultimate goals of seismology, be it in relation to understanding tectonics, improving assessment of seismic hazard or discriminating between natural and anthropogenic events. Earthquakes can be quantified with respect to various geometrical and physical parameters such as time and location of the (initial) rupture and orientation of the fault plane and slip, fault length, rupture area, amount of slip, magnitude, seismic moment, radiated energy, stress drop, duration and time-history (complexity) of faulting, particle velocity, acceleration of fault motion etc. It is impossible, to represent this complexity with just a single number or a few parameters.

There are different approaches to tackle the problem. One aims at the detailed analysis of a given event, both in the near- and far-field, analyzing waveforms and spectra of various kinds of seismic waves in a broad frequency range up to the static displacement field, complemented by field investigations into macroseismic effects and surface expressions of fault rupture. Such detailed and complex investigations usually require a lot of time and effort. They may be feasible only for selected important events and are usually beyond the scope of routine seismological observatory practice. Nonetheless, we have deliberately dwelled on the issue of source complexity and the multitude of parameters required for describing them adequately. Because many of these parameter have to be derived by detailed analysis of high quality data collected by seismological observatories in a wider sense, permanent or temporary ones, physical or virtual seismic networks (Chapter 8) or seismic arrays (Chapter 9) of local, regional or even global scale or range of operation (see Chapter 8), measuring weak or strong motions.

With dense strong-motion networks deployed in source areas of potentially large earthquakes, as they become now increasingly available in many regions at risk, detailed pictures of both the fracture process may already be obtained in near real-time. They are of greatest importance for more reliable shake-map calculations, and thus for a better guidance of relief efforts and as empirical references of utmost importance for both earthquake engineers, land-use planners and others involved in disaster preparedness and mitigation (see Chapter 15).

The second, more simple approach is usually taken at seismological observatories and data centers for the routine analysis of mass data. They describe the seismic source only by a limited number of parameters such as the origin time and (initial rupture) location, magnitude, intensity or acceleration of measured ground shaking, sometimes complemented by fault-plane solutions. These parameters can easily be obtained and have the advantage of rough but quick information being given to the public and concerned authorities. Furthermore, this approach provides standardized data for comprehensive earthquake catalogs which are fundamental for other kinds of research such as earthquake statistics and seismic hazard assessment. But we need to be aware that these simplified, often purely empirical parameters can not give a full description of the true nature and geometry, the time history nor the energy release of a seismic source. In the following we will focus on the most common procedures in routine seismological practice.

3.2 Magnitude of seismic events (P. Bormann)

3.2.1 History, scope and limitations of the magnitude concept

The concept of *magnitude* was introduced by Richter (1935) to provide an objective instrumental measure of the size of earthquakes. The term magnitude was recommended to Richter by H. O. Wood in distinction to the name *intensity* scale, which is based on the assessment and classification of shaking damage and human perceptions of shaking and thus depends on the distance and depth of the seismic source (see Chapter 13). In contrast, the magnitude M uses instrumental measurements of the ground motion adjusted for epicentral distance and source depth. Standardized instrument characteristics were originally used to avoid instrumental effects on the magnitude estimates. Thus it was hoped that M could provide a single number to measure earthquake size which is related to the seismic energy, E_S. However, as outlined in 3.1 above, such a simple empirical parameter is not directly related to any physical parameter of the source. Rather, the magnitude scale aims at providing a quickly

determined simple " ... parameter which can be used for first-cut reconnaissance analysis of earthquake data (catalog) for various geophysical and engineering investigations; special precaution should be exercised in using the magnitude beyond the reconnaissance purpose" (Kanamori, 1983).

In the following we will use mainly the magnitude symbols, sometimes with slight modification, as they have historically developed and are still predominantly applied in common practice. However, as will be shown later, such “generic” magnitude symbols are often not explicit enough as to recognize on what type of records, components and phases these magnitudes are based. This requires more “specific” magnitude names where higher precision is required (see IS 3.2). Moreover, in order to assure in future a unique nomenclature, at least for the recently recommended IASPEI standards for widely used magnitudes (see IASPEI 2005 and 2011 as well as IS 3.3), we will use this new nomenclature only when the respective new procedures and so derived data are presented in the following.

The original Richter magnitude, ML or M_L, was based on maximum amplitudes measured on records of the standardized short-period Wood-Anderson (WA) seismometer network in Southern California that are displacement-proportional at periods less than 0.8 s. Such records were suitable for the classification of local shocks in that region. In the following we will name it Ml (with “l” for “local”) in order to avoid on the one hand confusion with more specific names for magnitudes from surface waves where the phase symbol L stands for unspecified long-period surface waves (e.g., in MLV or MLH), but also, in order to differentiate between local magnitudes scales in general with often unknown scaling, respectively calibration, to the Southern California standard, and those which have been derived and properly scaled according to the new IASPEI recommendations, which are written ML or M_L, respectively.

Gutenberg and Richter (1936) and Gutenberg (1945a, b and c) then extended the magnitude concept so as to be applicable to ground motion measurements from medium- and long-period seismographic recordings of both surface waves (written Ms or M_s) and different types of body waves (mB or m_B) in the teleseismic distance range. For the magnitude to be a better estimate of the seismic energy Es, they proposed for mB to divide the measured displacement amplitudes by the associated periods to obtain ground velocities and presented in Gutenberg and Richter (1956) the first energy-magnitude relationship log Es = 2.4 mB – 1.2 (when Es is given in Joule). Although they tried to mutually scale the different types of magnitudes in order to match at certain magnitude values, it was realized that these scales are only imperfectly consistent with each other. Therefore, Gutenberg and Richter (1956a and b) provided correlation relations between various magnitude scales (see 3.2.9.2).

After the deployment of the World Wide Standardized Seismograph Network (WWSSN) in the 1960s it became customary to determine the body-wave magnitude only on the basis of short-period narrow-band vertical component P-wave recordings only. This short-period body-wave magnitude was termed mb (or m_b). The introduction of mb increased the inconsistency between the magnitude estimates from body and surface waves. The main reasons for this are:

- different magnitude scales use different periods and wave types which carry different information about the source process and the radiated source spectra;

- the spectral amplitudes radiated from a seismic source increase linearly with its seismic moment for frequencies $f < f_c$ (f_c – corner frequency). This increase with moment, however, is reduced for $f > f_c$ (see Fig. 3.5). This changes the balance between high- and low-frequency content in the radiated source spectra as a function of event size;

- the maximum seismic energy is released around the corner frequency of the displacement spectrum because this relates to the maximum of the ground-velocity spectrum (see Fig. 3.5). Accordingly, M, when supposed to be a measure of the seismic energy released, strongly depends on the position of the corner frequency in the source spectrum with respect to the pass-band of the seismometer used for the magnitude determination;

- for a given level of long-period displacement amplitude and thus seismic moment M_0, the position of the corner frequency is mainly controlled by the stress drop in the source (see section 3.1.2.5). Accordingly, high stress drop results in the excitation of more high frequencies (Fig. 3.15) and thus earthquakes with equal Mw may have rather different energy magnitudes Me or short-period magnitudes such as mb or Ml.

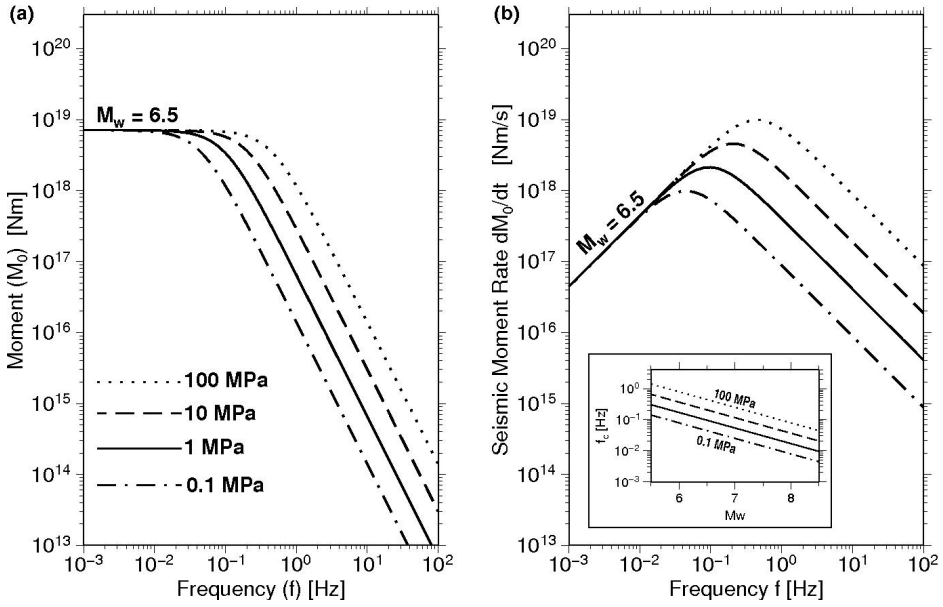

Fig. 3.15 (a) Far-field displacement and (b) velocity source spectra scaled to seismic moment and moment rate, respectively, for a model earthquake with Mw = 6.5 but different stress drop $\Delta\sigma$ in units of MPa. The spectra were calculated based on the model assumptions explained for Fig. 3.5. The inset in Fig. 3.16(b) shows the variation of the corner frequency f_c obtained according to the Brune (1970) equation $f_c = c\ v_s\ (\Delta\sigma/M_0)^{1/3}$ in a wider range of Mw for varying $\Delta\sigma$ in increments of one order between 0.1 and 100 MPa. (Copy of Fig. 2, p. 415 in Bormann and Di Giacomo 2011: The moment magnitude Mw and the energy magnitude Me: common roots and differences. J. Seismology, **15** (2), 411-427; © Springer Publishers).

- seismographs with different transfer functions sample the ground motion in different frequency bands with different bandwidth. Therefore, no general agreement of the magnitudes determined on the basis of their records can be expected;

- additionally, band-pass recordings distort the recording amplitudes of transient seismic signals, the more so the narrower the bandwidth is. This can not be fully compensated by correcting only the frequency-dependent magnification of different seismographs based on their amplitude-frequency response. Although this is common seismological practice in order to determine so-called "true ground motion" amplitudes for magnitude calculation, it is not fully correct. The reason is that the instrument magnification or amplitude-frequency response curves are valid only for steady-state oscillation conditions, i.e., after the decay of the seismograph's transient response to an input signal (see section 4.2 in Chapter 4). True ground motion amplitudes can be determined only by taking into account the complex transfer function of the seismograph (see Chapter 5) and, in the case of short transient signals, by signal restitution in a very wide frequency band (Seidl, 1980; Seidl and Stammler, 1984; Seidl and Hellweg, 1988). Only recently a calibration function for very broadband P-wave recordings has been published (Nolet et al., 1998), however it has not yet been widely applied, tested and approved (see section 3.2.6.1).

Efforts to unify or homogenize the results obtained by different methods of magnitude determination into a common measure of earthquake size or energy have generally been unsuccessful (e.g., Gutenberg and Richter, 1956a; Christoskov et al., 1985). Others, aware of the above mentioned reasons for systematic differences, have used these differences for better understanding the specifics of various seismic sources, e.g., for discriminating between tectonic earthquakes and underground nuclear explosions on the basis of the ratio mb/Ms. Duda and Kaiser (1989) recommend the determination of different spectral magnitudes, based on measurements of the spectral amplitudes from one-octave bandpass-filtered digital broadband velocity records (see section 3.2.6.1).

Another effort to provide a single measure of the earthquake size was made by Kanamori (1977). He developed the seismic moment magnitude Mw. It is tied to Ms but does not saturate for big events because it is based on seismic moment M_0, which is determined via the asymptotic plateau of low-frequency spectral displacement amplitudes for $f << f_c$. This level increases linearly with M_0. According to Eq. (3.1), M_0 is proportional to the average static displacement and the area of the fault rupture and is so a good measure of the total deformation in the source region. On the other hand it is (see the above discussion on corner frequency and high-frequency content) neither a good measure of earthquake size in terms of seismic energy release nor a good measure of specifying seismic hazard since most earthquake damage is usually related to medium and low-rise structures with eigenfrequencies $f > 0.5$ Hz (i.e., lower than about 20 stories) and mainly caused by high-frequency strong ground motion. Consequently, there is no single number parameter available which could serve as a good estimate of earthquake "size" in all its different aspects.

What is needed in practice are at least two parameters to characterize roughly both the size and related hazard of a seismic event, namely M_0 and f_c or Mw together with mb or Ml (based on short-period measurements), respectively, or a comparison between the moment magnitude Mw and the energy magnitude Me (e.g., Choy and Kirby; Bormann and Di Giacomo, 2011; and IS 3.5 by G. Choy in this Manual). Me can today be determined from direct energy calculations based on the integration of digitally recorded waveforms of broadband velocity (Seidl and Berckhemer, 1982; Berckhemer and Lindenfeld, 1986; Boatwright and Choy 1986; Kanamori et al. 1993; Choy and Boatwright 1995) (see section 3.2.7.2 and IS 3.6).

Despite their limitations, common magnitude estimates have proved to be suitable also for getting, via empirical relationships, quick but rough estimates of other seismic source parameters such as the seismic moment M_0, stress drop, amount of radiated seismic energy E_S, length L, radius r or area A of the fault rupture, as well as the intensity of ground shaking, I_0, in the epicentral area and the probable extent of the area of felt shaking (see sections 3.2.6.6 and 3.3.4).

Magnitudes are also crucial for the quantitative classification and statistical treatment of seismic events aimed at assessing seismic activity and hazard, studying variations of seismic energy release in space and time, etc. Accordingly, they are also relevant in earthquake prediction research. All these studies have to be based on well-defined and stable long-term data. Therefore, magnitude values – notwithstanding their inherent systematic biases as discussed above - have to be determined over decades and even centuries by applying rigorously clear and well documented stable procedures and well calibrated instruments. Any changes in instrumentation, gain and filter characteristics have to be precisely documented in station log-books or event catalogs and data corrected accordingly. Otherwise, wrong conclusions may be drawn from research based on incompatible data.

Being aware, on the one hand, of the inherent problems and limitations of the magnitude concept in general and specific magnitude estimates in particular and, on the other hand, of the urgent need to strictly observe reproducible long-term standardized procedures of magnitude determination, we will review below most of the magnitude scales applied in seismological practice. We will then introduce the newly recommended IASPEI measurement standards for some of the widely used magnitude scales. The have been outlined in more detail and commented with respect to their relationship to the classical magnitude scales in IS 3.3. An older comprehensive review of the complex magnitude issue was published by Båth (1981), the most recent condensed ones were authored by Bormann and Saul (2009a) and Bormann (2011). Various special volumes with selected papers from symposia and workshops on the magnitude problem appeared in Tectonophysics (Vol. 93, No.3/4 (1983); Vol. 166, No. 1-3 (1989); Vol. 217, No. 3/4 (1993). Yet, in the light of the newly recommended IASPEI standard procedures aimed at reducing procedure-dependent inconsistencies and the arguments and data provided in sections 3.1.2, 3.2.2, IS 3.3 and by Bormann et al. (2009), these earlier publications should be read with critical caution.

3.2.2. General assumptions and definition of magnitude

Magnitude scales are based on a few simple assumptions, e.g.:

- for a given source-receiver geometry "larger" events will produce wave arrivals of larger amplitudes at the seismic station. The logarithm of ground motion amplitudes A is used because of the enormous variability of earthquake generated amplitudes;
- magnitudes should, as preferred by Gutenberg when proposing the mB scale, be a measure of radiated seismic energy and thus be proportional to the velocity of ground motion, i.e., to A/T with T as the period of the considered wave;
- the decay of ground displacement amplitudes A with epicentral distance Δ and their dependence on source depth h, i.e., the effects of geometric spreading and attenuation of the considered seismic waves, is known at least empirically in a statistical sense. It can be

compensated for by a calibration function $\sigma(\Delta, h)$. The latter is the log of the inverse of the reference amplitude $A_0(\Delta, h)$ of an event of zero magnitude, i.e., $\sigma(\Delta, h) = -\log A_0(\Delta, h)$;

- the maximum value $(A/T)_{max}$ measured on the recorded waveform radiated by a point source of a seismic phase for which $\sigma(\Delta, h)$ is known should provide the best and most stable estimate of the event magnitude;
- regionally variable preferred source *directivity* and/or focusing/defocusing conditions, which may be significant especially in the case of surface waves, may be corrected by (a) regional source correction term(s), C_r, and the influence of local site effects on amplitudes (which depend on local crustal structure, near-surface rock type, soft-soil cover and/or topography) may be accounted for by a station correction, C_S, which is assumed not to depend on azimuth.

Accordingly, the general form of all magnitude scales based on measurements of ground *displacement amplitudes* A_d and periods T is:

$$M = \log(A_d/T)_{max} + \sigma(\Delta, h) + C_r + C_S. \quad (3.13)$$

Problem 1: Calibration functions used in common practice do not consider a frequency dependence of $\sigma(\Delta, h)$

Theoretical calculations by Duda and Janovskaya (1993) for different attenuation models and by Di Giacomo et al. (2008) for P waves, based on the assumption of Q values that do not depend on frequency, show that differences in $A(\Delta,T)$ may become > 0.6 m.u. for T < 3 s, however they are < 0.2 for T > 4 s and thus they are more or less negligible for magnitude determinations in the medium- and long-period range. Yet, magnitude determinations based on the measured ratio A/T, respectively A x f, largely compensate for the frequency-dependent attenuation of A. Accordingly, A/T based magnitudes are more stable in a wider range of periods than A based magnitudes.

In section 3.2.5.2 we will show that the differences in magnitude estimates between short-period mb, when A is measured as the maximum amplitude in the whole P-wave train, and the more long-period magnitude estimates (mB and Ms) can fully be explained by differences in the frequency at which the amplitudes are measured with respect to the corner frequency of the radiated source spectrum (see Figs. 3.5 and 3.15). We term this effect the *spectral component of saturation*. Accounting additionally for excessively large attenuation differences at higher frequencies, as proposed by some of the models, would result in even larger differences between teleseismic mb, mostly measured at 0.5 to 2 Hz, mB (mostly measured between 0.03 Hz < f < 0.3 Hz) and Ms measured around 20 s period. Therefore, the assumption of frequency-dependent Q according to the absorption model of Liu et al. (1976) seems better to explain both the differences in mb and mB as well as field observations by Der et al. (1982). For the time being, this relaxes the necessity to introduce into the general magnitude formula (3.13) an additional frequency-dependent attenuation term, neither for the two standard body-wave magnitudes nor for the broadband surface-wave magnitude Ms(BB), until better empirical data become available. Yet, this matter requires further studies.

Problem 2: $(A/T)_{max}$ or (A_{max}/T)?

For ease of record analysis it has become widespread practice to measure the easily recognizable largest record amplitude with its period T, to correct it for the period-dependent displacement response and only then to determine the ratio A_{dmax}/T. This, however, may not be the real $(A_d/T)_{max}$ intended by Gutenberg as a measure of maximum ground motion velocity and thus a close estimator of the radiated seismic energy. Especially, when T is measured in the period range of already steeply dropping amplification of the response curve differences in magnitude estimates may then reach several tenth of magnitude units with respect to the correct procedure (m.u.). This has been identified at the NEIC as a major problem when measuring in records of the WWSSN-SP type (see Fig. 3.19 below) the largest P-wave amplitude at period between about 2 to 3 s. The average deviations as compared to network averages may then reach about +0.5 m.u. (see Fig. 3.16), also when measuring at periods around 0.3 s, which is, however, rarely the case. This lead to the agency decision to calculate mb only from amplitudes measured at periods T < 2 s instead of up to < 3 s, as recommended by the classical mb measurement standard. The reason is that correcting the measured trace amplitudes for the period-dependent instrument response may in the range of the very strong decay of the WWSSN-SP response with 3rd order for periods larger than about 1.5 s yield much too large ground amplitudes at already slightly too large measured periods.

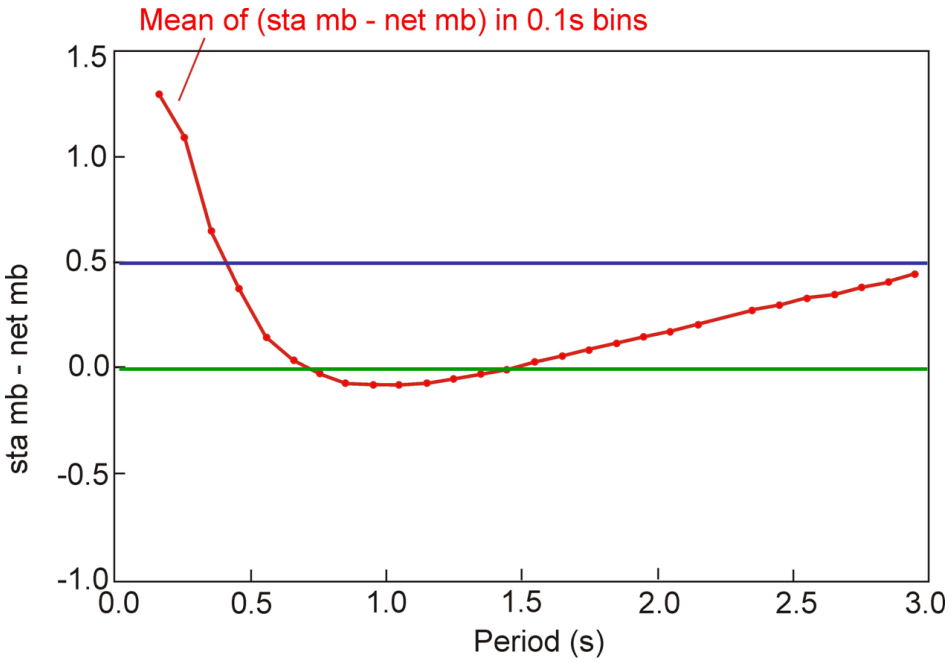

Fig. 3.16 Mean difference between individual station mb and network mb in 0.1 m.u. bins as determined by the NEIC of the US Geological Survey as a function of period at which the maximum amplitude A for mb has been measured (simplified redrow from a Figure by J. W. Dewey et al., 2011).

Although not yet fully understood in detail, this problem can obviously be reduced by measuring instead of Amax on the WWSSN-SP filtered record trace the largest velocity amplitude $V_{max} = 2\pi(A/T)_{max}$ in the time-differentiated WWSSN-SP record trace (see, e.g., Fig. 3.46).. One reason seems to be that - in comparison to WWSSN-SP records – their time-derivatives are more high-frequency with more harmonically looking oscillations and easier

to identify related maximum peak-to-trough deflections that really relate to $(A/T)_{max}$. In contrast, WWSSN-SP records tend to be more complex, making it sometimes more difficult to properly read the period which relates to the largest trace amplitude, respectively to the proper $(A/T)_{max}$. This may, as in the case of Fig. 3.17, result in overestimating the T related to the largest trace amplitude and thus in strong overestimation of the ground motion amplitude A and thus mb. Another reason may be that the ground velocity magnification of the WWSSN-SP response decays only with the 2nd order towards longer periods. This reduces the adverse effect of measurement errors in T when converting the measured velocity trace amplitude into ground velocity amplitude.

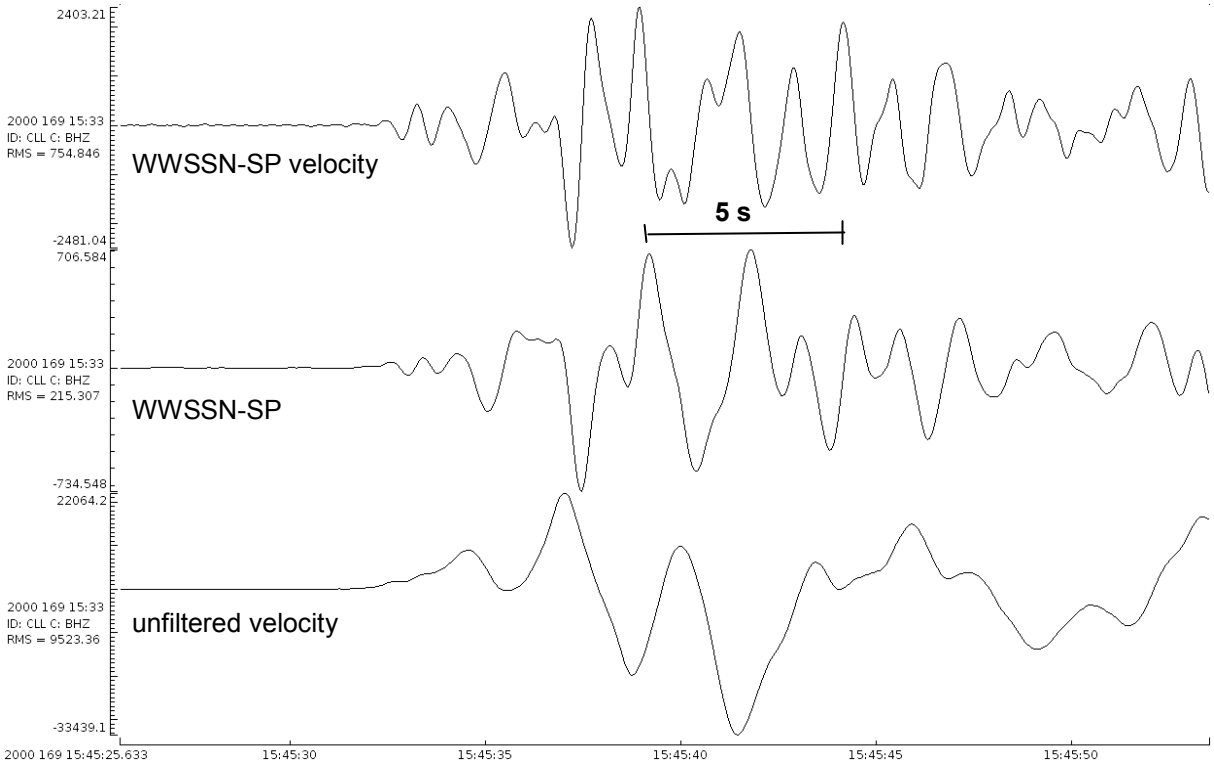

Fig 3.17 Comparison of a P waveforms in an unfiltered velocity broadband record (bottom), in the respective WWSSN-SP simulated record (middle), and as a WWSSN-SP velocity trace. Figure amended according to a record plot kindly provided by J. Saul, 2012.

Fig. 3.18a plots the difference $mb(V_{max})$ - $mb(A_{max}/T)$ for a test data set, both measured automatically. The cluster of strongly negative residuals between -0.4 and -0.65 m.u. relates to standard mb values measured at periods between 2.1 s and 2.8 s. For shorter periods the deviations between these two versions of mb measurement have been generally less than 0.2 m.u. with an average absolute deviation of only 0.07 m.u., but 0.11 m.u., when the outliers are included. The mean deviation is about -0.02 with the outliers and slightly positive, + 0.03 m.u., without them. This make $mb(V_{max})$ measurements a strong candidate procedure that holds promise to yields with greater ease (no period measurement required) on average mb values that are compatible with standard mb yet with greater stability and reduced data scatter. Further studies and documentation on this problem are encouraged.

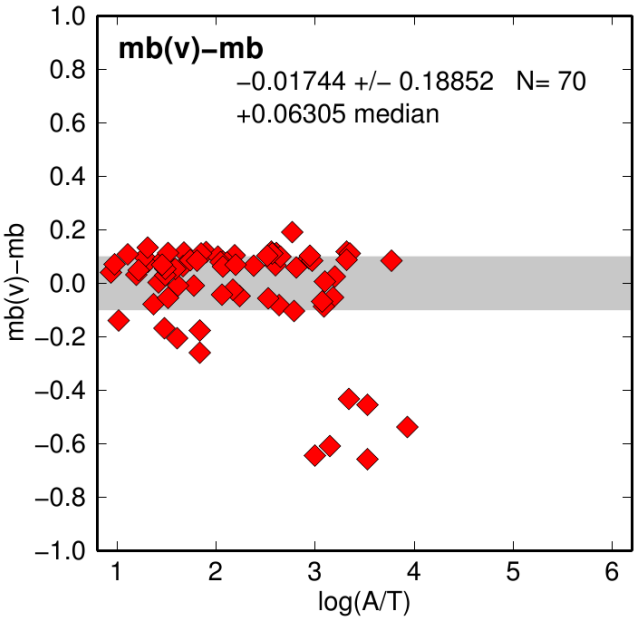

Fig. 3.18a Difference between automatically measured mb values based on measuring the maximum velocity amplitude V/2π on time differentiated WWSSN-SP filtered traces minus mb based on A/T measurement in a wide range of log(A/T) of 4 magnitude units. Note the strong outliers despite generally good agreement between these two ways. For explanation see text. (Figure by courtesy J. Saul, GFZ Potsdam).

As one step in this direction, Alberto Michelini from the Istituto Nazionale di Geofisica e Volcanologia, Rome, Italy, compared on the request of the Editor for 1155 earthquakes between February 1st, 2012, and January 28th, 2013, mb(INGV), which is in fact an WWSSN-SP based mb(V_{max}), with mb(USGS), which is supposed to be a IASPEI standard mb. The results have been plotted in Fig. 3.18b, One recognizes that the two magnitudes agree on average for the overwhelming majority of data with mb(USGS) < 6.0 better than 0.1 m.u., zet the difference grows with magnitude up to about 0.3 m.u. The average difference as well as the median of mb(USGS)-mb(INGV) is 0.06 m.u., the standard deviation ±0.174 m.u. and the average absolute deviation 0.145 m.u.

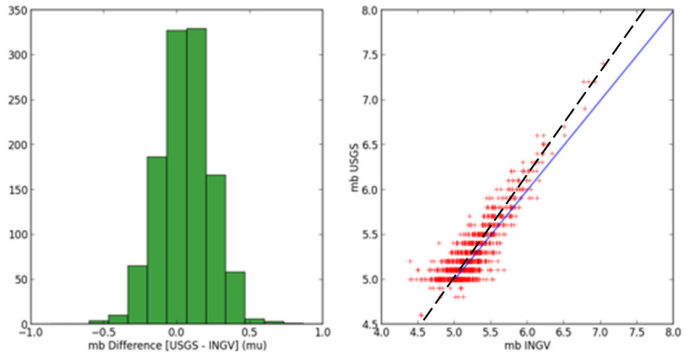

Fig. 3.18b **Left:** Histogram of the difference mb(USGS)-mb(INGV); **right:** data plot of mb(USGS) over mb(INGV) for 1155 earthquakes with 4.5 < mb(USGS) < 7.5. The blue line is the 1:1 relationship, the broken black line an eye fit. Figure by courtesy of Alberto Michelini, INGV (2013).

3.2.3 General rules and procedures for magnitude measurement

3.2.3.1 General procedures when working with analog data or on digital screen plots

Magnitudes can be determined on the basis of Eq. (3.13) by reading the displacement amplitudes A_d and their related periods T for calculating $(A/T)_{max}$ for body waves (e.g., P, S, PP) or surface waves (LQ or Lg, LR or Rg) for which calibration functions for either vertical (V) and/or horizontal (H) component records are available. If the period is measured on a seismogram recorded by an instrument whose response is in the considered period range already proportional to velocity, then $(A_d/T)_{max} = A_{vmax}/2\pi$, i.e., the measurement can be directly determined from the maximum trace amplitude of this wave or wave group with only a correction for the velocity gain. In contrast, with displacement proportional records one may not know with certainty where $(A/T)_{max}$ is largest in the displacement waveform. Sometimes smaller amplitudes but associated also with shorter periods may yield larger $(A/T)_{max}$. In the following we will always use A for A_d, and V for A_v, if not otherwise explicitely specified.

In measuring A and T from seismograms for magnitude determinations and reporting them to national or international data centers, **the following definitions and respective instructions** given in the Manual of Seismological Observatory Practice (Willmore, 1979) as well as in the recommendations by the IASPEI Commission on Practice from its Canberra meeting in 1979 (slightly modified and amended below) **should have been observed in the past:**

- The trace amplitude B of a seismic signal on a record is defined as its largest peak (or trough) deflection from the base-line of the record trace.
- For many phases, surface waves in particular, the recorded oscillations are more or less symmetrical about the zero line. B should then be measured either by direct measurement from the base-line or - preferably - by halving the peak-to-trough deflection (Figs. 3.19 a and c - e). For phases that are strongly asymmetrical (or clipped on one side) B should be measured as the maximum deflection from the base-line (Fig. 3.19 b).
- The corresponding period T is measured in seconds between those two neighboring peaks (or troughs) - or from (doubled!) trace crossings of the base-line - where the amplitude has been measured (Fig. 3.19);
- The trace amplitudes B measured on the record should be converted to ground displacement amplitudes A in nanometers (nm) or some other stated SI unit, using the A-T response (magnification) curve Mag(T) of the given seismograph (see Fig.3.20); i.e., A = B/Mag(T). (**Note:** In most computer programs for the analysis of digital seismograms, the measurement of period and amplitude is done automatically after marking the position on the record where A and T should be determined).
- Amplitude and period measurements from the vertical component (Z = V) are most important. If horizontal components (N - north-south; E - east-west) are available, readings from both records should be made at the same time (and noted or reported separately) so that the amplitudes can be combined vectorially, i.e., $A_H = \sqrt{(A_N^2 + A_E^2)}$.
- When several instruments of different frequency response are available (or in the case of the analysis of digital broadband records filtered so as to match different standard responses), A_{max} and T measurements from each should be reported separately and the type of instrument used should be stated clearly (short-, medium- or long-period,

broadband, Kirnos, Wood-Anderson, etc., or related abbreviations given for instrument classes with standardized response characteristics as in Tab. 3.1 and Fig. 3.20 left). For this the classification given in the old Manual of Seismological Observatory Practice (Willmore 1979) may be used.

- Broadband instruments are preferred for all measurements of amplitude and period.
- Note that earthquakes are often complex multiple ruptures. Accordingly, the time, t_{max} , at which a given seismic body wave phase has its maximum amplitude may be quite some time after its first onset. Accordingly, in the case of P and S waves, the measurement should normally be taken within the first 25 s and 40-60 s, respectively, but in the case of very large earthquakes this interval may need to be extended to more than a minute. For subsequent earthquake studies it is also essential to report the measurement time t_{max} (see Fig. 3.19).
- For teleseismic surface waves (i.e., $\Delta > 20°$) the procedures are basically the same as for body waves. However, $(A/T)_{max}$, often in the Airy phase of the dispersed surface wave train, occurs much later and should normally be measured in the period range between 16 and 24 s although both shorter and longer periods may be associated with the maximum surface wave amplitudes (see section 2.3 in Chapter 2 and Fig. 3.35 in section 3.2.5.1).
- Note that in displacement proportional records $(A/T)_{max}$ may not coincide in time with $B_{max.}$ Sometimes, in dispersed surface wave records in particular, smaller amplitudes associated with significantly smaller periods may yield larger $(A/T)_{max}$. In such cases also A_{max} should be reported separately. In order to find $(A/T)_{max}$ on horizontal component records it might be necessary to calculate A/T for several amplitudes on both record components and select the largest vectorially combined value. In records proportional to ground velocity, the maximum trace amplitude is always related to $(A/T)_{max}$. Note, however, that as compared to the displacement amplitude A_d the velocity amplitude is $A_v = V = A_d\, 2\pi/T$.
- If mantle surface waves are observed, especially for large earthquakes (see section 2.3.4 of Chapter 2), amplitudes and periods of the vertical and horizontal components with the periods in the neighborhood of 200 s should also be measured.
- On some types of short-period instruments (in particular analog) with insufficient resolutions it is not possible to measure the period of seismic waves recorded from nearby local events and thus to convert trace deflections properly to ground motion. In such cases magnitude scales should be used which depend on measurements of maximum trace amplitudes only.
- Local earthquakes were often clipped in analog records of high-gain short-period seismographs with insufficient dynamic range. This made amplitude readings impossible. In this case magnitude scales based on record duration (see 3.2.4.5) might be used instead, provided that they have been properly scaled with magnitudes based on amplitude measurements.

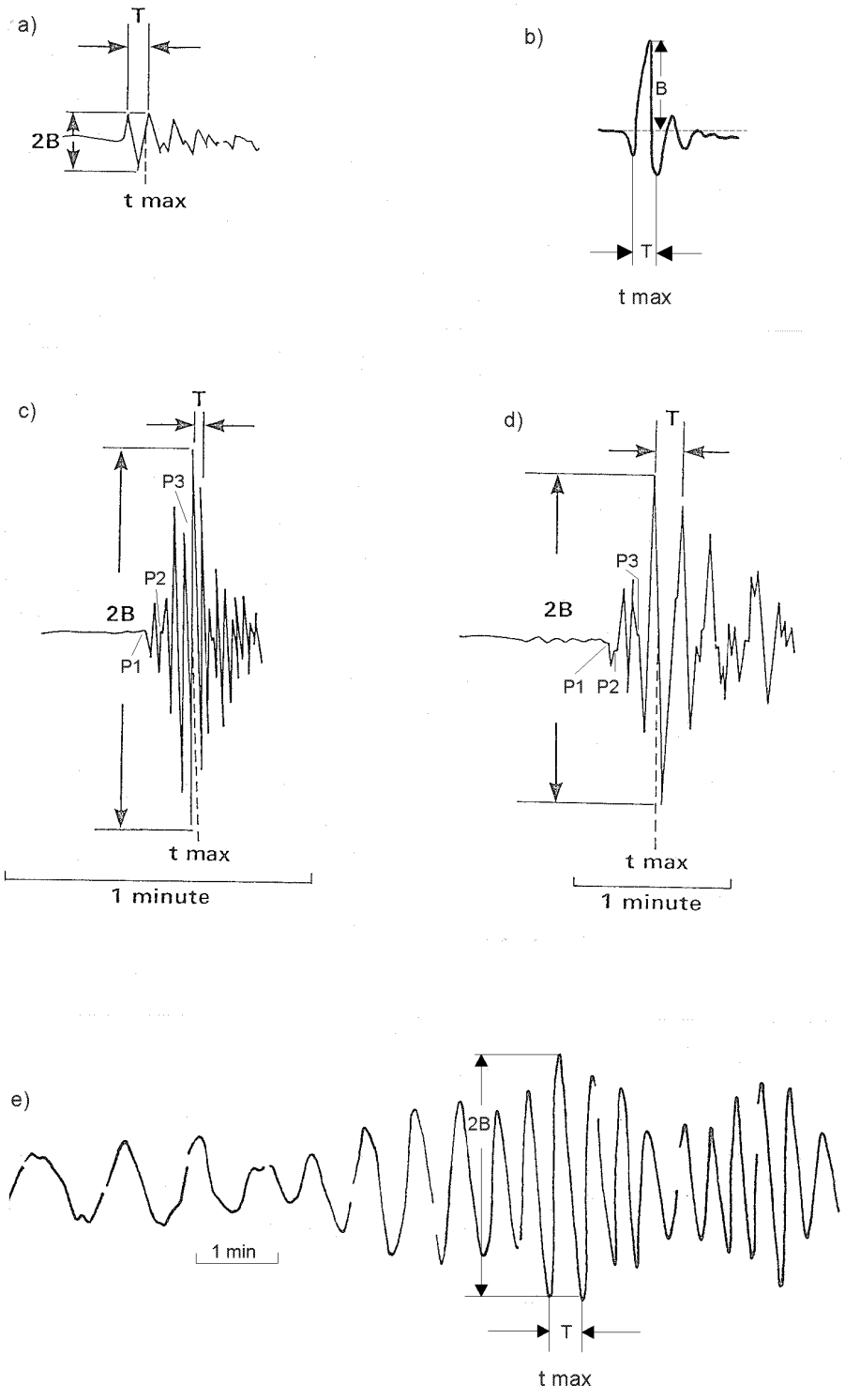

Fig. 3.19 Examples for measurements of trace amplitudes B and periods T in seismic records for magnitude determination: a) the case of a short wavelet with symmetric and b) with asymmetric deflections, c) and d) the case of a more complex P-wave group of longer duration (multiple rupture process) and e) the case of a dispersed surface wave train. Note: c) and d) are P-wave sections of the same event but recorded with different seismographs (classes A4 and C) while e) was recorded by a seismograph of class B3 (see Fig. 3.20).

Tab. 3.1 Example from the former bulletin of station Moxa (MOX), Germany, based on the analysis of analog photographic recordings. The event occurred on January 1967. Note the unambiguous annotation of the type of instruments used for the determination of onset times, amplitudes and periods. Multiple body wave onsets of distinctly different amplitudes, which are indicative of a multiple rupture process, have been separated. Types of analog standard seismographs used: A = A4 in Willmore (1979) = short-period with flat displacement response between 0.7 and 10 Hz, B = B3 = in Willmore (1979) = long-period 30-to-80 s seismograph, C = KIRNOS displacement broadband seismograph with flat response between 10 Hz and 20 s as in Fig. 3.20. Components: V = Z = vertical component; H = vectorially combined horizontal components; Lm - maximum of the long-period surface wave train.

Day	Phase	Seismograph	h m s	Remarks
5.	+eiP1	A	00 24 15.5	Mongolia 48.08°N 102.80°E
	iP2	A	24 21.5	H = 00 14 40.4 h = normal MAG = 6.4
	iP3	A,C	24 28.0	Δ = 55.7° Az = 309.6° (USCGS)
	Pmax	C	24 31	
	ePP2	C	26 27.5	PV1 A 1.2s 71.8nm MPV1(A)=5.6
	ePP3	C	26 34	PV2 A 1.8s 1120nm MPV2(A)=6.6
	eS2	C	32 04	PV3 A 1.6s 1575nm MPV3(A)=6.8
	i S3	C	32 11	PV3 C 8s 16.3µm MPV3(B)=7.1
	eiSS	B	35 56	SH3 C 18s 60µm MSH3(B)=7.3
	iSSS	B	36 44	LmV C 17s 610µm MLV(B) =7.8
	LmH	C	48.0	Note: P has a period of about 23s in the long-period seismograph of type B!

Note in Tab. 3.1 the distinct differences between the different types of magnitude and the clear underestimation of short-period (type A $\rightarrow$ mb) magnitudes. This early practice of specifying magnitude annotation has been officially recommended already by the IASPEI Sub-Committee on Magnitudes in 1977 (see Willmore, 1979) but has, regrettably, not become global standard. However, current deliberations in IASPEI stress again the need for more specific magnitude measurements and reports to databases along these lines (see IS 3.2) if the measured data deviate more than 0.1 m.u. from the ones derived for the same type of magnitude calculated by adherence to the newly recommended IASPEI measurement standards. The latter are explained in detail in IS 3.3 of this Manual. Some essential deviations from the above outlined recommendations of the IASPEI Canberra meeting in 1979 are presented in the relevant subsections below with respect to the specific type of magnitude. Determining magnitudes according to more modern and physically based concepts, such as radiated energy or seismic moment, requires special procedures (see IS 3.6 and 3.8-3.10).

Global or regional data analysis centers calculate mean magnitudes on the basis of many A , T and/or M data reported by seismic stations from different distances and azimuths with respect to the source. This will more or less average out the influence of regional, source and local station conditions. Therefore, A, A/T or M data reported by individual stations to such centers should not yet be corrected for C_r and C_S. These corrections can be determined best by network centers themselves when comparing the uncorrected data from many stations (e.g., Hutton and Boore, 1987). They may then use such corrections for reducing the scatter of individual readings and thus improve the average estimate.

When determining new calibration functions for the local magnitude Ml, station corrections have to be applied before the final data fit in order to reduce the influence of systematic biases on the data scatter. According to the procedure proposed by Richter (1958) these station corrections for Ml are sometimes determined independently for readings in the N-S and E-W components (e.g., Hutton and Boore, 1987). When calculating network magnitudes some centers prefer the median value of individual station reports of Ml as the best network estimate. As compared to the arithmetic mean it minimizes the influence of widely diverging individual station estimates due to outliers or wrong readings (Hutton and Jones, 1993).

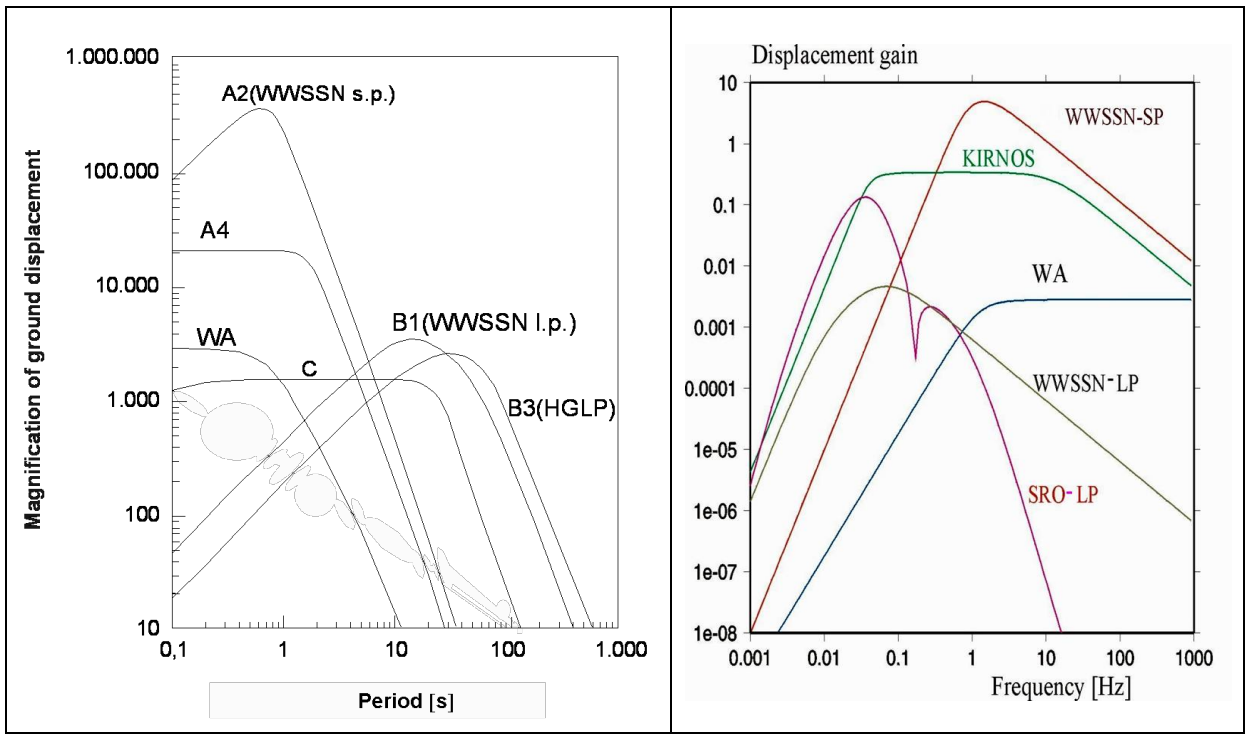

Fig. 3.20 Relative magnification curves for ground displacement for various types of standardized classical seismographs. **Left:** as a function of period according to Willmore (1979) and **right:** as a function of frequency as in Chapter 11.
WA = Wood-Anderson seismograph, which was instrumental in the definition of the local magnitude scale;
C = KIRNOS – short-to-medium-/long-period Russian broadband seismograph operated at all first-rate stations of the former Soviet Union and its allied countries as well as in China, which was instrumental in developing the Moscow-Prague Ms magnitude calibration function applicable in a wide range of surface-wave periods;
A4 = Kirnos SKM short-period seismograph of relatively broad bandwidth;
A2 = WWSSN-SP = short-period and
B1 = WWSSN-LP = longperiod seismograph of the World Wide Standardized Seismograph Network (WWSSN), set up by the United States Geological Survey (USGS) in the 1960s and 1970s, which were instrumental for measuring short-period P-wave magnitude mb and the long-period Ms around 20 s periods;
B3 = US High Gain Long-Period seismograph with maximum magnification around 40 s;
SRO-LP – long-period high-gain seismograph of the U.S. Seismological Research Observatories (SRO) for measuring 20 s surface-wave amplitudes and magnitudes with best signal-to-noise ratio by strongly filtering out 6 s ocean microseisms.

3.2.3.2 Aim and specified general procedures for IASPEI standard magnitudes and possible modifications in automated procedures (P. Bormann, J. Saul, and S. Wendt)

IASPEI has established in 2002 within its Commission on Seismic Observation and Interpretation (CoSOI) a Working Group on Magnitude Measurements (in the following for short named the WG Magnitude) in an effort to assure

- homogeneity and long-term global compatibility of magnitude data and their usefulness for seismic hazard assessment and research and therefore
- best possible agreement with magnitudes of the same type that have been measured for decades from analog seismograms according to original definitions, as well as
- unambiguity in the nomenclature of magnitude data of similar type but measured with different procedures

aiming at

- minimizing bulletin magnitude biases that result from procedure-dependent single-station or network magnitude biases,
- increasing the number of seismological stations and networks with well-defined procedures and
- promoting the best possible use of the advantages of digital data and processing.

As of now, this WG has agreed on standard measurement procedures for five widely used magnitudes: ML, mb, mb(Lg), Ms(20), mB(BB) and Ms(BB). For details see the latest version IASPEI (2013) of the recommendations of the Working Group of Magnitude Measurements as well as a more elaborated version with comments in IS 3.3.

Of general importance is that these standard magnitudes have to be measured on either simulated records of classical analog seismographs or on unfiltered digital broadband records:

- ML on Wood-Anderson (WA) records;
- mb and mb-Lg on WWSSN-SP records;
- Ms(20) on WWSSN-SP records.
- mB(BB) and Ms(BB) on unfiltered broadband records with a velocity-proportional response over at least the period range in which mB(BB) (T = 0.2 s to 30 s) and Ms(BB) (T = 3 s to 60 s) should be measured.

For the approximate shape of the response curves of WA, WWSSN-SP and –LP see Fig. 3.20 above, for the more precise normalized response curves and their respective poles and zeros see Figure 1 and Table 1 in IS 3.3.

Note that for the international data exchange and archiving the nomenclature of the standard magnitudes should be written in the (for magnitude data maximum of) 5-character IASPEI Standard Format (ISF; see Chapter 10), which would be ML, mb, mb_Lg, Ms_20, mB_BB and Ms_BB.

In contrast to the classical magnitude formulas, which are based on displacement amplitudes A measured in units of μm, amplitude readings for standard magnitudes should all be reported in units of nm (for A) or in nm/s (for velocity amplitudes V measured on unfiltered BB records). Therefore, the commonly known classical calibration relationships have been modified for the standard magnitudes to be consistent with these new units.

The measured amplitudes have to be reported following their so-called **amplitude phase names**, which are specified for the respective magnitudes as: IAML, IAmb, IAmb_Lg, IAMs_20, IVmB_BB and IVMs_BB. Tab. 10.5 in Chapter 10 gives an example how these amplitude data, also for other non-standard magnitudes, appear now in IMS1.0/ISF parameter format in the event and station parameter plots produced by the USGS/NEIC HYDRA automatic location and analysis system.

The current recommendations for amplitude and period measurements for the new **IASPEI magnitude standards** orientate themselves essentially on what has been described above with Fig. 3.18 and is still dominating practice when analyzing analog records or digital screen plots. According to IS 3.3 these recommendations read as follows:

"The amplitudes used in the magnitude formulas ... are in most circumstances to be measured as one-half the maximum peak-to-adjacent-trough (sometimes called "peak-to-peak") deflection of the seismogram trace. None of the magnitude formulas presented in this article are intended to be used with the full peak-to-trough deflection as the amplitude. The periods normally are to be measured as twice the time-intervals separating the peak and adjacent-trough from which the amplitudes are measured. The amplitude-phase arrival-times are normally to be measured as the time of the zero-crossing between the peak and adjacent-trough from which the amplitudes are measured."

Although the calculation of the broadband magnitudes mB_BB and Ms_BB, now based on direct measurement of V_{max}, do no longer require that the periods are measured, the WG Magnitude strongly encourages their complementary measurement and reporting, since the period at which V_{max} appears in broadband records is closely related to the corner frequency of the radiated source spectrum and thus is of interest also for other users of these data.

Furthermore, **we have to accept that their might be agency-specific circumstances that may lead to the modification of standard procedures, e.g., of measuring amplitudes and periods or using modified types of responses. But then certain rules should be obeyed** (see sections 3.5 and 5 in IS 3.3) **and a careful documentation of station/agency magnitude procedures be assured (see questionnaire in Annex 2 to IS 3.4).** The latter should be posted on the station/agency website and also be deposited and kept updated at the ISC for the information of data users.

While the visual recognition and picking of the dominating amplitudes and related periods is relatively easy interactively for an experienced analyst on a computer screen or record plot, even in the case of rather complex superimposed waveforms as in Fig. 3.17, or 3.21b below, it is much more difficult for a definite algorithm to handle properly all possible ramifications of such a measurement problem. Agencies which run automatic procedures of data analysis, may therefore prefer to measure as amplitude just the maximum positive or negative deflection between two zero crossings of the record trace and to estimate the zero position from the long-term average prior to the respective wave onset. The related period is then taken, e.g., as twice the timedifference between the respective zero crossings. This may be easier to handle

automatically. However, in order to check whether such a modified automatic measurement procedure, but also an automatic procedure which is supposed to mimic best the recommended measurement standards, yield indeed magnitude estimates within ± 0.1 m.u. of standard magnitudes measured manually or interactively by an expert analyst, this has to be tested and documented by comparative measurements. They should use an identical representative test data set in a wide range of magnitudes or log(A/T) and log(V/2π) values, respectively. Only when the results agree with an average absolute deviation less than about 0.1 m.u., the automatic data, or those derived with any other modified measurement procedure, can be accepted as being in agreement with the standards and thus can be reported to international agencies or in agency bulletins with the IASPEI amplitude-phase-name nomenclature.

We demonstrate this by way of example for period and amplitude measurements for mb, mB_BB, Ms_20 and Ms_BB The interactive analysis has been carried out by S. Wendt, CLL observatory of the University Leipzig, Germany, and the automatic analysis by J. Saul, GFZ German Research Centre for Geosciences at Potsdam. The latter tested two versions of rather simple but very fast and stable test algorithms, intended to be used with masses of globally retrieved waveform data in the tsunami early warning context. This sets limits with respect to algorithm flexibility and sophistication.

Fig. 3.21 gives an example of period measurements on a WWSSN-SP waveform for mb and on a velocity broadband waveform for mB_BB. Fig. 3.22 summarises the median and average ratios $T_{manual}/T_{automatic}$ and their standard deviations when measuring mb, mB_BB, Ms_20 and Ms_BB.

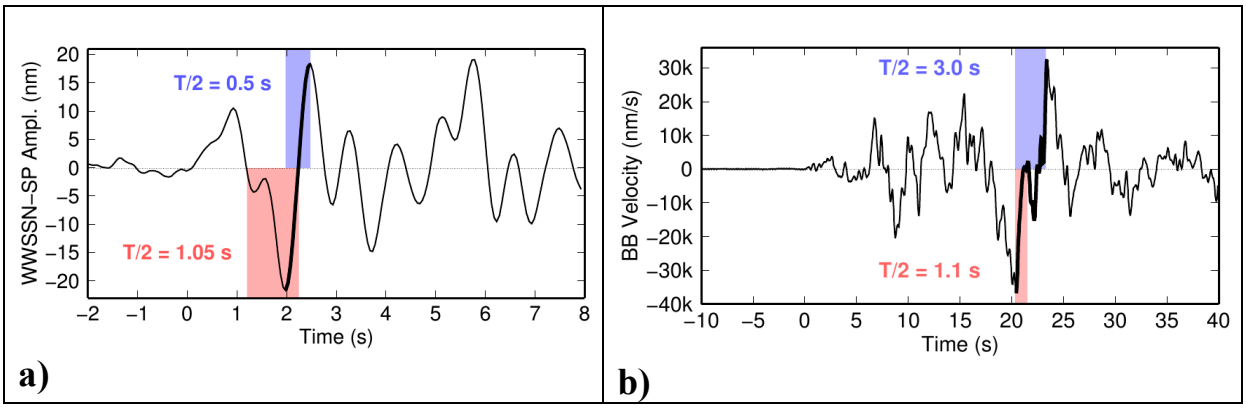

Fig. 3.21 P waveforms on **a)** a simulated WWSSN-SP record and **b)** on an unfiltered velocity broadband record to explain some of the possible complications of automatic amplitude and period measurements as compared to manual readings. The width of the **blue column** corresponds to T/2 when measuring as amplitude half of the vertical distance between the maximum peak and the maximum adjacent trough (for short peak-to-trough = ptp; marked as **bold black record trace**) and as period twice the time difference between ptp, as recommended by the standard. In contrast, the width of the **red column** corresponds to reading T/2 between the two adjacent zero crossings related to the largest (here negative) swing, when measuring as amplitude the largest zero-to-peak (or trough) deflection, in the following termed ztp for short. For comments on Fig. 3.21 see text.

When looking at the two waveforms in Fig. 3.21 one realizes that for an analyst there is no difficulty at all to properly determine A and T according to the standard recommendation based on ptp readings, even on the broadband trace with a distinct superposition of various periods. The dominant one, related to the absolute V_{max}, is without any doubt. Yet, in the BB velocity record of Fig. 3.21b T/2 manual peak-to-trough (= ptp in blue) is about 3 times T/2 ptp automatic (in red), because the simple algorithm got trapped in a secondary adjacent peak just after the zero crossing from below. A more sophisticated algorithm, which would recognize the difference between a secondary adjacent and the **maximum** adjacent peak would surely have got about the same period as an analyst.

Luckily, differences in T at which V_{max} is measured do not matter when calculating mB_BB. Only asymmetry between the corresponding largest positive and negative half cycle amplitudes makes a difference when comparing ptp/2 with zero-to-peak (ztp) amplitude measurements. In our case, however, the difference between **manual** ptp/2 and automatic ztp is minimal (**0.02 m.u**.). In contrast, the difference between the tested **automatic** ptp/2 and automatic ztp results is nearly **0.3 m.u**., which would be the theoretical maximum for single-sided swings. Yet, on the smoother P waveform in Fig. 3.21a the current ptp/2-algorithm had not difficulties to correctly read A and T. In contrast, the automatic ztp-algorithm measured on this waveform a much too large period between the related two zero crossings. In view of the steep WWSSN-SP response drop for periods larger than 1.5 s, a much too large A was calculated, resulting in a **0.6 m.u. larger mb value than mb(IASPEI)** (see section 3.2.2, ***Problem 2,*** Figs. 3.16 and 3.18 and related discussion).

Fig. 3.22 summarizes the results of our comparative period measurements for all four teleseismic standard magnitudes. The average ratios $T_{automatic}/T_{manual}$ are close to 1 for mb, Ms_20 and Ms_BB with very small standard deviation SD. Worst are the mean and SD for mB_BB. On the other hand the median ratio is best for the two broadband magnitudes mB_BB and Ms_BB. This indicates that outliers in period estimates in conjunction with mB_BB measurements, which can not be prevented with the here tested automatic ptp/2 algorithm, seem to bias both the mean and SD significantly. However, the generally good agreement between manual and automatic period determinations according to the standard recommendation is very encouraging.

Period ratios:

mb:	$T_{automatic}$ / T_{manual}	mean = 1.025 ± 0.004 median = 1.007
mB_BB:		mean = 0.850 ± 0.023 median = 1.000
Ms_20:		mean = 0.996 ± 0.001 median = 0.997
Ms_BB:		mean = 1.027 ± 0.003 median = 1.000

Fig. 3.22 Period ratios $T_{automatic}/T_{manual}$ (median, mean and standard deviation) for the teleseismic standard magnitudes mb, mB_BB, Ms_20 and Ms_BB when measured according to the 2 times peak-to-trough rule.

Next we compare in Fig. 3.23 various combinations of automatic and manual mB_BB measurements.

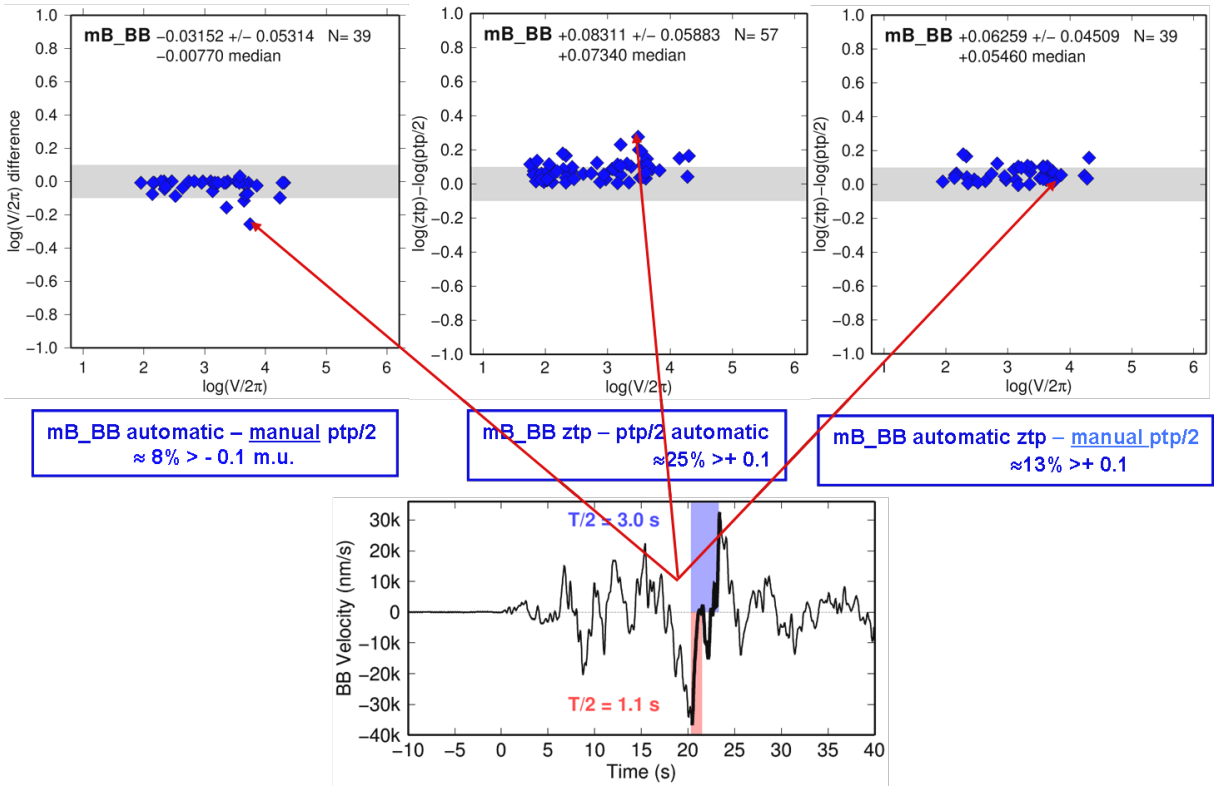

Fig. 3.23 Differences of mB_BB values (ordinates of the upper three figures) between automatic and manual ptp/2 procedures (upper left), fully automatic ztp and ptp/2 procedure (upper middle), and automatic ztp compared with manual ptp/2 procedure (upper right). The analyzed records cover a wide range of earthquakes with magnitudes 5.3 ≤ mB_BB ≤ 8.3. In the middle row the percentage of differences > ±0.1 m.u. is given. The long red arrows point to the respective magnitude difference values in the uppermost three diagrams that result from applying the respective procedure combination to the waveform depicted in the bottom diagram.

From Fig. 3.23 the following conclusions can be drawn:

- Different algorithms of automatic mB_BB determination may yield results which significantly differ from each other or from competent manual mB_BB measurements.
- Best agreement between automatic and manual mB_BB calculations is achieved with the current ptp/2 test algorithm. The single outlier of nearly – 0.3 m.u. is due to the algorithm getting stuck in a secondary peak near to the zero line. Only in two more cases the difference between automatic and interactive readings is slightly larger than 0.1 m.u., probably again due to taking some secondary maxima/minima as largest adjacent peak or trough, yet further away from the zero line. In summary, it is most likely, that the tested automatic ptp/2 procedure yields overwhelmingly standard compatible mB_BB data. The median difference in our test with 39 events is +0.01 m.u. and the average absolute difference 0.03 m.u., reducing to 0.02 m.u. without the single large outlier.
- If the algorithm could be upgraded so as to avoid getting trapped in secondary extrema of different polarity adjacent to the primary amplitude maxima or minima then the automatic mB_BB measurements would be perfectly compatible with manual standard measurements.

- The agreement between automatic ztp and manual ptp/2 measurements is somewhat inferior. In about 13% of the studied cases residuals are > 0.1 m.u., but always < 0.2 m.u. with the average absolute deviation 0.04 m.u.
- The disagreement is largest between fully automatic ztp and ptp/2 derived mB_BB values. In about 25% of the cases the difference is > 0.1 m.u. and may reach about 0.3 m.u. with a median of 0.07 and an average absolute deviation of almost 0.05 m.u. This is not compatible with IASPEI standard requirements.

Fig. 3.24 show a similar comparison of automatic and manual mb procedures.

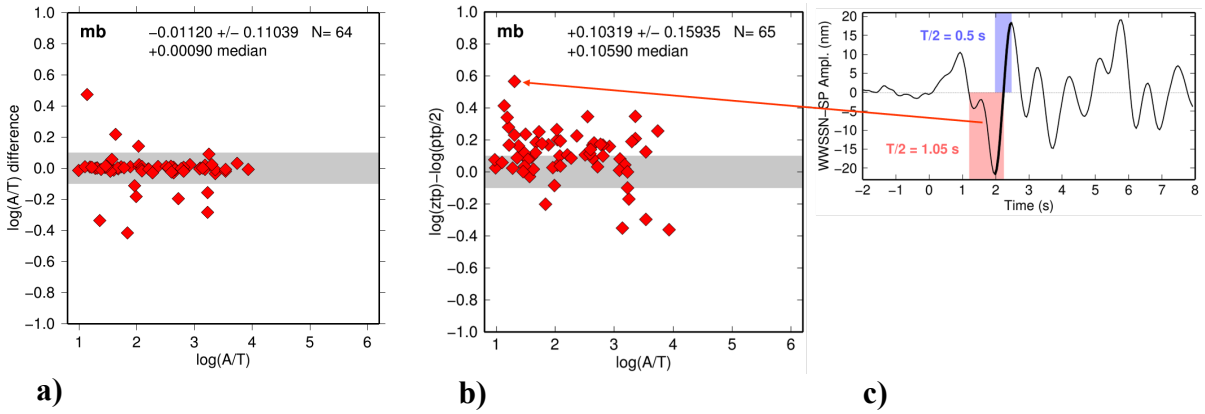

Fig. 3.24 Difference in m.u. between automatically and manually determined mb values in the magnitude range 5.0 ≤ mb ≤ 7.6: **a)** automatic – manual ptp/2 measurement; **b)** automatic ztp – manual ptp/2 measurement; **c)** WWSSN-SP waveform with the ztp negative half swing marked in red from which A and T were measured that produced the data point with the largest difference of almost 0.6 m.u. in diagram b).

From Fig. 3.24 the following conclusions can be drawn:

- mb yields more data than mB_BB for smaller events but with much larger scatter.
- For about 84% of the analyzed waveforms, **the ptp/2 test algorithm yielded mb values that agreed within 0.1 m.u. with those determined by manual expert analysis**. Both arithmetic mean and median difference are within 0.01 m.u. from zero Therefore, the ptp/2 algorithms hold promise to produce overwhelmingly mb values that are compatible with IASPEI standard mb. Despite sometimes large outliers the median difference is zero and the the average absolute deviation between automatic and manual ptp/2 measurements for mb only 0.05 m.u.
- Yet, outliers up to 0.6 m.u. are not acceptable for standard magnitude data that aim at drastically reducing procedure-dependent errors. Therefore, for assuring IASPEI compatible amplitude, period and mb values in the agency bulletins and data reports to international data centers either the algorithm has to be improved or expert control of the final data is indispensible.
- The negative outliers of mb are again due to the ptp/2 algorithm getting occacionally trapped in secondary adjacent maxima or minima (see above discussion for mB_BB).
- Significant positive outliers may be due to overestimating the period T (see the 2-3s problem discussed above), usually at rather small log(A/T) values due to superposition

with more long-period noise amplitudes which is not recognized and properly accounted for by the automatic algorithm.

- **The ztp-algorithm**, which still worked reasonably well for mB_BB, **does not yield standard compatible results for mb**. Average and median difference are already about 0.1 m.u., the standard deviation is ±0.16 m.u. and the average absolute difference to ptp/2-based manual analysis 0.11 m.u. Accordingly, for about ¾ of the analyzed waveforms the difference to manual ptp/2 measurement was larger than 0.1 m.u., with positive and negative outliers up to about 0.4-0.6 m.u.

Figs. 3.25 and 3.26 show such comparisons also for broadband Ms_BB and narrowband Ms_20.

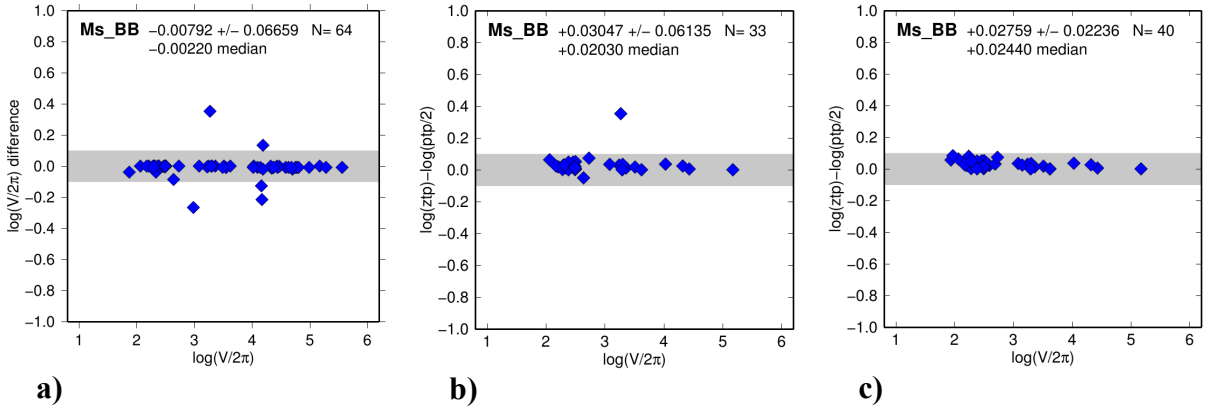

Fig. 3.25 Difference in m.u. between automatically and manually determined velocity broadband Ms_BB values in the magnitude range 4.6 ≤ Ms_BB ≤ 9.0: **a)** automatic – manual ptp/2 measurement; **b)** automatic ztp – manual ptp/2 measurement; c) automatic ztp – ptp/2 measurement.

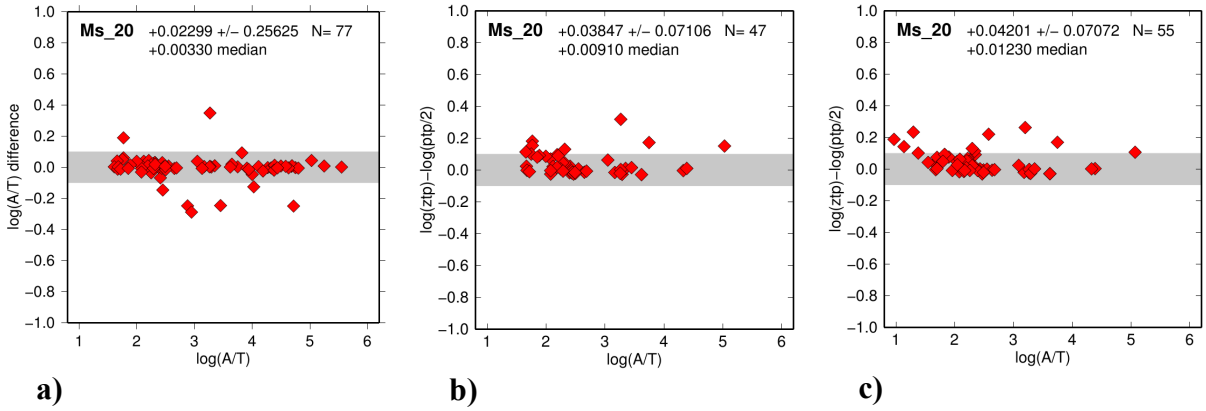

Fig. 3.26 Difference in m.u. between automatically and manually determined velocity broadband Ms_20 values in the magnitude range 4.8 ≤ Ms_20 ≤ 9.0: **a)** automatic – manual ptp/2 measurement; **b)** automatic ztp – manual ptp/2 measurement; **c)** automatic ztp – ptp/2 measurement.

Comments and conclusions related to Fig. 3.25 and 3.26 are the following:

- For both Ms magnitudes automatic and manual A/T and V_{max} readings based on ptp/2 yield in most cases comparable values, yet the average agreement is clearly better and the data scatter less for Ms_BB (mean difference -0.01 m.u., SD = ±0.07 m.u. and average absolute deviation of 0.02 m.u. only, as compared to Ms_20 with -0.02, ±0.25 and 0.07 m.u. respectively).
- For only about 8% of the data automatic ptp/2 Ms_BB differed more than ± 0.1 m.u. from the manually measured ones, for Ms_20 this applied to about 10% of the data.
- **The differences between automatic ztp and manual ptp/2 are even less**. For Ms_BB the agreement is even perfect, with the exception of a single but relatively large (+0.35 m.u.) outlier, which is in fact the same for Ms_20.
- The reason for this single large outlier turned out to be an event association error by the automatic algorithm. It searches for the maximum surface-wave amplitude within a given time window after the P-wave onset. The time window depends on distance and a fixed group-velocity window assumed for the surface waves. In the current algorithm, the group velocity window covers the range between 2.5 and 4.5 km/s. With this wide window, applied to two Chile earthquake aftershocks, following each other within 17 min, the algorithm measured as the largest surface-wave amplitude for both Ms_BB and Ms_20 that of the about 0.3 m.u. larger later aftershock, the analyst, however, the surface-wave maxima measured by the analyst, however, related correctly to the earlier aftershock. This wrong association accounts also for the identically large positive outlier when comparing the automatic and manual ptp/2 results for Ms_BB and Ms_20 in Figs. 3.25 and 3.26. The lesson is, that proper association of surface-wave maxima related to closely following events are generally more difficult for an algorithm which has to operate blind with a fixed set of parameters than for an off-line working intelligent analyst. Therefore, before final data cataloguing and reporting to international data centers automatically calculated magnitude data should go through an expert review.
- While there are no negative residuals at all for Ms_BB when comparing automatic ztp with manual ptp/2, there are 3 negative ones when comparing automatic and manual ptp/2, and even 6 in the case of Ms_20. One of the negative outliers for both Ms_BB (-0.27 m.u.) and Ms_20 (-0.25 m.u.) was again due to the wrong association of the automatically measured surface-wave maximum to another event that occurred within the same hour but at rather different distance and thus arrived at the recording station again close to the surface-wave maximum of another event. And one more of the 3 negative Ms_BB residuals (-0.22 m.u.) was caused by missing the later arriving absolute V_{max} for Ms_BB within the preset group velocity and measurement time window, which, however, worked fine for this event for the earlier arriving Ms_20 amplitude maximum..
- **Only for Ms_BB the tested automatic ztp and ptp/2 algorithms yielded practically identical results within < 0.1 m.u.**

Tab. 3.2 summarizes the essential statistical results of the above procedure comparison.

Tab. 3.2 Statistic parameters of comparing automatic magnitude calculations based on ztp and ptp/2 amplitude measurements with manual ptp/2 measurements according to IASPEI standard procedures. **Mauto** = type of magnitude, measured automatically, **N** = number of measured differences between automatic and manual magnitude determinations; **Median** = median difference, **Mean** = arithmetic mean of differences, **SD** = standard deviation from the mean, **Avad** = average absolute difference, **% > 0.1** = approximate percentage of differences larger than 0.1 m.u., **Max outliers**. **Note:** all calculated median, mean, SD and avad values have been rounded to the nearest second decimal. Since the distribution of differences is not Gaussian the median and avad values are more relevant to assess the agreement with the strict standard procedure. Mauto procedures in best agreement with the manual standard procedure have been written in bold letters.

Mauto	N	Median m.u.	Avad m.u.	Mean m.u.	SD m.u.	% > 0.1.u.m	Max outliers m.u.
mb(ztp)	65	+0.10	0.11	+010	±0.16	55	+0.6 and -0.4
mb(ptp/2)	64	0.00	0.05	-0.01	±0.11	18	+0.5 and – 0.5
mB_BB(ztp)	39	+0.05	0.04	+0.06	±0.05	13	+0.3
mB_BB(ptp/2)	39	-0.01	0.03	-0.03	±0.05	8	-0.15
Ms_20 (ztp)	47	+0.01	0.05	+0.04	±0.07	18	+0.3
Ms_20(ptp/2)	77	0.00	0.07	+0.02	**±0.26**	10	+0.4 and -0.3
Ms_BB(ztp)	33	+0.02	0.02	+0.03	±0.06	3	+0.4
Ms_BB(ptp/2)	64	0.00	0.03	-0.01	±0.07	8	+0.4 and -0.3

Summarizing our procedure comparison test we conclude:

- The current automatic GFZ algorithm for determining teleseismic magnitudes of the types mb, mB_BB, Ms_20 and Ms_BB have been developed in the first instance for application in the tsunami early warning systems, i.e., for very fast and stable applications to great amounts of globally accessible waveform data. Therefore, ztp has so far been given preference for ptp/2 in operational applications.
- Yet, our investigations showed, that the ztp algorithm is – with the exception for Ms_BB – inferior (often not much but worst for mb) to the ptp/2 algorithm, which is closer to the preferred IASPEI standard procedure.
- However, with the exception for mb, both algorithms yield (when taking into account the median, respectively the mean differences, standard deviations, and average absolute differences as well as the real distribution of residuals) magnitude estimates which differ in less than 20%, for the ptp/2 version even in less than 10% of the cases, magnitude values that are within 0.1 m.u of manual expert estimates.
- The differences could be further reduced, for body-wave magnitude estimates in particular, by using a more sophisticated ptp/2 algorithm that avoids getting trapped in

a secondary maximum or minimum by searching for the **largest adjacent** amplitude with opposite polarity to the primary maximum deflection from the zero line..

- Automatic algorithms for surface waves have to search for the maximum amplitude within a flexible time window, depending on distance and a preset group velocity window. If the latter is chosen too small it may fail or yield to small values when applied to Ms_BB measurements in a wide range of periods and distances. And when the group velocity window is chosen too wide, the algorithm may measure instead of the searched for surface-wave maximum of an earlier and/or weaker event the later following larger maximum of an overlapping event, closely spaced in time of arrival. Our data have been affected by such cases.
- Event association errors, and likely also mistakes in proper peak-to-trough association in the case of complex waveforms, can hardly be excluded for sure in automatic procedures of magnitude determination that are based on preset algorithm parameters. Therefore, automatically determined magnitude data should be critically checked by expert analysts before they enter final bulletins or are reported to international data centers for final use and archiving.
- Generally, in any such comparison of different magnitude measurement procedures, differences beyond the acceptable level of measurement errors of about 0.10-0.15 m.u. should not be considered as random noise. Usually they have a non-random cause. Therefore, one should strive to identify their reasons. This requires, however, that one goes back for the specific data points to their respective waveforms and compare which amplitudes and periods have been measured by what method and at which time. If the reasons for significant residuals have become clear this may also offers the chance to reduce the data scatter by modifying the algorithm. This we have tried to demonstrate by way of example.
- Another lesson from our demonstration is that one should avoid in such comparisons that the selected reference waveform data contain overlapping wave groups belonging to different events in order to avoid large outliers due to wrong associations.

In the following we will outline the origin, general features, formulae and specific differences of various magnitude scales that are currently in use or recommended by the IASPEI WG on Magnitudes. We will highlight which of these scales are at present already accepted as world-wide standards and will also spell out related problems which still require further consideration, clarifying discussion, recommendations or decisions by CoSOI. Data tables and diagrams on calibration functions used in actual magnitude determinations are given in Datasheet 3.1.

3.2.4 Magnitude scales for local and regional events

The large variability of velocity and attenuation structure of the crust does in fact not permit the development of a unique, internationally standardized calibration function for local events. However, the original definition of magnitude by Richter (1935) did lead to the development of a local magnitude scale Ml (original nomenclature ML) for California. Ml scales for other areas are usually scaled to Richter's or Hutton and Boore´s (1987) definition and also the procedure of measurement is more or less standardized. With slight modification, the Hutton and Boore formula has now been accepted by IAPEI as the reference formula for standard ML to which other regional Ml scales should be scaled in order to yield compatible results within about 0.1 m.u. for equal measurement values at different distances.

3.2.4.1 The original Richter magnitude scale Ml

In his 1935 landmark paper Richter stated:

*„...it is frequently desirable **to have a scale** for rating these shocks in terms of their original energy, independently of the effects which may be produced at any particular point of observation."*

For his measurements he used Wood-Anderson (WA) horizontal component torsion seismometers which had become available and widely deployed as a standard instrument in the 1930s in Southern California. According to the manufacturer the **WA seismometers** had the following parameters: natural period T_S = 0.8 s, damping factor D_S = 0.8, **static magnification V_{max} = 2800**. The resulting response is sketched in Fig. 3.27 left..

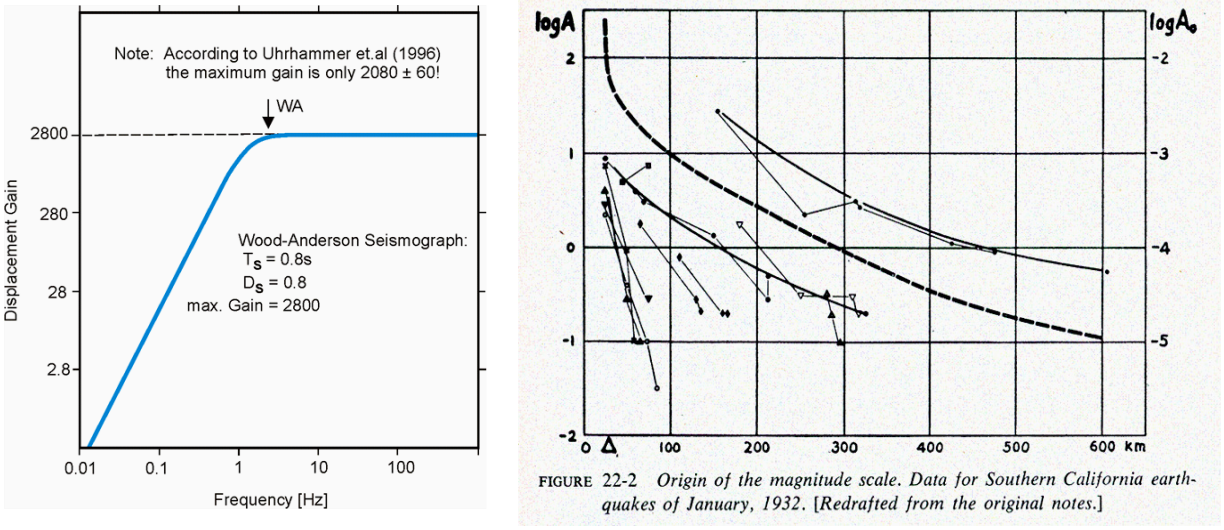

Fig. 3.27 Left: Wood-Anderson response according to manufacturer´s instrument data; **Right:** Plot of original data measured by Richter; copy of Figure 22-2 in Richter (1958)..

Following a recommendation by Wadati, Richter plotted the logarithm of maximum **trace amplitudes**, A_{max}, measured on WA records as a function of epicentral distance Δ. He found that $\log A_{max}$ decreased with distance along more or less parallel curves for earthquakes of different size (Fig. 3.20 (right). This led him to propose the following definition for the magnitude as a quantitative measure of earthquake size (Richter 1935, p. 7):

"The magnitude of any shock is taken as the logarithm of the maximum trace amplitude, expressed in microns, with which the standard short-period torsion seismometer ... would register that shock at an epicentral distance of 100 km".

This local magnitude was later given the symbol ML (Gutenberg and Richter, 1956b). In order to calculate ML also for other epicentral distances, Δ, between 30 and 600 km, Richter (1935) provided attenuation corrections. They were later complemented by attenuation

corrections for Δ < 30 km assuming a focal depth h of 18 km (Gutenberg and Richter, 1942; Hutton and Boore, 1987). Accordingly, one gets

$$ML = \log A_{max} - \log A_0 \qquad (3.14)$$

with A_{max} in mm of measured zero-to-peak trace amplitude in a Wood-Anderson seismogram. The respective calibration values $-\log A_0$ were published in tabulated form by Richter (1958) (see Table 1 in DS 3.1). Fig. 3.28 summarizes the classical procedure of ML determination.

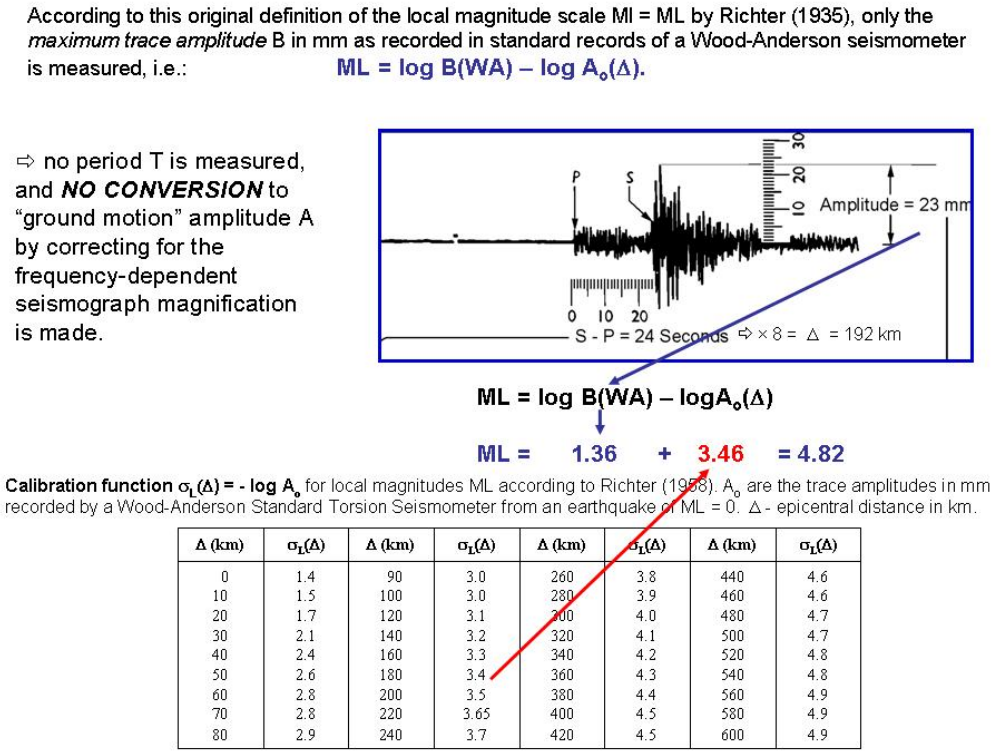

Δ (km)	$\sigma_L(\Delta)$	Δ (km)	$\sigma_L(\Delta)$	Δ (km)	$\sigma_L(\Delta)$	Δ (km)	$\sigma_L(\Delta)$
0	1.4	90	3.0	260	3.8	440	4.6
10	1.5	100	3.0	280	3.9	460	4.6
20	1.7	120	3.1	300	4.0	480	4.7
30	2.1	140	3.2	320	4.1	500	4.7
40	2.4	160	3.3	340	4.2	520	4.8
50	2.6	180	3.4	360	4.3	540	4.8
60	2.8	200	3.5	380	4.4	560	4.9
70	2.8	220	3.65	400	4.5	580	4.9
80	2.9	240	3.7	420	4.5	600	4.9

Fig. 3.28 Summary of the classical procedure of measuring ML. Note that the letter B was given here to record trace amplitudes, highlighting that they were not been converted to ground motion displacement amplitudes A.

Note 1: According to Uhrhammer and Collins (1990) the magnification of 2800 of WA seismometers had been calculated on the basis of wrong assumptions on the suspension geometry. **More correct values** for the static magnification and the damping of the seismometer are **2080 ± 60 and Ds = 0.7**, respectively (see also Uhrhammer et al., 1996). Accordingly, **magnitude estimates based on synthesized WA records** assuming the original WA parameters systematically underestimate the size of the event. This underestimation depends on the frequency at which the amplitude is measured. It is on average at typical periods about 0.1 m.u., has its minimum around the corner frequency of 0.128 Hz (T = 0.8 s; 0.065 m.u.) and is largest (up to 0.13 m.u.) at significantly lower and higher frequencies (Fig. 3.29). However, as long as records of original WA seismographs are used this bias plays no role.

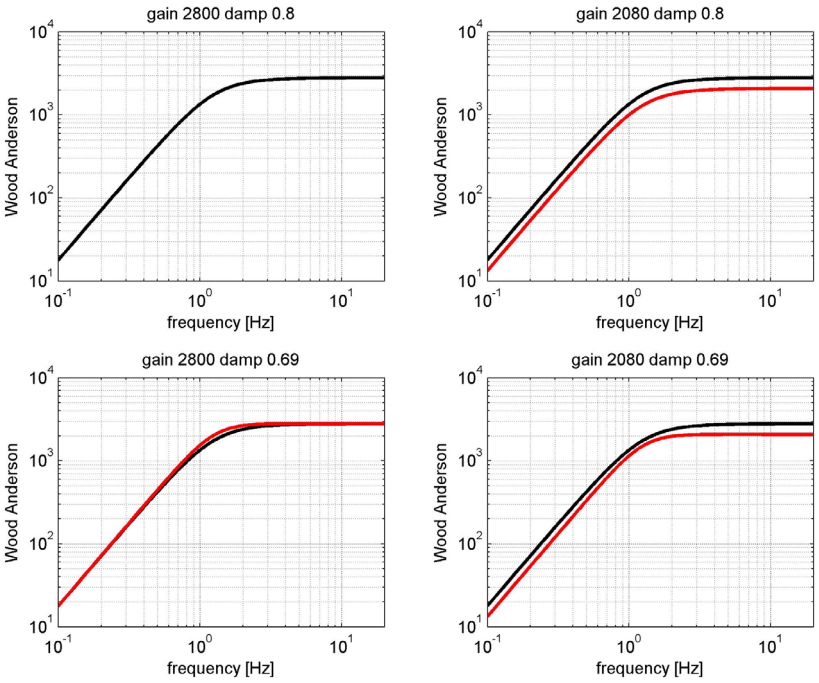

a)

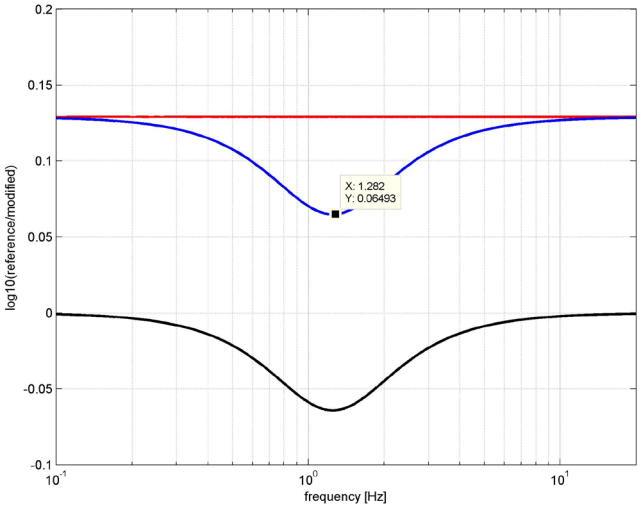

b)

Fig. 3.29 **a)** Response curves of Wood-Anderson seismometers calculated for different static magnification and damping. Upper left: Original manufacturer´s response; upper right: **red** response curve according to Uhrhammer and Collins (1990) when correcting only for the difference in static magnification; lower right: red curve: as upper right but additionally accounting for the difference in seismometer attenuation. **b)** differences in ML (m.u.): red line – correcting only for difference in static magnification; blue curve – accounting additionally for the difference in seismometer attenuation; black curve – difference between red and blue. (Figure by courtesy of D. Bindi, 2011).

Note 2: In contrast to the general magnitude formula (3.13), Eq. (3.14) considers only the maximum displacement-proportional record amplitudes but not their periods. Reason: WA instruments are short-period and their traditional analog recorders had a limited paper speed. Proper reading of the period was difficult. It was assumed, therefore, that the maximum

amplitude phase (in case of local events generally Sg, Lg or Rg) had always about the same dominant period within the plateau range of the response. Also, - log A_0 does not consider a depth dependence of $\sigma(\Delta, h)$. Seismicity in southern California is generally shallow (mostly less than 15 km). Eq. (3.14) also does not give regional or station correction terms. They were already taken into account when determining -log A_0 for southern California.

Note 3: In the following we use as the general NMSOP nomenclature for local magnitude data Ml (with l = local), unless the respective data have been measured and calibrated for sure according to the new IASPEI ML standard or they relate directly to the original Richter scale.

Note 4: The smallest events recorded in local microearthquake studies have negative values of Ml while the largest Ml is about 7, i.e., the Ml scale also suffers "*saturation"* (see Fig. 3.47). Despite these limitations, Ml estimates of earthquake size are relevant for earthquake engineers and risk assessment since they are closely related to earthquake damage. The main reason is that many structures have natural periods close to that of the WA seismometer (0.8s) or are within the range of its pass-band (about 0.1 - 1 s).

Problems and conclusions:

1) In 3.2.3 it was said that in the case of horizontal component recordings, as a general IASPEI rule, A_{Hmax} should be the maximum vector sum amplitude measured at t_{max} in both the N and E component. Deviating from this, Richter (1958) says: *"... In using ...both horizontal components it is correct to determine magnitude independently from each and to take the mean of the two determinations. This method is preferable to combining the components vectorially, for the maximum motion need not represent the same wave on the two seismograms, and it even may occur at different times*." In most investigations aimed at deriving local Ml scales $A_{Hmax} = (A_N + A_E)/2$ has been used instead to calculate ML although this is not fully identical with $Ml = (Ml_N + Ml_E)/2$ and might give differences in magnitude of up to about 0.1.m.u.

2) The Richter Ml from arithmetically averaged horizontal component amplitude readings will be smaller by at least 0.15 magnitude units as compared to Ml from A_{Hmax} vector sum. In the case of significantly different amplitudes A_{Nmax} and A_{Emax} this difference might reach even several tenths of magnitude units. However, the method of combining vectorially the N and E component amplitudes, as generally practiced in other procedures for magnitude determination from horizontal component recordings, is hardly used for Ml because of reasons of continuity in earthquake catalogs, even though it would be easy nowadays with digital data.

3) According to Hutton and Boore (1987) the *distance corrections developed by Richter for local earthquakes (Δ < 30 km) are incorrect*. Bakun and Joyner (1984) had come to the same conclusion for weak events recorded in Central California at distances of less than 30 km. This leads to magnitude estimates from nearby stations that are smaller than those from more distant stations. Therefore, Hutton and Boore (1987) proposed that local magnitude scales be redefined such that Ml = 3 corresponds to 10 mm of motion on a WA record at 17 km hypocentral distance. This is consistent with the original definition of the scale for Southern California and will also allow a better comparison of earthquakes in regions with very different wave attenuation within the first 100 km.

4) According to Hutton and Jones (1993) redetermination of local magnitudes recorded by the Southern California Seicmographic Network (SCSN) from 1932 t0 1990 has shown that the magnitudes have not been consistently determined over that period of time. The amplitudes recorded on WA instruments were systematically overestimated prior to 1944 compared to present reading procedures, leading to a significant overestimation of Ml. Moreover, the change to computerized estimation in 1975 led to slightly lower event magnitudes for the time after. These obviously not well documented, thought over and agreed upon changes contributed to an apparently higher rate of seismicity in the 1930s and 1940s than later in the catalog, which had been misinterpreted as a decrease in seismicity rate after the 1952 Mw7.5 Kern County earthquake. Rereading WA amplitudes for moderate earthquakes (Ml ≥ 4.5) for the whole time span resulted in magnitudes which proved to be Poissonian distributed with no significant change in seismicity above the 90% level.

5) Similar experiences with other local and global catalogues led Habermann (1995) to state: " ... the heterogeneity of these catalogues makes characterizing the long-term behaviour of seismic regions extremely difficult and interpreting time-dependent changes in those regions hazardous at best.... Several proposed precursory seismicity behaviors (activation and quiescence) can be caused by simple errors in the catalogues used to identify them. ....Such mistakes have the potential to undermine the relationship between the seismological community and the public we serve."

The points stated above highlight the urgency for standardization of measurement procedures and of careful documentation of introduced changes and their reasons. Only this can assure the unambiguous reproduction of so important event parameters such as magnitude and enable - if required – their correction for assuring long-term stability and representativeness of earthquake catalogs.

For a review of the development and use of the Richter scale see Boore (1989).

3.2.4.2 The new IASPEI standard ML

In order to avoid several of the above mentioned problems and inconsistencies in Ml determination and to reduce related data scatter and/or level discrepancies the IASPEI/CoSOI Working Group on Magnitude Measurements recommends the following for **IASPEI standard ML** (for more details and discussions see IS 3.3):

*"For crustal earthquakes in regions with attenuative properties **similar** to those of Southern California, the proposed standard equation is*

$$ML = \log_{10}(A) + 1.11 \log_{10}R + 0.00189*R - 2.09, \qquad (3.15)$$

*where A = maximum **trace** amplitude in **nm** that is measured on output from a **horizontal-component** instrument that is filtered so that the response of the seismograph/filter system replicates that of a **Wood-Anderson standard seismograph** but with a static magnification of 1 (see Table 1 and Figure 1 in IS 3.3) and R = **hypocentral distance in km**, typically less than 1000 km."*

Note that equation (3.15) is an expansion of that proposed by Hutton and Boore (1987). The constant term -2.09 is based on the experimentally determined attenuation and static magnification of the Wood-Anderson instrument by Uhrhammer and Collins (1990), rather than on the respective parameters specified earlier by the manufacturer (see discussion and Fig. 3.29 in 3.2.4.1). Further, the WG states:

"For seismographic stations containing two horizontal components, amplitudes are measured independently from each horizontal component, and each amplitude is treated as a single datum. There is no effort to measure the two observations at the same time, and there is no attempt to compute a vector average.

*For crustal earthquakes in regions with attenuative properties that are **different** than those of coastal California, and for measuring magnitudes with vertical-component seismographs, the standard equation is of the form:*

$$ML = \log_{10}(A) + C(R) + D, \qquad (3.16)$$

where A and R are as defined in equation (here 3.15)*, except that A may be measured from a **vertical-component** instrument, and where C(R) and D have been **calibrated** to adjust for the different regional attenuation and to adjust for any systematic differences between amplitudes measured on horizontal seismographs and those measured on vertical seismographs."*

Procedures to synthesize the responses of other seismographs from digital broadband recordings are meanwhile common knowledge (e.g., Plešinger et al., 1995 and 1996). Therefore, WA seismographs are no longer required for carrying out Ml determinations. Savage and Anderson (1995) and Uhrhammer, et al. (1996) demonstrated the ability to determine an unbiased measure of local magnitude from synthetic WA seismograms. Thus, a seamless catalog of Ml could be maintained at Berkeley, California. In a first approximation (although not identical) this may also be achieved by converting record amplitudes from another seismograph with a displacement frequency response $Mag(T_i)$ into respective WA trace amplitudes by multiplying them with the ratio $Mag_{WA}(T_i)/Mag(T_i)$ for the given period of A_{max} (see EX 3.1). Sufficient time resolution of today's high-frequency digital records is likewise no longer a problem.

Note: For differences between Richter´s (1935) and the now standard formula (3.15) as well as for admissible modifications of the WA response for improving the SNR and still enabling unbiased ML estimates of very weak earthquakes see sections 4.1 and 5.1.1 in IS 3.3.

3.2.4.3 Other Ml scales based on amplitude measurements

As highlighted by the IASPEI recommendation for an ML standard, Richter's and also Hutton and Boore´s attenuation corrections are valid for Southern California only. More recently, a new calibration function has been agreed upon for all California and vicinity (Uhrhammer et al., 2011). But shape and level of these California calibration functions may be different from those applicable in other regions of the world with different velocity and attenuation structure, crustal age and composition, heat-flow conditions and depth distribution of earthquakes. Accordingly, when determining Ml calibration functions for other regions, the amplitude attenuation law has to be determined first and then this curve has to be scaled to the original

definition of ML at 100 km epicentral distance (or at closer distance as recommended by Hutton and Boore, 1987; see Problem 3 in 3.2.4.1). Some examples for other regional Ml calibration functions have been plotted in Fig. 3.30. Formulas for these and many more regional calibration functions are given in Table 2 of DS 3.1 together with comments on their scaling, components to be used and the distance range of applicability. Those for continental shield areas revealed significantly lower body-wave attenuation when compared with Southern California (e.g., the calibration curve of Alsaker et al., 1991, in Fig. 3.30. Therefore, despite proper scaling to California ML at or near to Δ = 100 km, their calibration and thus derived Ml values for equal amplitude input data may already be several tenths of magnitude units smaller at several 100 km distance.

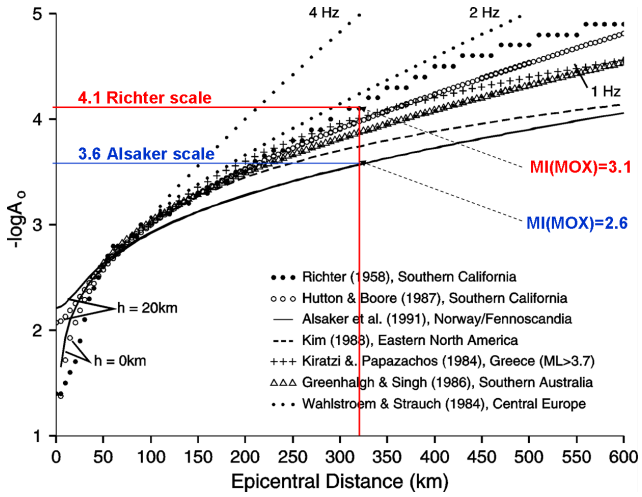

Fig. 3.30 Calibration functions for Ml determination in different regions. Some of them extend well beyond the 600 km distance plotted here, e.g., that of Alsaker et al. (1991) up to 1500 km. At this distance -log A_0 differs by 1.7 magnitude units from the extrapolated calibration curve for southern California. Even at much shorter distance, such as 320 km for a demonstration event recorded at station MOX, the difference is already to 0.5 m.u.

The problem of vector summing of amplitudes in horizontal component records or of arithmetic averaging of independent Ml determinations in N and E components can be avoided by measuring the maximum amplitude on vertical component recordings instead, provided that the respective -log A_0 curves are properly scaled to the original definition of Richter at Δ = 100 km or at shorter distances, as proposed by Hutton and Boore (1987) and done, e.g., for Tanzania (Langston et al., 1998), for better compensation of near range differences in attenuation properties and in the depth distribution of earthquakes. Several vertical component formulas have been proposed also for other regions (see. Table 2 of DS 3.1). At large distances, sometimes well beyond the distance of 600 km for which -log A_0 was defined by Richter (1958), they mostly measure on Lg waves. Alsaker et al. (1991) and Greenhalgh and Singh (1986) showed that A_{Zmax} is ≈ 1 to 1.2 times A_{Hmax} = 0.5 (A_{Nmax} + A_{Emax}) and thus yields practically the same magnitudes.

Note 1: Station corrections in some of these studies varied between -0.6 to +0.3 magnitude units (Bakun and Joyner, 1984; Greenhalgh and Singh, 1986; Hutton and Jones, 1993) and correlated broadly with regional geology. This points to the urgent need to determine both calibration functions and station corrections for Ml on a regional basis.

Note 2: Since sources in other regions may be significantly deeper than in southern California, either $\sigma(\Delta, h)$ should be determined or at least the epicentral distance Δ be replaced in the magnitude formulas by the "slant" or hypocentral distance $R = \sqrt{(\Delta^2 + h^2)}$. The latter is now common practice. E.g., the Ml scale for Kamchatka is based on Fedotov's (1968) K-scale (see IS 3.7, Figure 5) and is defined as $Ml = 0.5\ K_S - 0.75$. It uses the maximum ratio A/T for S-waves scaled against the S-P traveltime (which is approximately proportional to R). The calibration curve σ(S-P) for the K-scale is the averaged one over three depth bins in the depth range 0-200 km. Ml defined in this way is well correlated en mass with event mb (A. Gusev, personal communication 2013).

Note 3: There have been efforts to develop frequency-dependent regional calibration functions, e.g., for Central Europe (Wahlström and Strauch, 1984; see Fig. 3.30). But this breaks with the required continuity of procedures and complicates the calibration relationship for Ml.

Note 4: Increasing availability of strong-motion records and their advantage of not being clipped even by very strong nearby events have led to the development of (partially) frequency-dependent Ml^{SM} scales for strong-motion data (Lee et al., 1990; Hatzidimitriou et al., 1993). The technique to calculate synthetic Wood-Anderson seismograms from strong-motion accelerograms was first introduced by Kanamori and Jennings (1978). In any event, the best way to make Ml^{SM} values best compatible with standard ML, the broadband strong-motion records have to be pre-processed by applying double integration so as to produce the respective broadband displacement equivalent (with the uncertainty of the unknown integration constants). Then a WA simulation filter should be applied (see section 3.1 in IS 3.3 and for a general application example Margaris and Papazachos, 1999) before measuring the amplitudes. And, most importantly, a local/regional displacement calibration function carefully scaled to that in (3.15) has to be available.

3.2.4.4 mb_Lg

Short-period Lg waves with periods $T < 3$ s (see Chapter 2, 2.3.3 and definition in IS 2.1) die out even along short oceanic travel path but they may travel far with comparably low attenuation (e.g., in comparison with Sg) through the continental crust. This applies especially to travel paths of Lg in cratonic platform areas, such as those in North America and Eurasia. Accordingly, while Sg may no longer be recognizable Lg may become the prominent phase at distances above a few hundred km (see Fig. 2.17 in Chapter 2) and well recordable up to about 30° epicentral distance.

The Lg phase is a complicated seismic signal. It is comprised of many surfache higher modes having group velocities around 3.5 km/s. Lg energy is strongly scattered by crustal heterogeneities (Knopoff et al., 1973; Bouchon, 1982; Kennett, 1985 and 1986; Xie and Lay, 1994 and 1995). This complexity of Lg results in a very effective averaging of both the source radiation and crustal wave propagation effects. Therefore, statistical measures of Lg, such as rms amplitudes over a specified group velocity window, yield for given propagation paths very stable and accurate relative estimates of source strength, e.g., Lg magnitude values, which are useful in nuclear test discrimination and yield estimation (Xie and Lay, 1995). However, regional calibration for different travel paths is a prerequisite.

Lg magnitudes are calibrated either with respect to (or in a similar way as) Ml or to teleseismic mb. In the latter case they are usually termed mbLg or Mn (Ebel, 1982). Thus, when scaled to match with teleseismic mb at larger distances, a respective mb_Lg scale, covering the range between 4° and 30° (as originally proposed by Nuttli (1973) can bridge the gap between more local Ml scales and teleseismic (D > 20°) mb.

Moreover, mb_Lg has proven to yield rather stable magnitude estimates, even for single stations (Mayeda, 1993), with low scatter and thus good input data for estimating the yield of underground nuclear explosions (UNE) (e.g., Nuttli, 1986, Hansen et al., 1990). Further, since teleseismic P-wave records from earthquakes with magnitudes mb around 4 or less usually suffer of very low signal-to-noise ratio, mb_Lg permits to extend the discrimination capability between UNE and natural earthquakes on the basis of the Ms-mb criterion down to Ms = 2.5 (Patton and Schlittenhardt, 2005; Richards, 2002). This has made mb_Lg to a preference magnitude in the test-ban control community (e.g., Zhao et al., 2008).Yet, mb_Lg has also become a favorite regional magnitude in general seismological practice of North America, southern Asia and in several northern European states such as Denmark, Finland and Norway (see **EMSC-CSEM Newsletter of Nov. 15, 1999** via http://www.emsc-csem.org/Documents/?d=newsl). One should note, however, that some of the so-called Lg scales are often not proper mb_Lg - as shortly sketched below - but rather extensions of Ml, scaled to California ML and not to teleseismic mb, yet measuring Lg amplitudes up to much greater distances than common for chiefly Sg-based Ml.

Nuttli (1973) was first to propose a conventional type of formulas for mb(Lg) for the eastern United States that have been routinely used at the NEIC:

$$mb(Lg) = 3.75 + 0.90 \cdot \log_{10} \Delta + \log (A/T) \quad \text{for} \quad 0.5° < \Delta < 4°, \tag{3.17}$$

and

$$mb(Lg) = 3.30 + 1.66 \cdot \log_{10} \Delta + \log (A/T) \quad \text{for} \quad 4° < \Delta < 30°, \tag{3.18}$$

where Δ = distance in degrees, A = ground motion amplitude of Lg waves in microns, and T = period in seconds in the rante 0.5 to 1.5 s.. A is the magnification-corrected, sustained (3rd largest peak) amplitude in the Lg train, measured on vertical-component, short-period (SP) WWSSN seismograms and corrected for period-dependent magnification.

The two log-linear formulas, which match at $\Delta = 4°$, were required in order to approximate the empirical (A/T) observations in the Central U.S., which the exponential decay laws of Ewing et al. (1957), sufficiently well. And the constants had to be chosen such that mb(Lg) agrees for moderate size earthquakes in the U.S. with teleseismic mb(P).

Båth et al. (1976) developed a similar Lg scale for Sweden which is widely used in Scandinavia. Street (1976) recommended a unified mbLg magnitude scale between central and northeastern North America. Herrmann and Nuttli (1982) showed (later also Kim, 1998) that mbLg values are commonly similar to Ml when based on amplitude readings with periods around 1 s. They also proposed to define regional attenuation relations so that mbLg/Mn from different regions predict the same near source ground motions,i.e., that the mbLg scale becomes “transportable”. This new magnitude equation employs two terms to correct for amplitude decay (2nd term = geometrical decay and 3rd term = attenuation) and it requires that the attenuation γ of 1-Hz Lg waves is known beforehand. The formula reads:

$$mb(Lg) = 3.81 + 0.83 \cdot \log_{10} \Delta + \gamma \cdot (\Delta - 0.09°) \cdot \log e + \log A, \qquad (3.19)$$

where e = 2.718. Note that in this formula just amplitude A and not (A/T) is measured, again on WWSSN-SP records but in an even narrower range of period (0.8 s to 1.2 s) The constant in this formula was also determined by scaling mb(Lg) to teleseismic mb(P). Specifically, for earthquakes in central United States, an Lg amplitude A of 115 μm at distance 0.09° had to yield an mb = 5.0 to be consistent with teleseismic magnitudes. This differs from the convertional mb(Lg) formula which yields at this distance an A/T of 155 μm/s for mb =5.

Herrmann and Kijko (1983) developed a frequency-dependent scale mLg(f) in order to broaden the frequency domain within which mbLg is applicable. Ebel (1994) proposed mLg(f), calibrated to mb and computed with appropriate Lg spatial attenuation functions, to become the standard for regional seismic networks in northeastern North America. Ambraseys (1985) published calibration Q_g (for Sg and Lg) and Q_R (for crustal Rayleigh waves), respectively that are applicable for northwestern European earthquakes in the distance range $0.5° < D < 11°$.

The final form of an amplitude-based mb(Lg) formula has been proposed by Nuttli (1986) and is written in two parts: First a corrected "hypothetical" Lg amplitude at distance 10 km = 0.09° is calculated on the basis of the general Ewing et al. (1957) decay law that fits best the empirical regional attenuation curves and then, in a second step, mb(Lg) using this hypothetical amplitude, normalized to 110 μm, and the calibration constant. These formulas read:

$$A(10) = A(\Delta) \cdot (\Delta/10)1/3 \cdot [\sin(\Delta/111.1) / \sin(10/111.1)]1/2 \cdot \exp[\gamma \cdot (\Delta - 10)] \qquad (3.20)$$

and

$$mb(Lg) = 5.0 + \log [A(10)/110] , \qquad (3.21)$$

where A(Δ) is sustained ground motion amplitude in μm and Δ is distance in km. The minor deviations from the earlier Herrmann and Nuttli (1982) formulas are, besides the scaling to 110 μm instead of 115 μm, that the acceptable period range has been somewhat relaxed (0.7 s to 1.3 s) and that only amplitudes in the group velocity window of 3.6 to 3.2 km/s should be measured.

Based on the formulas developed by Nuttli (1986) and Herrmann and Nuttli (1982) the CoSOI Working Group on Magnitude Measurement recommended now (see IASPEI, 2013 and/or IS 3.3) the following **IASPEI standard formula for mb(Lg) = mb_Lg**:

$$\text{“} \qquad \boldsymbol{mb\_Lg = \log_{10}(A) + 0.833\log_{10}[r] + 0.4343\gamma(r - 10) - 0.87} \qquad \textbf{(3.22)}$$

*where A = "sustained ground-motion amplitude" in **nm**, defined as the third largest amplitude in the time window corresponding to group velocities of 3.6 to 3.2 km/s, in the period (T) range 0.7 s to 1.3 s; r = **epicentral distance** in **km;** γ = coefficient of attenuation in km^{-1}. γ is related to the quality factor Q through the equation $\gamma = \pi/(Q \cdot U \cdot T)$, where U is group velocity and T is the wave period of the L_g wave.*

*A and T are measured on output from a **vertical-component** instrument that is filtered so that the frequency response of the seismograph/filter system replicates that of a WWSSN **short-period** seismograph. Arrival times with respect to the origin of the seismic disturbance are used, along with epicentral distance, to compute group velocity U."*

Note: ***"γ is a strong function of crustal structure and should be determined specifically for the region in which the mb_Lg is to be used."***

Benz et al. (1997) describe in detail the procedure applied and the values derived in a comprehensive regional Lg attenuation survey for the continental United States.

The approximate equations (3.17) and (3.18) of Nuttli (1973) yield mb_Lg that are about 0.1 m.u. smaller than those of the proposed standard procedure when γ = 0.00063 km^{-1} in equation (3.22). Yet, preference is given to the proposed standard formula because of its transportability to regions with attenuation different than that of eastern North America (Nuttli, 1986; Patton, 2001).

Recent researches on mb_Lg and regional variation of Lg attenuation **commonly use root-mean-square (RMS) amplitude measurements** rather than measurements made at a single peak (e.g., Patton and Schlittenhardt, 2005; Phillips and Stead, 2008), The use of RMS amplitudes offers the promise of more precise mb_Lg measurements (according to Mayeda, 1993, with roughly 25% smaller residuals as compared to single amplitude mb_Lg), but will require the development of a new formula, which should then be calibrated with respect to equation (3.22). See in this contest also the last paragraph in the next section on Md and Mc. Developing the mb(Lg) scale for central Europe, Patton and Schlittenhardt (2005) had to calibrate all GRSN stations for site terms and for differences in Lg attenuation, because lateral variations in Lg Q turned out to be significant across the study area. Therefore, a regional Q model consisting of constant-Q partitions north, south and in the central Alps had to be developed.

3.2.4.5 Duration and coda magnitudes (Md or Mc)

The simplest magnitude to use for local earthquakes is the duration or coda magnitude (Md or Mc). Md scales have been developed as a complement or alternative to single-amplitude based Ml. Signal codas are formed by scattered waves, i.e., waves which did not travel the minimum paths between seismic source and receiver, being reflected and diffracted by lateral inhomogeneities of the propagation medium. The stronger the primary signal, the larger the signal-to-noise ratio and thus the coda duration d. Different procedures are applied for determining signal or coda duration such as:

- duration from the P-wave onset to the end of the coda, i.e., where the signal disappears in the seismic noise of equal frequency, as in Fig. 3.31);
- duration from the P-wave onset to that time when the coda amplitudes have decayed to a certain threshold level, given in terms of average or RMS signal-to-noise ratio or of absolute signal amplitudes or signal level. This is objective, reproducible and best suited for automatic coda length determination, not, however, for manual ones.
- total elapsed time = coda threshold time minus origin time of the event.

Thus d becomes a good estimator of signal strength or event magnitude, which is in the local range, in agreement with single scatter theories, even independent on recording distance when the total elapse time is taken (Aki and Chouet, 1975). Yet, it is also possible to estimate the magnitude of large earthquakes even at teleseismic distances by using the P-wave coda (Houston and Kanamori, 1986). Another distinct advantage of Md is that coda amplitudes

depend much less than maximum phase amplitudes on source radiation pattern and directivity (Masuda, 1992).

One of the main reasons, however, for developing Md scales was that analog paper or film recordings had a very limited dynamic range of only about 40 dB and analog tape recordings of about 60 dB. Even the dynamic range of early digital recorders with 12 or 16 bit A-D converters and thus 66 dB or 90 dB, respectively, was not yet enough to assure unclipped seismic records and A_{max}-based magnitude determinations in the case of strong earthquakes recorded at local and regional distances.

In contrast, Md (or Mc) scales are based on either the total signal duration or the duration of the most pronounced coda of the Sg and/or Lg phase of an event. Coda length can easily be estimated even on clipped records of low dynamic range. However, with 24 bit A-D converters and ≈140 dB usable dynamic range now being standard, clipping is usually no longer a pressing problem. It is rare that an event is not considered for analysis because of clipped record traces.

Note that scattering efficiency on small-scale heterogeneities depends on wavelength. Codas of seismic phases (also termed *signal-generated noise*) are well developed in short-period but not in long-period records and more pronounced in bandlimited than in broadband records (see Figs. 4.11-13???) in Chapter 4). Moreover, SNR conditions at station and network sites influence the Coda-SNR and thus the measured coda length above noise level. Therefore, Md scales should be developed for networks with given instrumentation (gain and bandpass range), noise conditions and practize a uniquely specified way of measuring signal duration and choosing the screen scaling appropriately. Fig. 3.31 illustrates to some extent, how variations in these parameters and related uncertainty in picking the coda end may influence the calculated Md values.

Moreover, one should also know that short coda length (< 10 s) are not a stable measure of earthquake size since they do not yet contain the backscattered energy from more distant heterogeneities (Aki and Chouet, 1975). Thus, one can not expect a generally valid relationship for Md calculation for both small (in the near range only recorded) and large events (recorded also at larger distances) (e.g., Bakun and Lindh, 1977).

According to Aki and Chouet (1975) coda waves from local earthquakes are commonly interpreted as back-scattered waves from numerous heterogeneities uniformly distributed in the crust and that only one scatterer has been met by not-minimum path rays before reaching the station. Therefore, for a given local earthquake **at epicentral distances shorter than 100 km** the total duration of a seismogram is almost independent of distance and azimuth and of structural details of the direct wave path from source to station. Also the shape of coda envelopes, which decay exponentially with time (see Fig. 3.22), remains practically unchanged. The dominating factor controlling the amplitude level of the coda envelope and signal duration is then the earthquake size. This allows development of duration magnitude scales without a distance term if coda duration is measured from the origin, i.e.:

$$Md = a_0 + a_1 \log d. \qquad (3.23)$$

Thus, quick magnitude estimates from local events are feasible even without knowing the exact distance of the stations to the source.

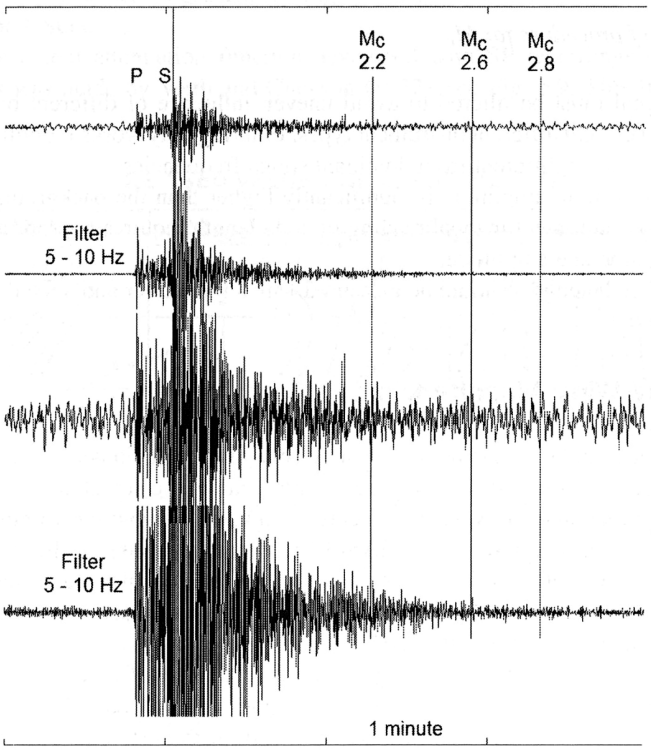

Fig. 3.31 Unfiltered (1st and 3rd trace) and filtered record traces of a local event with Ml = 2.8 at station FOO in Norway in 117 km epicentral distance, with the 3rd and 4th traces being amplified for better noise resolution. Note the significant differences in Mc = Md estimates using formula (3.27) below, depending on where one picks the end of the coda. High-pass filtering and record amplification may aid a more realistic picking. (Copy of Fig. 6.7 in Havskov and Ottemöller (2010); © Springer publishers).

At larger distances and with multi-scattering involved, also distance comes into play. A theoretical description of the coda envelopes as an exponentially decaying function with time and linear dependence on distance was presented by Herrmann (1975). He proposed a duration magnitude formula of the more general form:

$$Md = a_0 + a_1 \log d + a_2 \Delta. \qquad (3.24)$$

Most coda wave magnitude relationships are of this general type and use measured coda lengths larger than 30 s.

Havskov and Ottemöller (2010) show by way of example that the large variations in the formula parameters determined for different regions and thus the great variability of calculated Md values for equal values of d are much larger than common for A_{max}-based ML scales. They also argue that most of these differences are due to different ways of measuring coda length and to differences in SNR conditions but not due to so different tectonics and attenuation conditions.

A very early formula for the determination of local magnitudes based on signal duration was developed for earthquakes in Kii Peninsula in **Central Japan** by Tsumura (1967) and scaled to the magnitudes M_{JMA} reported by the Japanese Meteorological Agency:

$$Md = 2.85 \log (F - P) + 0.0014\,\Delta - 2.53 \qquad \text{for } 3 < M_{JMA} < 5 \qquad (3.25)$$

with P as the onset time of the P wave and F as the end of the event record (i.e., where the signal has dropped down to be just above the noise level), F – P in s and Δ in km (also in all later following relationships)

Another duration magnitude equation of the same structure has been defined by Lee et al. (1972) for the **Northern California** Seismic Network (NCSN). The event duration, d (in s), is measured from the onset of the P wave to the point on the seismogram where the coda amplitude has diminished to 1 cm on the Develocorder film viewer screen with its 20 times magnification. With Δ in km these authors give:

$$Md = 2.00 \log d + 0.0035\,\Delta - 0.87 \qquad \text{for } 0.5 < Ml < 5. \qquad (3.26)$$

The location program HYPO71 (Lee and Lahr, 1975) employs Eq. (3.25) to compute duration magnitudes, called FMAG. But it was found that Eq. (3.25) yields seriously underestimated magnitudes of events Ml > 3.5. Havskov and Ottemöller (2010) also calculated the greatest differences of this formula as compared to other formulas developed for other regions. Therefore, several new duration magnitude formulae have been developed for the **NCSN**, all scaled to Ml. One of the latest versions by Eaton (1992) uses short-period vertical-component records, a normalization of instrument sensitivity, different distant correction terms for $\Delta < 40$ km, $40 \text{ km} \le \Delta \le 350$ km and $\Delta > 350$ km, as well as a depth correction for h > 10 km.

Formulas according to (3.24) were also derived for **Norway by** Havskov and Sørensen (2006):

$$Md = 3.16 \log d + 0.0003\,\Delta - 4.28 \qquad \text{for } 0.5 \le Ml \le 5, \qquad (3.27a)$$

for **Mexico** by Havskov and Macias (1983):

$$Md = 2.40 \log d + 0.00046\,\Delta - 1.59 \qquad \text{for } 3 \le Ml \le 6, \qquad (3.27b)$$

for **East Africa** Dindi et al. (1995):

$$Md = 1.9 \log d + 0.0004\,\Delta - 1.2 \qquad \text{for} 3 \le Ml \le 5, \qquad (3.27c)$$

and for Northwestern Italy by Bindi et al. (2005) with signifantly different coefficients for each stations of a network of 12 stations, ranging for the constant term between -1,7 and -2.7, for the distance term between (2.8 and 4.9)×10exp-3 and for the duration term between 1.77 and 2.61.

In contrast, other formulas, mostly for smaller earthquakes recorded at shorter distances, were developed according to the general relationship (3.23), i.e., without a distance term for scaling smaller earthquakes recorded at closer distances, such as

by Bakun and Lindh (1977) for **California**:

$$Md = 0.71 \log d + 0.28 \qquad \text{for} 0.5 \le Ml \le 1.5, \qquad (3.28a)$$

by Viret (1980) for the **eastern USA**:

$$Md = 2.74 \log d - 3.38, \qquad (3.28b)$$

and by Castello et al. (2007) for **Italy,** with mostly large station corrections Scj for stations in Southern Italy:

$$Md = 2.49 \log d - 2.31 + Scj \qquad \text{for } 1.5 \le Ml \le 4.5, \qquad (3.29)$$

Other Md formulas used in **Albania, France, Italy, Portugal** and former **Yugoslavia** can be found in the **EMSC-CSEM Newsletter of Nov. 15, 1999** via http://www.emsc-csem.org/Documents/?d=newsl), for **Greece** in Kiratzi and Papazachos (1985), for **Sweden** in Wahlström (1979), for the Vogtland swarm earthquakes in **Germany** in Klinge (1989), for the **Caucasus** area in Rautian et al. (1979) and for **Japan** in Masuda (1992).

According to Eaton (1992), average station residuals between amplitude- and duration-based local magnitude estimates are practically independent of distance from the epicenter to at least 800 km. Moreover, when properly scaled mutually, the difference between these two independent estimates is, when averaged over 0.5 m.u. intervals, less than 0.05 in the magnitude range M = 0.5 to M = 5.5.

Note: Crustal structure, scattering and attenuation conditions vary from region to region and even from station to station (local site effects). The latter seem to dominate both amplitude-based and duration-based magnitude residuals. Older well-consolidated rocks produce negative residuals (due to smaller amplitudes and shorter durations) and younger unconsolidated rocks produce positive residuals (Eaton, 1992). No general formulas can therefore be given. They must to be determined locally for any given station or regionally for every network and be properly scaled to the best available amplitude-based Ml scale. In addition, the resulting specific equation will depend on the chosen definition for d, the local noise conditions, the sensor response and gain operated at the considered seismic station(s) of a network.

Moreover, with mb_Lg scales using increasingly instead of third peak or RMS amplitudes coda envelopes, they become a version of coda magnitudes scales Mc. Mayeda (1993), using 1-Hz Lg-coda envelopes, thus made very stable single-station estimates of magnitudes from Nevada test site underground nuclear explosions. Rautian et al. proposed already in 1981 the use of coda amplitude, not of duration, in the definition of coda-based magnitudes, since coda spectral amplitudes are closely related to the earthquake source spectrum (Rautian and Khalturin, 1978). Coda-amplitude based Lg-magnitude estimates have generally a five times smaller scatter. Rautian et al. (1981) designed two particular scales based on the records of short-period (SP) and medium-period (MP) instruments. A scale of this kind is still used routinely by the Kamchatka seismic network (Lemzikov and Gusev, 1989 and 1991; see also IS 3.7). The main advantage of such magnitude scales is their unique intrinsic accuracy; even a single-station estimate has a root-mean-square (RMS) error of only 0.1 or even less.

3.2.4.6 The Russian K-class system for classifying earthquakes

For quantifying the size of local and regional earthquakes in terms of released seismic energy the energy class (K-class) system has been developed since the late 1950s in the former Soviet Union (FSU). For small and moderate earthquakes in the catalog *"Earthquakes in the USSR"* only K values are given, supplemented by magnitude values based on body and surface-wave readings only for larger, world-wide recorded earthquakes (see section 3.2.5 on common teleseismic magnitude scales and Table 4 in DS 3.1).

Nature, origin, and methodology of the K-class system are poorly known to western seismologists studying Soviet and Russian seismological data, yet they are of great interest and importance to those conducting detailed research on the seismicity of the former USSR (FSU) with the aim to make it also quantitatively compatible with other seismicity data and maps on a regional and global scale (Rautian et al., 2007; Mackey et al., 2010). We have, therefore, added to NMSOP-2 an elaborate new information sheet **IS 3.7**. It outlines in detail the conditions to be met and the assumptions made in developing the K-scale, looks into the conversion relationships between different regional K-scales and ISC mb and Ms as well as Mw and Me magnitude.

K-class was defined as $K = \log_{10} E_S$ with E_S in units of Joules. Yet, available instrumentation and analysis tools as well as simplifications introduced in the interest of mass routine measurements by technical personal resulted in the development of various regional K-scales which mostly do not measure $(A/T)_{max}$ (proportional to ground motion velocity) but displacement amplitudes A only. This, however, made in fact K to be a size estimator which is more closely related to Ml and for small to moderate size earthquakes also to Mw rather than being a good estimator of released seismic energy E_S or modern energy magnitude Me. An exception is the Kamchatka K, which is based on measuring $(A/T)_{max}$ (see Figure 5 in IS 3.7). Therefore, it scales also reasonably well with teleseismic Me based on the integration of squared velocity amplitudes on broadband records (see Figure 11 in IS 3.7).

Generally, there exist significant differences between the various local to regional K-scales, as they exist for any local-regional magnitude scale (see sections 3.2.4.3 to 3.2.4.5 for Ml, Md and mb(Lg)). This makes a simple and globally valid conversion of published K values into relevant magnitude equivalents impossible. For a very rough orientation, however, which K value would approximately correspond to a given "western" magnitude, or vice versa, Bormann derived, on the basis of a figure published by Riznichenko (1992) (see Figure 8 in IS 3.7), the following "conservative" formulas

$$\log E_S \approx K = 1.8\ M + 4.1, \tag{3.30a}$$

or, when resolved for M,

$$M = 0.556\ K - 2.3 \tag{3.30b}$$

where M, depending on distance and event size, is supposed to relate either to Ml (for values << 4 to about 6), mb (for > 4 to about 5.5), mB (between about 5.5 to 7.5) or Ms (> 6 to about 8.5).

However, according to Fig. 3.32, the Eqs.(3.30a) and (3.30b) generally estimates for a given Mw a higher K than any of the other K or magnitudes scales, or, for a given K underestimates Mw or the respective other magnitude values.. The differences in K are smallest and in the

range 3 < Mw < 6.5 almost negligible when calculating K according to the linear Rautian (1960) formula for Tadshikistan, which is practically identical with Eq. (3.30b).:

$$M = (M_L) = 0.56\ K - 2.22. \qquad (3.31)$$

Yet, when lowering in Eq.(3.30) K by about 1.5 units this would result in a better **average** M to K conversion estimate, although with a large average deviation in the order of 1 unit in K with respect to other specific regional conversion relationships.

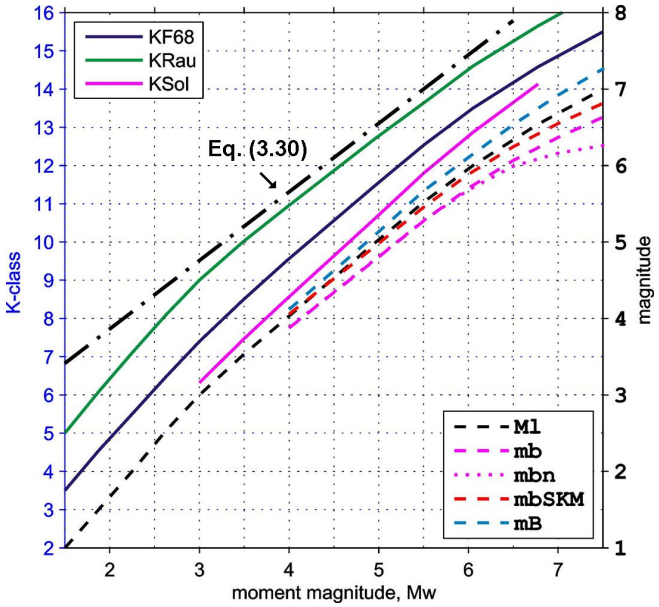

Fig. 3.32 Non-linear relationships between K-class, Mw, Ml and different kinds of P-wave magnitudes according to Figure 9 in IS 3.7, provided by A. Gusev, in comparison with the linear M-K relationship of Eq. (3.30). For explanation of legend and references see IS 3.7.

This is confirmed when comparing Eq. (3.31) with the linear regressions between K and short-period mb = Mb in Figure 7a of IS 3.7, however Eq. (3.31)) is for the various linear K-Ms relationships a somewhat better average estimator (Fig. 3.33). Thus, one should be aware of the uncertainty of K to M and M to K conversions which depend on the type of magnitude and the sometimes large differences between the various regional K scales. The causes of these differences may not even be of pure seismological reasons, such as differences in prevailing source and wave propagation processes. E.g., the discrepancy between KF68 and KSol in Fig. 3.32 is mainly due to an error in the absolute scaling constant of KSol, which result in K values that are 0.6 units too low (Fedotov, 1972). Also assumptions made about the shear wave velocity for calculating the wave energy density on the reference sphere have been somewhat different, e.g., for the Rautian and Fedotov K scales (see related discussion in IS 3.7). Such inconsistencies in K procedures and scaling may significantly biases the seismological conclusions which could be drawn from the data and should be eliminated.

None the less, the authors of IS 3.7 see great potential for modernizing and homogenizing the K-class procedures with the aim to establish an empirically founded simple and very useful energy-related complement to both teleseismic Me as well as to local and regional Ml. Proper Me calculations, which are chiefly based on model assumptions and full-fledged energy

integration, are hardly possible on a mass routine basis and at the higher frequencies at which small to moderate local and regional earthqakes are recorded. On the other hand Ml is, in contrast to **what K is supposed to be**, more closely related to seismic moment and Mw than to **released seismic energy**. But, in order to bring up K to what it was originally intended for, requires that future K is consistently calculated only on the basis of maximum measured ground motion velocity amplitudes V_{max} instead of displacement amplitudes A_{max}. And V_{max} should be measured directly on standardized, in all regions compatible short-period records with identical (real or simulated) transfer functions that are velocity proportional in a sufficiently wide bandpass range that covers the expected corner frequencies of the source spectra of all earthquakes in the K or magnitude range of interest. Similarly, a unique model and elastic parameter set used for calculating energy density as well as the procedures for calibrating regional K-scales to a standard reference K-scale have to be developed, agreed upon and carefully documented, as they exist for standard ML (see 3.2.4.3). Otherwise, no interregional compatibility of K values can be achieved.

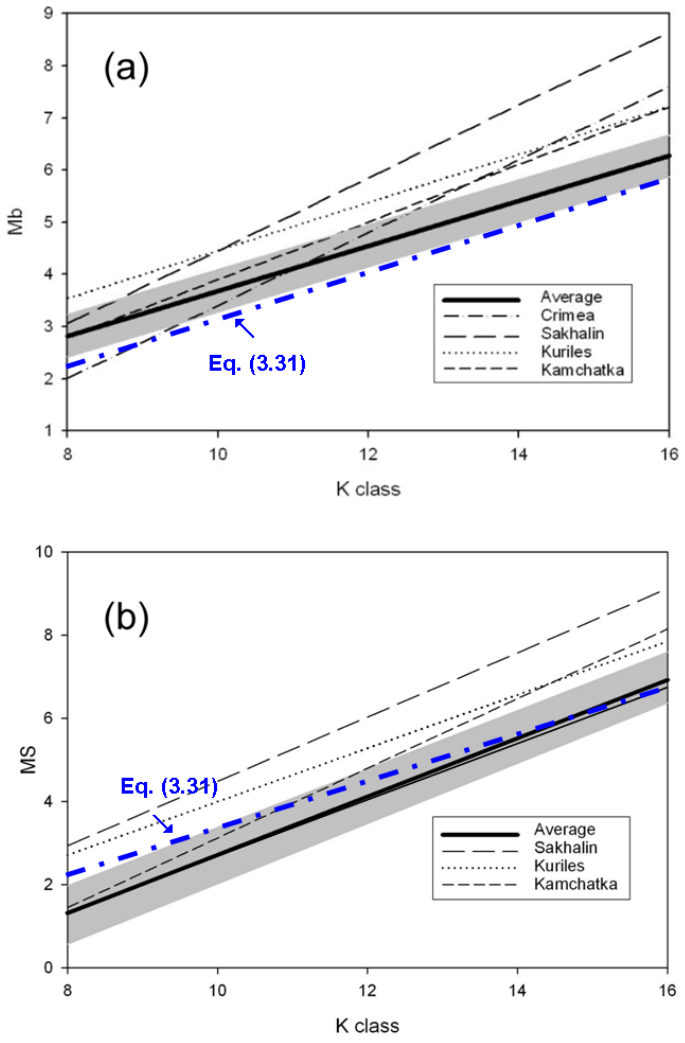

Fig. 3.33 Linear orthogonal regression relationships between (a) ISC mb = Mb and (b) ISC Ms = MS with different regional K scales (according to Figure 7 in IS 3.7) and their comparison with Eq. (3.31).

3.2.4.7 The Japanese M_{JMA} scale

The Japan Meteorological Agency (JMA) uses routinely its own magnitude scale. M_{JMA} magnitudes are determined from the maximum ground displacement amplitude A of the total seismic event record trace and measured at any station at epicentral distance $\Delta < 2000$ km. The maximum amplitude may be either that of a surface wave or of a body wave recorded by a seismograph with an eigenperiod of 5 s. According to Katsumata (1996) two calibration functions are used:

a) for earthquakes at focal depth h < 60 km Tsuboi´s (1954) formula, which is said to be well calibrated with the Gutenberg and Richter (1954) magnitudes. It reads

$$M_{JMA} = \log \sqrt{(A_N^2 + A_E^2)} + 1.73 \log \Delta - 0.83 \qquad (3.32a)$$

where A_N and A_E are half of the maximum peak-to-trough amplitudes in μm with periods $T \leq 10$ s in the two horizontal components and Δ is given in km, and

b) for earthquakes deeper than 60 km Katsumata´s (1964) formula

$$M_{JMA} = \log A + K \qquad (3.32b)$$

where K is a function of Δ and h and given as a table by Katsumata (1964). Also this formula was scaled so that it gives almost the same magnitude values as that of Gutenberg and Richter (1954). Both Koyama et al. (1982) and Nuttli (1985) give rather similar (average graphical) relationships between Ms and M_{JMA}. The agreement is almost perfect at magnitude 7, however M_{JMA} tends to be increasingly larger than Ms(20) for smaller magnitudes, up to about 1 m.u. at $M_{JMA} = 5$.

Interestingly, the Tsuboi formula (3.32a) was derived on the basis of records of the astatic medium-period Wiechert horizontal pendulum records (see *Dedication to Wiechert and Galitzin* via the NMSOP-2 cover page), which had a flat displacement response for periods between about 0.1 and 5 s. All later introduced instruments or simulation filter responses used for measuring M_{JMA} mimic approximately the original Wiechert response. However, for earthquakes with Mw < 5.5 nowadays also velocity proportional responses, flat between about 1 and 30 Hz may be used for measuring an M_{JMA}(velocity). Further, station magnitudes that deviate from the average network magnitude more than 0.5 m.u. are not taken into account in calculation the event magnitudes and mean values of the latter with standard deviations ≥0.35 m.u. are not given as event magnitudes (personal communication by Yasuhiro Yoshida, 1996).

3.2.5 Common teleseismic magnitude scales (P. Bormann and S. Wendt)

Wave propagation in deeper parts of the Earth is, within a few percent of lateral velocity perturbations (see Chapter 2, Fig. 2.80), more regular than in the crust and can for most purposes be described sufficiently well by 1-D velocity and attenuation models. This permits derivation of globally applicable teleseismic magnitude scales. Fig. 3.34 shows smoothed A-Δ relationships for short-period P and PKP waves as well as for long-period surface waves for teleseismic distances, normalized to a magnitude of 4.

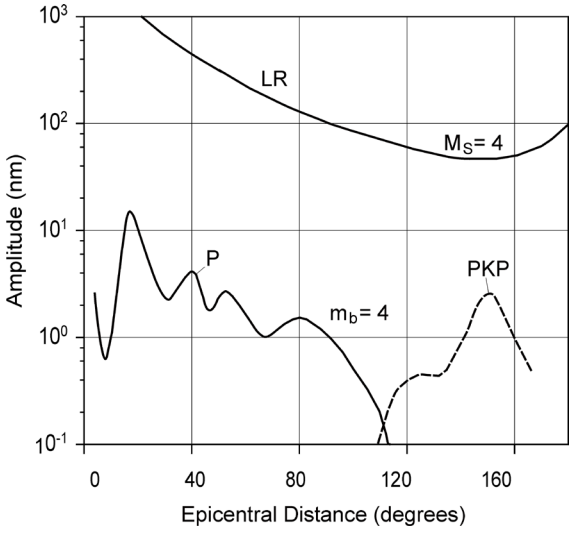

Fig. 3.34 Approximate smoothed amplitude-distance functions for P and PKP body waves (at about 1 Hz) and of long-period Rayleigh surface waves LR at periods T ≈ 20 s for an event of magnitude 4.

From Fig. 3.34 the following general conclusions can be drawn:

- Surface waves and body waves have a different geometric spreading and attenuation. While the former propagate in two dimensions only, with amplitudes A decaying with distance Δ roughly ~ $\sqrt{\Delta}$ the latter propagate three-dimensionally, with amplitudes decaying in a homogeneous full space ~ **Δ.** Therefore, for shallow seismic events of the same magnitude, surface waves have generally larger amplitudes than body waves.
- Surface wave amplitudes change smoothly with distance. They generally decay up to about 140° and increase again beyond about 150°-160°. The latter is due to the increased geometric focusing towards the antipodes of the spherical Earth's surface which then overwhelms the amplitude decay due to attenuation.
- In contrast to surface waves, the A-Δ relations for first arriving longitudinal waves (P and PKP) show significant amplitude variations. The latter are mainly caused by energy focusing and defocusing due to velocity discontinuities in deeper parts of the Earth. Thus the amplitude peaks at around 20° and 40° are related to discontinuities in the upper mantle at 410 km and 670 km depth, the rapid decay of short-period P-wave amplitudes beyond 90° is due to the strong velocity decrease at the core-mantle boundary ("core shadow"), and the amplitude peak for PKP near 145° is caused by the focusing effect of the outer core (see Fig. 11.59???).

Other body wave candidates for magnitude determinations again behave differently, e.g. PP which is reflected at the Earth's surface half way between the source and receiver. PP does not have a core shadow problem and is well observed up to antipode distances. Furthermore, one has to consider that body waves are generated efficiently by both shallow and deep earthquakes. This is not the case for surface waves. Accordingly, the different A-Δ-h behavior of surface and body waves requires different calibration functions if one wants to use them for magnitude determination.

3.2.5.1 Surface-wave magnitude scales Ms and the new IASPEI standards

Gutenberg (1945a) developed the magnitude scale Ms for teleseismic surface waves:

$$Ms = \log A_{Hmax}(\Delta) + \sigma_S(\Delta). \quad (3.33)$$

It is based on measurements of the maximum horizontal ground motion displacement amplitudes $A_{Hmax} = \sqrt{(A_N^2 + A_E^2)}$ of the surface wave train at "periods of about" 20 s although Gutenberg used occasionally also periods as low as 12 s and as high as 23 s (Abe, 1981a; Lienkaemper, 1984; see section 4.4 in IS 3.3). The surface-wave maximum usually corresponds to the Airy phase, a local minimum in the group velocity dispersion curve of Rayleigh surface waves which arises from the existence of a low-velocity layer in the upper mantle (see Fig. 2.10 in Chapter 2).

It should be noted, however, that according to Geller and Kanamori (1977) Gutenberg did not measure the true maximum horizontal motion vector with both components measured at the same time. Rather, he combined the largest amplitude in the A_N component with the largest amplitude of A_E, although they might occur at different time and belong to different types of surface waves (see Figure 5 in Section 4.4 of IS 3.3). There was no corresponding formula given for using vertical component surface waves, which would have avoided this problem, because no comparably sensitive and stable vertical component long-period seismographs were available at that time.

The calibration function $\sigma_S(\Delta)$ is the inverse of a semi-empirically determined A-Δ-relationship scaled to an event of Ms = 0, thus compensating for the decay of amplitude with distance. The specified Gutenberg (1945a) formula, applicable between $20° \leq \Delta < 130°$ epicentral distance, reads:

$$Ms = \log A + 1.656 \log \Delta° + 1.818 \quad (3.34)$$

where Δ° is in degrees and A the ground motion displacement amplitudes in μm. Differences in the calibration term are <0.05 m.u. as compared to respective tabulated calibration values published by Richter (1958) (see DS 3.1). The latter, however, account better than the simple formula for the energy focusing of surface waves towards the antipodes. The differences between Ms values calculated for distances >130° according to (3.33) or by using the tabulated calibration values are 0.07 m.u. at 140°, 0.12 m.u. at 160° and 0.55 m.u. at 180°.

The Gutenberg relationship was further developed by Eastern European scientists. Soloviev (1955) proposed to use instead of the maximum ground displacement A_{max} the maximum ground particle velocity $V_{max} = 2\pi(A/T)_{max}$ since the latter is more closely related to seismic energy. Moreover, $(A/T)_{max}$ also better accounts for the large variability of periods at which surface-waves have their largest amplitudes, depending on distance of travel, crustal structure but also on magnitude and source depth, i.e., on the primary conditions of wave excitation. And finally, measuring $(A/T)_{max}$ permits rather stable magnitude estimates in a wider range of distances than the Gutenberg relationship which requires to read only periods around 20 s at teleseismic distances.

Although for most continental Rayleigh waves the Airy phase periods are around 10 to 15 s and for dominatingly oceanic travel paths periods around 20 s and more (Bullen and Bolt,

1985; Marshall and Basham, 1972), the actual range of periods at which $(A/T)_{max}$ in the surface-wave trains is observed in seismic broadband records is much larger. Respective periods, measured at the China Earthquake Network Center (CENC), have been plotted over epicenter distance in Fig. 3.35. Despite the great data scatter an average distance trend is obvious.

Based on much earlier observations of this kind by Soloviev and Shebalin (1957) and Karnik (1956), a team of researchers from Moscow and Prague proposed a new Ms scale and calibration function (Karnik et al., 1962 ; Vanek et al., 1962):

$$Ms = \log (A/T)_{max} + \sigma_S(\Delta) = \log (A/T)_{max} + 1.66 \log \Delta + 3.3. \qquad (3.35)$$

It is applicable at epicentral distances $2° < \Delta < 160°$, for sources that are less than 60 km deep and to surface-wave amplitude readings with periods above 3 s. The IASPEI Committee on Magnitudes recommended at its Zürich meeting in 1967 the use of "the Moscow-Prague 1962 formula" as **standard for Ms determination.**

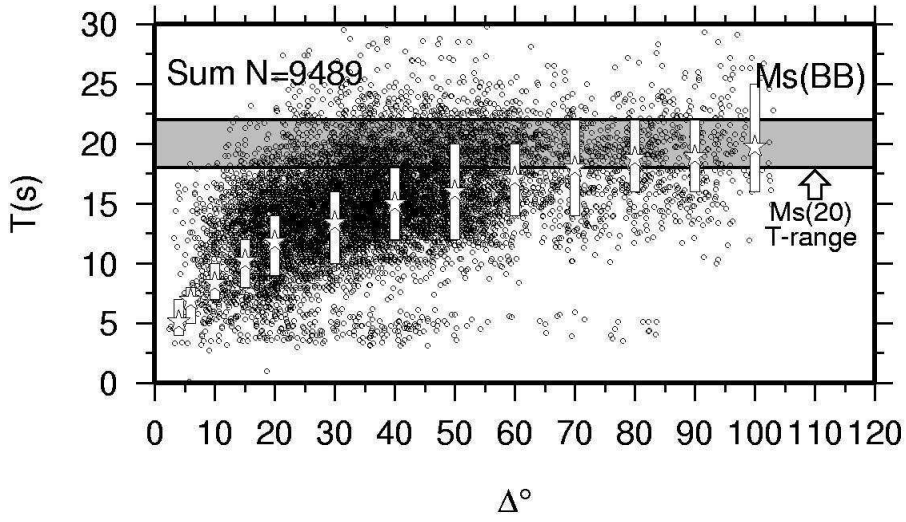

Figure 3.35 Variability of periods associated with V_{max} of the Rayleigh wave group depending on distance Δ. The gray shaded stripe marks the period range for which traditional Ms measurements at the U.S. Geological Survey´s National Earthquake Information Center (NEIC) are carried out. Light gray columns give the observed range of average periods as published by Vaněk et al. (1962) and Willmore (1979), and the stars give the respective average periods of the plotted open circle data points within the related magnitude segment. Copy of Figure 8 in Bormann et al. (2009), p. 1874, © Seismological Society of America.

The recommendation to use the Prague formula as standard for Ms calculation has generally been accepted by the global seismological community. However, as outlined by Bormann et al. (2009) there have been widespread misunterstanding and wrong statements in publications by other authors about how and in which ranges of distance and periods this formula should be used. No wonder that the concerned U.S. agencies decided to use it only at teleseismic distances and for amplitude readings in the period range 18s to 22 s in keeping with Gutenberg´s original formula and recommendations. This, however, made the deliberate

introduction of $(A/T)_{max}$ in the Prague formula practically meaningless, because differences in period readings in this narrow period range make for less then 0.1 m.u. difference. Yet, this U.S. practice, based on amplitude readings on records of the long-period WWSSN-LP instrument (see response in Fig. 3.20), became standard throughout the western seismological community.

In contrast, seismological observatories in the former Soviet Union (FSU) and its allied countries used formula (3.35), as recommended in the original publications and in the Willmore (1979) Manual of Seismological Practice. And A and T values were read on records of type Kirnos seismographs with displacement proportional response between about 0.1 and 10 to 20 s (see response Fig. 3.20), as most of the earlier data readings which had led to the derivation of the Prague formula.

In China, however, Ms values were routinely determined according to both Ms concepts. This provided to the IASPEI/CoSOI WG on Magnitudes a unique opportunity to compare the respective data measured on the same stations of the China National Seismic Network and analyzed by the same personnel at the China Earthquake Network Center (CENC). The results, published by Bormann et al. (2007), revealed both similarities and relevant differences of the respective Ms values and encouraged the WG to propose the following two **IASPEI standards for Ms** (see IASPEI 2005 and its updates of 20011 and 2013):

Ms(20), or Ms_20 in the ISF format (see Chapter 10) for data exchange and archiving, and Ms(BB), or Ms_BB, respectively. Their abridged definitions read as follows (for more details see IS 3.3):

$$\boldsymbol{Ms\_20 = \log_{10}(A/T) + 1.66\log_{10}\Delta + 0.3,} \qquad \textbf{(3.36)}$$

"where A = ***vertical-component*** *ground displacement in* ***nm*** *measured from the maximum trace-amplitude of a surface-wave phase having a period between* ***18 s and 22 s*** *on a waveform that has been filtered so that the frequency response of the seismograph/filter system replicates that of a World-Wide Standardized Seismograph Network (WWSSN)* ***long-period seismograph …*** *with A being determined by dividing the maximum trace amplitude by the magnification of the simulated WWSSN-LP response at period T, Δ =* ***epicentral*** *distance in degrees,* $\boldsymbol{20° \le \Delta \le 160°}$*".*

Equation (3.36) is formally equivalent to the Ms equation proposed by Vaněk et al. (1962) but is here applied to vertical motion measurements in a narrow range of periods. Moreover, formula (3.36) should be applied only to shallow earthquakes. *Ms_20* is expected to significantly underrepresent the energy released by intermediate- and deep-focus earthquakes due to their less effective generation of 20 s surface waves. Therefore, some agencies generally compute Ms_20 only for shallow-focus earthquakes, typically those whose confidence-intervals on focal-depth would allow them to be shallower than 50 or 60 km. For deeper earthquakes adjustment would need to be made, e.g., in accordance with Herak et al. (2001) (see also Question 4 below) in order to assure compatibility of Ms_20 data within the acceptable uncertainty limit of about 0.1 m.u. for IASPEI standard magnitudes.

For Ms_BB the standard formula reads:

$$\boldsymbol{Ms\_BB = \log_{10}(V_{max}/2\pi) + 1.66\,\log_{10}\Delta + 0.3,} \qquad \textbf{(3.37)}$$

*"where V_{max} = ground **velocity in nm/s** associated with the maximum trace-amplitude in the surface-wave train, as recorded on a **vertical-component** seismogram that is **proportional to velocity**, where the period of the surface-wave, T, should satisfy the condition **3 s < T < 60 s**, and where T should be preserved together with V_{max} in bulletin data-bases; Δ = **epicentral** distance in degrees, **2° ≤ Δ ≤ 160°**"*

Formula (3.37) is based on the Ms equation proposed by Vaněk et al. (1962), but is here applied to vertical motion measurements and is used with the $\log_{10}(V_{max}/2\pi)$ term replacing the $\log_{10}(A/T)_{max}$ term of the original. (3.37) could be further simplified by including $-\log_{10}2\pi = -0.8$ into the constant, thus sparing one operation and reading

$$Ms\_BB = \log_{10}V_{max} + 1.66\ \log_{10}\Delta - 0.5. \qquad (3.37a)$$

Also Ms_BB should be calculated for shallow focus earthquakes only, unless appropriate depth corrections are made (see Question 4 below).

As of now (2012), both the ISC and NEIC use Eq. (3.36) for the determination of Ms from events with focal depth h < 60 km without specifying the type of waves or components considered. The ISC accepts both vertical or resultant horizontal amplitudes of surface waves, with periods between 10 - 60 s from stations in the distance range 5° - 160° but calculated the representative average Ms only from observations between 20° - 160°. In contrast, the NEIC calculated so far only Ms_20 from vertical component readings of stations between 20° ≤ Δ ≤ 160° and for reported periods of 18 s ≤ T ≤ 22 s. This limitation in period range is not necessary and limits the possibility of Ms determinations from weaker and regional earthquakes. However, both agencies are now introducing the IASPEI standard procedures according to the above definitions, besides calculating complementary magnitude data (see, e.g., Tab. 10.5 in Chapter 10).

Recently, there has been again a tendency to determine the surface-wave magnitude by specifying the type of the waves and/or components used, e.g., MLRH or MLRV from Rayleigh waves and MLQH from Love waves or simply MLH and MLV as was the practice in Eastern Germany in the 1960's (see Tab. 3.1) and recommended already in 1967 by the IASPEI Committee on Magnitude at Zürich. Since the newly proposed IASPEI Seismic Format (see 10.2.5) accepts such specifications (in the case that they require more than 5 characters in the metadata reported to data centers), the IASPEI WG on Magnitudes intends to elaborate recommendations for unambiguous standards and "specific" magnitude names. For a preliminary version see IS 3.2.

Question 1: Are the new IASPEI Ms standards compatible with Gutenberg Ms?

For 20 s surface waves of the same amplitudes Eqs. (3.35) and (3.36) yield about 0.18 m.u. (0.19 m.u. at Δ = 100°) units larger Ms values than the original Gutenberg formula (3.34). Therefore, Abe (1981a) gave the following relationship between Ms determinations by NEIC using Eq. (3.35) and M_{GR} values published by Gutenberg and Richter (1954):

$$Ms(\text{"Prague"}, NEIC) = M_{GR}(\text{Gutenberg-Richter}) + 0.18. \qquad (3.38)$$

This conclusion, however, could **not be confirmed** by Lienkaemper (1984). Recomputations with the Moscow-Prague formula for the same events were only 0.03 m.u. higher on average

than M_{GR}. In section 4.4 of IS 3.3, Bormann and Dewey give additional reasons for the good agreement. Moreover, Bormann et al. (2009) compared Ms(NEIC) with strict Ms_20 determinations and found an excellent agreement (Fig. 3.36). Thus the **compatibility with earliest available and future Ms determinations at periods around 20 s is quantitatively assured** despite several changes in instrumentation and in the procedure of reading amplitudes on horizontal and later vertical-component recordings.

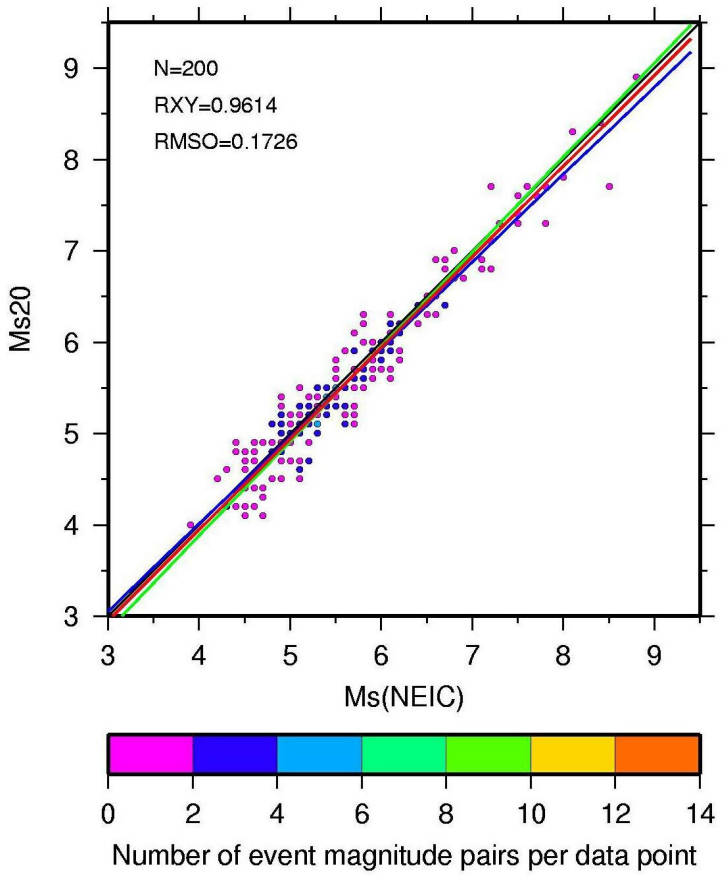

Fig. 3.36 Data and linear regression relations (standard and orthogonal) between the new IASPEI standard Ms_20, measured at the China Earthquake Network Centre (CENC) by using China network data alone for earthquakes in the years 2001-2007, and the respective event Ms(NEIC) based on global data. RXY – correlation coefficient; RMSO – orthogonal rms error, based on data published in Bormann et al. (2009).

NEIC never measured Ms in a wider range of period and distance. Therefore, a similar comparison can not be made with Ms_BB. But Fig. 3.37 shows an excellent overall correlation between Ms_20 and Ms_BB, yet with a slight systematic difference in trend: For magnitudes less than about 6.5 Ms_BB tends to be increasingly larger, reaching on average 0.3 m.u. at Ms_BB = 4.5 (Fig. 3.37). The main reason is that the average period at which the surface waves have their largest V_{max}, respectively $(A/T)_{max}$, depends also on magnitude, dropping from about 16 s at Ms_BB = 6.5 down to about 11 s at Ms_BB = 4.5, i.e., well below the 18 to 22 s period range at which Ms_20 is measured (see Figure 7 in Bormann et al., 2009). Accordingly, at T = 11 s the ratio A/T is twice as large as at T = 22 s. This makes for a difference of 0.3 m.u.

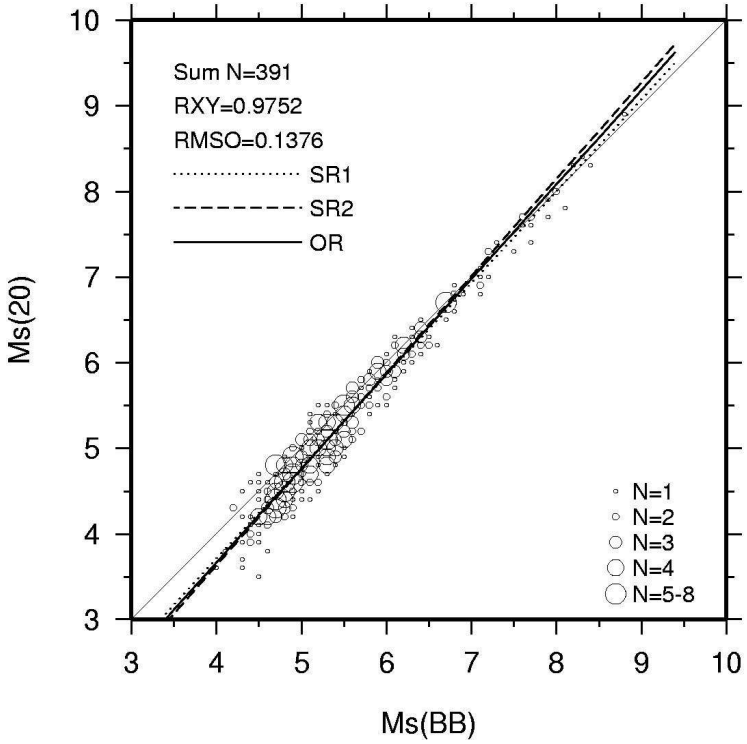

Fig. 3.37 Data and linear regression relations (standard and orthogonal) between the new IASPEI standard magnitudes Ms_20 and Ms_BB, measured at CENC. RXY = correlation coefficient, RMSO = orthogonal root mean square error. Figure compiled from data published in Bormann et al. (2009).

Figure 7 in IS 3.3 illustrates how in general (although not in each single case) the difference between Ms(BB) and Ms(20) grows with growing deviation of the periods at which V_{max} is measured in BB records from the narrow period range of Ms_20. Since surface waves of weaker earthquakes are recorded only at shorter distances with dominatingly shorter periods this magnitude dependence on the measured surface-wave periods translates also into a distance dependence (see Fig. 3.35). One consequence is that Ms_20 data systematically underestimate Mw at magnitudes below about 6.5 at which long-period energy is systematically less radiated than at shorter periods (see Fig. 3.5 right; Kanamori and Anderson, 1975; Ekström and Dziewonsky, 1988). The then larger Ms_BB values reduce this difference by almost 50% (Fig. 3.38). Therefore, **Ms_BB,** being in best tune with the Ms standard Eq. (3.35), **provides essential complementary information to Ms_20** and allows for more Ms determinations **also in the near regional range.**

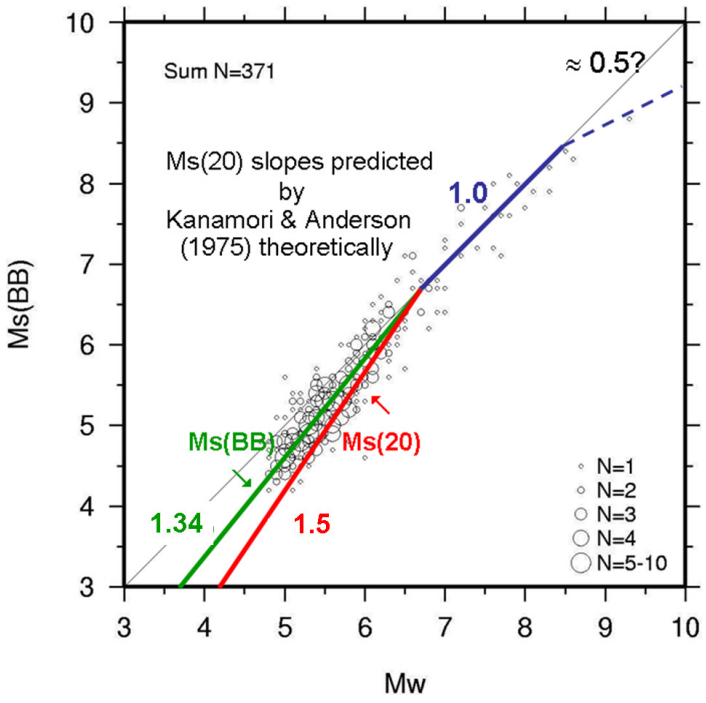

Fig. 3.38 Data and linear regressions between the new IASPEI standard Ms_BB, measured at CENC, and Mw(GCMT) as well as the approximate respective regression line of Ms_20 for Mw < 6.5. Figure compiled according to data published in Bormann et al. (2009).

Question 2: Is Ms measured on horizontal and vertical components compatible?

The calibration terms in both the Gutenberg and the Moscow-Prague formula for Ms determination had been derived for the correction of amplitude readings in horizontal (H) component records only. The introduction of stable long-period vertical component (V) seismometers into global seismological practice in the 1960s introduced another change in Ms measurement practice. According to Hunter (1972) the differences between Ms(V) and Ms(H) are negligible. This was confirmed by Bormann and Wylegalla (1975). According to their orthogonal regression relationship

$$MLV = 0.97MLH + 0.19, \qquad (3.39)$$

with a correlation coefficient of 0.98 and a standard deviation of ± 0.11m.u. only, the two magnitudes differ on average in the magnitude range between 4 to 8.5 less than 0.07 m.u. Thus, both findings **confirm the continuity and compatibility of old and modern Ms data**. Therefore, from May 1975 onwards, the USGS decided to calculate their Ms exclusively from vertical component readings. Since that time, Ms(NEIC) is in fact identical with the IASPEI confirmed standard magnitude Ms_20.

Question 3: How reliable the calibration formulas for Ms_determination compensate for the distance dependence of amplitudes?

Both the original Gutenberg relationship (3.33) and the Moscow-Prague IASPEI standard relationship (3.35) are rather simple and supposed to be used up to 140°, respectively 160°

epicentral distance only. Reason: Both formulas do not well account for the amplitude increase beyond 140° (see Fig. 3.34). This, however, can be avoided by using the respective tabulated calibration values instead (see DS 3.1., Tables 3 and 4). For Ms_BB determination the tabulated Moscow-Prague calibration values agree at epicentral distances between 1° and 140° within 0.05 magnitude units with the values calculated from the calibration term in formula (3.35). For larger distances, however, this formula overestimates the magnitude between 0.05 and 0.55 (at 180°) m.u. About the same applies when comparing values calculated with the Gutenberg formula (3.33) with the related tabulated calibration values published by Richter (1958). Therefore, **preference should be given to the use of the tabulated values, at least for distances >140°.**

However, several authors realized that using standard formula (3.35) for calculating 20 s Ms results in systematic distance-dependent biases (van Seggern, 1977; Herak and Herak, 1993; Rezapour and Pearce, 1998). Therefore, they proposed revised formulas for Ms_20 calculation. The revised formula of Herak and Herak for Ms_20 is:

$$Ms = \log (A/T)_{max} + 1.094 \log \Delta + 4.429. \qquad (3.40)$$

It is based on USGS data, i.e., on amplitude readings in the period range 18 to 22 s. It provides distance-independent estimates of Ms over the whole distance range $4° < \Delta < 180°$. Ms values according to Eq. (3.40) are equal to those from Eq. (3.35) at $\Delta = 100°$, larger by 0.39 magnitude units at $\Delta = 20°$ and smaller by 0.12 units for $\Delta = 160°$. Eq. (3.40) is practically equal to the formulae earlier proposed by von Seggern (1977) and similar to the more recent formula (18) obtained by Rezapour and Pearce (1998) on the basis of all ISC Ms data between 1978 and 1993:

$$Ms = \log (A/T)_{max} + 1/3 \log(\Delta) + 1/2 \log(\sin\Delta) + 0.0046\Delta + 5.370. \qquad (3.41)$$

Formula (3.41) makes allowance for the theoretically known contribution of both dispersion and the distance-dependent geometrical spreading, thus providing an improved overall distance correction, especially beyond $\Delta = 145°$ and reduces for intermediate size earthquakes the scatter against log M_0 as compared to Ms_20 calculated with the Moscow-Prague formula.

Developing new calibration formulas for Ms_20 is principally correct, because the IASPEI standard Moscow-Prague formula had not been developed for calibrating displacement amplitudes at periods around 20 s but for calibrating $(A/T)_{max}$ in a much wider range of periods and distances. Already Gutenberg (1945a) wrote in his Ms paper, that the 20 s condition "is not fulfilled for distances less than 20°." Therefore, reported distance-dependent biases may reach at near regional distances up to about 0.5 m.u. and are in perfect agreement with the observed trend to shorter surface-wave periods as presented in Fig. 3.35, whereas for stronger earthquakes recorded at larger distances the difference between Ms_20 and Ms_BB is in most cases negligible (Fig. 3.37). Yet, with the exception of formula (18) in Rezapour and Pearce (1998), which has become the standard Ms formula at the International Data Center (IDC) of the CTBTO (see Chapter 17), none of these alternative Ms_20 calibration relationships has already been accepted as a global standard. However, there is a need for it and it will surely reduce the currently existing systematic difference between Ms_20 and Ms_BB in certain distance and magnitude ranges. There is hope that the now beginning global collection of standardized Ms_20 data with likely reduced procedure-dependent errors will finally result in a globally accepted new calibration function for standard Ms_20.

Question 4: Why there is no depth term in the Ms calibration functions?

The amplitudes of the fundamental surface-wave mode decay exponentially with depth (see Chapter 2) and routine depth determinations for shallow earthquakes (< 70 km) are still rather uncertain (at present with errors in the order of 10-20 km, at Gutenberg´s time even worse or undetermined). This limited both the derivation and the meaningful application of depth corrections. On the other hand, more than 95% of the global seismicity goes on the account of shallow earthquakes. Therefore, Gutenberg (1945a) proposed to use his formula only for earthquakes at source depths not exceeding 40 km and to use only surface waves around 20 s which are also less sensitive to uncertainties in source depth than those with shorter periods. He even specified: *"...it seems that for shocks with a depth of focus of about 35 km, 0.1 should be added to the magnitude calculated from (1)* [here Eq. (3.33)] *to bring the resulting M into agreement with the original zero point of Richter´s scale, and that the values given in table 4 are not affected by more than ± 0.2 by variations in focal depth so long as this does not exceed 40 km."* And in Gutenberg (1945b) he even wrote: "*The determination of the magnitude of shocks with a focal depth in excess of about 30 km must be based on the amplitudes of the body waves".* For the same reasons also Vanek et al. (1992) did not include depth corrections in their formula but relaxed somewhat the upper depth limit being aware of the uncertainties both of the initial hypocenter depth determinations at his times and their limited relevance with respect to the hypocenter position of maximum seismic energy release in the case of large finite source ruptures.

Question 5: Are depth correction terms for Ms available and feasible?

Empirically derived corrections for intermediate and deep earthquakes were published by Båth (1985). They range between 0.1 and 0.5 magnitude units for focal depths of 50 - 100 km and between 0.5 and 0.7 units for depths of 100 - 700 km.

Based on model calculation and their comparison with real observations of 20 s surface waves from earthquakes down to h = 530 km depth, Herak et al. (2001) proposed the following corrections $\Delta Ms(h)$ for 20 s surface waves, which are in the same range as the empirical data by Båth (1985), i.e., up to about 0.75 m.u. near 600 km depth (see also Fig. 3.39):

$$\begin{aligned}
&\Delta Ms(h) = 0 && \text{for } h < 20 \text{ km} \\
&\Delta Ms(h) = 0.314\log(h) - 0.409 && \text{for } 20 \text{ km} \le h < 60 \text{ km} \\
&\Delta Ms(h) = 1.351\log(h) - 2.253 && \text{for } 60 \text{ km} \le h < 100 \text{ km} \\
&\Delta Ms(h) = 0.400\log(h) - 0.350 && \text{for } 100 \text{ km} \le h < 600 \text{ km}.
\end{aligned} \qquad (3.42)$$

It would be desirable to test the feasibility of these correction terms globally based on type IAMs_20 amplitude readings also for deeper earthquakes, maybe put in brackets, and to investigate their compatibility with mb, mB and Mw estimates for these earthquakes. If such comparisons demonstrate the reliability, stability and thus feasibility of these depth corrections for Ms they may in future be integrated in a new Ms_20 standard.

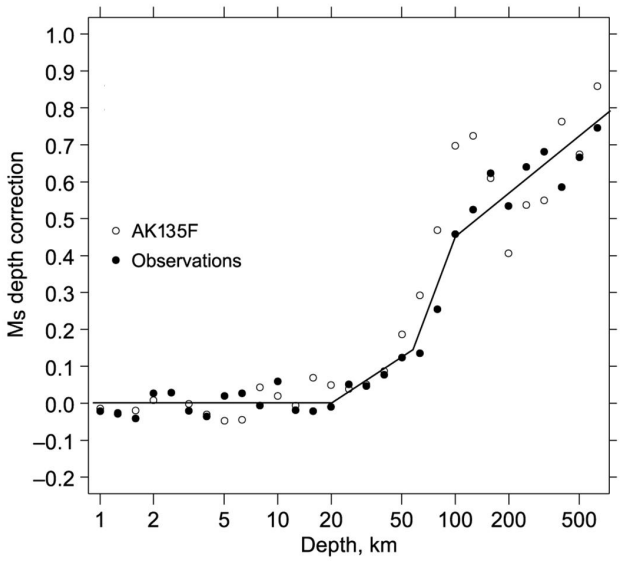

Fig. 3.39 Ms_20 depth correction based in observations and theoretical modeling (AK 135 model; see DS 2.1 and Fig. 2.79 in Chapter 2). The solid line represents the proposed Ms depth corrections according to formulas (3.42). (Modified version of Figure 7 on page 1527 of Herak et al. (2001). Theoretical and observed depth corrections for Ms. Pure appl. Geophys, **158**, 1517-1530; © Birkhäuser Verlag).

If V_{max} is also found at periods around 20 s, than the Herak et al. (2001) corrections could be applied to Ms_BB as well. However, the penetration depth of surface waves and therefore also the efficiency of surface-wave excitation depends on wavelength and thus period. If V_{max} is measured at T >> 20 s (up to about 60 s) depth corrections may not be needed for source depth up to about 100 km. For periods of only about 5 s, however, the underestimation may become significant already for source depth larger than about 15 to 20 km. Regrettably, period-dependent source-depth correction terms have not yet been derived. With standard V_{max} and related period data expected to become available en mass in future in the bulletins of international data centers it should be possible to determine such period-dependent empirical corrections in relation to those for Ms_20.

Question 6: How does travel paths affect the period at which Ms_BB is measured?

Marshall and Basham (1972) investigated how much the travel paths of Rayleigh (LR) surface waves affect their measured displacement amplitudes at different periods. They found *"…that for an impulsive input into a North American path the amplitudes at 10 secs are eight times larger than the amplitudes at 20 seconds, due to the dispersion characteristics of the path alone;…"* In contrast: *"…over a Eurasian path the amplitude difference between 10 and 20 seconds is only a factor of two. The predicted amplitude at 20 seconds period for both paths is however almost equal, …"* Moreover they showed that both oceanic and mixed intercontinental paths LR waves exhibit relatively low amplitudes at the shorter periods below 20 s, yet, for 20 s < T < 45 s oceanic path LR amplitudes dominate those with continental or mixed intercontinental paths. Therefore, the periods at which the largest LR velocity amplitudes were measured at stations of the China National Seismic Network (CNSN) up to epicenter distance of 100° on LR waves with dominatingly continental or mixed paths were in 79% of the cases outside of the 18-22 s period band at which Ms_20 is measured (see Fig.

3.35). In contrast, Ms_BB determined at stations of the German Regional Seismic Network (GRSN) up to D = 160°, which include a larger share of LR of mixed or even dominatingly oceanic paths than in records of the CNSN, "only" 62% of the LR_{max} were measured at periods outside of the 18-22 s range, again being mostly shorter but with a larger share of T > 22 s, up to 62 s (see Fig. 3.40).

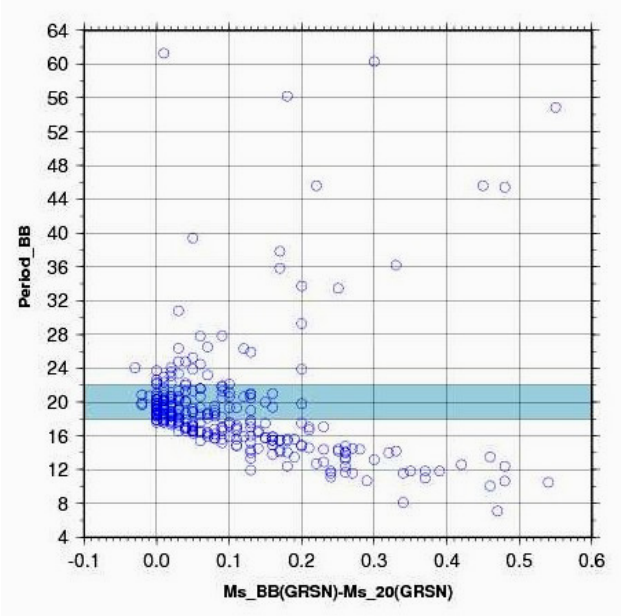

Fig. 3.40 Difference between Ms_BB and Ms_20 in relation to the period at which V_{max} was measured on velocity broadband records at GRSN stations in Germany.

Figs. 3.41 shows for different source locations, magnitude ranges and paths the periods at which LR V_{max} has been measured with T < 35 s at station CLL of the GRSN and Fig. 3.42 for some average regional paths LR V_{max} measured at even longer periods up to 60 s.

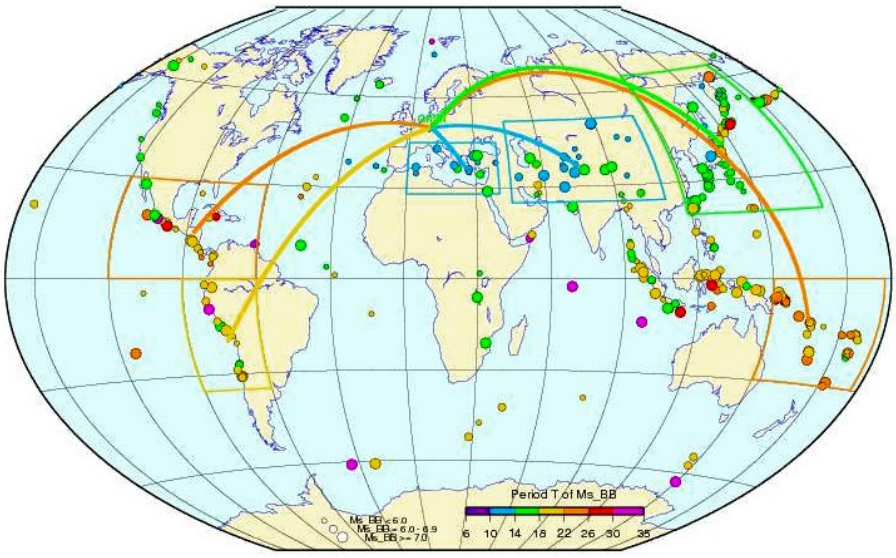

Fig. 3.41 Periods at which V_{max} of LR waves has been measured on velocity broadband records at station CLL, Germany, depending on source location, event Ms and travel path.

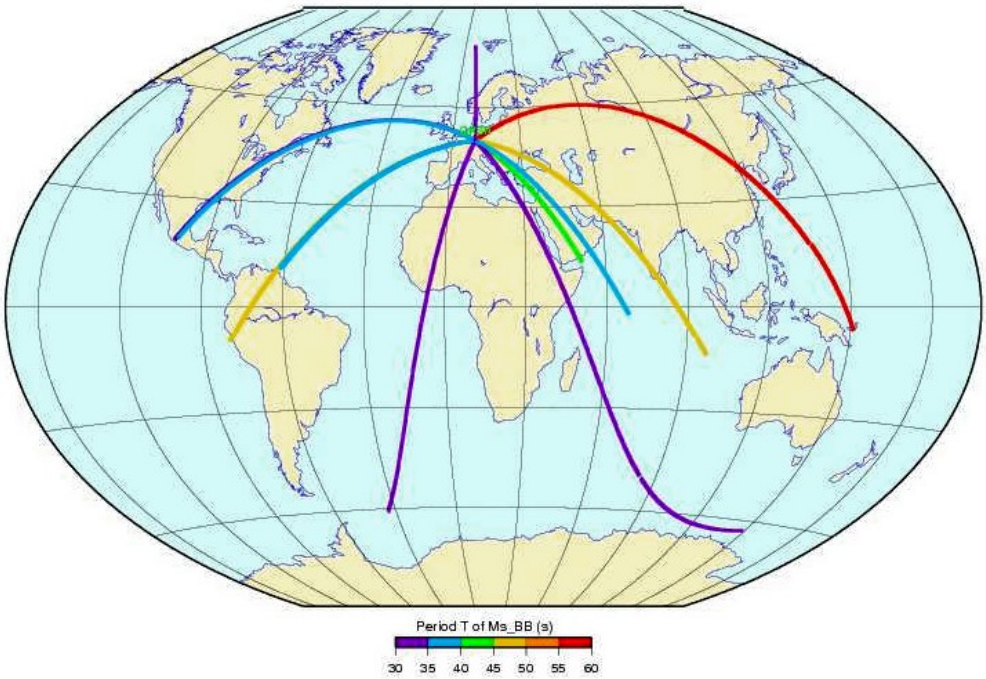

Fig. 3.42 Periods between 30 s and 60 s at which V_{max} of LR waves has been measured on velocity broadband records at station CLL, Germany, along some prevailing average regional paths.

From Fig. 3.41 it is obvious that the periods at which V_{max} is measured are:

- Generally less than 18 s for pure Eurasian path up to about 80° long, and mostly even shorter (between some 6 to 14 s) for distances less than 30-50°, also when travelling through the African continent via the Mediterranean Sea to Central Europe;
- Mixed Rayleigh-wave paths arriving from comparable backazimuth, e.g., New Zealand, travelling through about half oceanic and half Eurasian continental crust, have already periods between 22 and 26 s.
- Mixed path intercontinental LR travelling from the western coasts of South America, Central America or North America, respectively, to Central Europe have typically periods between 18-22s, 22-26 s (more oceanic) and 14-18 s, respectively;
- Periods longer than 26 s have been measured for some individual earthquakes with either dominating oceanic paths or even for mixed paths, e.g. for the slow 17 July 2006 Mw7.7 Java tsunami earthquake (red dot in Fig. 3.41), whereas from other, faster rupturing earthquakes in the same region (green dots) LR_{max} is often recorded at periods between 14 and 18 s.

Interesting in Fig. 3.42 is the rather different and somehow unexpected behavior of the even more long-period LR and mantle Rayleigh waves with periods between 30 s and 60 s. Practically all paths from the relevant source regions are mixed paths to CLL station. The shortest periods between 30 s and 35 s may occur along both the shortest as well as the longest paths. And the longest periods, up to about 60 s, have been measured for mantle Rayleigh wave maxima arriving on the long teleseismic mixed path from SE Asia (e.g., off-coast Papua New Guinea earthquake).

Question 7: Why the IASPEI Ms formula does not include a period dependence?

Since Gutenberg restricted the use of his empirically determined Ms formula to amplitude readings around 20 s, for which according to the later finding by Marshall and Basham (1972) there is also the best agreement between the maximum LR amplitudes for different continental and mixed paths, there was no need for introducing a period-dependent attenuation term.

The situation, however, is different for Ms_BB which is measured at periods 3 s < T < 60 s. Although attenuation losses for periods > 20 s may become increasingly negligible, this is not the case for much shorter period. Yet, interestingly, the empirical data collected by Soloviev and Shebalin (1956) and Karnik (1957) revealed a much higher stability of the read velocity amplitudes - or ratio $(A/T)_{max}$ - as compared to the respective displacement amplitudes, in a wide period range and still a high overall compatibility of their data with Gutenbergs´s Ms.. And since the authors of the Moscow-Prague formula, in the interest of best possible data continuity, scaled their data to the Gutenberg relationship they neither investigated nor introduced a period-dependence in their formula.

Ambraseys (1985) confirmed the stability and broad applicability of Moscow-Prague formula (3.35) when applied to European recordings of medium-period instruments at distances ≥ 4° Quote: *The data available from Northwester European earthquakes of the last 70 years recorded mainly by light and heavy Wiecherts, Galitzin, Mainka, Quervain-Picard, Milne-Shaw, Grenet and modern medium-period instruments, suggest that on the average for D ≥* 4°, *M values calculated from equation (1)* (here 3.35) *do not exhibit an unequivocal distance dependence. ... The fit does not improve if we include distance and path corrections following, say, Marshall and Basham. ...Consequently, equation (1) was used over any distance and without any restriction for measurements to a fixed period other than the restrictions imposed on D and T by the data proper. ...neither a period constraint nor distance effects for the regional conditions considered seem to play an important role."*

Also Okal (1989) came to the conclusion that the use of (A/T) in the Moscow-Prague calibration formula is **a partial and ad hoc compensation** for a large number of frequency-dependent terms ignored by it. The simplest explanation is that attenuation terms which linearly increase with frequency are compensated by multiplying A with f = 1/T. When looking at the tremendous range of period variations in Fig. 3.35 at which surface wave V_{max} has been measured by seismic stations at distances between 2° and 100° one can hardly believe that they yielded the stable and with Ms_20 generally compatible Ms_BB data plotted in Fig. 3.37, and this with even slightly smaller average standard deviation than for Ms_20 data (see Table 5 in IS 3.3).

How much $(A/T)_{max} = V\pi/2\pi$ readings may stabilized the Ms estimate has been illustrated by Bormann et al. (2009) with an example observed at the German Regional Seismic Network:

> *05 Feb. 2006, Alaska, average network $\Delta \approx 61°$, 15-station network $M_S(BB) = 4.91 \pm 0.08$ at average network T = 15.4 ± 8.3 sec, station BFO $M_S(BB) = 5.0$ at T = 7.1 sec, station CLZ $M_S(BB) = 4.9$ at T = 28.6 sec, i.e., within 0.1 unit the same $M_S(BB)$ despite $T_{CLZ} \approx 4 \times T_{BFO}$.*

Moreover, Ambraseys (1985) also found, that medium-period $(A/T)_{max}$ Ms data correlate well with local magnitudes estimated by a number of European stations. This has been confirmed by S. Wendt for Ms_BB data of station CLL too.

Yet, the phrasing "partial" compensation by Okal (1989) may be reason enough to look closer into the need – or not – of introducing for different seismotectonic environments, especially in the regional distance range, frequency-, path- and/or distance-dependent corrections into the current standard Ms_BB formula (3.37). Mass data of standard Ms_BB, expected to become available in future together with the periods at which V_{max} has been measured, would be ideal for such studies.

Question 8: Exist Ms scales with a frequency-dependent calibration term?

Yes, they do. E.g., Yacoub (1998) presented a method for accurate estimation of Rayleigh-wave spectral magnitudes M_R by velocity and frequency window analysis of digital records. He applied it to records of underground nuclear explosions in the distance range 5° to 110° and compared M_R with the classical time-window magnitude estimates, Ms, according to Eq. (3.35). While **both agreed well**, in general M_R had smaller standard deviations. Another advantage is that the procedure for M_R determination can easily be implemented for on-line automated magnitude measurements.

More recently, Bonner et al. (2006) reported about the application of their time-domain variable-period surface-wave magnitude measurement procedure at regional and teleseismic distances. It is based on multi-bandpass filtering in the period range from 8 to 24 s in increments of 4 s, selecting the maximum bandpass amplitude and correcting it with a period-dependent correction term. Yet, also these authors found a generally good agreement of their Ms(VMAX), on average better than 0.1 m.u., with the formulas of Rezapour and Pearce (1998) and Vanek et al. (1992) when applied at teleseismic distances, with the exception of a small distance-dependent trend of -0.002 m.u./° and a standard deviation of 0.21 m.u. of carefully measured station magnitudes for a subset of 33 events from the Mediterranean region.

Yet, Bormann et al. (2009) got similar results for Ms_BB with almost negligible differences when plotting for a much larger global event set and routine station readings the difference between Ms(BB) and Ms(NEIC) for earthquakes at depth h < 60 km over the distance range 2° to 103°. When considering all measured periods of V_{max} in the range 3 s to 30 s (as compared to the 8-24 s data of Bonner et al.) the standard deviation of 0.33 m.u. and distance-dependent trend of -0.0029 m.u./° where only somewhat larger. However, when using only periods < 15 s in the whole distance range, for which larger attenuation effects would be expected, then the trend even reduced to merely -0.0009 m.u./° and the standard deviation to 0.29 m.u.

Therefore, for the time being, all these comparisons still question the practical relevance of introducing frequency-dependent corrections in the Ms formulas in view of the generally large data scatter which due to station site effects depending also on epicentral distance and backazimuth (see Question 9 on focusing and defocusing of LR waves). Probably the largest positive effect of the multi-bandpass filtering prior to Ms(VMAX) measurement for periods > 8 s is, when compared with readings on unfiltered broadband records, that on stormy days ocean microseisms are strongly reduced and thus the SNR improved. This surely will reduce

the standard deviation of Ms measurements. Since NEIC is now routinely calculating both Ms_BB and Ms(VMAX) there may in future be more and better data available to assess the relative performance of these two kinds of variable frequency Ms procedures in different ranges of distance, backazimuth and source depth. This may help to decide about the necessity of introducing frequency-dependent attenuation terms also in the Ms_BB formula. Maybe, the frequency-dependence of the quality factor Q, which we discus below in conjunction with P-wave periods below 5 s, is another reason, why also surface-wave amplitudes measured at periods larger than 3 s for Ms_BB or 8 s for Ms(VMAX) are less affected by attenuation towards shorter periods than expected from frequency-independent Q models. If this can be proved then no urgent need may be felt for introducing frequency-dependent attenuation corrections in the standard formula for Ms_BB as long as the dominating station site and non-attenuative path effects due to unconsidered lateral velocity anomalies remain uncorrected.

Question 9: How lateral velocity inhomogeneities may affect the Ms estimates?

There may be significant regional and also station residual biases due to surface-wave path effects. Lateral velocity variations in the crust and upper mantle as well as refraction at plate boundaries may result in significant focusing and de-focusing effects and thus regional over- or underestimation of station Ms or regional Ms averages as compared to global Ms event averages (Lazareva and Yanovskaya, 1975; Yanovskaya, 2012; Figs. 3.43, 3.44 a and b).

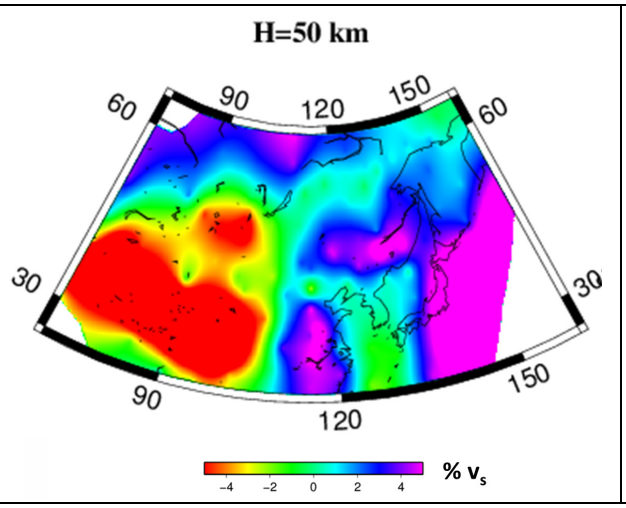

Fig. 3.43 S-wave velocity tomography for the uppermost 50 km of Central and NE Asia according to T. B. Yanovskaya (2012) (by courtesy of the author).

This is confirmed by comparing Ms_BB measured at Collm (CLL) station in Germany with global Ms(NEIC) event averages (Fig. 3.44a). The Ms-residuals of CLL have been plotted over epicenter distance D. They show both a positive trend with growing distance as well as oscillations with average amplitudes up to +0.55 m.u. and individual data scatter up to more than one m.u. The large scatter also hints to another dependence on the backazimuth BAZ of the source region. This is confirmed by Fig. 3.44b when comparing the different average Ms residuals from the Kamchatka, Kuriles and Japan source region with those from SW North America, Central America and NW South America, all being about the same epicentral distance D ≈ 85° away from CLL but mostly with smaller and even negative residuals.

Relating Ms anomalies as a function of D and BAZ to major lithosphere velocity anomalies or plate boundaries along the way of travel would be a very important result. For enabling such

investigations primary station residual data should be preserved and not be manipulated by trying to reduce them by applying station corrections before reporting the data to national or international seismological data or network centers.

According to Abercrombie (1994) surface-wave focusing seems to be the main cause for the anomalously high Ms magnitudes of continental earthquakes relative to their seismic moments, rather than differences in the source process. Therefore, he suggests that in order to obtain reliable, unbiased estimates of regional seismic strain rate and hazard, local/regional moment-magnitude relationships should be preferred to global ones.

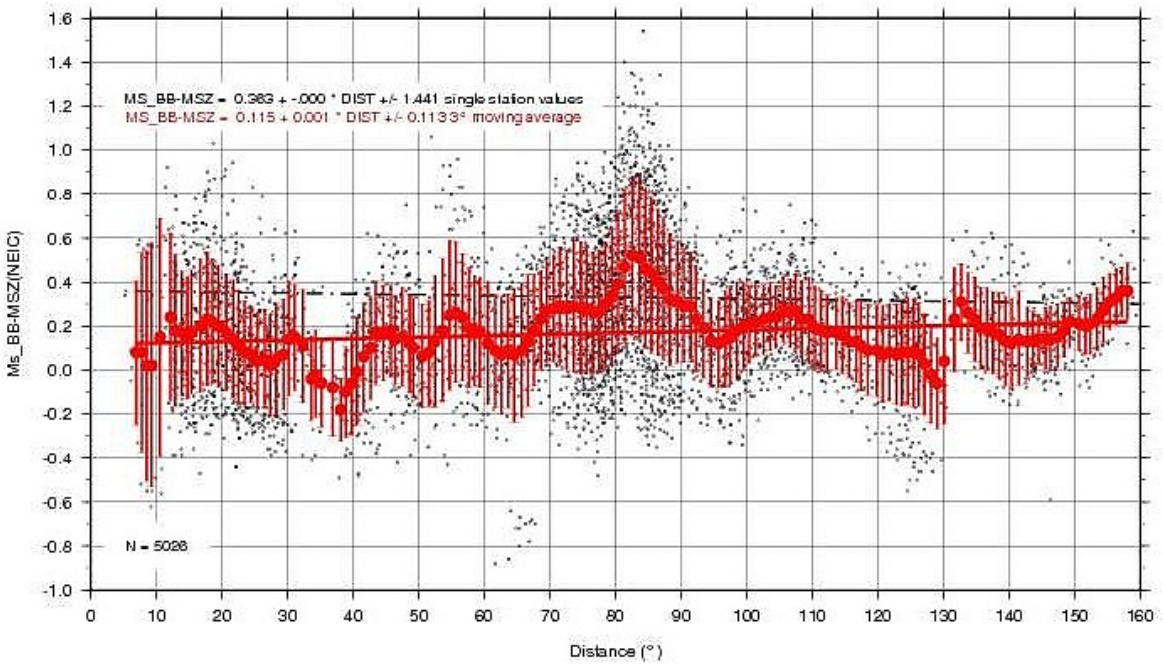

Fig. 3.44a Difference between Ms_BB(CLL)–Ms(NEIC), based on earthquakes recorded between September 1992 and December 2007. Black dots - individual measurements, bold red dots – average values over increments of 1° in distance together with their standard deviation (vertical red bars). Red line - moving average trend. On average CLL Ms_BB is 0.36 m.u. larger than Ms(NEIC).

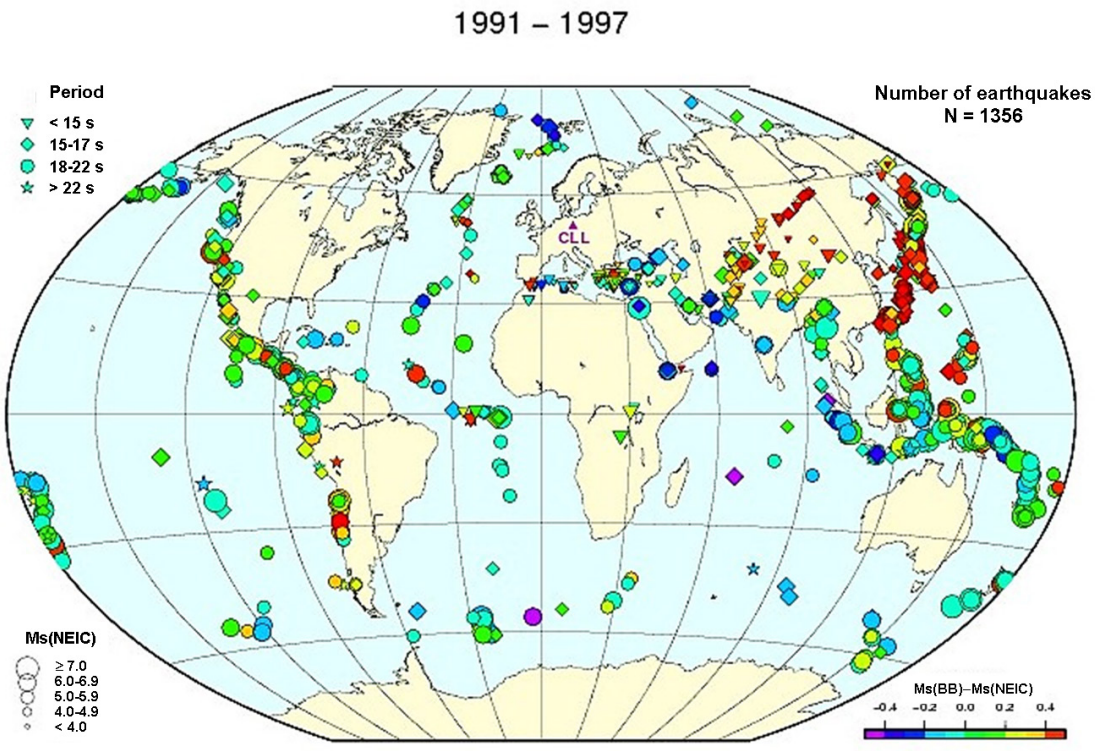

Fig. 3.44b Differences between station Ms_BB(CLL) and global Ms(NEIC) event averages for different source regions.

Question 10: How affect deviations from the standard responses Ms_BB and Ms_20?

There is no adverse effect on the measured values of V_{max} for Ms_BB if the passband range of the velocity-proportional BB response covers the range of periods within which V_{max} for Ms_BB should be measured, i.e., between about 3 s and 60 s. At least periods up to 40 s, which make for the vast majority of data, should becovered (see Fig. 3.40).

With respect to Ms_20 we show in IS 3.3 that even large deviations in the LP response from the recommended WWSSN-LP standard may not bias Ms_20 magnitudes as long as it is assured, that the passband range of the alternative response covers with its maximum magnification the period range of 18 to 22 s. This could be demonstrated by filtering the BB records so that they simulate SRO-LP records. The SRO-LP response differs very much from the WWSSN-LP response (see Fig. 3.20) and has the advantage of strongly reducing ocean microseisms with periods between about 3 to 8 s, thus improving the SNR and increasing the number of events for which Ms_20 can be measured. None the less, the derived Ms_20 values agree within 0.1 m.u. with standard Ms_20 (see Figure 14 in IS 3.3) and thus can be reported as such and also their amplitude readings with the nomenclature IAMs_20.

3.2.5.2 Body-wave magnitude scales and the new IASPEI standards

Gutenberg (1945b and c) developed a magnitude relationship for teleseismic body waves such as P, PP and S, measured on broadband or long-period instruments at periods of 2-20 s (Abe, 1981a and 1984; Abe and Kanamori, 1979 and 1980). It is based on theoretical amplitude

calculations from a point source, corrected for geometric spreading and only distance-dependent attenuation and then adjusted to empirical observations from shallow and deep-focus earthquakes, mostly in intermediate-period records:

$$mB = \log (A/T)_{max} + Q(\Delta, h). \qquad (3.43)$$

Gutenberg and Richter (1956a) published a table with Q(Δ) values for P-, PP- and S-wave observations in vertical (V=Z) and horizontal (H) components for shallow shocks (see Tab. 7 in DS 3.1), complemented by diagrams Q(Δ, h) for PV, PPV and SH (Figures 1a-c in DS 3.1) which enable also a compatible magnitude determinations for both shallow and intermediate to deep earthquakes (see Abe and Kanamori, 1979).

On the basis of the scanned diagram for PV the NEIC has produced a new table with increments of source depth (see Table 2 in IS 3.3) and a computer program for interpolation between these values (PD 3.1). Both are now used by the NEIC and the ISC as the common basis for calibrating P-wave magnitudes, thus eliminating earlier slight discrepancies in their magnitude calculations due to somewhat different scanning and interpolation. Therefore, these calibration values and the interpolation program should be used in future by other seismological agencies and observatories as well. The Q(Δ, h) values are correct when amplitudes are given in micrometers (10^{-6} m).

Gutenberg and Richter (1956a) also proposed a *unified magnitude m* as a weighted average of the individual mB values determined for the different types of body waves. Because of their different nature and/or propagation paths they also differ in their frequency content. In addition, these body waves leave the source at different take-off angles and/or have different radiation pattern coefficients. Using these body waves jointly for the computation of magnitude significantly reduces the effect of the source mechanism on the magnitude estimate. Gutenberg and Richter (1956a) also scaled *m* (in a first approximation = mB) to the earlier magnitude scales Ml and Ms so as to match them at magnitudes between about 6 to 7.

Later, with the introduction on a global scale of the WWSSN short-period 1s-seismometers (for response see Fig. 3.20), it became common practice at the NEIC to use the calibration function Q(Δ, h), developed for medium-period amplitude readings on relatively broadband recording, for band-limited short-period PV measurements only. According to Fig. 3.45, this results in the case of strong earthquakes and when compared with their Ms_20 or mB estimates, in an about 1 m.u. lower mb value (termed *spectral component of saturation*). In addition, it was recommended in the early 1960s that the largest amplitude be taken within the first few cycles (Engdahl and Gunst, 1966; Willmore, 1979) instead of measuring the maximum amplitude in the whole P-wave train. To measure the largest amplitude within the first 5.5 s after the P onset is still the standard practice at the IDC of the CTBTO (see Chapter 17). Since the average rupture duration of earthquakes of magnitude 6, according to relationship (3.3), is about 6 s, such a fixed measurement time-window will add for larger earthquakes additionally a *time-window component of saturation* (see Fig. 3.46).

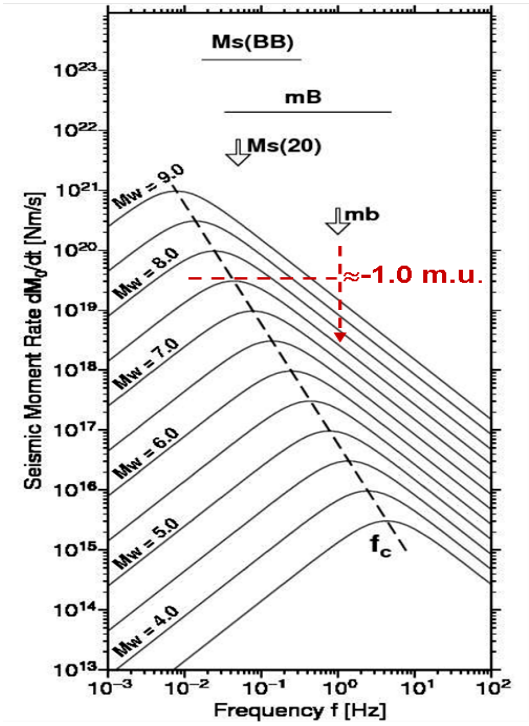

Fig. 3.45 Illustration of estimating approximately the average amount of spectral magnitude saturation of mb with respect to Ms_20 or mB_BB on the basis of the scaling law in Fig. 3.5.

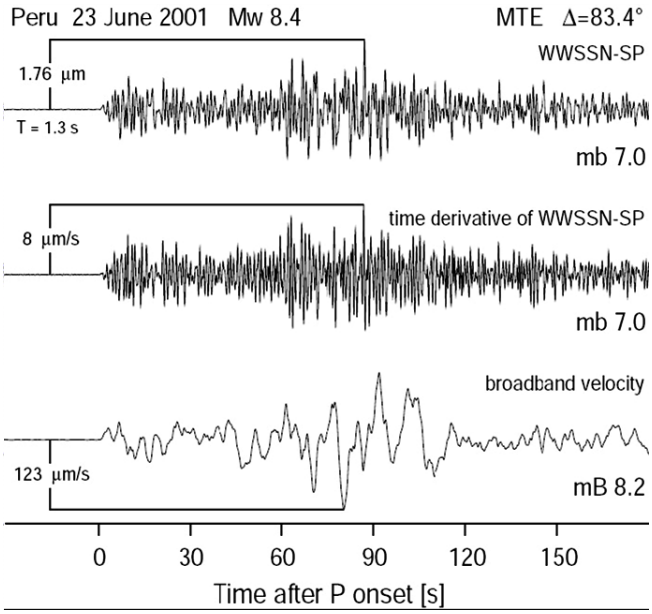

Fig. 3.46 Short-period WWSSN and broadband (BB) records of a strong Mw8.4 Peru earthquake. They illustrate the measurement of mb and mB at the largest amplitudes in the P-wave train near 90 s after the P-wave onset. The difference in velocity amplitude of 123µm/s in the BB record and 8 µm/s in the time-differentiated WWSSN-SP record is due to spectral saturation according to Fig. 3.31, explaining the difference mb-mB = - 1.2. If one would measure for mb A_{max} within the first 5.5 s, then this difference would increase by -0.5 m.u. (time-window component of saturation). (Copy of Figure 1 in Bormann and Saul, 2008, Seism. Res. Lett. 79, No. 5, p. 699; © Seismological Society of America).

One should be aware that the practice of measuring the P-wave amplitude so early in so short a window was due to the focused interest in the 1960s on discriminating between earthquakes and underground nuclear explosions (UNE). For the latter, having source durations in the order of milliseconds only, their maximum P-wave amplitudes are always observed within the first few seconds after the P onset. Therefore, such a short time-window even improved the discrimination between earthquakes and UNE based on the Ms-mb criterion (see section 11.2.5.2??? of Chapter 11).

Yet, Bormann and Khalturin (1975) argued against it in the more general interests of earthquake seismology and recommended (quote):
"We are of the opinion that the extension of the time interval for the measurement of (A/T)max up to 15 or 25 sec., as proposed ...in the Report of the first meeting of the IASPEI Commission on Practice (1972) ...is not sufficient in all practical cases, especially not for the strongest earthquakes with M > 7.5....To reduce the systematic differences between magnitude determinations from body waves and surface waves, short-period or medium-period broad-band records should be preferred to short-period narrow-band ones for the MB-determination and the time interval for measuring the maximum value of A/T should be extended to about 1 minute for the strongest earthquakes."

In response, the IASPEI Commission on Practice revised its earlier 1972 measurement recommendation in 1978, stating that the maximum P-wave amplitude for earthquakes of small to medium size should be measured within 20 s from the time of the first onset and for very large earthquakes up to 60 s (see also Willmore, 1979, p. 85). This somewhat reduced the discrepancy between mB and mb but in any event both are differently scaled to Ms and Mw with the short-period mb necessarily saturating earlier than medium-period mB (see Fig. 3.47).

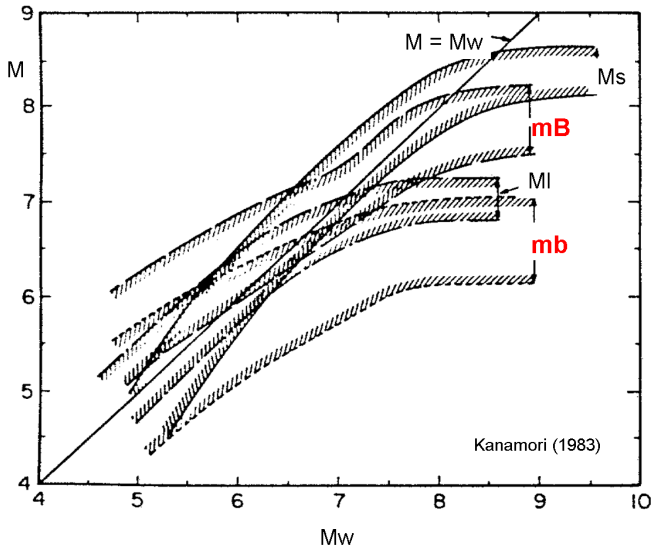

Fig. 3.47 Approximate relationships and ranges of variability between Ml, mb, mB and Ms with respect to non-saturating Mw (redrawn and modified from Fig. 4, p. 193, in Kanamori 1983; based on the kind permission of Elsevier Science Publishers for reprinting in NMSOP 2002).

However, some of the national and international agencies have only much later or not even as of now changed their practice of measuring $(A/T)_{max}$ for mb in a very limited time-window. E.g., the International Data Centre for the monitoring of the CTBTO still uses a time window of only 6 s (5.5s after the P onset), regardless of the event size. In contrast, the former Soviet/Russian practice (but also the East German practice, see Tab. 3.1 and Fig. 3.69 in section 3.2.5.2) of analyzing short-period records was always to measure the true P-wave maximum on the entire record. These magnitudes, reaching values between 7.3 to 7.6 for the strongest earthquakes, were denoted as MPV(A) or mSKM, because of using modified, relatively broadband short-period Kirnos type of instruments with a response as in Figure 1 of IS 3.7). Similar "whole P-wave train" mb magnitudes were later determined also by Koyama and Zeng (1985), denoted m_b^*, and by Houston and Kanamori (1986), denoted $\widehat{m}_b$, which also reached values up to 7.6. With respect to saturation, mSKM, m_b^* and $\widehat{m}_b$ behave much like Ml, as could be expected from their common frequency band used and considering that Ml is determined also from the maximum amplitude in the whole short-period event record. Ml saturates around 7.5 as well (see Fig. 3.47).

Taking into account the above facts, the CoSOI WG on Magnitudes recommends two P-wave **IASPEI standard magnitudes, mb and mB_BB,** with suitably modified measurement procedures (IASPEI 2005, 2011 and 2012). In short they are defined as follows:

$$\boldsymbol{mb = \log_{10}(A/T) + Q(\Delta, h) - 3.0}, \qquad (3.44)$$

where A = P-wave ground amplitude in ***nm*** *calculated from the maximum trace-amplitude in the* ***entire P-phase train*** *(time spanned by P, pP, sP, and possibly PcP and their codas, and ending preferably before PP); T = period in seconds,* ***T < 3 s****; of the maximum P-wave trace amplitude.*

Q(Δ,h) = attenuation function for ***PZ*** *(P-waves recorded on vertical component seismographs) established by* ***Gutenberg and Richter (1956a)*** *in the tabulated or algorithmic form as used by the U.S. Geological Survey/National Earthquake Information Center (USGS/NEIC)* (see Table 2 in IS 3.3 and PD 3.1); *Δ =* ***epicentral*** *distance in degrees,* ***20° ≤ Δ ≤ 100°****; h = focal depth in* ***km****;*

and where both T and the maximum trace amplitude are measured on output from a ***vertical-component*** *instrument that is filtered so that the frequency response of the seismograph/filter system replicates that of a WWSSN* ***short-period*** *seismograph (see Figure 1 and Table 1 in IS 3.3) with A being determined by dividing the maximum trace amplitude by the magnification of the simulated WWSSN-SP response at period T.*

Note that Fig. 3.7 in section 3.1.2.4 shows how new standard mb data relate to mb measured within the first 6 s after the P onset.

The standard relationship for mB_BB reads as follows:

$$\boldsymbol{mB\_BB = \log_{10}(V_{max}/2\pi) + Q(\Delta, h) - 3.0}, \qquad (3.45)$$

where V_{max} = ground ***velocity in nm/s*** *associated with the maximum trace-amplitude in* ***the entire P-phase train*** *(…as for mb…), as recorded on a vertical-component seismogram that is* ***proportional to velocity,*** *where the period of the measured phase, T, should satisfy the*

*condition **0.2 s < T < 30 s**, and where T should be preserved together with V_{max} in bulletin data-bases;* and Q(Δ, h), Δ and h as for mb. *Equation (3.45) differs from the equation for m_B of Gutenberg and Richter (1956a) by virtue of the $\log_{10}(V_{max}/2\pi)$ term, which replaces the classical $\log_{10}(A/T)_{max}$ term.*

Formula (3.43) can be simplified by including $-\log_{10}(2\pi) = -0.8$ into the constant, then reading

$$mB\_BB = \log_{10}V_{max} + Q(\Delta, h) - 3.8. \qquad (3.45a)$$

For more details and comments on mb and mB_BB see IS 3.3.

Question 1: Is modern mB_B compatible with the classical Gutenberg mB?

Gutenberg measured himself or used measurements of P-wave amplitudes and periods published in other station bulletins that were commonly based in these years on relatively broadband medium-period instruments with responses that resemble that of the classical Russian Kirnos instruments of type SK and SKD (see the relative response curves 6 and 7 in Figure 1 of IS 3.7; for SKD also the Kirnos response in Fig. 3.20). Most of these response curves were more or less displacement proportional in the period range between 0.1 s < T < 10-2 s, such as Mainka, Wiechert, Galitzin or Bosch-Omori (Kanamori, 1988, or Figure 5.6 in Lay and Wallace, 1995). Periods of A_{max} measured in displacement records (and thus relating to (A_{max}/T) tend to be somewhat larger than periods of V_{max} in velocity records which correspond to $(A/T)_{max}$. Although Gutenberg aimed at the latter, common practice has been to measure (A_{max}/T) instead. This is obvious from Fig. 3.48 too, which compares traditional and period-wise more noisy measurements of P-wave A_{max} for classical mB at the CENC with related measurements of T at V_{max} for mB_BB. Notable in both figures is the exponential increase of T for mB > 6. On average this is related to the exponential increase of the corner period of seismic source spectra with magnitude. The great scatter of measured periods at individual stations is both due to the stress drop-dependence of the corner period (see Fig. 3.15) and local station site effects. In records of weaker earthquakes with low SNR, however, the measured values of T may already be biased by the prevailing periods of ocean storm microseisms with periods between about 3 to 8 s.

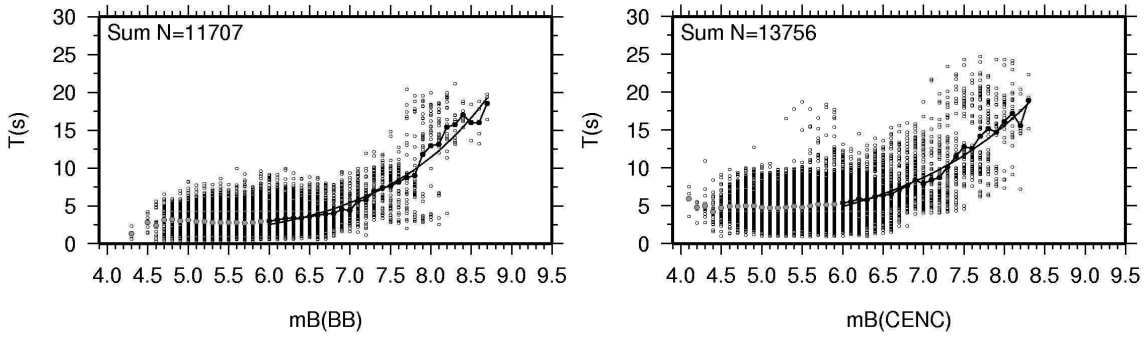

Fig. 3.48 Dependence on mB_BB (left-hand panel) and on mB_CENC (right-hand panel) of the P-wave periods observed at individual stations when measureing V_{max} on broadband-velocity records or A_{max} on broadband displacement records of SK (Kirnos) type. The polygon line connects the average periods measured at the considered magnitude, the curved line is the exponential fit to it. (Copy of Figure 6 in Bormann et al. (2009), Seism. Res. Lett. 99, 3, p. 1873; © Seismological Society of America).

A consequence of this procedural difference of measuring directly V_{max} (as for Ms_BB too) may be the not perfect 1:1 trend of the regression relations between mB(BB) and mB(CEN) (see Fig. 3.49). For magnitudes < 6.5 mB(BB) yields somewhat larger values than mB. However, in the range mB > 6, in which Gutenberg measured this magnitude only, the average difference is ≤0.1 m.u. and the overall correlation coefficient is very high. Therefore, we can conclude that modern mB(BB) = mB_BB is compatible with the mB intended and practized by Gutenberg within the acceptable error limit of 0.1 m.u. for the standard.

Question 2: How relates standard mb to mb(NEIC)?

Short-period narrow-band mb is not a body-wave magnitude recommended by Gutenberg. It has unilaterally been introduced by the concerned U.S. agencies in conjunction with the deployment of their World Wide Standard Seismograph Network (WWSSN) in the 1960s and 1970s. Since, however, the vast majority of global magnitude data is now mb, it is an indispensible de facto standard magnitude although its measurement procedures have changed several times. Early U.S. mb values were measured within the first few P-wave cycles in short-period records. They saturated already near to 6 (see Fig. 3.7). However, following the IASPEI resolution of 1978, the USGS/NEIC changed practice laterone and measured A_{max} routinely either in the first 20 s or, after automation of the analysis procedure, within the first 10 cycles. Yet, analysts were instructed to extend this window in the final review for the PDE up 60 s in the case of strong earthquakes. Moreover, the early WWSSN-SP records where later substituted by filtering with the PDE response, which has a steeper roll-off for f > 1 Hz, a slightly larger relative bandwidth and period of maximum gain (see Figure 3 in IS 3.3). Nevertheless, one can expect standard mb to be close to post-1978 mb(NEIC), at least for the vast majority of data. According to Fig. 3.50 this is true for mb between about 4 and 6.5, for larger magnitudes, however, again mb(NEIC) tends to be somewhat smaller, saturating around 7 instead around 7.5 as standard mb. Also, when comparing these two data sets, the data scatter is significantly larger and the correlation coefficient much smaller than in the comparison of standard Ms_20 with Ms(NEIC) (Fig. 3.37).

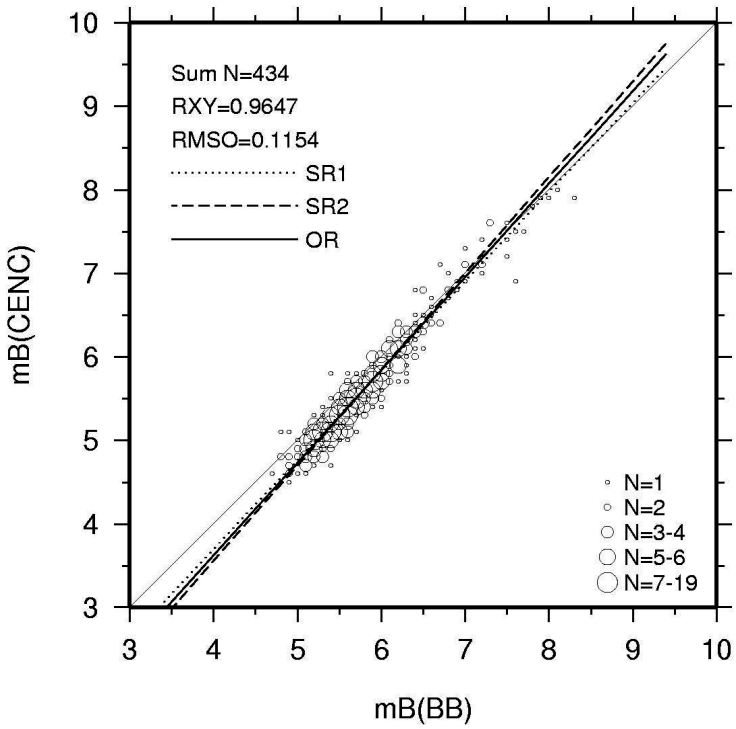

Fig. 3.49 Regression relationships (standard and orthogonal) between mB(BB) and classical mB(CENC). RXY = correlation coefficient, RMSO = orthogonal root mean square error. Figure based on data published in Bormann et al. (2009).

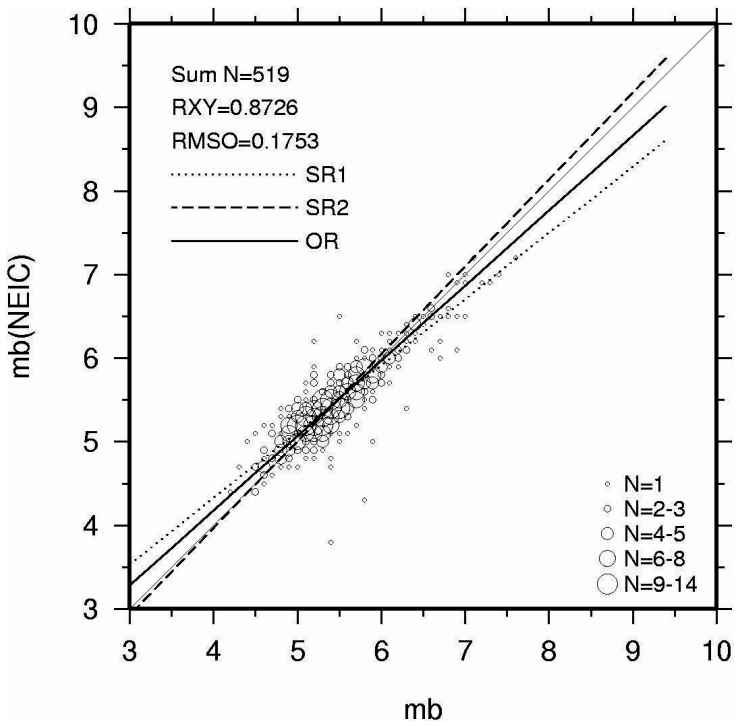

Fig. 3.50 Regression relationships (standard and orthogonal) between standard mb, measured at the China Earthquake Network Center (CENC), and mb(NEIC) for the same events. Legend as in Fig. 3.49. Figure based on data published in Bormann et al. (2009).

Question 3: How relate standard mb and mB_BB to each other?

Fig. 3.51 compares event standard magnitudes mb and mB_BB, as measured at (CENC) on records of the China National Seismograph Network, and Fig. 3.52 the same but based on records of the German Regional Seismic Network (GRSN), analyzed by S. Wendt.

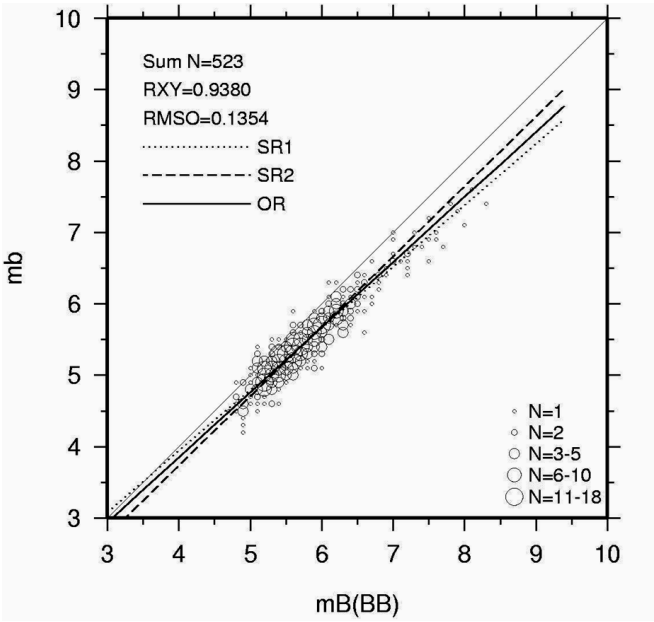

Fig. 3.51 Regression relationships (standard and orthogonal) between standard mb and mB(BB), measured at CENC. Legend as in Fig. 3.49. Figure based on data published in Bormann et al. (2009).

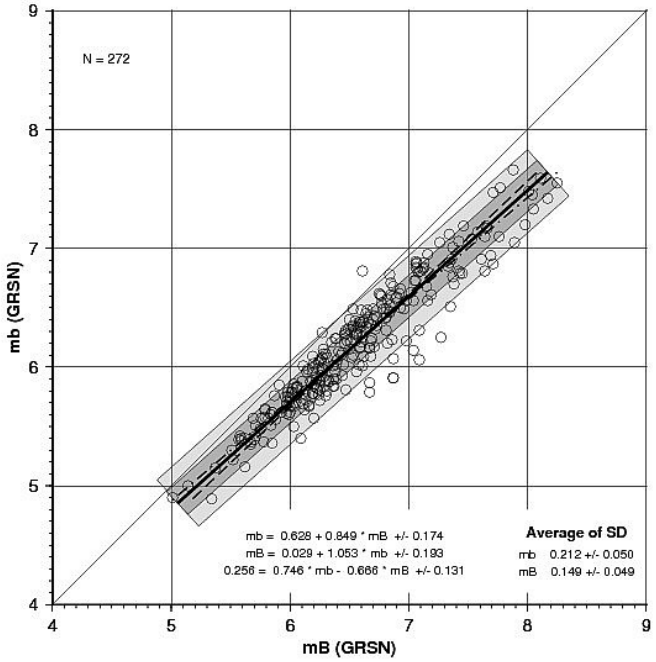

Fig. 3.52 Data and regression relationships (standard and **orthogonal = thick black line**) between the event standard mb and mB_BB as determined with records of the German Regional Seismic Network (GRSN). The medium and light grey shaded bands limit the 1σ and 2σ standard deviation (SD) range of the OR relationship.

Both Fig. 3.51 and 3.52 show the same tendency, namely, that

- mB_BB is always larger than mb and differs the more the stronger the earthquake;
- the difference is smallest (around +0.1 m.u.) at magnitude 5, grows on average to about +0.5 m.u. around mB(BB) = 8, and may reach in individual cases about one m.u.(see also Fig. 3.31).

Moreover, the average SD values for the calculated event mb and mB, given in the lower right corner of Fig. 3.52, indicate that on average the measurement errors for mB (0.15 m.u.) are significantly smaller than for mb (0.21 m.u.), less smaller at shorter periods but much smaller for stronger earthquakes with V_{max} recorded at longer periods.

Question 4: How affects the large scatter of period readings in BB records the estimate of mB_BB?

Fig. 3.48 revealed the large scatter of periods at which V_{max} is measured in all magnitude ranges. Yet, Fig. 3.53 shows a systematic trend, namely, that the difference mB_BB-mb grows on average with the measured period which is related to the corner frequency of the seismic source spectrum and thus to earthquake magnitude itself. The difference between these two magnitudes is less than +0.3 m.u. when the mB periods fall into the range at which also mb is measured. The then still positive mB residuals are likely due to the larger relative bandwidth of the BB records as compared to WWSSN-SP records (see Chapter 4). Yet, the difference between mB_BB and mb may reach 1 m.u. for great earthquakes measured at period around 15 to 25 s, which is in agreement with Fig. 3.45.

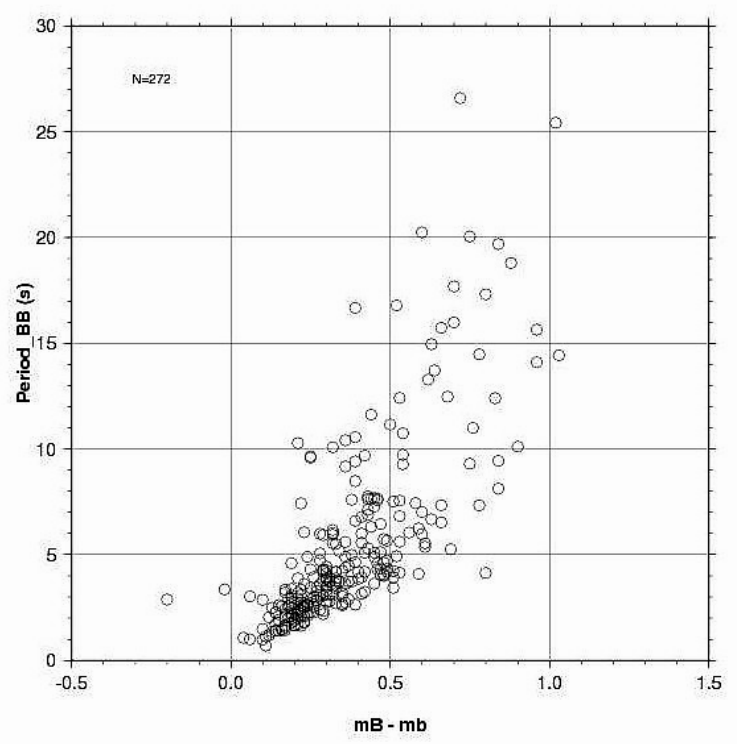

Fig. 3.53 Relationship between the difference of mB(BB)-mb on the period at which the V_{max} for mB(BB) calculation was measured. The data have been measured on velocity-proportional records of the broadband German Regional Seismic Network (GRSN).

The large data scatter in Fig. 3.53 at comparable magnitude differences is most likely due to both stress-drop and thus corner-frequency differences of earthquakes with comparable moment release as well as to local station site effects. This, however, does not essentially bias the stability and representativeness of the V_{max} readings for reliable mB_BB estimates, as the following case, observed on teleseismic station records of the GRSN, illustrates (according to Bormann et al., 2009):

- Earthquake off the east coast of Honshu, 18 January 2006, average network distance $\Delta \approx 82°$, 16-station network mB_BB = 6.06 ± 0.23 with an average T = 2.4 ± 1.4 s; station IBBN mB_BB = 6.10 at T = 0.7 s and station BUG mB_BB = 6.10 at T = 5.0 s; i.e., equal mB_BB although $T_{BUG} \approx 7 \times T_{IBBN}$.

Thus we can conclude, that the variability of period measurements in BB records on often not very harmonic oscillations does not essentially bias the readings of V_{max}. Generally, measurement errors of mB are significantly smaller than for short-period mb (compare also Figs. 3.23 and 3.24).

Question 5: How deviations from the standard responses affect mb and mB_BB?

V_{max} and T readings for mB_BB will not be biased if the velocity-proportional passband range of the broadband records covers fully the range of periods within which mB_BB is supposed to be measured, i.e., between 0.2 s to 30 s. In fact, however, periods below 1 s are rarely observed, usually for deep earthquakes only.

mb measurements on narrowband short-period records are more strongly affected by the effective relative bandwidth, the steepness of gain roll-off beyond the corner periods of the passband and by the exact period at which the response reaches its maximum gain. Therefore, it is advisable to adhere to the WWSSN-SP simulation filter parameters prescribed for standard mb. Yet slight differences in the high-frequency roll-off, as they had originally been implemented in some analysis software, my be acceptable within the 0.1 m.u. tolerance range for standard magnitudes (see Fig. 11 and discussion in IS 3.3).

Question 6: To what extent differences between mb and mB_BB are due to frequency-dependent attenuation?

Up to now, both mb and mB are calibrated with the Gutenberg and Richter (1956a) $Q(\Delta,h)_{PZ}$ functions although the latter had been derived from readings with periods between about 2 and 20 s (Abe and Kanamori, 1979) and were intended to be used for calibrating mainly intermediate-period amplitude readings within this range. This raises the question whether it is acceptable at all to use these calibration functions for 1 s P-wave mb as well or whether the observed systematic differences between mb and mB are – at least partially - due to the neglectance of frequency-dependent attenuation. One should note, however, that Gutenberg and Richter obviously did not believe in the applicability of the frequency-dependent attenuation model for their problem of magnitude determination. Because by measuring A/T instead of A they compensated in fact largely for the exponential frequency-proportional increase of displacement amplitude attenuation by multiplying A with f = 1/T. Thus they

derived a linear model of attenuation proportional to exp-0.00006 L, where L is the total length of the ray path from the station to the source. This explains the stability of the G&R Q(Δ, h) functions, making them theoretically even equally applicable to 10 s data and 10 Hz data. Although this may not fully be true for frequencies above about 0.5 Hz, various studies have shown (see section 2.5.4.2 on *wave attenuation* in Chapter 2) that there is no clear empirical evidence for frequency-dependent Q for periods above 2 – 4 s and that for higher frequencies the expected exponential increase in displacement amplitude attenuation is strongly reduced by absorption-band effects. Moreover, it is a matter of fact that the observed differences between mb and mB depend chiefly on magnitude itself and that they can almost perfectly be explained by the magnitude-dependent shift of the corner frequency of the source spectrum towards lower frequency and the average decay of the velocity amplitudes for f > fc with the first order (see Fig. 3.45).

With the same reasoning, the IASPEI standard calibration function for Ms, measuring A/T or nowedays directly velocity amplitudes for Ms_BB in a wide range of periods is rather stable and reliable as well without accounting for frequency-dependent attenuation. When, however, measuring surface-wave displacement amplitudes in narrow bandpass ranges for Ms determination, as done in the Bonner et al. (2006) Ms(VMAX) procedure, then it is indeed indispensible to correct such amplitudes for frequency-dependent attenuation to make them on average compatible with Ms_BB or the so-called Prague-Ms. That this is indeed the case has been demonstrated by both Bonner et al. (2006) and Bormann et al. (2009).

Regrettably, reliable experimental data on frequency-dependent attenuation are still rare and model calculations may yield rather different results depending on whether one uses attenuation models with the ***quality factor Q*** depending on frequency for shorter periods or not. Therefore, until more reliable empirical spectral attenuation data for ground-motion velocities measurements become available, it is still justified to use the Gutenberg-Richter calibration functions for both mb and mB_BB determinations.

Question 7: How reliable are the Gutenberg-Richter $Q(\Delta, h)_{PV}$ curves/tables?

The Gutenberg and Richter (1956a) calibration curves show many details, probably too many in view of the interpolation through rather noisy data measured with instruments of different response, often not well known gain and station site effects (see Veith, 1998) and less accurate estimates of epicentral distance and depth they had available in their days. Already efforts by Christoskov et al. (e.g., 1978, 1985 and 1991) for the development of a homogeneous magnitude system (HMS) based on carefully selected first-order stations over Eurasia and accounting for station site corrections showed that the average P-wave calibration curve for shallow events is much smoother than the respective Gutenberg-Richter Q(Δ). Differences between medium-period P(Δ) and Q(Δ) reach up to 0.3 m.u. in some limited distance ranges between 20° and 100°. Saul and Bormann (2007) came to the same preliminary result and additionally showed that the differences in the regional range between 5° and 20° epicentral distance may be even larger, up to about 0.8 m.u. around 10° (see Figure 16 in IS 3.3). These differences, especially in the regional distance range, may however differ from region to region. Further investigations are required to clarify this. Standardized mB measurements will ease this task.

Nolet et al. (1998a) also derived new depth-distance corrections for deep earthquakes in the ranges $20° \leq \Delta < 90°$ and $100 \text{ km} \leq h \leq 700 \text{ km}$, based on readings of V_{max} in velocity

broadband records as for standard mB_BB. They published their revised $Q_b(\Delta,h)^{NKC}$ both as a diagram plot and as a Fourier expansion formula which yields values that generally differ less than 0.1 m.u. from those derived via the curve plot. The plot curve looks much smoother (see Fig. 3.54 in section 3.2.6.1 and related discussion) than the Gutenberg-Richter $Q(\Delta,h)_{PZ}$ plot (Fig. 1a in DS 3.1), showing less details but the same main features and trends as well as low scatter and no bias with depth with respect to $\log M_0$ when normalized to 0 for shallow events (Nolet et al., 1998b). However, only after a rigorous comparison of mb and mB_BB values calculated for deep earthquakes by using both the Gutenberg-Richter and the Nolet et al. Q-values and their confrontation with independent accurate and stable magnitude measurements such as Mw one might be able to decide which calibration data are better suited for calculating the two standard body-wave magnitudes for deep earthquakes, i.e., by not introducing a systematic bias but reducing data scatter.

Still open problems:

Despite the strong recommendation of the Committee on Magnitudes at the IASPEI General Assembly in Zürich (1967) to report the magnitude for all waves for which calibration functions are available, the ISC and NEIC determine no body-wave magnitudes from PP or S waves despite their merits discussed above and the fact that digital broadband records now allow easier identification and parameter determination of these later phases.
1) At distances beyond 100° the P-wave core shadow prevents to measure mb and mB. Yet, good PP readings from strong earthquakes are possible and calibration functions $Q(\Delta, h)$ available for PPH and PPV up to 170°. According to Bormann and Khalturin (1975), mB determined from P and PP waves scale perfectly. The orthogonal regression is

$$mB(PP) = mB(P) + 0.05 \pm 0.15 \text{ m.u.} \qquad (3.46)$$

If, however, short-period amplitude readings for P and PP are used instead, the orthogonal relationship is magnitude-dependent (mb(PP) = 1.25 mb(P) -1.22) and the standard deviation is much larger (±0.26 m.u.). This again testifies the greater stability of body-wave magnitudes based on medium- to long-period readings.

2) The suitability of large amplitude readings of PKP in the distance range of the core caustic around 145° and beyond for magnitude determinations has also been ignored so far (see 3.2.6.3 and EX 11.3).

3) No proper discrimination had been made in the past at the international data centers between data readings from different kinds of instruments or filters, although respective recommendations were made already at the joint IASPEI/IAVCEI General Assembly in Durham, 1977. However, with the step-wise introduction of the new IASPEI standards since 2010 for some of the most widely used magnitudes both the measurement parameters as well as the related unique nomenclature for measured amplitudes and magnitudes have now been fixed (see Table 4 in IS 3.3). On the other hand, this necessitates that magnitude data resulting from non-standard procedures, which can – on average - not reproduce for the same type of magnitude the standard results within 0.1 m.u., be reported with a specified nomenclature. First proposals have been made in IS 3.2 and are expected to be refined in future.

3.2.6 Other amplitude, period, intensity or tsunami based magnitude scales (P. Bormann)

Below we describe several other complementary procedures for magnitude estimation. They are not (yet) based on IASPEI recommended standards but are (or my become) also useful for applications in seismological practice.

3.2.6.1 Broadband and spectral P-wave magnitude scales

Broadband P-wave magnitude scale for intermediate and deep earthquakes

A calibration function $Q_b(\Delta,h)^{NKC}$ has been derived by Nolet et al. (1998a). It is based on V_{max} measurement on broadband velocity recordings of P waves (bandpass between 0.01 and 2 Hz) and applicable to intermediate and deep earthquakes in the ranges $20° \le \Delta \le 90°$ and 100 km $\le h <$ 700 km. For deriving this calibration function, the measured amplitudes have been normalized to a scalar seismic moment $M_0 = 10^{18}$ NM, which corresponds to a **short-period** mb = 5.7 according to a relationship $mb = (\log M_0 - 4.3)/2.4$ for deep earthquakes published by Giardini (1988) and to Mw = 5.9 according to the IASPEI standard Mw-M_0 relationship $Mw = \log(M_0 - 9.1)/1.5$.

The $Q_b(\Delta,h)^{NKC}$ plot looks much smoother (Fig. 3.54) than the Gutenberg and Richter (1956a) plot of $Q(\Delta,h)_{PZ}$ (see Figure 1a in DS 3.1). Even some of the larger details in the Gutenberg-Richter plot are missing, yet the isolines follow the main feature of $Q(\Delta, h)_{PZ}$ (around 300 to 400 km depth) and the trend with distance, have small standard deviations and no bias with depth with respect to $\log M_0$ when normalized to 0 for shallow events (Nolet et al., 1998b).

Quantitatively, the values of $Q_b(\Delta,h)^{NKC}$ are generally lower than those of $Q(\Delta,h)_{PZ}$ because Nolet et al. (1998a) wrote their mb formula in the way as we wrote also (3.37a) for Ms_BB and (3.45a) for mB_BB, i.e., by including $-\log 2\pi = -0.8$ into the constant. But it remains an average difference of about -0.3 m.u. with quite some scatter. The scatter may be due to the many local details in the G-R plot that could - partially at least – be related to uncorrected station site effects (Veith, 1998) (see discussion in section 3.2.5.2 related to Question 7). The negative average residual with respect to $Q(\Delta,h)_{PZ}$, however, is obviously due the scaling of mb to mb = 5.7 (or Mw = 5.9 for $M_0 = 10^{18}$ Nm), which on average corresponds according to Bormann et al. (2009) to an mB_BB = 6.0 (see also Fig. 3.53 and the average difference of mB-mb of about 0.3 m.u. for periods of P around 3 s in broadband records. According to Nolet et al. (1998a) the dominant periods of the maximum velocity pulses of deep earthquakes in broadband records fall in the range between 1 – 4 s but are occasionally even larger. Thus they are longer than the dominant periods around 1 s of the short-period P waveforms on which the amplitudes for mb are commonly read. Therefore, in order to make on average the numbers given on the isolines of Fig. 3.54 comparable with the Gutenberg-Richter (1956a) Q-values, which were derived for scaling medium-period mB measurements, one would need to correct for the downscaling to short-period mb.

No results of a systematic comparison of mb(Nolet) with standard mB_BB for identical V_{max} readings have become known to us so far. This, however, would be necessary and the reasons for differences better be understood before one can judge on the potential advantage (or not) of replacing for earthquakes deeper than 100 km the Gutenberg-Richter $Q(\Delta,h)_{PZ}$ by $Q_b(\Delta,h)^{NKC}$. Such an investigation should be encouraged.

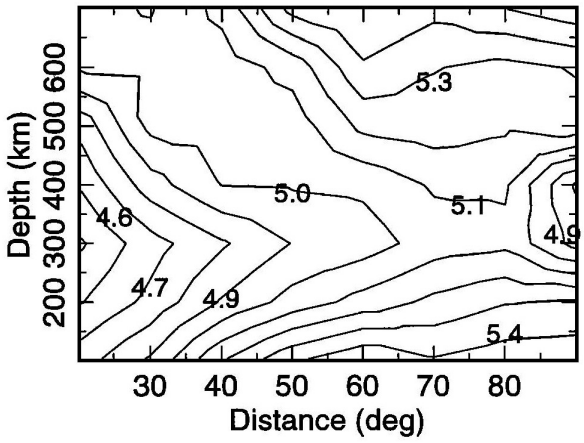

Fig. 3.54 $Q_b(\Delta,h)^{NKC}$ calibration values, averaged over 20° and 200 km depth range. Copy of Fig. 3 in Nolet et al. (1998), Geophys. Res. Lett., **25**, 9, p. 1453; © American Geophysical Society.

Spectral P-wave magnitudes

Duda and Kaiser (1989) recommended the determination of spectral magnitudes based on measurements of largest amplitudes in one-octave filtered digital broadband records of P waves. Fig. 3.55 show such bandpass records of two earthquakes with comparable magnitude mb, recorded at comparable distance, but having different source depth and mechanism. Accordingly, the amplitudes in different spectral ranges differ a lot. This is due to regional differences in ambient stress conditions and related stress drop.

Duda and Yanovskaya (1993) calculated theoretical spectral amplitude-distance curves based on the IASP91 velocity model (Kennett and Engdahl, 1991) using two different attenuation models aiming at magnitude calibration of spectral amplitude measurements (see Fig. 2.39 in Chapter 2). This effort is a response to the "saturation" problems discussed above. By combining the spectral magnitude estimates yields smoothed average values of the radiated seismic spectrum, its spectral plateau, corner frequency and high-frequency decay and thus of M_0 and stress drop of the given event. Thus one may draw inferences on systematic differences in the prevailing source processes (e.g., low, normal or high stress drop), related ambient stress conditions in different source regions but also on the amount and relative share of radiated high and low frequencies and thus of the potential of the earthquake to cause either strong shaking damage or generate a tsunami.

This, however, has so far not yet been the main concern of common seismological routine practice, which aimed at providing just a simple one (or two) parameter size-scaling of seismic events for general earthquake statistics and hazard assessment. Rather, spectral magnitudes were more considered a research issue, which could be tackled even more directly by calculating both M_0 and the radiated seismic energy E_S proper, by estimating the corner frequency and shape of the overall source spectra from the corrected broadband record spectra and by determining and interpreting jointly both energy magnitude Me and moment magnitude Mw and their difference (see IS 3.5). Good Mw and Me estimates can nowadays already be done fully automatic within about 10-20 min after origin time and allow essentially the same inferences to be drawn then from the multi-bandpass filtering of broadband records

(see, e.g., Choy and Kirby, 2004; Di Giacomo et al., 2010a; Bormann and Di Giacomo, 2011). Therefore, this educationally very appealing concept of spectral magnitudes has not yet found broad application in observatory practice. A fine example is presented in Fig. 3.55.

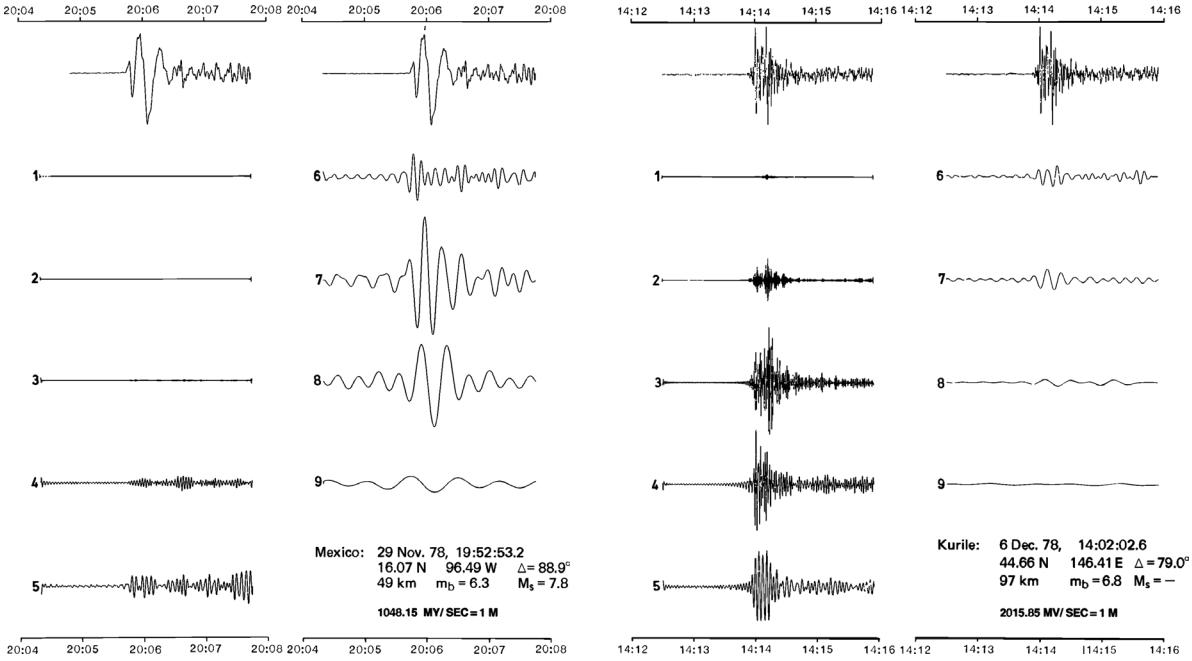

Fig. 3.55 Examples of broadband digital records proportional to ground velocity of the P-wave group from two earthquakes with mb = 6.3 and h = 49 km (left), and mb = 6.8 and h = 97 km (right), respectively. The earthquakes occurred in different source regions (Mexico and Kuriles). Below their BB records (uppermost traces) their one-octave bandpass-filtered outputs are plotted. The numbers 1 to 9 on the filtered traces relate to the different center periods between 0.25 s (1) and 64 s (9) in one-octave distance. Note that the somewhat "weaker" event on the left has its maximum recorded ground velocity in trace 7, corresponding to a center period of 16 s. In contrast, the mb-wise stronger event on the right, for which one would on average expect an even longer corner period, has its V_{max} at 1 s (trace 3). Thus, the 1-Hz spectral magnitude in the case of the Kurile earthquake would be much larger than for the Mexico earthquake, hinting to strong felt shaking and potential damage of exposed objects, not, however in the case of the Mexico earthquake with a very small amount of 1-Hz energy released. (Copied from Duda, 1986; with permission of the BGR Hannover).

3.2.6.2 1-Hz P-wave magnitude m(P) and mb(IDC)

Veith and Clawson (1972) developed a calibration function, termed $P(\Delta,h)_{SP}$ (see Fig. 3.56), using short-period WWSSN vertical-component P-wave records of underground nuclear explosions, thus avoiding data scatter due to uncorrected source radiation pattern effects. The $P(\Delta,h)_{SP}$ plot looks much smoother than the $Q(\Delta, h)_{PZ}$ curves published by Gutenberg and Richter (1956a) and resemble, also at depth, much more an inverse A-Δ relationship for short-period P waves as depicted in Figs 2.39 or 3.34. However, using only very shallow-depth sources, the calibration curves at depth are empirically not well constrained. They have been model-derived using still debatable attenuation models and therefore differ often significantly from both the Gutenberg and Richter (1956a) and the Nolet et al. (1998a) calibration curves

for vertical component P waves (compare with Figure 1a in DS 3.1 and Fig. 3.54 above, respectively). Yet, for shallow events mb(P) values agree well with mb(Q) (according to Veith, 2001, with an average difference of -0.03 m.u.) but have less scatter. Therefore, no wonder that the International Data Center (IDC) of the Comprehensive Test-Ban Treaty Organization (CTBTO) uses $P(\Delta,h)_{SP}$ as standard calibration curve for calculating its mb(IDC) values (see Chapter 17).

For deeper events, however, mb(P) is systematically lower than mb(Q) (up to about 0.4 magnitude units at 450 to 640 km depth) due to a different attenuation law assumed in the upper mantle and transition zone (Veith, 2001). For more details on pros and cons see Nolet et al. (1998b) and Veith (1998). Also note, that deviating from the use of the Gutenberg-Richter $Q(\Delta,h)_{PZ}$ functions, the calibration values given in Fig. 3.56 have to be applied to maximum P-wave peak-to-trough (2A) displacement amplitudes in units of nm = 10^{-9} m (instead of peak-to-trough/2 amplitudes in μm = 10^{-6} m). Accordingly, the Veith and Clawson formula reads:

$$mb(P) = \log (A_{max;peak\text{-}to\text{-}trough}/T) + P(\Delta,h) \qquad (3.47)$$

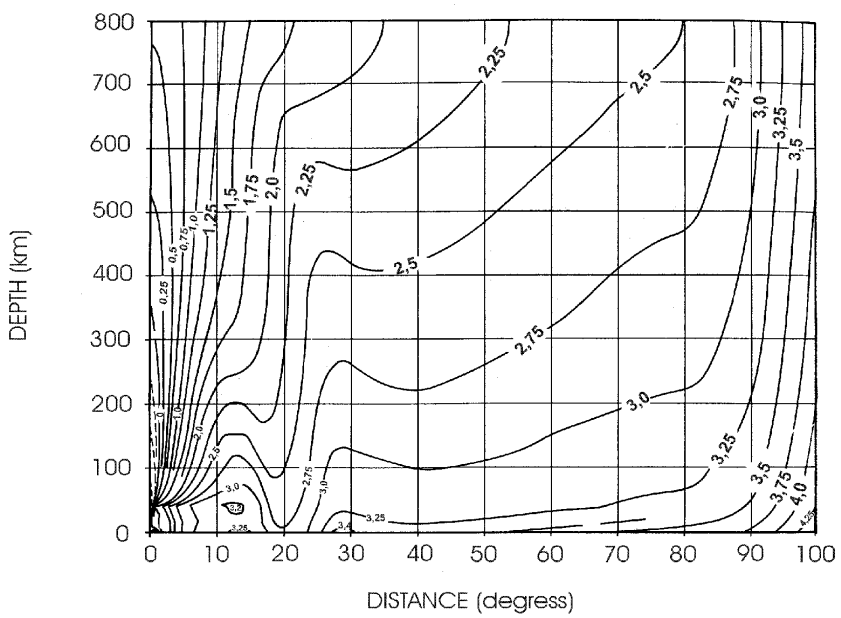

Fig. 3.56 Calibration functions P(Δ,h) for mb determination from narrow-band vertical-component short-period records with peak displacement magnification near 1 Hz (WWSSN-SP characteristic). (Modified according to Veith and Clawson (1972), Magnitude from short-period P-wave data, BSSA, **62**, 2, p. 446, © Seismological Society of America).

The Veith-Clawson magnitude calibration functions are officially used by the IDC in Vienna for mb determination although the IDC filter applied to the digital velocity-proportional broadband data prior to the amplitude measurements for mb results in a displacement response peaked around 3.4 Hz (Granville et al., 2005) instead of around 1 Hz, as required for the use of P(Δ, h) (Veith, 2001). According to the spectral logA-D curves calculated by Duda and Yanovskaya (1993) for the modified PREM attenuation model (see Fig. 2.39 in Chapter 2), logA is in the distance range between 10° and 100° at 4 Hz about 0.15 to 0.5 units smaller

than at 1 Hz. . Thus, the use of P(Δ, h) in conjunction with the IDC filter response is physically not correct and tends to systematically underestimate mb. This is further aggravated by the fact that the IDC determines A_{max} within a time window of only 5.5 s after the P onset (Granville et al., 2005). This heuristic procedure, although very suitable for a best possible discrimination between earthquakes and underground explosions on the basis of the mb-Ms criterion (see 11.2.5.2??), is not appropriate for proper earthquake scaling, at least for events with magnitudes larger than 6 and thus average rupture durations of more than 6 s [see relationship (3.3)].

According to the above, the difference between mb(IDC) and other mb values calculated with a more low-frequent response and longer measurement-time window will grow with magnitude. According to Bormann et al. (2007), based on data kindly provided by S. Wendt (2005), the difference between NEIC mb(PDE)–mb(IDC) is on average:

- 0.06 m.u. for mb(PDE) < 4.0
- 0.37 m.u. for mb(PDE) = 4.0-4.9,
- 0.48 m.u. for mb(PDE) = 5.0 -5.9,
- 0.61 for mb(PDE) ≥ 6,

and reached 1.5 m.u. for the great 2004 Mw9.0 Sumatra-Andaman earthquake.

Granville et al. (2002) analyzed 10 medium-size earthquakes in the depth range > 0 km to 530 km and with magnitudes mb between 6.4 and 6.8 according to the PDE (Preliminary Determination of Epicenters) reports of the United States Geological Survey (USGS) and 13 underground nuclear tests (UNTs) with PDE magnitudes mb between 4.6 and 6.1. They compared these data, which were derived from simulated WWSSN-SP records, by using the traditional procedure of mb determination based on the Gutenberg-Richter Q-functions, with a) the mb for the same WWSSN-SP data but calibrated with the Veith-Clawson relationship; b) the body-wave magnitudes reported in the REB (Reviewed Event Bulletin) of the (preliminary) PIDC based on the IDC filter with peak magnification around 3.4 Hz For comparison of the responses see Figure 4 in Granville et al., 2005, or Figure 3 in IS 3.3).

From this study the following conclusions were drawn:

- The agreement between mb(Q) (Gutenberg-Richter) and mb(P) (Veith-Clawson) based on WWSSN-SP data was still reasonably good for the earthquakes (average difference mb(Q)-mb(P) = 0.2);
- For underground explosions (only shallow-depth events!) the agreement was even better (average mb(P)-mb(Q) = 0.09);
- Yet, the average discrepancy between mb(P) and mb(PIDC/REB) is much larger (0.5 magnitude units), although the latter are also scaled with the Veith-Clawson calibration functions. For 63% of the earthquake observations the difference was at least 0.4 mb units, and several of them had even an mb offset greater than 1 magnitude unit!;
- In contrast, the average discrepancy between mb(P) and mb(PIDC/REB) is 0.0 and 75% of the observations fall between – 0.1 and +0.1;
- The PIDC (now IDC in Vienna) procedure is adequate for mb determination of underground nuclear explosions, but not for earthquakes.

3.2.6.3 Short-period PKP-wave magnitude

Calibration functions $Q(\Delta,h)_{PKP}$ for short-period amplitude and period readings from all three types of direct core phases (PKPab, PKPbc and PKPdf) have been developed by Wendt (see Bormann and Wendt, 1999; also explanations and Figure 3 in DS 3.1). These phases appear in the distance range $\Delta = 145° - 164°$ (see Fig. 3.34, Figs. 11.62-63 ??? in Chapter 11 and Figure 1 in EX 11.3) with amplitude levels comparable to those of P waves in the distance range $25° < \Delta < 80°$. Many earthquakes, especially in the Pacific (e.g., Tonga-Fiji-Kermadec Islands) occur in areas with no good local or regional seismic networks. Often these events, especially the weaker ones, are also not well recorded by more remote stations in the P-wave range but often excellently observed in the PKP distance range, e.g., in Central Europe. This also applies to several other event-station configurations. Available seismic information from PKP wave recordings could, therefore, improve magnitude estimates of events not well covered by P-wave observations at distances below 100°.

Earlier investigations on the use of PKP phases for magnitude determination have been published by Miyamura (1974), Mizone, (1977), Tittel (1977), Janský et al. (1977), Kowalle et al. (1983) and Janský and Kvasnička (1992).

3.2.6.4 High-frequency moments and magnitudes

Koyama and Zheng (1985) developed a kind of short-period seismic moment M_1 which is related to the source excitation of short-period seismic waves and scaled to mb according to

$$\log M_1 = 1.24\ mb + 10.9 \quad (\text{with } M_1 \text{ in J = Nm}). \tag{3.48}$$

They determined M_1 from WWSSN short-period analog recordings by applying an innovative approximation of spectral amplitudes

$$Y(f) = 1.07\ A_{max}\ (\tau/f_0)^{1/2} \tag{3.49}$$

with A_{max} - maximum amplitude, f_0 - dominant frequency and τ - a characteristic duration of the complicated wave-packets. They analyzed more than 900 short-period recordings from 79 large earthquakes throughout the world in the moment range $7.5 \times 10^{17} \le M_0 \le 7.5 \times 10^{22}$ Nm. M_1 did not saturate in this range!

More recently, Atkinson and Hanks (1995) proposed a high-frequency magnitude scale

$$\mathbf{m} = 2 \log a_{hf} + 3 \tag{3.50}$$

with a_{hf} as the high-frequency level of the Fourier amplitude spectrum of acceleration in cm/s, i.e., for $f >> f_c$. They use average or random horizontal component accelerometer amplitudes at a distance of 10 km from the hypocenter or from the closest fault segment. **m** has been scaled to the moment magnitude **M** = Mw for events of average stress drop in eastern North America and California. When **M** is known, **m** is a measure of stress drop. For large pre-instrumental earthquakes **m** can more reliably be estimated than **M** from the felt area of earthquake shaking (see 3.2.6.6). When used together, **m** and **M** provide a good index of ground motion over the entire engineering frequency band, allow better estimates of response spectra and peak ground motions and thus of seismic hazard.

3.2.6.5 Earthquake early-warning magnitudes

In recent years great attention has been paid to the development of earthquake early warning systems (EEWS) which allow – besides very quick event location - near real-time magnitude estimates from the very first few seconds of acceleration, velocity or displacement records (e.g., Nakamura 1988, 2007; Espinoza-Aranda et al., 1995; Teng et al., 1997; Wu et al., 1997; Allan and Kanamori, 2003; Kanamori, 2005; Simons et al., 2006; Zollo et al., 2006; Gasparini et al., 2007). Based on such data rapid public alarms may be issued and/or automatically triggered risk mitigation actions after strong earthquakes with damage potential be taken. EEWS aim at minimizing the area of so-called "blind zones" which are left without advanced warning before the arrival of the S waves which have usually the largest strong-motion amplitudes. This necessitates very dense and robust seismic sensor networks within a few tens of km from potentially strong earthquake sources. Such dense networks are at present available only in a very countries, e.g. California, Japan, Taiwan, and Italy. Their principles of rapid magnitude estimates are rather different from those mentioned above and below and the data analysis from such systems is largely based on much debated concepts such as the hypothesis of the deterministic nature of earthquake rupturing. Olson and Allen (2005), e.g., claim to be able to estimate with an average absolute deviation of 0.54 magnitude units the size of earthquakes up to magnitude 8 from the maximum period of the first arriving P waves within the first 4 s from many low-pass filtered velocity records within 100 km from the epicenter. However, Rydelek and Horiuchi (2006), who analyzed waveform data recorded by the Japanese Hi-net seismic network (see Chapter 8, section 8.7.3), could not confirm that such a dominant frequency scaling with magnitude exists. Also Kanamori et al. (1997), together with Nakamura (1988) one of the fathers of this idea, expressed much more caution about the prospects of this method after he had run together with Wu an extensive experiment with the Taiwan Early Warning System which has presently a 22-s reporting time for first location and magnitude estimates with magnitude uncertainty of ±0.25 m.u. (Wu and Kanamori, 2005). To reduce this reporting time even further down to about 8 s and thus the "blind zone", they used only the records of the first 8 station within less than 21 km epicentral distance to estimated the magnitude via the magnitude dependence of the average period τ_c of the P-wave, as well as the peak displacement amplitudes, if > 0.1 cm, within the first 3 s of the low-pass filtered displacement signal after the P-wave onset. Wu and Kanamori (2005) summarized their experience as follows: "… the slip motion is in general complex and even a large event often begins with a small short-period motion, followed by a long-period motion. Consequently, it is important to define the average period …during the first motion." However, after applying the τ_c concept to the Taiwan EWS they concluded: "…For EWS applications, if $\tau_c < 1$ sec, the event has already ended or is not likely to grow beyond M > 6. If $\tau_c > 1$ sec, it is likely to grow, but how large it will eventually become, cannot be determined. In this sense, the method provides a **threshold warning**". Moreover: "If $\tau_c > 1$ sec, the event is potentially damaging. If it is larger than 2 sec, the event is almost certainly damaging. Combining this information with other data, such as the initial velocity and displacement amplitudes, would allow the damage potential of the event to be assessed more accurately." More can indeed not be expected to be said within the first 3 s of a record, especially not for strong and great earthquakes. Only for earthquakes with M ≤ 6 and thus total rupture durations that are according to formula (3.5) on average not more than about twice the τ_c measurement time windows of Kanamori (3 s) or Olson and Allen (4 s), these new concepts seem to yield reasonably good magnitude estimates, comparable with those provided by tsunami early warning systems (TEWS) in the case of strong to great

tsunamigenic earthquakes within some 5 to 30 min (e.g., Lomax and Michelini, 2012). This is illustrated by short reference to and discussion of several representative EEWS.

The Nakamura UrEDAS (Urgent Earthquake Detection and Alarm System) predicts the magnitude from the dominating period Td within a few seconds of the initial P-wave motion. According to Nakamura and Saita (2007) these dominiating periods, when observed at hypocentral distances between about 50 to 850 km, increase for earthquakes with M_{JMA} 3 to 7 from an average of about 0.2 s to 4 s. However, due to the large scatter of Td by a factor of about 3 measured at individual stations for the same event, the event magnitude M_{JMA} the latter can only be estimated with a possible error of about 0.5 m.u.

The ElarmS system (Allen and Kanamori, 2003), an adaptation of UrEDAS for Southern California, uses TriNet and California Integrated Seismic Network stations (see IS 8.4, and Simons et al., 2006). For estimating the magnitude it measures the **predominant period** $\mathbf{T^P_{max}}$ (between 0.1 and 3 s) in broadband velocity records within the first few seconds (1 to 4 s, depending on event size) after the P-wave onset. Yet, again due to the large variability of the individual station T^P_{max} (up to a factor of about 10) the average absolute error in the estimated magnitude is ± 0.7 m.u when measured only at the closest station to the epicenter. However, when the closest 10 stations within 100 km of the epicenter are used, this error drops to ±0.35 m.u. Allen and Kanamori (2003) give two regression relationships for estimating the magnitude via T^P_{max}, one for events with magnitudes between 3 and 5, the other one for magnitudes between 4.5 and 7.

Grecksch and Kümpel (1997) estimated the magnitudes using the rise time of the first complete peak amplitude, the **predominant period**, and the related Fourier amplitude of the initial part of strong-motion signals. Yet, with this approach the magnitude uncertainty may even be as large as ±1.35 m.u. with a single accelerogram and ±0.5 m.u. with more than eight accelerograms.

A different approach had been taken by Wu et al. (1998). Using strong-motion records from moderate size earthquakes with $5.0 \leq Ml \leq 6.5$ and 10 s waveforms after the P-wave onset they derived an Ml_{10} estimator from the strong-motion signal duration which allows to estimate local magnitude $\mathbf{Ml = 1.28Ml_{10} - 0.85 \pm 0.13}$ with a correlation coefficient of 0.96. The slope of 1.28 indicates that small earthquakes require smaller and bigger earthquakes larger adjustments at 10 s to be made. With this procedure the Taiwan Central Weather Bureau determines epicenters and rather reliable magnitudes in about 20 to 30 s after the occurrence of moderate size earthquakes.

For larger crustal earthquakes Wu and Teng (2004) developed another method of estimating the moment magnitude with a standard deviation of about ±0.30 m.u. up to magnitudes of about 7.5 by integration of near source strong-motion amplitudes over the **whole rupture duration.** Yet, such magnitude estimates require more time, and are available only within some 30 to 60 s after origin time. This time lag is not suitable for advanced early warning anymore, however quite adequate for rapid response services (RRS).

In order to reduce the time lag Wu and Zhao (2006) again dealt with estimating the magnitude by using the **P-wave amplitudes** within the first three seconds of the record. Applied to earthquakes in Southern California they found out that their *"Pd magnitudes"* agree with catalog magnitudes with a **standard deviation of ±0.18 m.u. for events with magnitudes <6.5** but that they saturate for larger ones and can not be used to estimate magnitudes ≥6.7.

The same problem of saturation of Pd amplitudes they had observed already for large earthquakes in Taiwan (Wu et al., 2006), thus proving that the deterministic earthquake initiation model of Olson and Allen (2005) is not applicable to large earthquakes with magnitudes up to 8 and more, with rupture durations up to several 100 s.

In Italy, with very dense accelerometer networks near to major active faults, a procedure has been developed and tested by Zollo et al. (2006) which determines for both P and S waves the distance corrected logarithm of peak displacement ($\log(PGD_t^{10km})$ within the first 2 s after the onset of P and S for events in the magnitude range between 4 and 7.3 (93% in the range 4 to 6). Most of the records have been made at distances less than 20 km from the source. The authors give weighted standard for their logPGD estimates of ± 0.13 (for S) to ± 0.22 (for P).

A very different approach has been taken by Simons et al. (2006). They determine the earthquake magnitude via a multiscale wavelet analysis from the first 3-4 s of the incoming P wave and analyzed 2272 seismograms recorded by the Southern California TriNet array at epicentral distances up to 150 km in the magnitude ranges from 3 to 5 and >5 to 7.3,respectively, as in Allen and Kanamori (2003). Yet also they could predict the true magnitude only within approximately one unit. These authors correctly state that "…the nature of wave propagation (which includes the effects on the P-wave amplitude due to focusing, attenuation and site amplification) as well as the complexities of the source mechanism, and its orientation with respect to the measurement stations, are all such that any predictive relationships between the observables gleaned from the P wave and earthquake magnitude are statistical at best."

This notwithstanding, much of the average potential as well as the principal shortcomings of the above EEW magnitude procedures could have been predicted and wrong claims as those by Olson and Allen (2005) be avoided by taking into account the approximate relationship (3.5) as well the average seismic source spectra in Fig. 3.5 of this Chapter.

According to relationship (3.5) the average rupture duration of magnitude M = 3 events is ≈ 0.1 s, for M = 5 ≈1.6 s, for M = 6 ≈6 s, and for M ≥ 7 ≈ 25 s up to about 400 s for M = 9. Moreover, the large and great earthquakes are usually very individual multiple rupture processes with complicated and often non-symmetric source-time functions (see, e.g., Figs. 3.5, 3.9 3.10, 3.13 in this Chapter). This may even require to approximate the moment-rate release function by multiple point sources to get correct Mw estimates (e.g., as Tsai et al., 2005, for the great 2004 Sumatra-Andaman earthquake). In view of these facts to speak of a deterministic nature of earthquake ruptures which allows to predict their size up to magnitude 8 from data within the first 4 s of a seismic records is daring. At best one can speak of a deterministic component in the rupture process. Suitable measurement parameters related to this deterministic componenent are the average **rupture duration**, uncertain by a factor of about 2-3 for a given event and magnitude (see, e.g., Fig. 3.5), and the approximate average corner frequency f_c of the source spectrum, also with a variability range at a given magnitude due to variations in stress drop and/or rupture velocity Magnitude is supposed to be an estimator of released seismic energy. The largest amount of energy is released around f_c. According to Fig. 3.5, right-hand panel, f_c is on average for Mw = 3 ≈10Hz, for M = 5 ≈1Hz, for M = 6 ≈0.3Hz, and the respective corner periods for M = 7, 8 and 9 ≈25 s, 100s and 400 s, respectively. But this means that up to M = 6 the dominating radiated periods are already contained in the first few second of the P-wave record. And since the rupture duration for M = 6 is on average only about 6 seconds, the related amplitude maximum will also appear within a time window of 3-4 s after the P-wave onset, a symmetric moment rate release function

provided. Thus there is no wonder, why the EEW magnitude procedures based on Pd and/or τ_c work reasonably well up to magnitudes 6-6.5, begin to saturate, however, for stronger earthquakes. And then it is understandable, why the strong-motion duration-based procedure by Wu and Teng (1998) works fine up to 7.5 when integrating over time windows between 30 s and 60 s.

And beyond, this principle discussion explains also why procedures as proposed, e.g., by Hara (2007 a and b), Bormann and Saul (2009), and Lomax and Michelini (2009 a and b) do not saturate at all. They relate maximum, summed-up or integrated amplitudes or, as Lomax and Michelini (2011 and 2012) the dominant period Td (up to 30 s and more) to estimates of the rupture duration. Lomax and Michelini (2012) even, measure Td by the peak of the τ_c algorithm of Nakamura (1988) and Wu and Kanamori (2005), applied with a 5 s sliding time-window from 0 to 55 s after the P arrival on velocity seismograms. I.e., essentially the same measument parameters are looked for as by the EEW community, but they avoid saturation by adopting the measurement time window after P to the growing rupture duration and the bandwidth of the record so as to surely cover f_c and thus Pd. And additionally, as by Wu et al. (1998) for magnitudes up to 7.5, the rupture duration itself is taken into account. Yet such principle considerations can not be not be found in any of the other above referenced EEW papers.

3.2.6.6 Macroseismic magnitude

In order to apply the useful concept of instrumentally determined magnitudes for earthquake size classification, statistics and seismic hazard assessment also to earthquakes that occurred in the pre-instrumental era relationships between earthquake magnitudes and macroseismic parameters determined in the instrumental era had to be developed. Some of these efforts aimed at developing specifically magnitude scales which are best suited for earthquake engineering assessment of potential damage and thus seismic risk. According to Grünthal (2011) "intensity data give a surprisingly robust measure of earthquake magnitudes." These efforts go in two directions: by relating M to macroseismic intensity I and/or shaking area A_I or by focusing on the high-frequency content of seismic records.

Macroseismic magnitudes, M_{ms} are particularly important for the analysis and statistical treatment of historical earthquakes. Gutenberg and Richter (1942) published already a few years after the introduction of the instrumental earthquake magnitude by Richter (1935) a first empirical relationship with the epicentral intensity I_0 followed by Kawasumi (1951) who related his magnitude scale M_K to the **intensity I in the JMA scale** (see Chapter 12) **at the 100 km distance**, following Richter's definition of Ml as closely as possible. This approach is physically quite reasonable because for most earthquakes a distance of 100 km is already the far field and source finiteness can be ignored. The Kawasumi intensity-magnitude conversion formula reads:

$$M_K = 0.5\ I_{100} + 4.85. \qquad (3.51)$$

This approach was further developed by Rautian et al. (1989).

Other approaches related either the maximum observed intensity I_{max} (e.g., Topppzada, 1975) or the epicentral intensiy I_0 to M (e.g., Karnik, 1969). Differences between I_0 and I_{max} are expected to be small, but there have been instances where I_{max}, due to extreme local site

effects exceeded I_0 as much as two degrees (Tinti et al., 1987). Therefore, relationships based on I_0 are nowadays generally preferred to I_{max}-based relationships. On the other hand, I_0-based definitions implicitly assume the point source model and must be often misleading. Of course, with historic catalogs, there is usually no other way. There are three main approaches to compute macroseismic magnitudes:

1) M_{ms} is derived from the epicentral intensity I_0 (or the maximum reported intensity, I_{max}) assuming that the earthquake effects in the epicentral area are more or less representative of the strength of the event (e.g., Karnik, 1969);

2) M_{ms} is derived from taking into consideration the whole macroseismic field, i.e., the size of the shaking is related to different degrees of intensity or the total area of perceptibility, A (e.g., Toppozada, 1975);

3) M_{ms} is related to the product $P = I_0 \times A$ which is nearly independent of the focal depth, h, which is often not reliably known (Toperczer, 1953).

Accordingly, formulae for M_{ms} have the general form of

$$M_{ms} = a\, I_0 + b\,, \tag{3.52}$$

or, whenever the focal depth h (in km) is known, which strongly controls I_0,

$$M_{ms} = c\, I_0 + \log h + d\,, \tag{3.53}$$

or, when using the shaking area A_{Ii} (in km^2) instead,

$$M_{ms} = e \log A_{Ii} + f \tag{3.54}$$

with A_{Ii} in km^2 shaken by intensities I_i with $i \geq$ III, ..., VIII, respectively.

Since dominating source depth and intensity-attenuation conditions may vary significantly from region to region, the relevant coefficients have to be determined regionally. E.g., in order to derive suitable relationships according to (3.52) for Italy, Tinti et al. (1987) had to subdevide the territory into eight distinct regions for which the constant **a** varies between 0.27 and 0.62 and the correlation coefficients between 0.79 and 0.92. Karnik (1969) published a widely used relationship according to (3.53) for Europe:

$$M_{ms} = 0.5\, I_0 + \log h + 0.35. \tag{3.55a}$$

Gutdeutsch et al. (2002), however, derived another **orthogonal** regression relationship for Central and Southern Europe, which differs considerably from Karnik´s formula:

$$M_{ms} = 0.654\, I_0 + 1.868 \log h - 1.682 \quad \text{with SD} = \pm 0.284. \tag{3.55b}$$

For a given magnitude I_0 depend on source depth h. Two extreme examples from Illionois earthquakes have been referred to by Nuttli et al. (1979): The same I_0 = VII has been observed both by an earthquake with mb = 3.8 at h = 1 km source depth and by another one with mb = 5.5 at 20 km depth.

In the above equations, M_{ms} is used for a generic macroseismic magnitude. Musson and Cecić (2002) emphasize, however, that for any particular equation it is important to specify what type of magnitude the equation is compatible with (Mw, Ml, Ms, or others). Moreover, it is also important to determine the standard error as a measure of uncertainty attached to the estimated magnitude values, as for the relationship (3.55b).

Relationships, according to formula (3.54), with the area of intensities of shaking from IV to VIII scaled to local magnitude Ml, have been developed by Toppozada (1975) for California and Western Nevada.

Sometimes the mean radius R_{Ii} of the shaking area related to a given isoseismal intensity is used instead of the area A_i and (3.52) is then written:

$$M_{ms} = g \log R_{Ii}^2 + h \log R_{Ii} + j. \qquad (3.56)$$

Greenhalgh et al. (1989) give such relationships for the radii of Modified Mercalli (MM) intensities III and IV as observed for Australian earthquakes and with M_{ms} scaled to Ml.

Thus, in the above relationships, the constants **a** through **j** have to be determined independently for different regions and accordingly, M_{ms} is mostly scaled to local/regional Ml. Also Ml requires local/regional scaling and has proven to be best related to earthquake damage and engineering applications because of A_{max} being measured in the most relevant frequency range for earthquake engineers between about 0.5 to 10 Hz. Yet, some M_{ms} relationships in the United States have been scaled instead to the near 1-Hz mb(Lg), e.g. by Street and Turcotte (1977) for the Northeastern North America and by Nuttli et al. (1979).

In recent years, however, it has become increasingly fashionable to unify magnitudes in earthquake catalogues to the moment magnitude Mw (for critiism see 3.2.10), although Mw is a static measure of earthquake size and derived from the long-period asymptotic plateau of the radiated source displacement spectrum instead of being measured around its corner frequency at which the maximum of seismic energy is radiated. Yet, as long as the considered magnitudes $Mw < 6.5$ and thus the corner frequencies according to Fig 3.5 on average > 0.3 Hz such an approach may still be acceptable, not, however, when much larger or slow earthquakes play a significant role in the area under consideration.

Grünthal et al. (2009) published such a relationship based on well constrained moment magnitude Mw, I_0, and h of European earthquakes. It reads

$$Mw = 0.667\ I_0 + 0.30 \log(h) - 0.10, \qquad (3.57)$$

or, when no reliable information about h is available

$$Mw = 0.682\ I_0 + 0.16. \qquad (3.58)$$

These two relations are valid in the ranges $5 < I_0 < 9.5$, $3.0 < Mw < 6.4$, and $5\ km \leq h < 22\ km$.

According to Musson and Cecić (2002), differences in spectral content for larger earthquakes may affect the way in which earthquake vibration is perceived, and a different scaling with

area appears then to apply. Therefore, Frankel (1994) uses for representing the full magnitude range the form

$$M_{ms} = n \log(A/\pi) + 2m/(2.3\sqrt{\pi})\sqrt{A} + a \qquad (3.59)$$

where n is the exponent of geometrical spreading, m = (πf)/(Qβ) with f = predominant frequency of earthquake motion at the limit of the felt area (probably 2-4 Hz), Q the shear-wave attenuation, and β = shear-wave velocity, taken as 3.5 km/s).

Frankel (1994) compared felt area and moment magnitudes for California with its young mountain ranges with a global data set of earthquakes in stable continental regions (SCRs) such as central USA (Fig. 3.57). The main reason for the large difference in felt area for equal moment magnitude Mw is that the average attenuation is at frequencies around 2-4 Hz, which is the range of best human perceptibility to ground shaking, much higher in California than in SCRs, with corresponding Q values of about 490 in California and 1600 in SCRs, respectively.

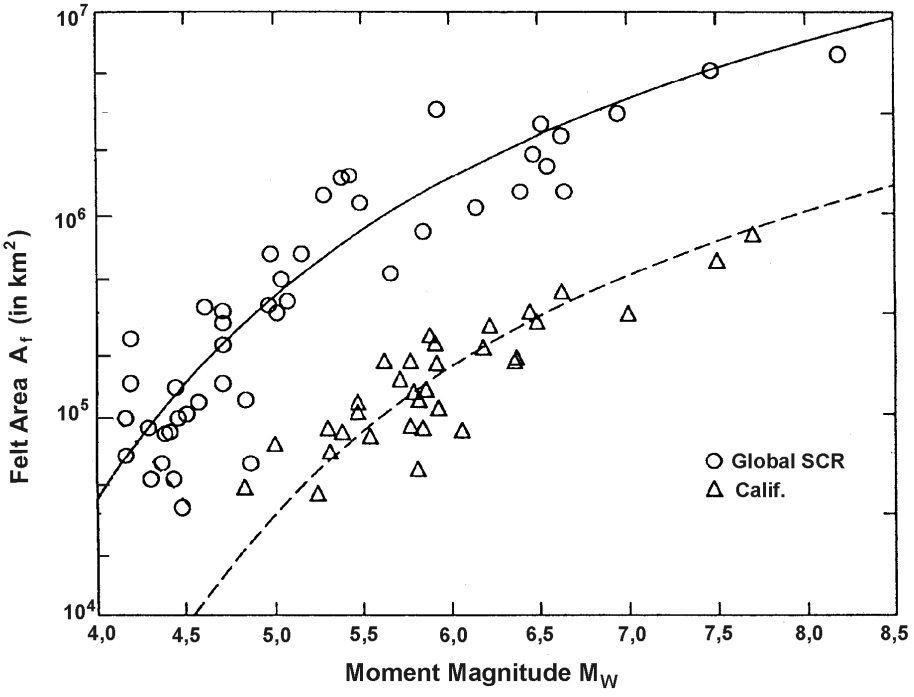

Fig. 3.57 Felt area A_f (in km^2) plotted against moment magnitude, M_w, for global data from stable continental regions (SCR) (open circles; from Johnston, 1993) and California data (triangles, from Hanks et al., 1975; Hanks and Johnston, 1992). Solid and dashed lines are fits according to an equation given by Frankel (1994) (modified from Frankel, Implications of felt area-magnitude relations for earthquake scaling and the average frequency of perceptible ground motion, Bull. Seism. Soc. Am., Vol. 84, No. 2, Fig. 1, p. 463, 1994; © Seismological Society of America).

Johnston (1996) derived a regression relation for the Modified Mercalli Intensity scale (MMI; see Chapter 12) for stable continental regions to predict seismic moments M_0 according to the functional regression form (3.59) proposed by Frankel (1994) with an uncertainty in the range

of ±0.15 to 0.23 Mw units, and another M_{ms} scale based on $P = I_0 \times A$ (in km^2) had been published by Galanopoulos (1961):

$$M_{ms} = \log P + 0.2\,(\log P - 6), \tag{3.60}$$

A macroseismic magnitude scaled to the body-wave magnitude of Central United States earthquakes in the range $2.7 \le mb \le 5.5$ was developed by Nuttli and Zollweg (1974):

$$mb = 2.65 + 0.098 \log A_f + 0.054\,(\log A_f)^2. \tag{3.61}$$

It is applicable for magnitude estimates of central United States earthquakes with felt areas of shaking $A_f \le 10^6$ km^2 for which there are intensity maps but no instrumental data available.

Other forms of these equations combine I_0 and the radius r of the total macroseismic field (Albarello et al., 1995), either in the way

$$M_{ms} = a\,I_0 + b\,\ln r + c, \tag{3.62a}$$

or, when using values for each available isoseismal I,

$$M_{ms} = a\,I_0 + \sum b_i\,\ln r_i + c. \tag{3.62b}$$

However, because of the subjectivity in isoseismal construction, modern opinion favours the direct use of the distribution of intensity **I** data points (IDPs) at epicentral distance D, without any isoseismals. This is particularly suitable in the case of sparse intensity data. An example are the two formulas given by Braunmiller et al. (2005) for earthquakes in Switzerland:

$$M_{ms} = [I(D) - 0.096 + 0.043D]/1.27 \quad \text{for shallow earthquakes } (h \approx 5 \text{ km}) \tag{3.63a}$$

and

$$M_{ms} = [I(D) + 1.173 + 0.030D]/1.4 \quad \text{for deeper earthquakes } (h \approx 12 \text{ km}). \tag{3.63b}$$

Currently three systems are available for the joint computation of the main earthquake parameters epicentre/hypocenter and magnitude from IDP sets: The Bakun-Wentworth (B-W) method, originally developed for California by Bakun and Wentworth (1997), the BOXER method for Italian earthquakes with Ms > 5.5 by Gasperini et al. (1999) and MEEP (Macroseismic Estimation of Earthquake Paramaters) by Musson and Jiménez (2008). In Chapter 12 (Fig. 12.8) of this Manual, Musson and Cecić compare the results of all three methods, applied to the same IDP set of an earthquake in the UK, with the instrumentally calculated epicentre and magnitude. All these methods require a well-calibrated intensity-attenuation model valid for the region under consideration.

A related problem is the determination of magnitudes of prehistoric and historic (pre-instrumental) earthquakes from dimensions (length L, width W and/or dislocation D) of observed seismo-dislocations (e.g., Khromovskikh, 1989; Wells and Coppersmith, 1994; Mason, 1996) based on correlation relationships between magnitudes and respective field data from recent events (see 3.3.4).

3.2.6.7 Tsunami magnitude

A different kind of magnitude is the tsunami magnitude scale M_t as defined by Abe (1979 and 1981b). The scale is so constructed that Mt agrees with the moment magnitude Mw. According to Abe (1989) holds

$$M_t = \log H_{max} + a \log \Delta + C \tag{3.64}$$

where H_{max} is the maximum single (crest or trough) amplitude of tsunami waves in m as measured by tide-gage records and /or as derived from maximum inundation height, Δ - epicentral distance in km to the respective tide station and a and C - constants (a was found to be almost 1). In case of the long-wave approximation, i.e., with tsunami wavelengths being much larger than the bathymetric depths, the maximum tsunami height is strictly related to the maximum *vertical* deformation of the ocean bottom, $D_{\perp max}$, and thus to the seismic moment M_0. M_t was calibrated, therefore, with the average condition $M_t = Mw$ for the calibration data set. This resulted in:

$$M_t = \log H_{max} + \log \Delta + 5.8. \tag{3.65}$$

(3.65) shows no saturation. For the Chile earthquake 1960 M_t = 9.4 while M_w = 9.5. Sometimes, very slow but large ruptures with a large seismic moment cause yet much stronger tsunami than would have been expected from their moment, surface wave, energy or body-wave magnitudes Mw, Ms, Me or mb, respectively. Such events are called "tsunami earthquakes" (Kanamori, 1972; Kanamori and Kikuchi, 1993; Polet and Kanamori, 2009). A striking example is the April 1, 1946 Aleutian earthquake with Ms = 7.3, Mw = 8.6 and M_t = 9.3. M_t avoids this underestimation of possible tsunami effects of such earthquakes by the common magnitude scales. Hara (2007b) gives two more examples for the 1992 Nicaragua earthquake (Mw = 7.6, M_t = 8.0) and the 1996 Peru earthquake (Mw = 7.5, M_t = 7.8). Such earthquakes have negligibly small energy in the high-frequency range and cause no or only minor shaking damage (see discussions in section 3.2.7.2 on energy magnitude Me).

3.2.7 Non-saturating magnitude scales Mw and Me

3.2.7.1 Moment magnitude Mw (P. Bormann)

The history of the derivation of the moment magnitude scale and the essential assumptions on which it is based have been outlined in detail by Bormann and Di Giacomo (2011) and in 3.1.2.5. Here we summarize only the essentials.

According to Eq. (3.2) and Fig. 3.5 the scalar seismic moment $M_0 = \mu \bar{D} A$ is determined from the asymptote of the displacement amplitude spectrum as frequency $f \rightarrow 0$ Hz. If this condition is fulfilled M_0 does not saturate. Kanamori (1977) proposed, therefore, a moment magnitude, Mw, which is tied to Ms but which would not saturate either. He reasoned as follows: According to Kostrov (1974) the radiated seismic strain energy is proportional to the stress drop $\Delta\sigma$, namely $E_S \approx \Delta\sigma \bar{D} A/2$. With Eq. (3.2) one can write $E_S \approx (\Delta\sigma/2\mu) M_0$. (For definition and determination of M_0 and $\Delta\sigma$ see also IS 3.1 and EX 3.4). Assuming a reasonable value for the shear modulus μ in the crust and upper mantle (about 3-6 $\times 10^4$ MPa) and assuming that, according to Kanamori and Anderson (1975) and Abe (1975), the stress

drop of large earthquakes is remarkably constant (ranging between about 2 and 6 MPa; see Fig. 3.37), one gets as an average $E_S \approx M_o/2\times10^4$ (see Fig. 3.88). Inserting this into the relationship proposed by Richter (1958) between the released seismic strain energy E_S and Ms, namely

$$\log E_S = 4.8 + 1.5\ Ms \text{ (in SI units Joule J = Newton meter Nm)} \qquad (3.66)$$

it follows:

$$\log M_0 = 1.5\ Ms + 9.1, \qquad (3.67)$$

which holds, however, according to empirical data by Ekström and Dziewonski (1988), for Ms > 6.8 only.

Solving (3.67) for the magnitude and replacing Ms with Mw one gets with M_0 in Nm

$$Mw = (\log M_0 - 9.1)/1.5 = (2/3)\ (\log M_0 - 9.1) \qquad (3.68)$$

and Mw = Ms for Ms > 6.8. This has been proved to be essentially correct by more recent empirical Mw-Ms regression relationships with slopes of 0.94 between 6.5 < Ms < 8.8 (Bormann et al., 2009), 0.99 between 6.2 ≤ Ms ≤ 8.2 (Scordilis, 2006), 1.06 between 6.2 < Ms ≤ 8.4 (Das et al., 2011) and 1.10 for Ms between 6.5 and 8.7 (Di Giacomo et al., 2013). Formula (3.68) is now the IASPEI (2005, 2011and 2013) accepted standard form of writing the moment magnitude formula. It avoids rounding errors and an ambiguity that arises if multiplication is performed prior to subtraction, which in a certain percentage of cases leads to Mw being different according to whether the moment is expressed in CGS or SI units (Utsu, 2002, and IS 3.3).

M_0 and Mw scales well with the logarithm of the rupture area [see Eqs. (3.165-3.167) and Figs. 3.94 and 3.95]. The determination of M_0 on the basis of digital broadband records is becoming increasingly standard at modern observatories and network centers. Yet, the source spectra of small to moderate earthquakes with magnitudes < 5 have usually corner frequencies higher than 0.5 Hz (see Fig. 3.5) and are often recorded at local to near regional distances with short-period instruments only. M_0 is then usually obtained in the spectral domain by determining the spectral plateau amplitude u_0 and using formula (3.2) (e.g., EX 3.4). For stronger up to great earthquakes (M > 8) however, recorded at teleseismic distances and much longer wavelengths, least-square waveform fitting of synthetic to long-period filtered seismograms is the preferred procedure. Dziewonski et al. (1981) developed such an algorithm for the full inversion of moment tensors from long-period body- and surface-waveforms with periods up to 45 s and 135 s, respectively. The automated version, which has become known as the Harvard Centroid Moment Tensor project and since 2006 as the Global CMT (http://www.globalcmt.org/), also yields the scalar seismic moment M_0 and Mw as spin-off parameters This method is still used, with some upgrading, e.g. those aiming at faster and more reliable solutions for very great complex mega-earthquakes. For such events the Harvard CMT moments turned out to be systematically too low because the longest periods considered were below the corner period of the single point source spectrum and the algorithm did not provide for fitting multiple source moment release functions (Stein and Okal, 2005; Tsai et al., 2005). Provisions have now been made to use longer periods for megaearthquakes. GCMT catalog data for events with Mw > 5.5 are considered to be available rather complete since 1977 but in more recent times also available down to Mw ≈ 4.5, although incomplete (see Figs. 3.81 and 3.82). For a most recent review about this project see Ekström et al. (2012).

Besides the GCMT also other agencies offer CMT solutions routinely for global and/or regional seismic events, such as the USGS NEIC, the GEOFON Big Alert Service of the GFZ German Research Centre for Geosciences (http://geofon.gfz-potsdam.de/eqinfo/gevn), the Swiss Earthquake Service (SED), the Japan Meteorological Survey (JMA), the Geophysical Survey of the Russian Academy of Sciences in Obninsk, to name just a few. In general, however, M_0, published by different authors or agencies, depends on details of the individual inversion methodologies and thus related event Mw may differ. Several alternative algorithms sharing the waveform inversion approach have been developed, e.g., by Aki and Patton (1978) and Kanamori and Given (1981) using surface waves and by Langston (1981), Sipkin (1982: 1986); and Nabelek (1984) using body waves. The USGS moment tensor solutions according to Sipkin (1986) use 15-55 s passband filtered waveform data. Therefore, this procedure also underestimates Mw for really great earthquakes. The code of Ammon (2001), developed for use on smaller magnitude earthquakes, works well with bandpass filtered waveform data between some 20 and 50 s. Thus, Mw methodologies and results have also to be critically checked for the range of their non-saturating applicability. For a detailed summary on the theory and methodologies of seismic moment tensor solutions and available services see IS 3.8, IS 3.10, and a related tutorial (IS/EX 3.11) (the latter two likely forthcoming).

3.2.7.2 Energy magnitude Me (D. DiGiacomo and P. Bormann)

Also the energy magnitude Me is in principle a non-saturating magnitude, provided that it can be measured by covering a sufficiently wide range of spectral velocity amplitudes. Bormann and Di Giacomo (2011) outlined in detail the common roots of Me and Mw as well as their differences both in theory and practical application (see also 3.1.2.5). In the following we recapitulate the essentials.

According to Kanamori (1977) Mw agrees very well with Ms for many earthquakes with a rupture length of about 100 km . Furthermore, he suggested that the log E_S-Ms relationship Eq. (3.66) also gives a correct value of the radiated seismic-wave energy for earthquakes with rupture dimensions larger than about 100 km. Therefore, Kanamori considered the Mw scale to be a natural continuation of the Ms scale for larger events. Thus, when inserting into Eq. (3.66) the value of Mw = 9.5 for the Chile 1960 earthquake instead of the saturated value Ms = 8.5 one gets a seismic energy release that is 30 times larger.

When substituting in Eq. (3.66) the surface-wave magnitude Ms by an energy magnitude Me, it follows

$$Me = (\log E_S - 4.8)/1.5 = (2/3)\,(\log E_S - 4.8). \qquad (3.69)$$

In the case that Kanamori´s condition $E_S/M_0 \approx 5 \cdot 10^{-5}$ holds, Eq. (3.69) reduces to Me = (2/3) (log M_0 – 9.1) = Mw. The latter has been published earlier by Purcaru and Berckhemer (1978), yet is valid only for the average apparent stresses (and related stress drop) on which the Kanamori condition is based. However, Choy and Boatwright (1995) showed that apparent stress, which is related to the ratio of E_S/M_0, may vary even for shallow events over a wide range between about 0.03 and 20.7 MPa. For deep earthquakes, the range is between about 0.03-7.4 MPa. They also found systematic variations in apparent stress as a function of focal mechanism, tectonic environment, and seismic setting. Oceanic intraplate and ridge-ridge transform earthquakes with strike-slip mechanisms tend to have higher stress drop and

E_S/M_0 ratio than interplate thrust earthquakes, with fault maturity obviously playing a major role (see IS 3.5). Accordingly, Me for the former will often be significantly larger than Mw. The opposite will be true for the majority of thrust earthquakes in subduction zones, for which Mw will be larger than Me. Therefore, Choy (2012) proposed $\Delta M = Me - Mw$, termed "differential magnitude", as a useful diagnostic parameter to discriminate between earthquakes with unusually high, intermediate and anomalously low energy radiation (see Figure 5 in IS 3.5). This point had repeatedly been made already in earlier publications (see next paragraph).

Riznichenko (1992) gave a correlation on the basis of data from various authors. It predicts (despite rather large scatter) an average increase of $\Delta\sigma$ with source depth h according to $\Delta\sigma = 1.7 + 0.2$ h, i.e., stress drops even larger than 100 MPa can be expected for very deep earthquakes. On the other hand, Kikuchi and Fukao (1988) found from analyzing 35 large earthquakes in all depth ranges that $E_S/M_0 \approx 5 \cdot 10^{-6}$, i.e., a ratio that is one order of magnitude less than the condition used by Kanamori for deriving Mw. Therefore, Me is not uniquely determined by Mw. Rather, Me and Mw are complementary descriptions of earthquake size and can be considerably different, up to 1 m.u. and even more. Striking examples have been published by Choy and Kirby (2004), Di Giacomo et al. (2009), Bormann and Di Giacomo (2011) and by G. Choy in IS 3.5 of this Manual.

The difference between Mw and Me reflects that Mw is nothing but a static measure of earthquake size [see relationship (3.1)] and thus of its overall tectonic effect. Thus, Mw does not contain any information about the dynamics of the source process. In contrast, Me is mainly controlled by the latter, namely by differences in stress drop and rupture velocity, which have a direct bearing also on the dominating frequency content of the radiated seismic energy (see also section 3.1.2.5).

Nowadays, with digital broadband recordings and fast computer programs, it is feasible to determine directly the seismic energy, E_S, by integrating the radiated energy flux in velocity-squared seismograms over the duration of the source process and correcting it for the effects of geometric spreading, attenuation and radiation pattern. According to Di Giacomo and Bormann (2011), via Venkatamaran and Kanamori (2004), it holds

$$\begin{aligned} E_S &= \left(\frac{1}{15\pi\rho\alpha^5} + \frac{1}{10\pi\rho\beta^5}\right) \int_{-\infty}^{\infty} \left|\dot{\hat{M}}(f)\right|^2 df \\ &= \left(\frac{2}{15\pi\rho\alpha^5} + \frac{1}{5\pi\rho\beta^5}\right) \int_{0}^{\infty} \left|\dot{\hat{M}}(f)\right|^2 df \\ &\approx \left(\frac{2}{15\pi\rho\alpha^5} + \frac{1}{5\pi\rho\beta^5}\right) \int_{f_1}^{f_2} \left|\dot{\hat{M}}(f)\right|^2 df \end{aligned} \qquad (3.70)$$

where ρ = density, α and β = *P*- and *S*-wave velocities of the medium, $\dot{\hat{M}}(f)$ = derivative of the seismic moment rate, f = frequency and f_1 and f_2 the lower and upper bounds of the integration, respectively.

A method, developed by Boatwright and Choy (1986) is now routinely applied at NEIC to compute radiated energies for shallow earthquakes of mb > 5.8 (see IS 3.6). Its application is not so trivial and not for use with single stations. Using almost 400 events, Choy and Boatwright (1995) derived the relationship for E_S-Ms as

$$\log E_S = 1.5\ Ms + 4.4. \quad (3.71)$$

It indicates that (3.66) slightly overestimates E_S. On the basis of such direct energy estimates these authors developed the energy magnitude relationship

$$Me = (2/3)\ (\log E_S - 4.4) \quad (3.72)$$

For earthquakes satisfying Kanamori´s condition $E_S/M_0 \approx 5 \cdot 10^{-5}$

$$Me = 2/3\ \log M_0 - 5.80 = Mw + 0.27 \quad (3.73)$$

i.e., an Me that is even larger than Mw. The Kanamori condition, however, is a narrow case.

To the contrary, according to the global average ratio E_S/M_0 in Choy et al. (2006) the average difference is $\Delta M = Me - Mw = -0.16$ and with respect to the newest data compilation in Figure 5 of IS 3.5 even less ($\Delta M = -0.36$), which corresponds to $E_S/M_0 = 5.75 \cdot 10^{-6}$ instead of $E_S/M_0 \approx 5 \cdot 10^{-5}$ assumed by Kanamori (1977) for deriving the Mw formula and in very good agreement with the $E_S/M_0 \approx 5 \cdot 10^{-6}$ by Kikuchi and Fukao (1988).

ΔM may become even much more negative, down to almost -1.5, for slow "tsunami earthquakes", corresponding to $E_S/M_0 \approx 1 \cdot 10^{-7}$. The latter may generate a strong (namely long-period) tsunami but only weak short-period ground motion, which may cause no shaking-damage and might not even be felt by people in the near field of the rupture. This has repeatedly been the case, e.g., on September 2nd, 1992 with the Mw7.6 Nicaragua earthquake, which had only an mb = 5.3 and an Me = 6.7, on June 2nd, 1994 with the Mw 7.8 Java tsunami earthquake and reported values for Me between 6.5 and 6.8, and on July 17th, 2006 with the Mw 7.7 Java earthquake with Me = 6.8. Moment-wise, all three earthquakes were comparably large, yet their rupture durations T_R ranged between about 100 s and 220 s (Kanamori and Kikuchi, 1993; Hara, 2007b; Lomax and Michelini, 2009a; Bormann and Saul, 2008 and 2009b). This is, according to the relationship $T_R \approx 0.6M - 2.8$ by Bormann et al. (2009), about 2-4 times longer than expected on average for earthquakes with Mw around 7.7.

This strongly contrasts with earthquakes Me >> Mw, e.g., for the 15 October 1997 M_w 7.1 Chile earthquake (Choy and Kirby, 2004) and the 12 January 2010 Mw 7.1 Haiti earthquake with Me values of 7.5 and 7.6, respectively, which caused major devastations and a large number of casualties due to strong ground shaking in conjuction with inferior building stocks. Other examples are given by Di Giacomo et al. (2010a and b). Thus, the difference $\Delta M = Me - Mw$ is an important diagnostic aid to quickly assess differences in the kind of seismic hazard and damages to be expected from strong earthquakes.

Another argument in favor of Me is that it follows more closely the original intent of the Gutenberg-Richter magnitude formula with $(A/T)_{max}$ as the input measurement parameter which relates magnitude to the velocity power spectrum and, thus, to energy. In contrast, Mw is related to the scalar seismic moment M_0 that is derived from the low-frequency asymptote of the displacement spectrum. Consequently, Me is more closely related to the seismic potential for damage while Mw is related to the final static displacement and the rupture area and thus related more to the overall tectonic effect of an earthquake.

However, one major advantage of non-saturating M_0 and thus Mw is that they have to be determined only from very long-period seismic waves with T >> Tc (= corner period of the radiated seismic spectrum). This is more easily done and less affected by small-scale complexities in the source process and inhomogeneities along the wave propagation path. Therefore, measurement errors in Mw are rather low, probably even less than 0.1 m.u. when based on good data.

In contrast, to assure a non-saturating Me the squared velocity spectrum would need to be measured widely enough towards both sides of f_c (respectively T_c) in Fig. 3.5 in order to assure that at least some 80% of the total E_S is obtained from the integration over the source spectrum. Me would then be underestimated by less than 0.06 m.u., which is negligible. When assuming that the low frequency part of the source spectrum is completely available, then - according to Singh and Ordaz (1994) - the highest frequency f_{max} still to be included should be 6 times f_c for an ω^{-2} model as in Fig. 3.5. However, the frequency range that can in practice be covered within the limits f_{min} and f_{max} may cut off significant amounts of seismic energy contained both in the low- and the high-frequency part of the source spectrum, especially, if the bandwidth of integration does not cover well frequencies around f_c. In the latter case Me may be underestimated up to a few tenths of magnitude units.

Current routine procedures operate in the period ranges between 0.2 and 100 s (procedure according to Choy and Boatwright, 1995). It is outlined in IS 3.6 and applied at the US Geological Survey (USGS), or 1 and 80 s (automatic near real-time procedure according to Di Giacomo et al., 2010a and b), applied by the GFZ German Research Centre for Geosciences (GFZ). The inclusion of frequencies above 1 Hz is generally difficult because of the then usually low SNR in teleseismic recordings and the difficulties to correct for frequency-dependent attenuation (see Chapter 2, section 2.5.4.2) and local site effects. But then, the condition $f_{max} = 6 \times f_c$ for the inclusion of higher frequencies is already difficult to meet for Mw < 5.5 in the case of an average stress drop ω^{-2} source model as assumed in Fig. 3.5. And since the average corner periods for magnitude 8.5 earthquakes is expected to be already around 100 s the current procedures will also not be able to sample the spectral amplitudes towards $T > T_c$. According to Bormann and Di Giacomo (2011) Eq. (3.72) can be written as

$$Me = Mw + [\log(\Delta\sigma/2\mu) + 4.7]/1.5. \quad (3.74)$$

This allows to roughly assess the possible influence of variations in stress drop on estimates of Me, using the scaling model in Fig. 3.5 but for varying in increments of one order for $\Delta\sigma$ between 0.1 and 100 MPa (see Tab. 3.2). This range of variations in $\Delta\sigma$ encompasses most of the published data (e.g., Abercrombie, 1995; Kanamori and Brodsky, 2004; Parolai et al., 2007; Venkataraman and Kanamori, 2004a). The related shift of f_c for these different $\Delta\sigma$ values has been plotted in Fig. 3.16 for an earthquake with Mw = 6.5, and in the inset for a wider magnitude range between Mw = 5.5 and 8.5. According to Fig. 3.16a, variations in $\Delta\sigma$ do not influence at all the displacement plateau of the source spectrum and thus estimates of M_0 as long as the basic condition of analysing only frequencies $f << f_c$ is observed. In contrast, according to Eq. (3.74) and in agreement with Fig. 3.16b, variations in stress drop by one order are - for a given seismic moment - expected to change the released energy by one order as well and thus the estimates of Me by almost 0.7 m.u.. This complicates matters even more.

In order to sample nearly 100% of the energy radiated by earthquakes with magnitudes between $5.5 \leq Mw \leq 8.5$ and stress drops between $0.1 \leq \Delta\sigma \leq 100$ MPa one would need to

consider a much wider range of frequencies between 0.001 Hz and 16 Hz instead. This is, however, not realistic, neither with respect to handling the very high-frequency part of the radiated energy nor for fast routine Me estimations using teleseismic P-wave records, taking also into account that the longest periods that can be used have to be shorter than the time difference between the onset of the P- and S-wave groups which can not be handled together. For a rough orientation Tab. 3.2 summarizes the magnitude-dependent underestimation of Me, -ΔMe, based on the source model of Fig. 3.5 but assuming variable stress drop between 0.1 and 100 MPa and integration over frequencies between 12.4 mHz and 1 Hz only, as in the GFZ procedure for quick Me estimation (see D. Di Giacomo et al., 2010 a and b).

Tab. 3.2 Estimates of –ΔMe for the GFZ procedure of Me determination according to Bormann and Di Giacomo, 2011).

$\Delta\sigma$ (MPa)	ΔM_e for $M_w = 5.5$	ΔM_e for $M_w = 6.5$	ΔM_e for $M_w = 7.5$	ΔM_e for $M_w = 8.5$
0.1	0.05	0.02	0.05	0.25
1	0.13	0.03	0.02	0.10
10	0.30	0.08	0.02	0.03
100	0.66	0.19	0.05	0.02

According to Tab. 3.2, an E_S procedure operating in the bandwidth range from 1 to 80 s may underestimate Me up to ≈0.66 m.u. for moderate (Mw ≈ 5.5) earthquakes with very high stress drop and thus $f_c > f_{max}$. But for most earthquakes with Mw between about 6.5 and 8.5 and intermediate $\Delta\sigma$ between about 1 to 10 MPa the underestimation is expected to be < 0.1 m.u. Yet, for great earthquakes (Mw > 8) with $\Delta\sigma$ < 1 MPa (possibly $f_c < f_{min}$), -ΔMe may also reach 0.2-0.3 m.u., or even more for extreme events. However, such estimates with respect to Me that are based on so simple a single point source rupture model must be used with caution. No models can account for all real source, propagation path and station site complexities, which luckily do not much affect teleseismic Mw estimates. Therefore, Tab. 3.2 can only for give a rough orientation of the possible range of Me uncertainties.

Underestimations for extreme events should be somewhat reduced by the more elaborate off-line USGS procedure that uses a slightly larger bandwidth and a residual integral for frequencies above f_c (see Boatwright and Choy, 1986). In summary, according to McGarr and Fletcher (2002), E_S released by earthquakes can probably be estimated only within a factor of 2-3 if multi-station high-quality seismic broadband data are available. This corresponds to an accuracy within 0.2 to 0.3 m.u. in Me. In the same range source directivity may affect related single station Me estimates (Venkataraman and Kanamori, 2004b)

Correcting for high-frequency attenuation is one of the most challenging tasks in calculating Me. It requires a detailed knowledge of the velocity and attenuation structure along the propagation paths, and also especially below the seismic stations. Available global attenuation models differ still significantly and are controversially discussed and empirical data show significant scatter. Fig. 3.58 compares empirical data of short-period spectral velocity amplitudes, measured on records of many world-wide distributed broadband stations. The respective spectral amplitude-distance curves have been calculated for two different Earth models, assuming frequency-independent quality factors Q: a) the AK135Q according to Montagner and Kennett (1996) and b) the Preliminary Earth Reference Model (PREM) according to Dziewonski and Anderson (1981). The inconsistencies for shorter periods are

obvious. The usually poor signal-to-noise-ratio at frequencies higher than 1 Hz in the teleseismic range represents another big limitation, especially for moderate and small earthquakes.

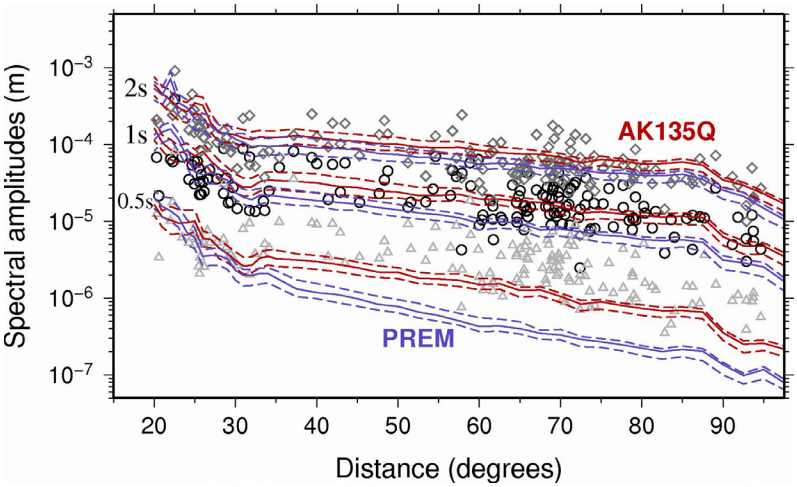

Fig. 3.58 Velocity spectral amplitudes at 0.5 s (2 Hz, light gray triangles), 1 s (1 Hz, black circles) and 2 s (0.5 Hz, gray diamonds) for the Mw = 7.9 Wenchuan, China, earthquake of 2008, May 12, superimposed to the theoretical spectral amplitude decay functions for the same frequencies for the AK135 model (median, 25th and 75th percentile in solid and dashed red lines, respectively) and the PREM model (median, 25th and 75th percentile in solid and dashed violet lines, respectively). An arbitrary offset has been added to the theoretical curves to make easier the comparison with the real data. (Courtesy of D. Di Giacomo, 2011).

These combined difficulties and thus - as compared to M_0 and Mw determinations - related larger possible errors are reasons that E_S and Me, despite their importance in assessing the damage potential of earthquakes, have rarely been used for this purpose so far. This, however, also means that one should not over-interpret differences between Mw and Me less than 0.2 m.u., yet larger ones may already be alarming because they may hint to different kinds of disaster consequences. Since Me for the Wenchuan earthquake was almost 0.4 m.u. larger than Mw (see Fig. 3.59) this may at least partially explain the extra ordinarily large shaking damages. In contrast, the great tsunamigenic Sumatra-Andaman Mw = 9,3 earthquake of 2004 was relatively slow with rupture velocities dropping down from 2.8 km/s at the beginning to 2.1 km/s in the Nicobar rupture segment. Accordingly, the related energy radiation efficiencies (see 3.1.2.5) were only 0.2 to 0.1 as compared to values between some 0.4 to 0.6 for other great earthquakes (Kanamori, 2006). Accordingly, energy magnitude Me(GFZ) = 8.8 is 0.5 m.u. units less than Mw for this earthquake (see Fig. 3.60a) which thus ranks between “normal” great earthquakes and the extremely slow tsunami earthquakes.

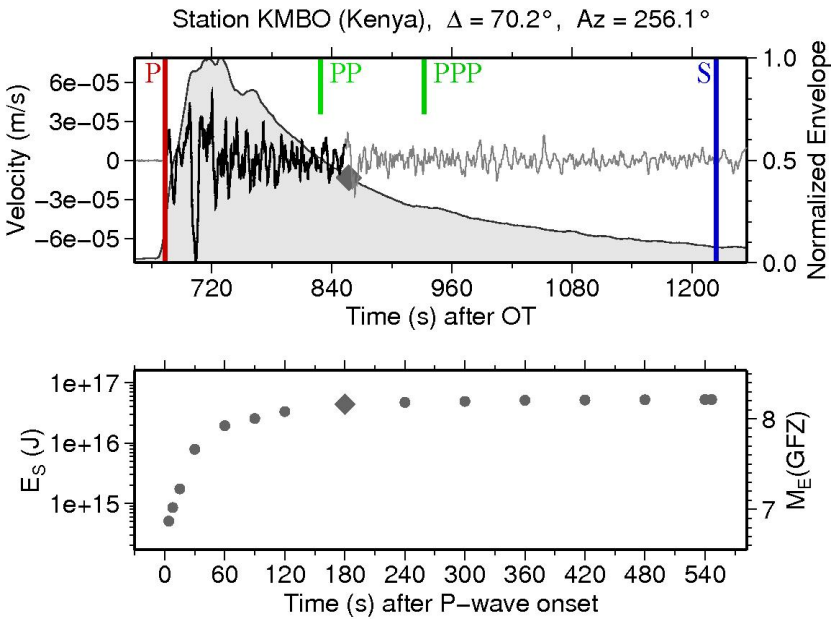

Fig. 3.59 Upper panel: vertical component velocity recording of the Mw = 7.9 12 May 2008 Wenchuan earthquake recorded at the station KMBO (Kenya). The theoretical P-, PP-, PPP- and S-wave arrival times have also been marked. The gray shaded area represents the envelope of high-frequency velocity amplitudes used to constrain the overall rupture time duration (Bormann and Saul, 2008), and the diamond at the end of the black record trace mark the end of the time window after the P-wave onset for which the final Me(GFZ) single station value is calculated. Thus, the full rupture duration is included in the E_S calculation. However, the rupture duration may last for several minutes (as for the great 26 December 2004 Sumatra earthquake). Then the entire S-P window should be considered. Lower panel: E_S (left y-axis) and Me (right y-axis) values for different cumulative P-wave windows. The diamond mark the end of the P-wave window that has been used for the single station M_E estimate. (Courtesy of D. Di Giacomo, 2011).

To evaluate the amount of time needed by this procedure to provide a stable Me in a real- or near-real time implementation, Fig. 3.60 shows the Me determinations at different times after OT for both the great 26 December 2004 Sumatra earthquake (Fig. 3.60a) and the 12 May 2008 Wenchuan earthquake (Fig. 3.60b). In the exceptional case of the 2004 Sumatra earthquake, for which the rupture duration as estimated from the duration of the P-wave train was about 500 s (Bormann and Wylegalla, 2005; Ni et al., 2005), this procedure could have yielded a stable Me already some 15 min after OT (Fig. 3.60a, right panel), since the major energy release occurred within the first 250 s of the rupture process (Choy and Boatwright, 2007). For the case of the Wenchuan earthquake, instead, using P-wave time windows of 180 s, more stations (24) could have been used already 10 min after OT, and a stable Me could have been released. Noticeably, in both cases the preliminary (alarm) Me(GFZ) available after 10 min are very close to the final values obtained by using all available stations. Of course, the time performance of this approach depends on the station availability with respect to the earthquake location. However, the worldwide station deployment is becoming increasingly dense, especially in areas for which a lack of instrumentation was still common a few years ago. Therefore, this procedure could yield in the near future rapid Me estimates within 10 min after OT also for great (Mw ≥ 8) earthquakes.

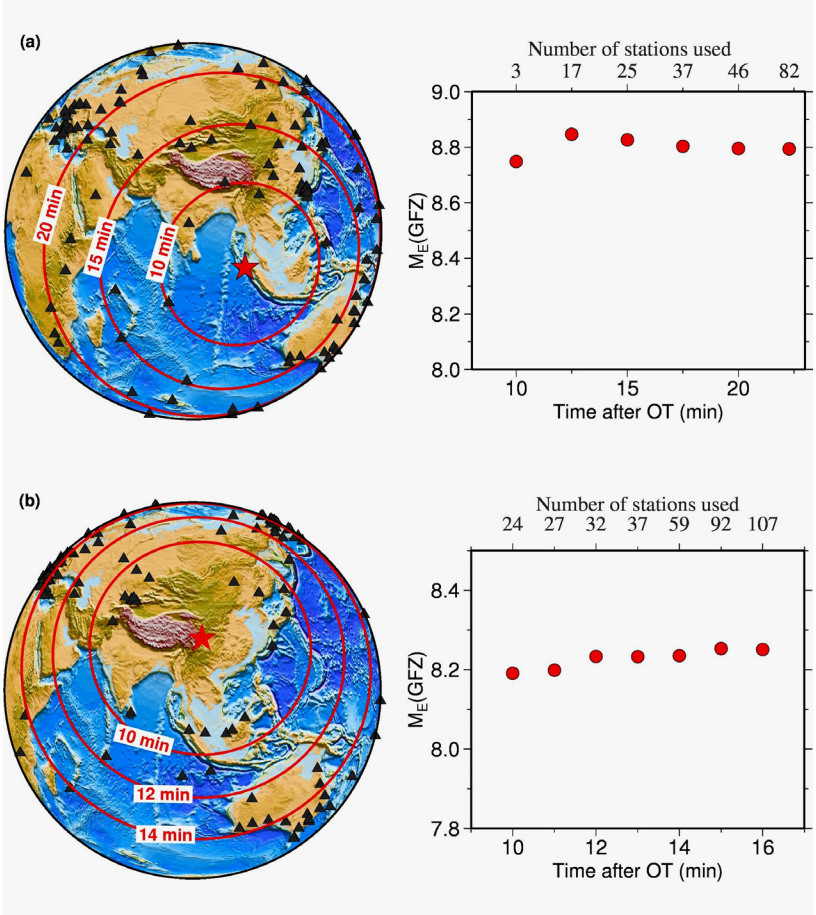

Fig. 3.60 a) Left: Map showing the location of the 26 December 2004 Mw = 9.3 Sumatra earthquake (red star), the broadband stations used to calculate Me(GFZ) (black triangles), and the red circles represent the S-wave arrival after OT. **Right:** Me(GFZ) determination of the Sumatra earthquake at different time after OT. The number of stations used to compute Me(GFZ) are also given; **b)** As for **a)** but for the 12 May 2008 Mw = 7.9 Wenchuan earthquake. Here the red circles on the map mark the time needed to record 180 s of P-waves.

3.2.8 Complementary non-saturating magnitude scales (P. Bormann)

3.2.8.1 Cumulative body-wave magnitude mBc

In their fundamental paper about energy and magnitude of earthquakes Gutenberg and Richter (1956a) shortly explain that their mB-logE_S relationship is based on the assumption of a point source which radiates a simple-shaped waveform whose largest amplitude and duration are related to each other. This makes it possible to estimate the seismic energy travelling with this waveform by scaling it to A_{max}, respectively $(A/T)_{max}$. They also mention that because of lacking data for stronger and likely more complex earthquakes the mB-logE_S relationship, which in fact is based on only 20 data points in the magnitude range between $5.3 \leq m \leq 8$ and one data point for $m = 2$ (see Fig. 3.83). may be less reliable. Indeed, larger earthquakes tend to be multiple source ruptures (see Figs. 3.9-3.13). Single-amplitude mB is then representative only for the largest sub-rupture. This let Bormann and Khalturin (1975) propose:

"In such cases we should determine the onset times and magnitudes of ***all clear successive P-wave onsets separately****, as they give a first rough impression of the temporal and energetic development of the complex rupture process."* **And further**: *„The magnitude* ***MP = log Σn (Ai /Ti) + Q(D,h)*** *(n is the number of successive P-wave onsets) could be considered as a more realistic measure of the P-wave energy released by such a multiple seismic event [...]."*

Bormann and Wylegalla (2005) demonstrated this by way of example for the great 2004 Mw9.3 Sumatra-Andaman earthquake. Just a single broadband station record near Berlin yielded a cumulative ΣmB, now termed mBc, of 9.4 and a rupture duration estimate of about 500 s. Meanwhile, this procedure has been fully automated (see Figs. 3.13 and 3.62, and for details Bormann and Saul, 2009b). Fig. 3.61 left shows the data and orthogonal regression relation (3.75) of Harvard CMT Mw(HRV) vs. mBc. Using Eq. (3.75) mBc can be converted into a proxy estimate of moment magnitude, Mw(mBc) = Mw*. Fig. 3.61 right compares Mw* with proper Mw(HRV). With SD_{OR} = orthogonal standard deviation and SD_Y in y direction holds:

$$Mw(HRV) = 1.22\ mBc - 2.11 \quad \text{with } SD_{OR} = 0.145 \text{ and } SD_Y = 0.23 \qquad (3.75)$$

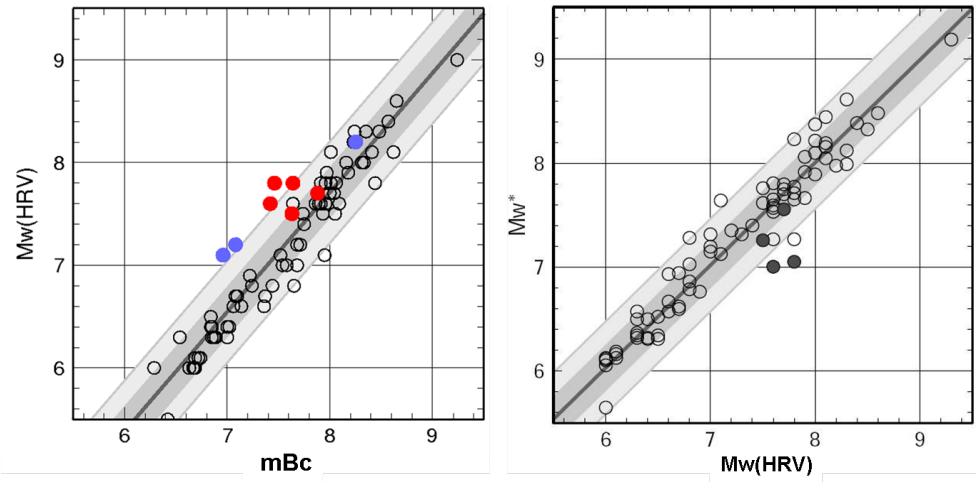

Fig. 3.61 Left: Orthogonal regression Mw(HRV) over mBc with 1-SD and 2-SD limits in dark and light grey; **red dots - tsunami earthquakes**, **blue dots – deep earthquakes**; **Right:** proxy Mw* = Mw(mBc) calculated via Eq. (3.75); **black dots – tsunami earthquakes**. Data according to Bormann and Saul (2009); Figure kindly provided by J. Saul, 2009.

Thus, equation (3.75) allows to compute a purely empirical Mw* estimator Mw(mBc), which is sufficiently accurate and quick to be used as a preliminary proxy Mw in tsunami early warning applications until Mw(HRV) (now Mw(GCMT) becomes available. Most events follow the two regressions well. For 80 percent of the events, $|Mw^* - Mw| < 0.25$ m.u. For only two events Mw* is significantly too low. They correspond to the very slow Mw 7.6 1992 Nicaragua and the Mw 7.8 1994 Java tsunami earthquakes. Yet, for two more tsunami earthquakes in our data set (M_w 7.5 Peru 1996; M_w 7.7 Java 2006, see Fig. 3.62) Mw* agrees within less than 0.25 m.u. with Mw, also for other major tsunamigenic events like the great 2004 and 2005 Sumatra earthquakes.

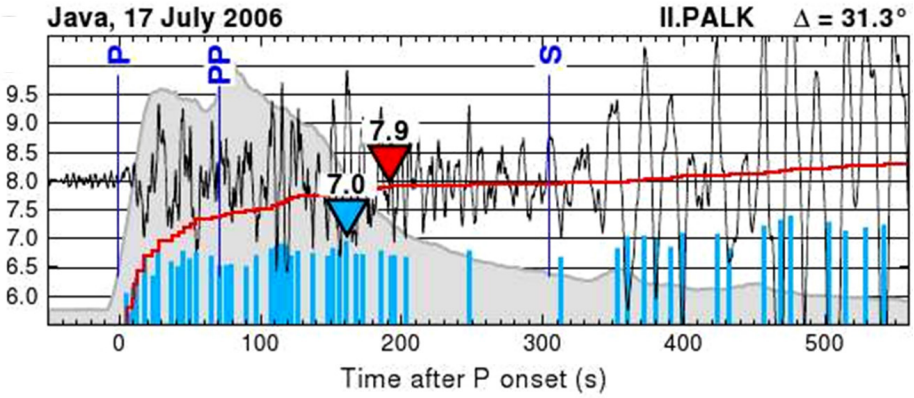

Fig. 3.62 Velocity-proportional broadband record of the Mw 7.7 July 2006 Java tsunami earthquake at station II.PALK processed with the automated mBc procedure by Bormann and Saul (2009b). Blue bars correspond to mB values of major amplitude onsets according to the condition $V_i \geq 0.6V_{max,t}$ with $V_{max,t}$ being the maximum velocity amplitude up to the time t. The largest sub-event single-amplitude mB = 7.0 has been marked by a blue triangle. The red curve shows the development of mBc with time and the red triangle the asymptotically saturated mBc value reached prior to the onset of S. The grey shaded area marks the high-frequency (HF) P-wave envelop. The apparent rupture duration d_{app} is measured from the P-onset up to the red triangle where the HF envelope amplitudes have dropped to 40% of their maximum value, corresponding to 16% energy wise.

From Fig. 3.61 left one realizes that mBc tends to overestimate increasingly magnitudes for Mw < 8. This means that for smaller earthquakes Gutenberg and Richter´s (1956a) original assumptions of a simple scaling of the maximum far-field P-wave amplitude to the duration of the waveform and its related seismic energy holds on average sufficiently well. Accordingly, summing up multiple P-wave onsets for smaller earthquakes tends to yield mBc > Mw and > mB. The apparent rupture duration estimates published by Bormann and Saul (2008 and 2009) agree for 90% of the investigate earthquakes within 10% with those published by Lomax and Michelini (2009a) for the same events, yet with a tendency of mB-mBc durations to be deliberately somewhat longer. This was necessary for assuring that the depth phases of P are included within this time window in order to satisfy IASPEI rules for mB measurements (see explanations to formulas (3.44 and 3.45). For the Java tsunami earthquake in Fig. 3.62 d_{app} = 190 s, which is almost three times longer than the rupture duration of 66 s estimated with formula (3.3) for an "average" Mw = 7.7 earthquake.

3.2.8.2 Mwp

A simple, fast and robust method of Mw determination from broadband P waveforms, termed Mwp, has originally been developed by Tsuboi et al. (1995) for quick estimation of the moment magnitude Mw and the tsunami potential of large near coastal earthquakes offshore of Japan. It has later been extended by Tsuboi et al. (1999) for application also to teleseismic earthquakes in general. Since then Mwp has become the main procedure at the Pacific Tsunami Warning Center (PTWC) for rapid rough Mw estimation. The procedure is based on the double integration of broadband P-wave velocity records and scaling of the maximum of the resulting source-time function via M_0 to Mw (Fig. 3.63).

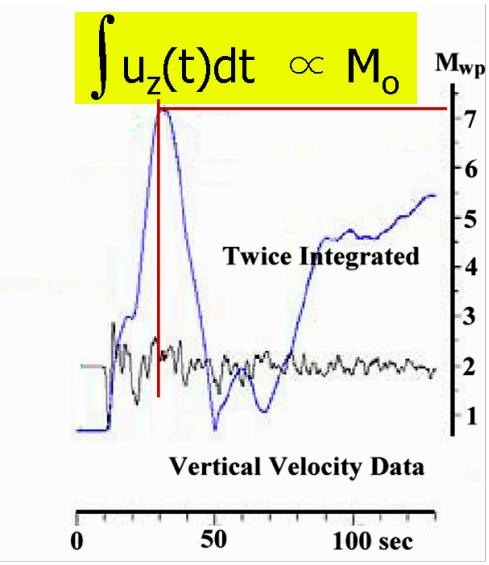

Principle of Mwp calculation

Fig. 3.63 **Black trace**: Original velocity-proportional vertical component P-wave record; **Blue trace:** Twice integrated record trace. According to Seidl and Berckhemer (1992) the **area** underneath the blue trace is proportional to M_0. For simplicity Tsuboi et al. (1995) scaled the first maximum of the blue trace to Mwp.

However, the original scaling as well as later introduced corrections were not so straightforward. Scaling to the first peak in the double integrated trace which is in fact the far-field source-time function, and not to the area underneath the total source-time function (see also Fig. 3.65a), assumes a single point source rupture model with a more or less symmetric moment-rate function and a simple relationship between the maximum amplitude and the area underneath the curve. Later, Tuboi et al. (1999) changed this by scaling Mwp to the largest of the first two maxima, accepting that this could relate either to a stronger depth phase (pP or sP) or to a stronger sub-event of the progressing rupture. Yet still, in the case of very large, more complex or very slow ruptures, Mwp tends to underestimate the true Mw, because even later sub-ruptures than the second one may have the largest amplitude, and most importantly, the rupture duration is not taken into account. For equal maximum amplitude of the source time function its duration and thus the area underneath the function may vary strongly, being much larger, e.g., in the case of slow earthquakes. Even with magnitude-dependent corrections introduced the Mwp = 8.2 for the great 2004 Sumatra earthquake turned out to be much too small (see Hirshorn and Weinstein, 2009). This value was later increased to Mwp = 8.5 by assuming a questionable variable apparent P-wave velocity (Kanjo et al., 2006).

Accordingly, Mwp turned out to be neither more efficient nor faster than the simple automated direct measurement of the traditional Gutenberg mB on velocity broadband records, which is now a new IASPEI body-wave standard. The reason is that also mB is based on the same simplified assumption, namely that the maximum amplitude of a single point source waveform in the far-field is scaled to the area underneath this waveform.

When plotting Mwp over mB (see section 3.2.8.1)) one gets almost a 1:1 orthogonal regression relationships whereas mBc is always larger but not saturating as do both the single amplitude mB and Mwp (Fig. 3.64). The regression relations are:

$$Mwp = 1.06\ mB - 0.09$$

and

$$Mwp = 0.95\ mBc - 0.47.$$

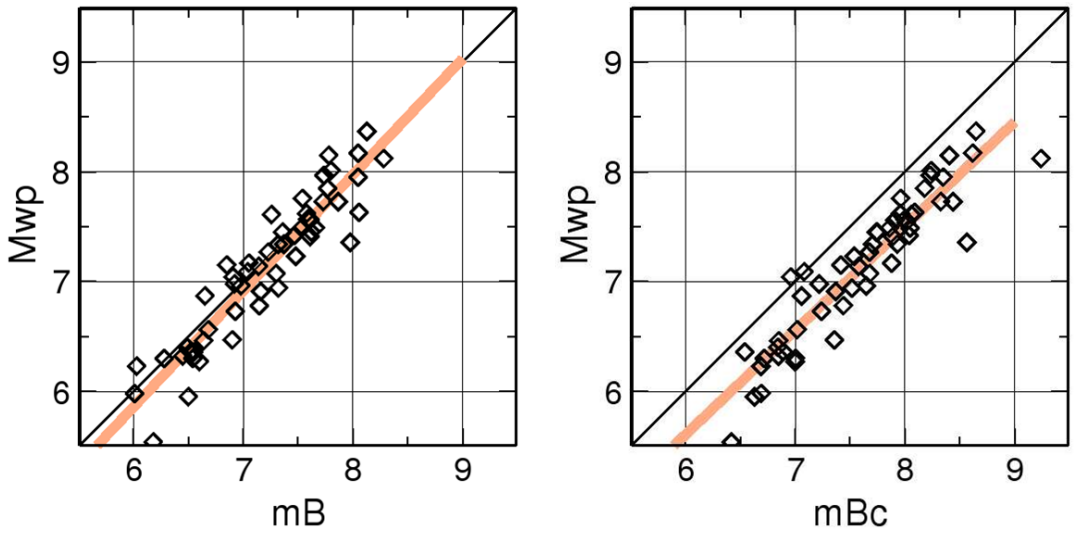

Fig. 3.64 Data and orthogonal regression relationships between Mwp of the Pacific Tsunami Warning Center and mB (left), respectively mBc (right), according to data of Bormann and Saul (2009). Figure courtesy of J. Saul, 2009.

3.2.8.3 M_{ED} and Mwpd

The main drawback of both Mwp and mB (in contrast to mBc) is that rupture duration and related major sub-events in seismic energy and moment release are not taken into account. The lack of these contributions, which may become very significant for great multi-source or extremely long-lasting ruptures (see Fig. 3.65a below), results in the underestimation of the overall event magnitude and thus of the tsunamigenic potential of really great earthquakes and of slow tsunami earthquakes in particular (e.g., Fig. 3.74 in section 3.2.9.4 and Hirshhorn and Weinstein, 2009).

To address this problem, and for rapid and accurate determination of the size and tsunamigenic potential of strong and great earthquakes, Lomax et al. (2007) and Lomax and Michelini (2009a) developed non-saturating, energy, M_{ED}, and moment, M_{wpd}, magnitudes, which explicitly take into account rupture duration. Similar to the procedures by Bormann and Saul (2008 and 2009) for measuring mB and mBc on velocity broadband records, the M_{ED} and M_{wpd} procedures estimate the apparent rupture duration, T_0, on high-frequency (HF;1-5Hz) filtered vertical component broadband seismograms. M_{ED} is based on an energy-duration procedure which cumulated energy in the time interval $t_{To} - t_P$ on vertical component, broadband velocity seismograms. The developed relationship between the estimated released seismic energy and the measured apparent rupture duration allowed a rapid estimation of $\Theta = \log(E_S/M_0)$ for identifying slow but dangerous tsunami earthquakes, namely, if Θ drops below -5.7.

Mwpd is based on a duration-amplitude procedure which is equivalent to cumulative application of the Mwp algorithm (i.e., moment determination) in the time interval $t_{To} - t_P$ on vertical component, broadband displacement seismograms. In operational application Mwpd values can be made available within about 10 min after origin time (OT) (Fig. 3.65a). First results showed, however, that additionally a scaling of the moment estimates was necessary in order to assure a better match with Mw(CMT). With such a scaling the difference $|$Mwpd – Mw(CMT)$|$ for events with magnitude $6.6 \leq Mw \leq 9.3$ was typically within ±0.2 m.u., with a standard deviation SD = 0.11 m.u. This moment correction has recently been simplified, along with other modifications, to enable faster, more robust real-time estimates of Mwpd (Lomax and Michelini, 2012).

Lomax and Michelini (2009b, 2011) show that neither Θ nor Mw alone proved to be good indicators for tsumanigenic earthquakes in general, while apparent rupture durations longer than about 50 s combined with predominant P-wave period Tp greater than about 10 s are good indicators. Lomax and Michelini (2009b) also show that measures on 1-5Hz HF filtered velocity broadband records alone can show for most earthquakes within 4-6 min after OT if the rupture duration is likely to exceed 50 s, indicative for tsunamigenic and tsunami earthquakes. Although less accurate than T_0, this rapidly available measure, T_{50EX}, is an important complement in operational tsunami early warning schemes. By combining T_{50EX} with a measurement of the predominant period, T_d, in the early part of the P-wave record, and later by estimating the apparent total rupture duration T_0, the products TdT_{50EX} and TdT_0 can be calculated (see Fig. 3.65b). These products proved to be reliable indicators for the tsunamigenic potential of earthquakes in general and for slow tsunami earthquakes in particular, superior to Mw(GCMT) (Lomax and Michelini, 2011, 2012). The reason is that the efficiency of tsunami generation by a shallow earthquake depends on the amount of sea floor displacement, which can be related to a finite-faulting model expressed by the *seismic potency*, LWD, where L is the length, W the width, and D the mean slip of the earthquake rupture (Kanamori 1972; Abe 1973; Polet and Kanamori, 2009). Mw is calculated from the seismic moment $M_0 = \mu LWD$ by assuming that μ, the shear modulus at the source, and thus also $LWD = M_0/\mu$ are constant and independent on source depth. This, however, is not the case, especially in shallow subduction zones. μ may there strongly decrease with source depth and fault rupture may occur close to the sea bottom on non-planar, lystric splay faults in water saturated sediments in the accretionary wedge (Fukao, 1979; Moore et al., 2007; Lay and Bilek, 2007). This will result in strongly reduced rupture velocity and stress drop and thus longer rupture duration with longer dominating periods of the radiated P-waves. In general, CMT algorithms, do not account for this low velocity and shear modulus. Accordingly, the seismic potency and tsunami potential may be underestimated, especially in the case of unusually slow ‘‘tsunami earthquakes’’, which, by definition, cause larger tsunami waves than one would expect from their Mw (Kanamori, 1972; Satake, 2002; Polet and Kanamori, 2009; Newman et al., 2011). Both Td and T_0, as well as the estimator of critical duration, T_{50EX}, “sense” these differences in source-depth dependent μ, and related reduced rupture velocity, increased rupture duration and potency LWD, and consequently increased sea surface displacement and tsunami potential.

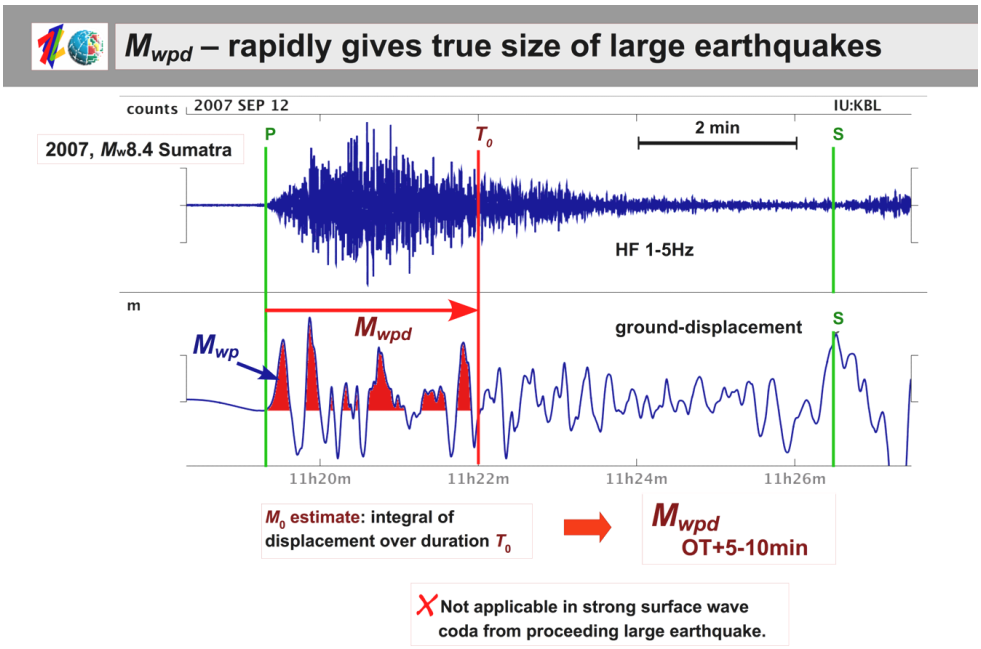

a)

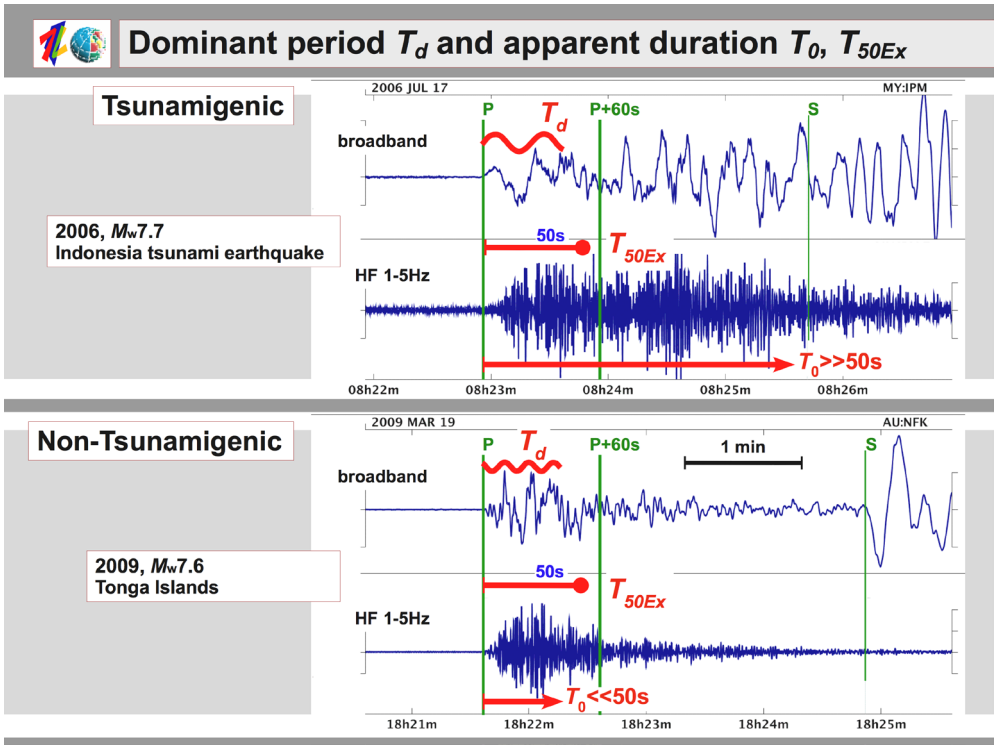

b)

Fig, 3.65 Illustration of a) the duration estimation and displacement integration for Mwpd determination and b) the estimation of the predominant period T_d, the duration exceedence probability parameter T_{50Ex} and of the total apparent rupture duration T_0 and their use for assessing the tsunamigenic potential of earthquakes. For details see text and Lomax and Michelini (2012). (Figure provided by courtesy of A. Lomax, 2013).

The Mwpd and TdT_{50EX}-Td T_0 procedures have been implemented operationally at the Istituto Nazionale di Geofisica e Vulcanologia (INGV) in Rome, Italy.

3.2.8.4 Hara´s maximum amplitude-duration magnitude M

In a slightly different and very straight forward empirical procedure Hara (2007a and b) combines measuring the high-frequency duration of the P-wave train with just the maximum P-wave displacement amplitude in broadband records to determine an empirical relation for a non-saturating magnitude M scaled to Mw in the Harvard CMT catalog:

$$M = 0.79 \log A + 0.83 \log \Delta + 0.69 \log t + 6.47$$

where A is the maximum displacement (in m) during the estimated duration t (in s) of high-frequency energy radiation since the P-wave first arrival time and Δ the epicentral distance (in km).

The Hara M matches with Mw(CMT) typically within ±0.3 m.u., with SD = 0.18. It is also applicable to tsunami earthquakes (2007b) that are characterized by relatively longer rupture duration but smaller amplitudes. However, in this case M underestimates, as Mw, the tsunami magnitude M_t.(see 3.2.6.7).

3.2.8.5 Mantle magnitude Mm

Another important teleseismic magnitude is called mantle magnitude Mm. It uses surface waves with periods between about 60 s and 410 s that penetrate into the Earth´s mantle (see section 2.3.4 in Chapter 2). The concept has been introduced by Brune and Engen (1969) and further developed by Okal and Talandier (1989 and 1990). Mm is firmly related to the seismic moment M_0 and thus avoids saturation. On the other hand, it is closer to the original philosophy of a magnitude scale by allowing quick, even one-station automated measurements (Hyvernaud et al., 1993), that do not require the knowledge of either the earthquake's focal geometry or its exact depth. The latter parameters would be crucial for refining a moment estimate and require (global) network recordings.

Mm is an estimate of ($\log M_0$ - 13) (when M_0 is given in Nm) and defined as:

$$Mm = \log X(\omega) + C_S + C_D - 0.90$$

where $X(\omega)$ is the spectral amplitude of a Rayleigh wave in μm-s, C_S a source correction, and C_D a frequency-dependent distance correction. For details of the correction terms, see Okal and Talandier (1989 and 1990).

Best results are achieved for Mw > 6 at distances > 15-20° although the Mm procedure has been tested down to distances of 1.5° (Talandier and Okal, 1992). However, at D < 3° the seismic sensors may be saturated in the case of big events. Also, at short distances one may not record the very long periods required for saturation-free magnitude estimates of very strong earthquakes, and for Mw < 6 the needed very long-period records may become too noisy. A signal-to-noise ratio larger than 3.0 is recommended for reliable magnitude estimates.

Mm determinations have been automated at the Pacific Tsunami Warning Center (PTWC) and the Centre Polynésien de Prévention des Tsunamis (CPPT) (Weinstein and Okal, 2005; Hyvernaud et al., 1993) so that values are available in near real-time within about 10 min after OT from near stations, however typically within about half an hour, plus a few minutes more for really great earthquakes measured at the longest periods. Mm does not – or only marginally – saturate, even for very great, slow or complex earthquakes.

Applications of Mm to the reassessment of the moment of shallow, intermediate and deep historical earthquakes are extensively described by Okal (1992 a and b).. For the Chile 1960 earthquake Okal (1992a) calculated values Mm ≈ 10 to 10.3 and for $M_0 = 3.2 \cdot 10^{23}$ Nm. Mm determinations were extensively verified and are said to be accurate by about ± 0.2 magnitude units (Hyvernaud et al., 1993).

3.2.8.6 W phase rapid Mw estimates and moment tensor solutions

In section 2.6.6 of Chapter 2 the nature and appearance of the very long-period W phase between the P and S-wave onsets have been shortly described (see Figs. 2.74 and 2.75). The inversion of the W phase for sufficiently strong earthquakes by optimizing the fit between W phase synthetics to empirical records (see Fig. 3.66) yields rather rapid (within about 25 minutes after the earthquake occurrence) and reliable first seismic moment tensor solutions and thus of both Mw (within about 0.1 m.u.) and the source mechanism of strong earthquakes (see Fig. 3.67). Therefore, such applications have recently gained immense practical importance for speeding up seismic tsunami warning, as proposed by Kanamori and Rivera (2008). First real-time implementations are operational at the U.S. Geological Survey's NEIC (Hayes et al., 2009) as well as at the GFZ Potsdam and the Indonesian Tsunami Early Warning System (InaTEWS) since 2011.

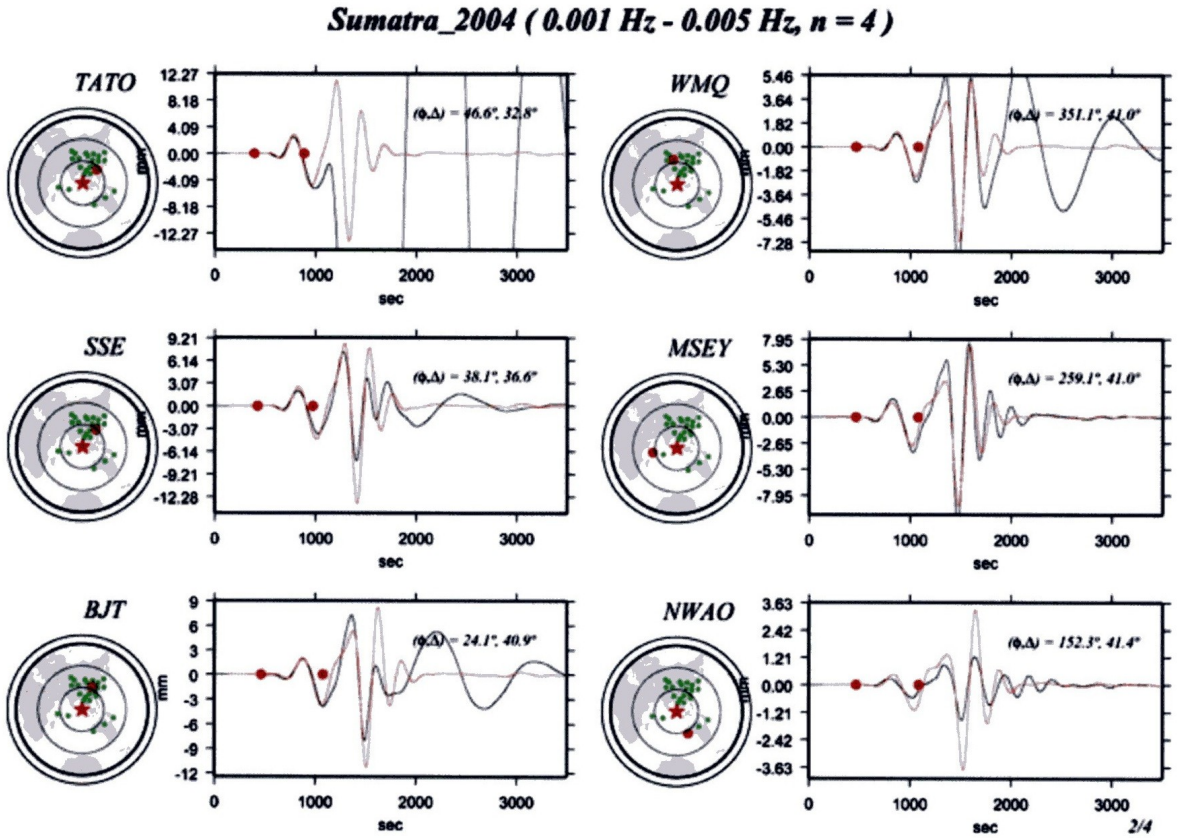

Fig. 3.66 Examples of fitting synthetic W waveforms (thick traces) to very long-period (200 to 1000 s) filtered observed waveforms at several seismic stations (thin traces). The two red dots on each trace indicate the time window over which the W-phase is inverted. From the overall best fitting solution the moment tensor parameters are estimated (Cut-out of Figure 11 of Kanamori and Rivera (2008); © Geophysical Journal International).

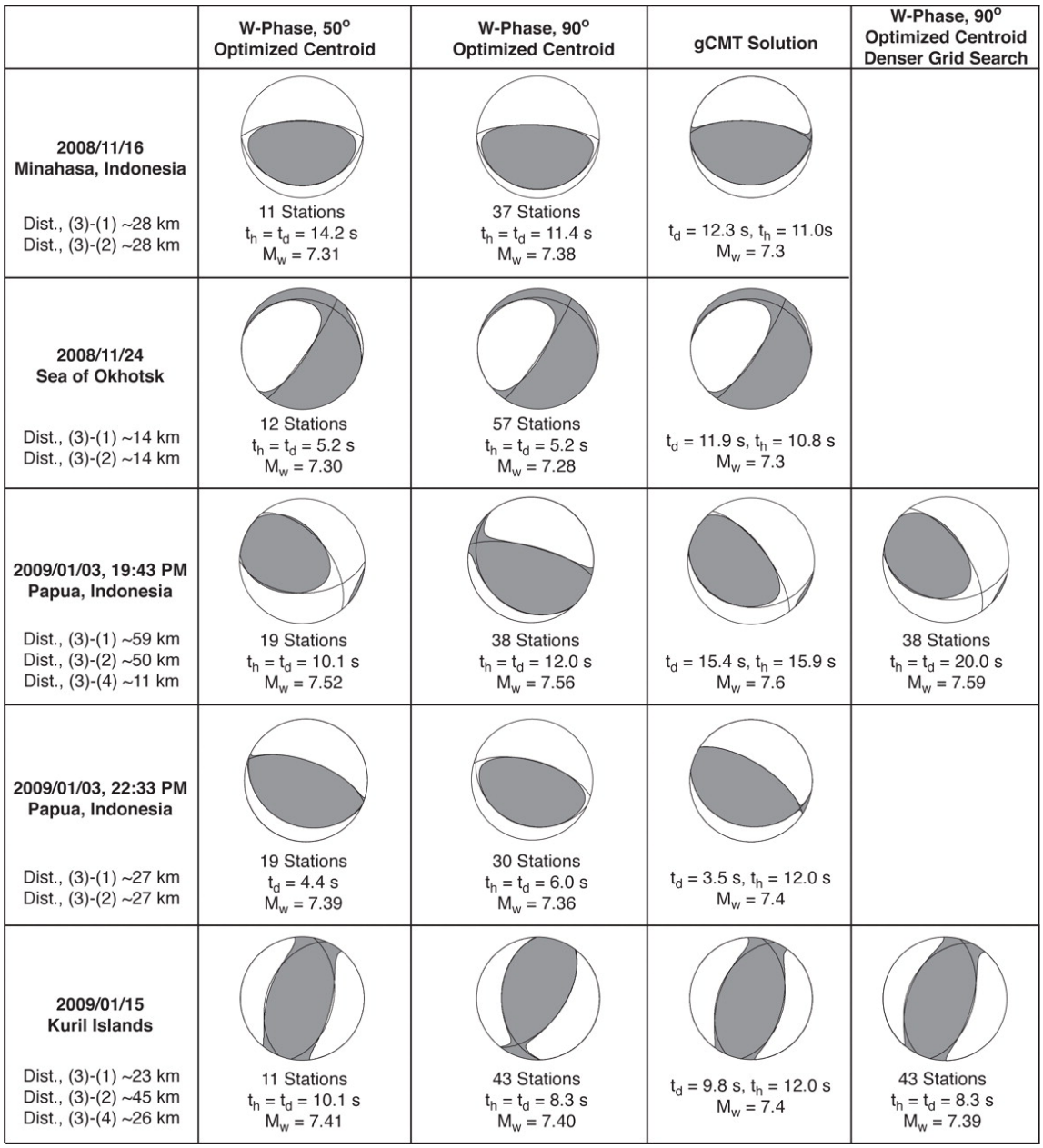

Fig. 3.67 Examples of operationally derived source parameters from W phase inversion in comparison to global Centroid Moment Tensor (gCMT) solutions. Solutions derived from station records at up to 50° epicental distance were on average available 24 min after OT and those from stations up to 90° epicenter distance within about 48 min. Optimized denser grid search takes more time with no significant difference. Copy of Figure 3 of Hayes et al. (2009), Seismological Research Letters, Vol. 80, No. 5, page 821; © Seismological Society of America.

3.2.9 Relationships among different magnitude scales
(P. Bormann, D. DiGiacomo and S. Wendt)

3.2.9.1 Remarks about regression and correlation relationships (P, Bormann)

Most of the published classical relationships between different types of magnitudes are simple linear standard regressions of type one (SR1), but often authors have not even specified in an unambiguous way the type of regression or data correlations they have applied. Yet, least-square fits may be done in very different ways. Sometimes even eye-fits, which are not the worst, because the intuitively accept that the data scatter relates to both compared variables. The approximate relationship (3.3) is such a best eye-fit through a largely scattering data cloud yielding a very simple and sufficiently reliable formula in the context of the great variability of individual data points. Also the famous Gutenberg-Richter log Es – m (respectively mB) relationship shown in Fig. 3.83 is obviously just an eye-fit but never stated explicitly as such. Moreover, some relationships, such as log E_S-Ms relationship by Choy and Boatwright (1995), are just a least-square fit to a prescribed slope, namely to the slope of 1.5 in the famous Richter (1958) logE_S-Ms relationship in the interest of assuring compatibility of the new relationships with already long-established and widely used and well established relationships, at least with respect to some essential parameters such as the slope or general trend. Yet proper linear regression through the same data set would yield both another slope and another constant (see section 3.3.3).

Standard regressions are least-square fits through the data cloud, which consider the scatter in plots of the (x_i, y_i) data pairs as being related solely to the dependent ordinate variable Y while assuming that the errors of the "independent" (or given) abscissa variable X are zero or negligibly small. In contrast, the inverse standard regression ISR (or standard regression SR2), is based on the opposite assumption that only X is afflicted with initial errors, but not Y. Accordingly, the slopes of SR1 and SR2 will differ, the more the larger the scatter of the data points and the smaller their correlation co-efficient.

Since generally all types of measured/calculated magnitude values are afflicted with initial errors, such standard regression relationships are not optimal. They can only be used in the way they have been derived, i.e., for converting a given magnitude, assumed to be error free, into another one by estimating its average value and related uncertainty such as its standard deviation. In fact, a standard regression projects the actual errors in the given variable into an increased error of the estimated dependent variable. Therefore, resolving an SR1 relationship Y over X for the variable X, as sometimes practiced when converting magnitudes, is not correct. Such a misuse of standard regressions easily results in conversion errors of 0.2 – 0.3 magnitude units (Gutdeutsch et al., 2011) but may become in the case of rather noisy, especially short-period magnitude data, as large as about 1 m.u. in some magnitude ranges (e.g. in Fig. 3.68 left), unless the initial errors of both variables are rather small and the correlation coefficient being close to 1 so that the difference in slope between SR1 and SR2 becomes negligible (see Fig. 3.68 right).

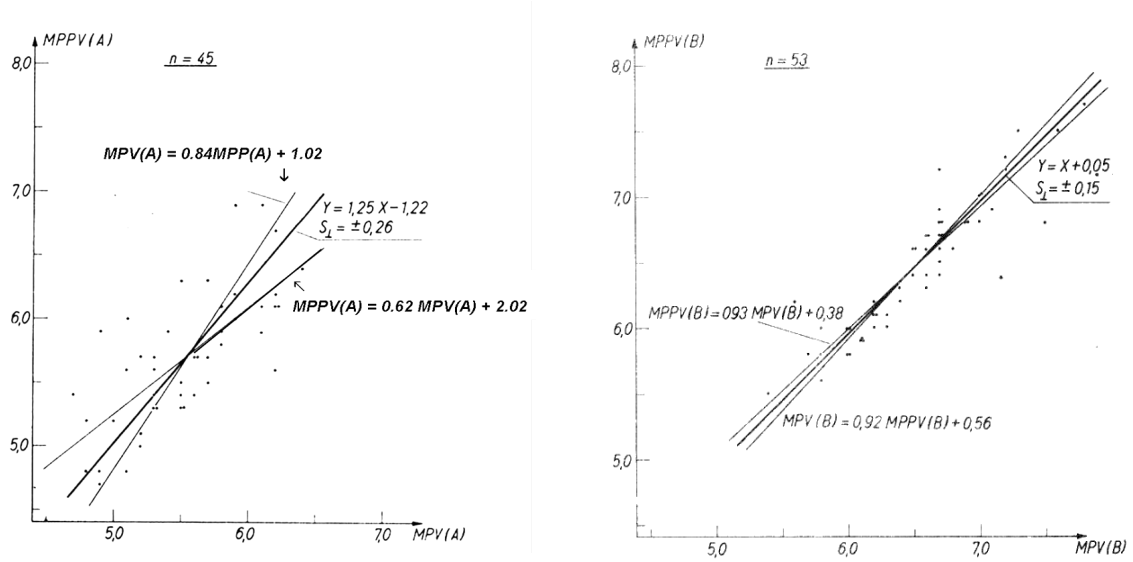

Fig. 3.68 Standard regressions SR1 of vertical component PP-wave magnitudes over vertical component P-wave magnitudes, measured on either short-period records of type A (left) or broadband records of type B (right), which correspond to type A4 and C, respectively, in Fig. 3.20 left). SR1 is compared with the respective inverse standard regression SR2 of MPV over MPPV and the common orthogonal regression OR, written in the form Y over X (see thick solid line between SR1 and SR2). Note the different slopes of SR1 and SR2, depending on the data scatter, which is much less for the broadband versions of MPV and MPPV. $S_{\perp}$ = orthogonal standard deviation. Copied from Figures 3 and 4 in Bormann and Khalturin (1975)

The simplest way to mitigate this problem is to calculate orthogonal standard regressions, OSR, assuming that both variables are afflicted with initial errors of the same size (ideally with an error ratio 1). This has been practiced, e.g., by Bormann and Khalturin (1975), Bormann and Wylegalla (1975), Ambrasseys (1990), Gusev (1991), Gutdeutsch et. al. (2001), Grünthal and Wahlström (2003), Bormann et al. (2007 and 2009), Ristau (2009) and Das et al. (2011). In the two papers by Bormann et al., the OSR solutions are presented together with SR1 and SR2 in order to see the differences and their dependence on the correlation coefficient (e.g., Figs. 3.49 and 3.50). In another publication, Castellaro and Bormann (2009) could show, that as long as the true error ratio, or the square root of the true variance ratio η_{true}, of the two variables ranges between $0.7 < \sqrt{\eta_{tru}} < 1.8$ this type of orthogonal regression under the assumption of $\eta = 1$ is superior to SR1 or SR2, but outside of this error ratio range, either SR1 or ISR = SR2 represent the data relationship better, depending also on their slope and how much it deviates from 1.

In reality, however, $\sqrt{\eta}$ may become as small as about 0.3, e.g. when comparing short-period mb with typical initial errors in the range between 0.2 and 0.3 (see also Table 5 in IS 3.3), with Mw(GCMT), for which initial errors are assumed to be not larger, often even less than 0.1 m.u. (personal communication by G. Ekström, 2009). Regrettably, in most classical papers the initial measurement errors of used event magnitudes are not given, probably not even known, also because the data reports, catalogs or bulletins of the de facto seismological World Data Centers such as the USGS-NEIC, the Global Centroid Moment Tensor (GCMT) project, or the International Seismological Centre (ISC) did not provide consistently such information. This problem is expected to disappear at the ISC thanks to the implementation of the new ISC locator (Bondár and Storchak, 2011) which computes Ms and mb with

uncertainties. Therefore, usually one could only estimate the approximate error ratio by own investigations. These may, however, yield different average measurement errors (standard deviations) even for equal types of magnitudes, depending on differences in instrument calibration, record reading accuracy, aperture and station site distribution of the network, regional variability of station site effects due to variable topographic and geologic conditions, etc. Table 5 in IS 3.3 compares such estimates for single expert readings of event magnitudes from records of the German Regional Seismic Network with those of an analyst team at the China Earthquake Network Center (CENC) based on records of the much larger China National Seismic Network.

If $\sqrt{\eta}$ differs from 1 and one knows sufficiently well this ratio, then a general orthogonal regression (GOR) (for procedures see Castellaro et al., 2006, Wason et al., 2012; Lolli and Gasparini, 2012, Das et al., 2013) would be closer to optimal than OSR. Yet, there has been another earlier approach in this direction by Stromeyer et al. (2004), applying a Chi-square regression for seismic strengths parameter relations. The *Chi-square* method is based on the theory of independent and normally distributed errors and provides a mathematical explanation for the results derived by Castellaro and Bormann (2009). Gutdeutsch et al. (2011) could show, that the results of these two different approaches agree well as long as the mean initial errors are < 0.5 m.u. Also Lolli and Gasparini (2012) investigated in detail the performance of GOR, the chi-square regression and the weighted total least squares. Although the formulations of these three approaches appear quite different, the authors showed that, under appropriate conditions, all compute almost exactly the same regression coefficients and very similar formal uncertainties. Thus, the availability of more general and theoretically correct tools for performing regression analysis and deriving conversion relationships between different types of magnitudes demonstrates the importance of knowing and taking into account their true average initial errors. Regrettably, these were commonly unknown so far. Therefore it would be highly desirable to complement current data parameter calculations and documentation at the most relevant seismological data centers accordingly. And in all publications about regression and conversion relationships the specifics of the applied procedure and its compatibility or incompatibility with other approaches should be unambiguously outlined and documented. One should also be aware, that GOR procedures developed or applied by different authors may differ significantly. E.g., a new methodology proposed by Wason et al. (2012) and applied by Das et al. (2013) for converting mb into Mw values for regional data from Japan, Mexico, the Indian Himalaya region and the Peninsula Indian region claims to reduce significantly both the average absolute difference as well as the standard deviation between the Mw proxy estimates and observed Mw(GCMT). Moreover, it is said to be less dependent on the usually not well known initial error ratio η.

Yet the issue is even more complicated because of the "saturation" tendency of several magnitude scales (see Fig. 3.47). Saturation is the larger the more narrowband the records are on which the amplitudes and related periods are measured and the more the measurement periods differ from the rupture duration. Therefore, all linear regression relations have only a limited value when comparing much less or not saturating magnitudes with strongly saturating ones, e.g., mb with Ms or Mw. Then only stepwise linear fits in limited magnitude ranges may yield still reasonable conversion relationships with not to large conversion errors (e.g., Fig. 3.69), or non-linear regression relationships as in Figs. 3.81-82 and 3.91-92.

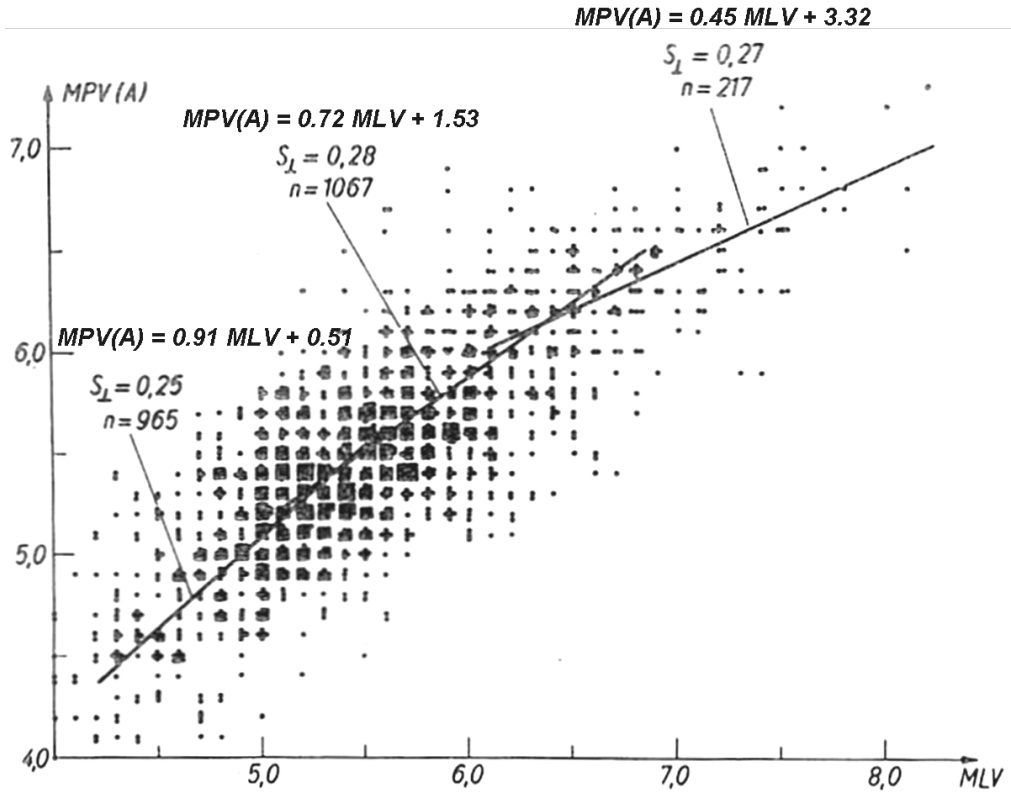

Fig. 3.69 Step-wise OR regression between vertical-component short-period mb (in a wide measurement time-window up to 1 min) and MLV(C) (of Ms_BB type) based on magnitude determinations at station MOX, Germany, for global earthquakes. Amended Fig. 5 of Bormann and Khalturin (1975).

When extrapolating the uppermost right OR relationship in Fig. 3.69 for 6.0 < MLV ≤ 8.3 up to the MLV = Ms_BB = 8.9 measured for the great Sumatra-Andaman Mw9.3 earthquake, one would "predict" an mb = MPV = 7.3, which agrees within 0.1 m.u. with the actual observation.

Non-linear "maximum-likelihood" regressions have been systematically applied for the first time by Gusev (1991) by investigating the relationships between Mw and the magnitudes mb (with A_{max} measured within first few seconds only), mSKM (with A_{max} measured in the whole P-wave group), mB, m_b^* (according to Koyama and Zeng, 1985), $\widehat{m}_b$ (according to Houston and Kanamori, 1986), Ml, Ms, and M(JMA) in both graphic and tabular form. Some of these relations are presented in Figure 9 of IS 3.7 in this Manual with respect to Mw and the Russian K = log Es class system of earthquake classification.

Another form of non-linear average eye-fit relationships of classical magnitudes with respect to Mw as a reference have also been derived by Utsu (2002) (see Fig. 3.70) and the specifics of the types of magnitudes and data, on which these relationships are based have been discussed in this paper extensively.

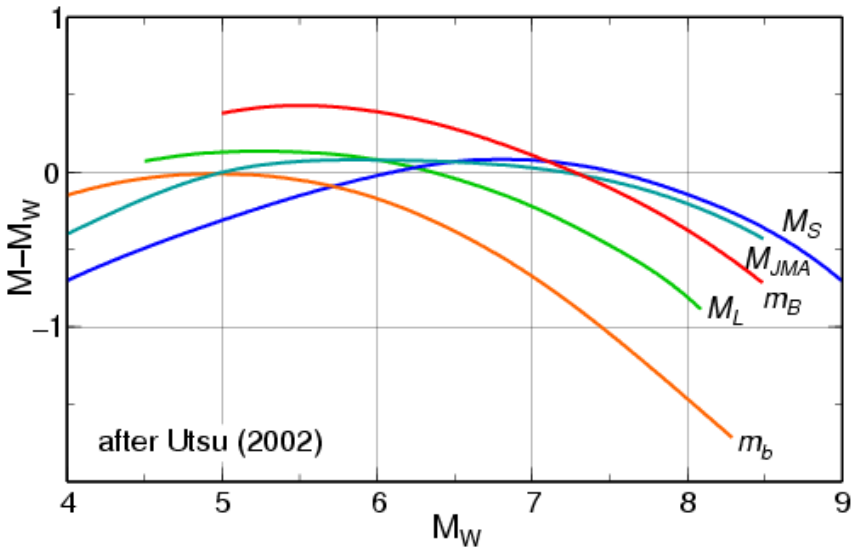

Fig. 3.70 Average relationships between different common types of magnitudes and the moment magnitude Mw. (Modified from Figure 1 in Utsu (2002): Relationship between magnitude scales. In: Lee W. H. K, Kanamori, H., Jennings, P. C., Kisslinger, C. (Eds) Earthquake and Engineering Seismology, Vol. A, 733-746; © Academic Press, London).

In conjunction with the elaboration of the ISC-GEM Global Instrumental Earthquake Catalogue (1900-2009) (see www.isc.ac.uk/iscgem/citing.php) new empirical relationships were derived by using both Generalized Orthogonal Linear and exponential non-linear models to obtain Mw proxies from Ms and mb. The new models were tested against true values of Mw, and the newly derived exponential models were found to be preferable to the linear ones (see section 3.2.9.5 for the data and comparison with GOR regression). Instead of the bi- or tri-linear regression (as in Fig. 3.69), the two data sets were optimally fit with single, continuous regression curves using an exponential model of the form $My = e^{(a+b\times Mx)} + c$. The regression was performed using the non-linear least square algorithm by Bates and Watts (1988) and Bates and Chambers (1992), which is freely available with the R-language.

3.2.9.2 Summary of classical magnitude relationships (P. Bormann)

Gutenberg and Richter (1956a, b) provided correlation relations between various magnitude scales:

$$m = mB = 2.5 + 0.63\ Ms \qquad (3.76a)$$

$$m = mB = 1.7 + 0.8\ Ml - 0.01\ Ml^2 \quad \text{and} \qquad (3.76b)$$

$$Ms = 1.27\ (Ml - 1) - 0.016\ Ml^2, \qquad (3.76c)$$

where m is the unified magnitude as the weighted mean of the body-wave magnitudes mB determined from medium-period broadband recordings. Practically the same relation as (3.70) based on some more data in a wider range of magnitudes between $5.5 \le mB \le 8.2$ was derived later by Abe and Kanamori (1980):

$$mB = 2.5 + 0.65\ Ms. \qquad (3.77)$$

It has only a slightly larger slope than (3.76a) and satisfies the mB and Ms data well between magnitude 5.2 and 8.7.

All these above regression relations are of the SR1 type. Sometimes they were wrongly applied, e.g. in a paper reviewed by the editor, were the author solved Eq. (3.70) for Ms, then converting short-period mb values as published by international data centers into Ms and finally calculated with these proxy Ms values the released seismic energy E_S via the Richter (1958) E_S-Ms relationships (3.66). Yet, Eq. (3.76a) is suitable only for converting Ms into mB and then applying the only energy-magnitude relationship logEs-mB which Gutenberg favored [see Eq. (3.95) in section 3.3.2], because he was aware that mB determined via $(A/T)_{max}$ in a wide range of periods is a much better estimator of released seismic energy than the long-period spectral magnitude Ms measured at periods around 20 s only.

When using **medium-to-long-period readings of P and surface waves in displacement broadband records of type C** (**Kirnos SKD**; see Fig. 3.20) and **SR1 regression**, practically identical relationships to Eq. (3.70) were found both by Bune et al. (1970) on the basis of records of the former **USSR-wide station network** and by Bormann and Wylegalla (1975) for the **single station MOX** in Germany (magnitude range 4.7 to 8.5). The latter is

$$MPV(C) = 2.5 + 0.60\ MLH(C). \qquad (3.78)$$

Relationship (3.76a) could also be reproduced more than 60 years later with practically identical SR1 relationships based on many more modern IASPEI standard mB_BB and Ms_BB measurements on velocity broadband readings of globally distributed earthquakes that were recorded by stations of both the China National Seismographic Network (CNSN) and the German Regional Seismic Network (GRSN) (see Bormann et al., 2009 and section 3.2.9.3).

Yet, the related **orthogonal regression** to Eq. (3.78), calculated for the same data set, is rather different:

$$MPV(C) = 1.83 + 0.70\ MLH(C) \qquad (3.75)$$

and the respective best fitting SR2 regression is

$$MLH\ (C) = -\ 1.54 + 1.25\ MPV(C). \qquad (3.79)$$

The latter is clearly different from

$$MLH\ (C) = -\ 4.17 + 1.67\ MPV(C)$$

when resolving incorrectly Eq. (3.78) for MLH. This would result in an overestimation of MLH by about 1.2 magnitude units for mB = 8 and an underestimation of 0.8 units for mB = 5.

The single random-parameter regression relationship between short-period mb and Ms based on **global WWSSN station-earthquake data** analyzed at NOAA (with amplitude measurement for mb within the first few cycles only after the P-wave onset) is very different from Eq. (3.76a), namely, according to Gordon (1971),

$$mb = (0.47 \pm 0.02)\, Ms + (2.79 \pm 0.09).$$

This agrees, with a constant offset of -0.16 m.u. (station correction?), with the **single-station** average formula derived by Karnik (1972) for the Czech station Pruhonice (PRU):

$$mb(sp, PRU) = 0.47\, MLH + 2.95.$$

On the other hand, when approximating vertical component short-period P-wave MPV(A) values plotted over the related MLV(C) values, both measured for globally distributed earthquakes at the **single station** MOX, Germany, in the wide magnitude range $4.0 \leq MLV(C) \leq 8.3$ by shorter overlapping tri-linear orthogonal regression relationships (see Fig. 3.69), Bormann and Khalturin (1975) derived

$$MPV(A) = 0.91\, MLV(C) + 0.51 \quad \text{between } 4.0 \leq MLV(C) \leq 5.5 \tag{3.80a}$$

$$MPV(A) = 0.72\, MLV(C) + 1.53, \quad \text{between } 5.1 < MLV(C) \leq 6.8 \tag{3.80b}$$

and

$$MPV(A) = 0.45\, MLV(C) + 3.32 \quad \text{between } 6.1 < MLV(C) \leq 8.3. \tag{3.80c}$$

The difference between short-period mb and long-period Ms strongly depends on the specifics of the seismic source process, e.g., on differences source size, source-time function, source depth, stress drop and thus radiated seismic spectra, especially the relative ratio of long-period to short-period spectral amplitudes. Therefore, plotting (20 s) Ms over (1 s) mb has become the most powerful discriminator between natural earthquakes and underground nuclear explosions (see, e.g., Chapter 11, section 11.2.5.2???, Fig. 11.22???; Figure 5 in Richards, 2002; Figure 2 in Richards and Wu, 2011). A relationship

$$Ms = 1.25\, mb - 2.45 \tag{3.81}$$

separates almost all shallow earthquakes globally from underground nuclear explosions (Richard, 2002). Interestingly, its slope is practically identical with the average slope of 1.23 in the Ms range between 4.0 and 6.8 when resolving the orthogonal relationships (3.80a and b) for MLV = Ms. However, the negative constant in (3.81) is 1.34 m.u. larger in order to account for the large data scatter around the average Ms-mb relationship for earthquakes.

Being aware of the even more general potential of Ms-mb, Prozorov and Hudson (1974) proposed a *creepex parameter*

$$c = Ms - a \times mb - b \tag{3.82}$$

with a and b being constants to be determined empirically for different source types, stress-drop conditions and seismotectonic regions. *Creep* stands for very slow rupture motions (see *slow* and *silent earthquakes* in the Glossary) and *ex* for explosions or other small seismic sources with extremely short source-time functions. Thus, *creepex* aims at discriminating between normal, very slow and explosion-like (fast rupture high-stress-drop) earthquakes. World-wide determination of this parameter for earthquakes in different regions revealed interesting relations of c to source-geometry and seismotectonic conditions. Global maps of *creepex* have been published by Prozorov et al. (1983) and Kaverina et al. (1996). Prozorov and Sabina (1984) could show that the regional earthquake catalog for Mexico contains earthquakes with rather different creepex values, that are related to three major types of

tectonic structurcs. E.g., *Creepex* is positive in zones of spreading and high heat flow, and negative in areas were relatively cold lithospheric plates are subducted into the mantle. Similar systematic regional differences were also reported for Ms – Mw (Ekström and Dziewonski, 1988; Patton, 1998) and Me – Mw (Choy and Boatwright, 1995; Choy and Kirby, 2004; Di Giacomo et al., 2010a; Bormann and Di Giacomo, 2011). Panza et al. (1993) extended the *creepex* concept to Md-ML and applied it to Italy.

Surface-wave magnitudes determined from vertical and horizontal component recordings using the so-called Prague-Moscow calibration function Eq. (3.35) correlated almost 1:1. According to Bormann and Wylegalla (1975), the orthogonal relationship is

$$MLV - 0.97\ MLH = 0.19 \tag{3.83}$$

with a standard deviation of only 0.11 and a correlation coefficient of r = 0.98. This clearly justifies the use of this calibration function, which was originally derived from horizontal amplitude readings, for vertical component (Rayleigh wave) magnitude determinations, too.

When using medium-period broadband data only, the orthogonal regression relation between magnitude determinations from PV and PPV or SH waves, respectively, are almost ideal. Gutenberg and Richter (1956a) had published Q-functions for all three phases (see Figures 1a-c and Table 6 in DS 3.1). Bormann and Wylegalla (1975) found for a global earthquake data set recorded at station MOX the orthogonal fits:

$$MPPV(C) – MPV(C) = 0.05 \tag{3.84}$$

with a standard deviation of only ± 0.15 magnitude units (see also Fig. 3.68 right) and

$$MSH(C) - 1.1\ MPV(C) = - 0.64, \tag{3.85}$$

with a standard deviation of ± 0.19 and magnitude values for P and S waves, which differ in the whole range of MPV(= mB) between 4 and 8 less than 0.25 units from each other. This confirms the good mutual scaling of these original body-wave calibration functions with each other, provided that they are correctly applied to medium-period data only. Regrettably, international data centers do no longer encourage data producers to report also amplitudes from PPV and SH waves for the determination of mB, which was Gutenberg´s original intention.

Kanamori (1983) summarized in graphical form the relationship between the various magnitude scales (see Fig. 3.47 in section 3.2.5.2 above). It also gives the ranges of uncertainty for the various magnitude scales due to observational errors and intrinsic variations in source properties related to differences in stress drop, complexity, fault geometry and size, source depth etc. The range of periods for which these magnitudes are usually determined are for mb: ≈1 s; for Ml: ≈ 0.1 - 3 s; for mB: ≈ 0.5 - 25 s; for Ms: ≈ 20 s and for Mw: ≈ 10 $\rightarrow \infty$ s. Accordingly, these different magnitude scales saturate differently: the shorter the measured periods the earlier "saturation", respectively underestimation of magnitude, occurs, i.e., according to the Kanamori graph for mb on average around 6.5, for Ml around 7, for mB around 8 and for Ms around 8.5 while Mw does not saturate. This is in good agreement with the general conclusions drawn on the basis of seismic source spectra (see Fig. 3.5). For mb, however, "saturation" will happen clearly later, when the maximum amplitudes are measured really within the whole P-wave train, as recommended by the new

IASPEI standards, and not within an a-priori fixed limited measurement time-window after the first arrival of P.

Ambrasseys (1990a and b), in an effort to arrive at uniform magnitudes for European earthquakes, re-evaluated magnitudes in the range $3 < M < 8$ and published in 1990b, with more data than in 1990a, the following updated *orthogonal regression relationships* between the various common magnitude scales:

$$0.76\ mb - 0.66\ mB = 0.31 \tag{3.86}$$

$$0.75\ mb - 0.66\ Ml = 0.51 \tag{3.87}$$

$$0.87\ mb - 0.50\ Ms = 1.91 \tag{3.88}$$

$$0.82\ Ml - 0.58\ Ms = 1.20 \tag{3.89}$$

with mb being determined according to the ISC procedure from short-period P-wave recordings and mB using medium-period P-wave records. These relations can be solved for either one of the two variables. Other relationships have been published by Nuttli (1985) which allow estimating Ms for plate-margin earthquakes when mb is known. For $mb > 5$ their results differ less than 0.2 magnitude units from those of Eq. (3.88) when solved for Ms.

The most recent GOR conversion relationships between more than 70.000 global ISC mb and Ms data during the period 1976-2007 have been published by Wason et al. (2012). This relationship reads, when rounded to the nearest second decimal:

$$Ms = 1.87\ mb - 4.44 \tag{3.90}$$

with a correlation coefficient RXY = 0.84 and a root mean square RMSO = 0.24. This relationship is rather close to the OSR relationship derived by Bormann et al. (2009) (next section) but differs more from Ambraseys (1990b) OSR relationship (3.88) for Europe and adjacent areas, when resolved for Ms:

$$Ms = 1.74\ mb - 3.02. \tag{3.91}$$

In the latter relationship Ms is of the Ms_BB type, measured also at regional distances down to 4° and at much shorter than 20 s periods which results in larger Ms values than the dominatingly 20 s Ms(ISC). At mb = 4 the difference is already 0.9 m.u.

Finally, we refer to a recent work by Ristau (2009), who gives both OSR. SR1 and SR2=ISR relationships between mb and Ml for all depth, shallow ($h < 30$ km) and deeper earthquakes in New Zealand. The average OSR relationship for all events reads:

$$mb = (0.94 \pm 0.07)\ Ml - (0.06 \pm 0.07) \tag{3.92}$$

with a distinct difference in slope (1.11 and 0.79, respectively) as well as scatter for shallow and deeper earthquakes.

3.2.9.3 Linear orthogonal and standard regressions between IASPEI standard magnitudes (P. Bormann, D. Di Giacomo and S. Wendt)

Bormann et al. (2009) derived the first OSR relationships between the four IASPEI standard magnitudes mb, mB_BB, Ms_20 and Ms_BB. They are based on data of some 400 to 500 globally distributed earthquakes that have been recorded by the China National Seismographic Network (CNSN) and analyzed at the China Earthquake Network Center (CENC) according to the standard procedures recommended by IASPEI (2005 and 2011) and in IS 3.3. Fig. 3.71 and Tab. 3.3 summarize the results. In the Table, besides the OSR relations, also the related SR1 and SR2 solutions are given with an ← instead of = sign in order to indicate that these relations can only be solved in this direction but not in the opposite one.

With reference to the Das et al. (2012) GOR relation (3.90) the standard Ms_20-mb OSR relation looks similar and reads:

$$Ms\_20 = 1.82\ mb - 4.75 \tag{3.93}$$

with RXY = 0.891 and an RMSO = 0.21. The somewhat steeper slope with a smaller constant in (3.90) is due to the fact that mb(ISC) saturates already around 7, standard mb, however, only around 7.5. Accordingly, an mb(ISC) = 7 relates with (3.90) already to an Ms = 8.6, a standard mb = 7, however, according to (3.91), only to an Ms = 7.8.

However, of much greater importance than the rather noisy and in fact rather non-linear (see section 3.2.9.5) relationship between short-period mb and Ms is the relationship between the new standard broadband mB_BB and Ms_BB with respect to the fundamental relationship between mB and Ms published by Gutenberg and Richter (1956a and b):

$$mB = 0.63\ Ms + 2.5. \tag{3.94}$$

This SR1 relationship is applicable for magnitudes between about 6 and <8.5. From it follows that mB = Ms at magnitude 6.75, yet mB is on average larger at smaller values of Ms and smaller at larger Ms. When substituting mB by (3.94) in the primary Gutenberg-Richter (1956 and b) relationship between body-wave magnitude and released seismic energy (with E_S in Joule):

$$\log E_S = 2.4\ mB - 1.2 \tag{3.95}$$

one arrives at the relationship (3.66) proposed by Richter (1958) (there with a typo) which has been instrumental in the derivation of both the moment magnitude and energy magnitude scales (see section 3.2.7 of this Chapter and Kanamori, 1977; Hanks and Kanamori, 1979; Choy and Boatwright, 1995; Bormann and Di Giacomo, 2011). Accordingly, the whole foundation of modern earthquake size, respectively strength classification essentially rests on it. Therefore, it is of great interest to know, whether the now proposed new IASPEI broadband magnitude standards mB_BB and Ms_BB, which differ slightly from the original Gutenberg mB and Ms, can reproduce this relationship nowadays with many more data in a wider magnitude range being now available than at Gutenberg´s time.

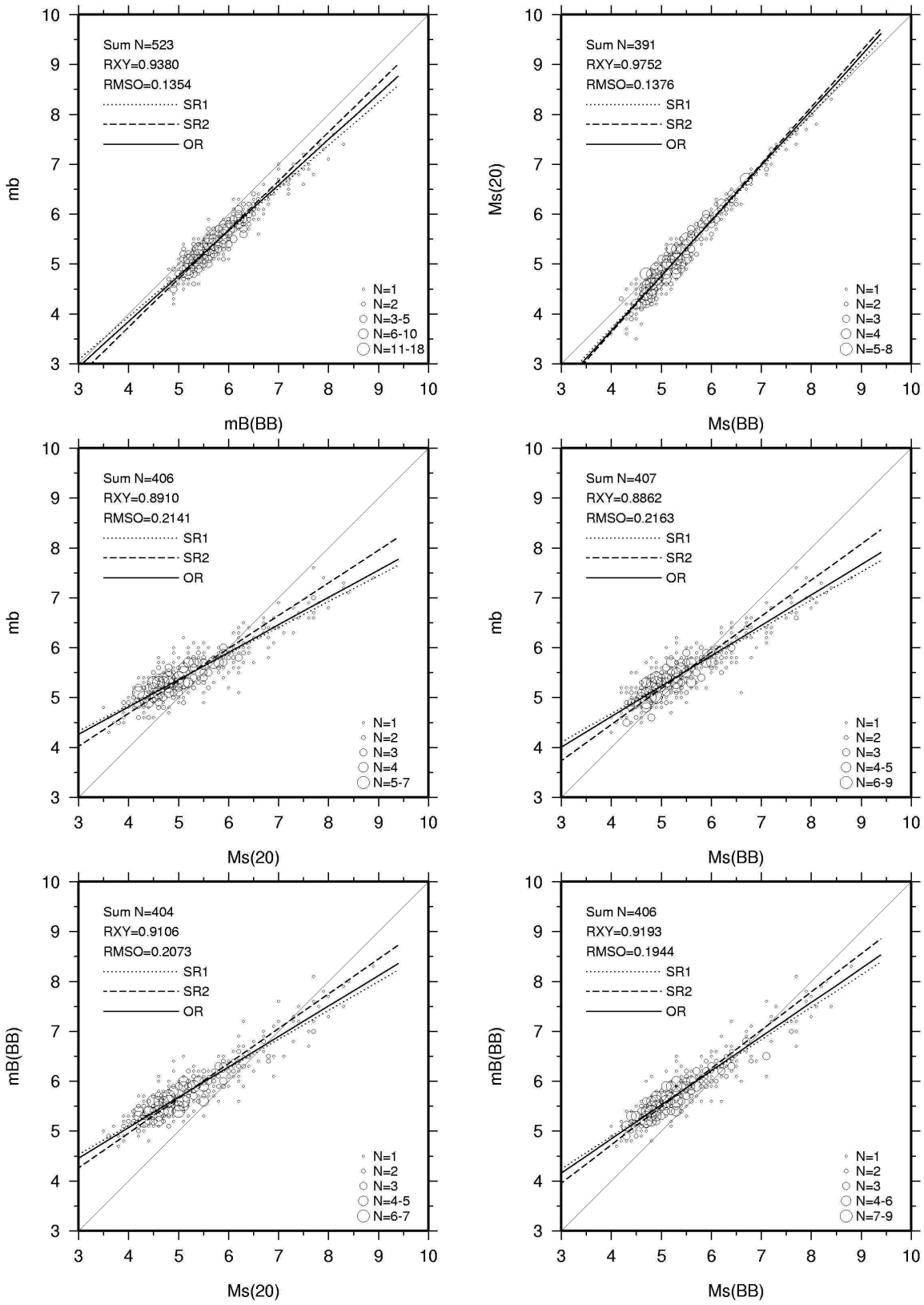

Fig. 3.71 Regression relations between new IASPEI standard magnitudes measured at CENC with respect to the ideal 1:1 line. N = number or (x,y) pairs, RXY = correlation coefficient, RMSO = orthogonal root-mean square error, OR = OSR, SR2 = ISR. For formulas see Tab. 3.3. Copy of Figure 11 by Bormann et al. (2009); © Seismological Society of America.

Tab. 3.3 Relationships between magnitudes determined from global earthquake CNSN data according to the IASPEI (2005) measurement standards. The unresolved OSR with RMSO are printed in bold letters, the rms for the resolved OSR are the uncertainty (standard error) of the estimated magnitude (modified and amended according to Bormann et al. (2009).

M_x-M_y N	Regression	Relationship	rms Error	Figure 3.71
mB_BB - mb 523	SR1 SR2 **OSR**	mb ← 0.86 mB_BB + 0.50 mB_BB ← 1.02mb + 0.18 **0.15 = -0.67 mB_BB + 0.74mb** mb = 0.91 mB_BB + 0.20 mB_BB = 1.10mb – 0.22	±0.18 ±0.20 **±0.14** ±0.19 ±0.21	upper left
Ms_BB - Ms_20 391	SR1 SR2 **OSR**	Ms_20 ← 1.07Ms_BB - 0.59 Ms_BB ← 0.89Ms_20 + 0.79 **0.50 = 0.74Ms_BB - 0.67Ms_20** Ms_20 = 1.10Ms_BB - 0.75 Ms_BB = 0.91Ms_20 + 1.47	±0.20 ±0.19 **±0.14** ±0.21 ±0.19	upper right
Ms_20 - mb 406	SR1 SR2 **OSR**	mb ← 0.52Ms_20 + 2.77 Ms_20 ← 1.53mb - 3.15 **2.29 = -0.48Ms_20 + 0.88mb** mb = 0.55Ms_20 + 2.61 Ms_20 = 1.82mb – 4.75	±0.24 ±0.41 **±0.21** ±0.24 ±0.44	middle left
Ms_BB - mb 407	SR1 SR2 **OSR**	mb ← 0.57Ms_BB + 2.40 Ms_BB ← 1.38 mb - 2.15 **1.86 = -0.52 Ms_BB + 0.85mb** mb = 0.61Ms_BB + 2.18 Ms_BB = 1.61mb – 3.57	±0.25 ±0.39 **±0.22** ±0.26 ±0.42	middle right
Ms_20 - mB_BB 404	SR1 SR2 **OSR**	mB_BB ← 0.58Ms_20 + 2.79 Ms_20 ← 1.43 mB_BB - 3.11 **2.25 = -0.52Ms_20 + 0.85mB_BB** mB_BB = 0.61Ms_20 + 2.63 Ms_20 = 1.61mB_BB – 4.31	±0.24 ±0.38 **±0.21** ±0.24 ±0.40	lower left
Ms_BB - mB_BB 406	**SR1** SR2 **OSR**	**mB_BB ← 0.65Ms_BB + 2.30** Ms_BB ← 1.31 mB_BB - 2.16 **1.74= -0.56Ms_BB + 0.83mB_BB** mB_BB = 0.68Ms_BB + 2.10 Ms_BB = 1.47mB_BB – 3.09	**±0.23** ±0.33 **±0.19** ±0.23 ±0.34	lower right

With reference to the GOR relation (3.90) by Das et al. (2012) the standard Ms_20-mb OSR relation looks similar and reads:

$$Ms\_20 = 1.82\ mb - 4.75 \qquad (3.93)$$

with RXY = 0.891 and an RMSO = 0.21.
However, of much greater importance than the rather noisy and in fact rather non-linear (see section 3.2.9.5) relationship between short-period mb and Ms is the relationship between the new standard broadband mB_BB and Ms_BB with respect to the fundamental relationship between mB and Ms published by Gutenberg and Richter (1956a and b):

$$mB = 0.63\ Ms + 2.5. \qquad (3.94)$$

This SR1 relationship is applicable for magnitudes between about 6 and <8.5. From it follows that mB = Ms at magnitude 6.75, yet mB is on average larger at smaller values of Ms and smaller at larger Ms. When substituting mB by (3.94) in the primary Gutenberg-Richter (1956 and b) relationship between body-wave magnitude and released seismic energy (with E_S in Joule):

$$\log E_S = 2.4\ mB - 1.2 \qquad (3.95)$$

one arrives at the relationship (3.66) proposed by Richter (1958) (there with a typo) which has been instrumental in the derivation of both the moment magnitude and energy magnitude scales (see section 3.2.7 of this Chapter and Kanamori, 1977; Hanks and Kanamori, 1979; Choy and Boatwright, 1995; Bormann and Di Giacomo, 2011). Accordingly, the whole foundation of modern earthquake size, respectively strength classification essentially rests on it. Therefore, it is of great interest to know, whether the now proposed new IASPEI broadband magnitude standards mB_BB and Ms_BB, which differ slightly from the original Gutenberg mB and Ms, can reproduce this relationship nowadays with many more data in a wider magnitude range being now available than at Gutenberg´s time.

The Chinese data presented in Fig. 3.71 (lower right) cover the magnitude range between 4 and 8.8 (with the great majority of magnitudes < 6), i.e., a much larger range than (3.94) or the slightly modified Abe and Kanamori (1980) formula based on strong earthquake records between 1953 and 1977:

$$mB = 0.65\ Ms + 2.5. \qquad (3.96)$$

None the less, the respective **standard regression SR1** between the two standard broadband magnitudes mB_BB and Ms_BB (**bold blue in Tab. 3.3**) is very similar to both of these formulas :

$$mB\_BB \leftarrow 0.65\ Ms\_BB + 2.30 \quad (\text{with } SD = \pm 0.23). \qquad (3.97)$$

Practically identical with (3.94), however, is a new mB_BB - Ms_BB SR1 relationship derived from a global set of 227 earthquakes in the range 4.7 < Ms_BB < 8.9 recorded by STS2 broadband seismographs of the GRSN network in Germany (see also Fig. 3.72 left):

$$mB\_BB \leftarrow 0.63\ Ms\_BB + 2.52 \quad (\text{with } SD = \pm 0.28). \qquad (3.98)$$

According to (3.97) and (3.98) mB_BB = Ms_BB for 6.5 and 6.8, respectively, i.e. close to the 6.75 according to (3.95). When converting values between Ms_BB = 6.0 and 8.5, i.e. magnitudes for which (3.95) holds, via the relationship (3.97) into mB_BB, then the

differences with respect to (3.95) vary between -0.08 and -0.03 m.u. And when using (3.98) instead, the difference to conversions based on the Gutenberg-Richter formula is constant + 0.02 m.u. for all magnitudes and thus practically negligible. And with relationship (3.74) Bormann and Wylegalla (1975) had already shown that **even single station BB body-wave and surface-wave magnitudes from global earthquakes** in the magnitude range 4.7 to 8.5 do essentially reproduce (3.95).

Also the SR1 between mB_BB and Ms_20, with slopes between 0.58 (Chinese data; Fig. 3.71 lower left and Tab. 3.3) and 0.62 (GRSN data; Fig. 3.72 right), still match rather well with Eq. (3.95). Conversion differences for Ms_20 between 6.0 and 8.5 range between - 0.04 and + 0.13 m.u., which is much smaller than the standard deviations for all these regressions that vary between ± 0.23 and ± 0.28 m.u.

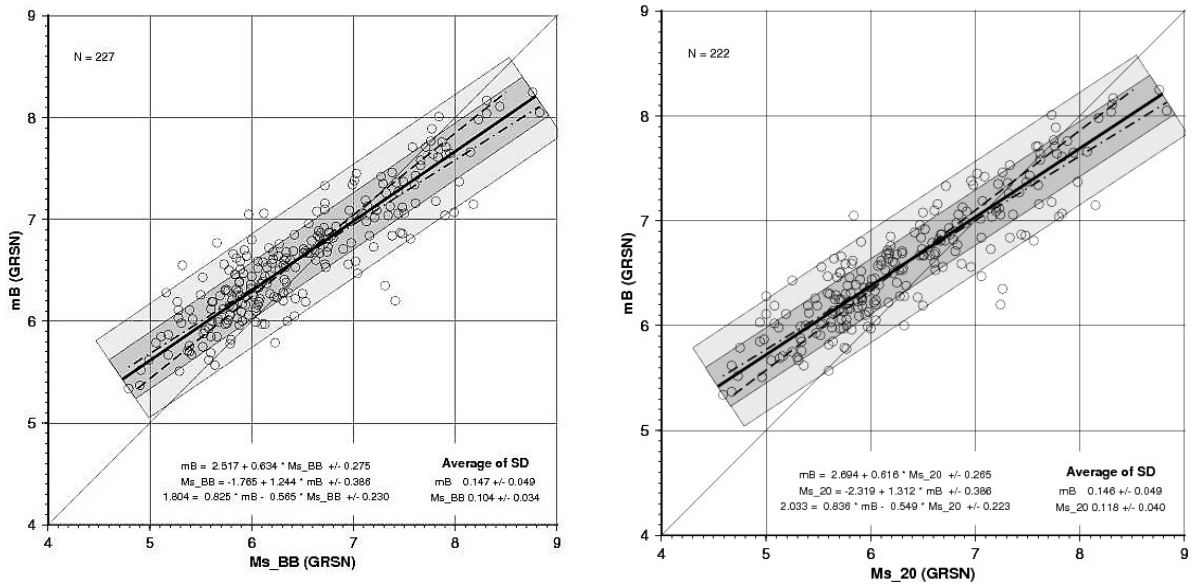

Fig. 3.72 Regression relationships between mB_BB and Ms_BB (left diagram), and Ms_20, respectively (right diagram) based on the analysis of global earthquakes recorded by the German Regional Seismic Network (GRSN):. SR1 (dot-broken line and upper inserted formula), SR2 (broken line and middle inserted formula) and OSR (bold black line and lower inserted formula). The gray and light-gray shaded bands indicate the 1- and 2-standard deviation limits around the OSR regression line. Given are also the average standard deviations with which the event magnitudes have been estimated.

The differences, however, to the Gutenberg-Richter (1956a) mB-Ms relationships is slightly larger when comparing a larger set (N = 931) of automatically determined global earthquake mB(GFZ) = mB_BB measured by the procedure described in Bormann and Saul (2008) and using stations globally distributed, with the respective Ms(USGS) data, which is in fact an Ms_20. According to Fig. 3.73 the SR1 relationship is

$$mB\_BB = 0.69\ Ms + 2.26 \qquad (\text{with } SD = \pm 0.28). \qquad (3.99)$$

In the magnitude range Ms = Ms_20 between 5.5 and 8.5 conversions of Ms into mB according to (3.99) yield values that are between 0.09 and 0.27 m.u. larger than those derived by using the G-R formula (3.94), however, agree perfectly with the later by Abe and Kanamori (1980) on the basis of more data revised relationship (3.96). The conversion

differences between (3.99) and (3.96) vary between –0.02 and +0.01 only. This is insignificant as compared to the measurement errors of these magnitudes.

Yet, the respective orthogonal regressions between mB and Ms differ clearly from these classical relationships. For the data in Fig. 3.73 the OSR is:

$$mB\_BB = 0.75\ Ms + 1.87 \quad \text{with RMSO} = \pm 0.17 \tag{3.100}$$

and an SD = ±0.21 m.u. of the mB_BB estimates.

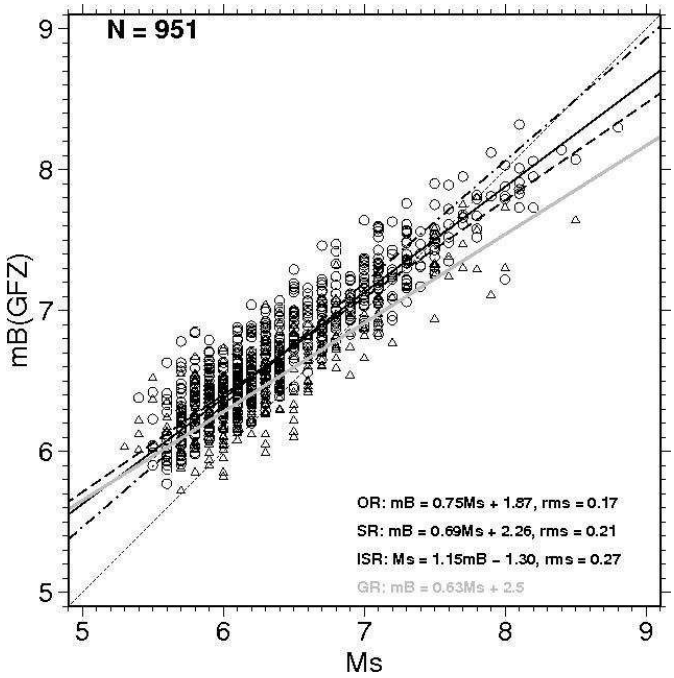

Fig. 3.73 mB(GFZ) = mB_BB over Ms(USGS) = Ms_20 for a global earthquake-station network data set compiled and processed by J. Saul and Di Giacomo (personal communication, 2010). Different point symbols relate to different types of source mechanism, e.g., the upright open triangles to strike-slip mechanism. The grey full line corresponds to the Gutenberg-Richter SR1 relationship (3.64).

In summary, we rest assured that the new standard magnitudes mB_BB and Ms_BB do not contradict with the inferences drawn by Richter (1958), and later by Kanamori and others on the basis of the Gutenberg-Richter SR1 relationship (3.94) leading to the derivation of the Mw standard formula. Modern Ms_20 and mB_BB data, however, do better agree with the Abe and Kanamori (1980) mB-Ms relationship.

3.2.9.4 Linear orthogonal and standard regressions between IASPEI standard magnitudes and classical mb and Ms with Mw and Me

(P. Bormann, D. DiGiacomo and S. Wendt)

Bormann and Saul (2008) and Bormann et al. (2009), supplemented by data provided by Di Giacomo (2010, personal communication), looked into the OSR and standard regression relationships between IASPEI standard magnitudes with Mw and Me for **global earthquakes**

recorded by world-wide distributed broadband stations. Fig. 3.73 plots Mw(GCMT) over mB(GFZ) which is an automatically determined mB_BB according to the procedure described by Bormann and Saul (2008), in the left panel for a limited early and in the right panel for a greatly extended data set compiled and processed by J. Saul and Di Giacomo (personal communication 2010).

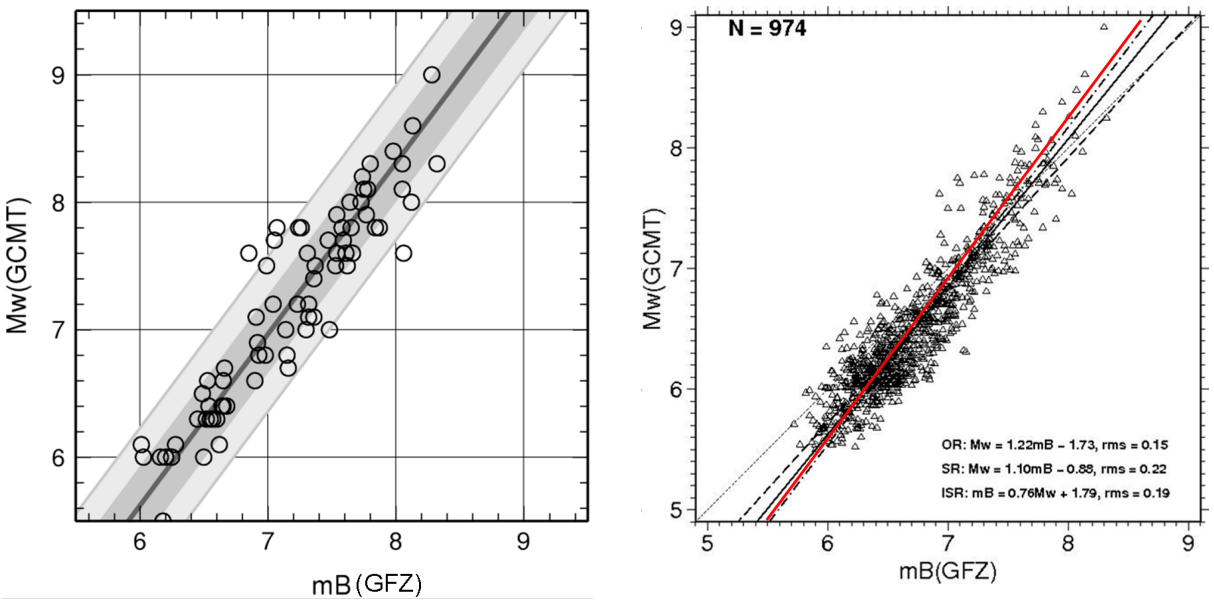

Fig. 3.74 Mw(GCMT) over mB(GFZ) for an initial limited data set (left-hand diagram) and a greatly expanded representative data set compiled and processed by J. Saul and Di Giacomo (personal communication 2010) (right hand diagram). The boundaries of the grey and light gray bands, respectively, in the left hand diagram correspond to one and two standard deviations. Larger positive outliers in Mw direction in both diagrams are relate to rare very slow tsunami earthquakes and large negative outliers to very fast ruptures. The read line in the right-hand diagram corresponds to the OSR relation in the left-hand panel according to Bormann and Saul (2008).

The OSR relationship in the left-hand panel of Fig. 3.73 is given by Bormann and Saul (2008) as

$$\mathrm{Mw(GCMT)} = 1.33\ \mathrm{mB(GFZ)} - 2.36, \qquad (3.101)$$

with RMSO = ±0.18 m.u. and an rms of ±0.30 m.u. in the estimated Mw. The related standard regression SR1, however, is

$$\mathrm{Mw(GCMT)} = 1.21\ \mathrm{mB(GFZ)} - 1.45 \text{ with rms} = \pm 0.29. \qquad (3.102)$$

and SR2

$$\mathrm{mB(GFZ)} = 0.71\ \mathrm{Mw(GCMT)} + 2.08 \quad \text{with rms} = \pm 0.22. \qquad (3.103)$$

We should note, however, that the conversion of available instrumentally measured Mw data into not available mB_BB values is not of practical importance at all. Relevant is only the need (or wish) to calculate proxy Mw estimates from measured mB_BB or other magnitudes if proper Mw values are not at all, or - because of longer required data acquisition and

processing times - not yet available, e.g., in the context of rapid early warning operations. And then, we have principally the choice to use either the SR1 or OSR regression relationship of Mw over mB_BB (or other magnitudes). When comparing long-period Mw data with other long-period or broadband magnitudes of comparably low initial measurement errors than in any event OSR relations are preferable because they represent more correctly the relationship between these two magnitudes, although the uncertainty in the estimated dependent variable is of the same order as for the SR1.

In Fig. 3.74 the regression relationships are remarkably good average representations for the vast majority of events despite the very different frequency ranges considered and methodologies applied to measure Mw and mB. According to the relationships (3.101) to (3.103) mB(GFZ) values are on average equal to Mw between 6.9 and 7.2, larger than Mw by 0.3 to 0.4 at Mw = 6.0, and smaller by the same amount at Mw = 8.5. But **automatically determined mB(GFZ)** from first arriving P waves is available much earlier than Mw(GCMT) derived from the analysis of very long-period P, S and surface waves. Therefore, by using relationship (3.101), which compensates best for the systematic trend difference between Mw and mB, the latter is used, e.g. in the operational German-Indonesian Tsunami Early Warning System (GITEWS; http://www.gitews.de), to get first rough proxy estimates of Mw within 5 min after origin time.

The respective formulas for the larger data set have been inserted in the right-hand diagram of Fig. 3.74. The OSR relationship reads:

$$Mw(GCMT) = 1.22\ mB(GFZ) - 1.73 \text{ with } RMSO = \pm 0.15. \quad (3.104)$$

The related uncertainty of Mw proxy estimates via mB(GFZ) is SD = ±0.24 m.u. and the average difference of Mw proxies calculated with either (3.101) or (3.104) is generally less than 0.2 m.u.

An almost identical OSR relationship has been derived by S. Wendt by comparing only 274 **manually derived mB_BB** values for global earthquakes recorded at stations of the German GRSN broadband network with Mw(GCMT):

$$Mw(GCMT) = 1.22\ mB(GRSN) - 1.68 \text{ with } RMSO = \pm 0.20. \quad (3.105)$$

Fig. 3.75 shows the related data plots together with the OSR, SR1 and ISR relationships and the one and two RMSO error intervals (gray and light gray bands).

Similar relationships have been derived by Di Giacomo (personal communication 2010) between mB(GFZ), Me(GFZ) and Me(USGS). The former Me data have been calculated with another fully automatic procedure described by Di Giacomo et al. (2008; 2010a and 2010b) while the USGS Me data are calculated by an off-line procedure described by Choy and Boatwright (1995) and in IS 3.6. In contrast to the GFZ procedure, which does not apply source-mechanism corrections to the measured values, in agreement with other classical magnitude procedures, the USGS procedure applies such corrections. Such theoretically based corrections, however, have the tendency to overestimate Me, especially for strike-slip events. Possible reasons have been discussed in section 3.2.7.2. Fig. 3.76 shows plots of Me(GFZ) and Me(USGS), respectively, over mB(GFZ) with the related OSR, SR1 and ISR = SR2 relationships, which are given as inserts together with their rms values.

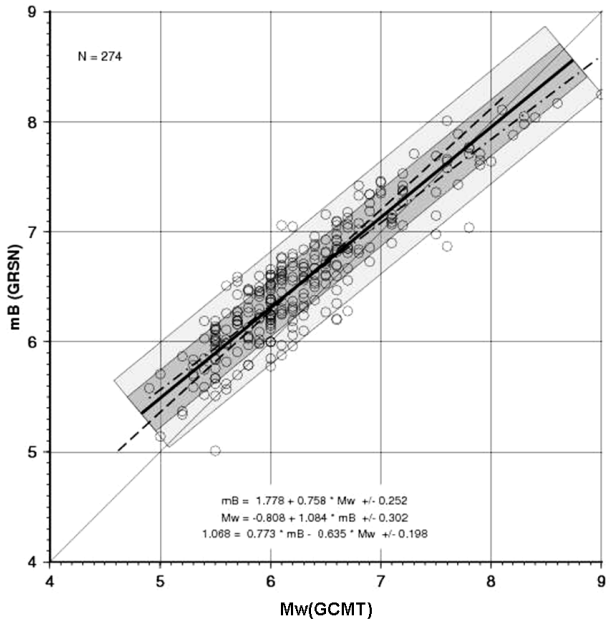

.

Fig. 3.75 Regression relationships SR1, SR2 = ISR and OSR (see inserted formulas from top to bottom) between mB_BB, calculated from broadband records at the German GRSN network, and Mw(GCMT). For legend see Fig. 3.72.

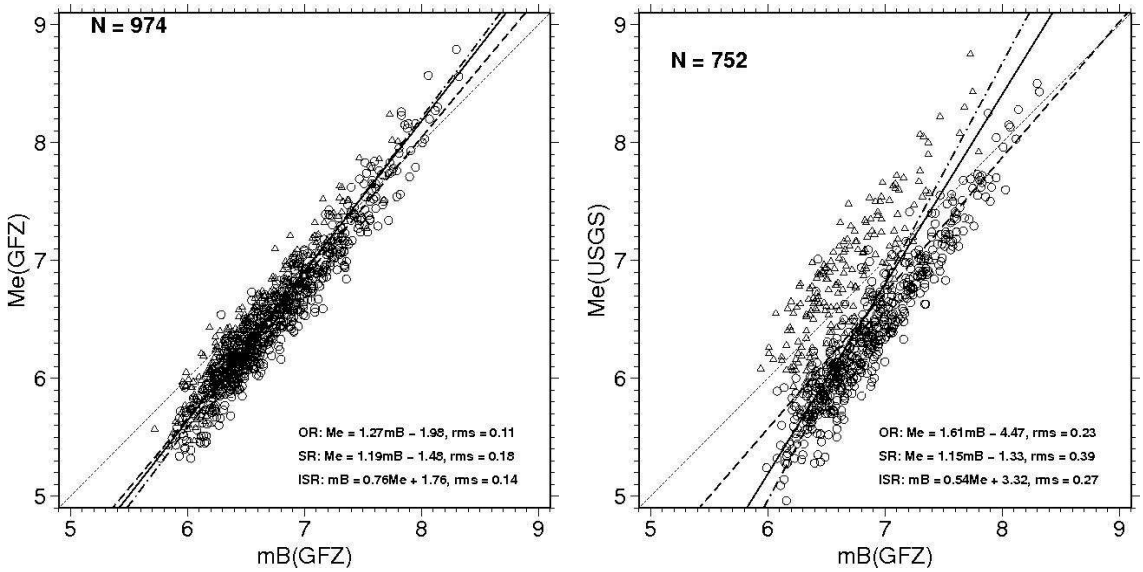

Fig. 3.76 Plots of Me(GFZ) (left-hand diagram) and Me(USGS) (right hand diagram) over mB(GFZ). Different point symbols relate to different types of source mechanism, e.g., the upright open triangles to strike-slip mechanism.

From Fig. 3.76 it is obvious that the data scatter doubles when accounting for theoretically expected yet purely model-based source-mechanism corrections, primarily for strike-slip (SS) earthquakes. Their share in the left-hand diagram are 323 and in the right-hand diagram 204. Note that in the left-hand diagram the difference between mB(GFZ)-Me(GFZ) for strike slip events is 0.13 ± 0.19 and for all types of source mechanisms 0.24 ± 0.19, i.e., an average difference of only 0.11 m.u. In contrast, for event magnitudes plotted in the right-hand diagram the difference between mB(GFZ)-Me(USGS) for strike slip events is -0.15 ± 0.34

and for all types of source mechanisms 0.50 ± 0.24, i.e., an average difference of 0.65 m.u. and a greatly increase data scatter.

Proxy estimates of Me(GFZ), however, could be made by using the OSR relationship with the automatically determined mB(GFZ):

$$Me(GFZ) = 1.27\ mB(GFZ) - 1.98 \quad \text{with RMSO} = \pm 0.11. \tag{3.106}$$

mB(GFZ) is available already within the first few minutes after origin time OT and the standard deviation of the Me estimate is only SD = ±0.18 m.u. This is much better than estimating Me(GFZ) or Me(USGS) via OSR conversion relationships with USGS Ms = Ms_20. Such proxy estimates would be uncertain, in terms of SD, by ±0.28 m.u. for Me(GFZ) and, even worse, ±0.39 m.u. for Me(USGS) (see Fig. 3.77), although Me(USGS) had been scaled to Ms(USGS) (see Choy and Boatwright, 1995; Choy et al., 2006). The very noisy relationship between Me and Ms illustrates, why Gutenberg favoured – intuitively - energy calculations via equation (3.95) based on ground motion velocity related $(A/T)_{max}$ measurements in a wide period range and not via the Richter $\log E_S$-Ms relationship (3.66) solely based on 20 s displacement amplitudes.

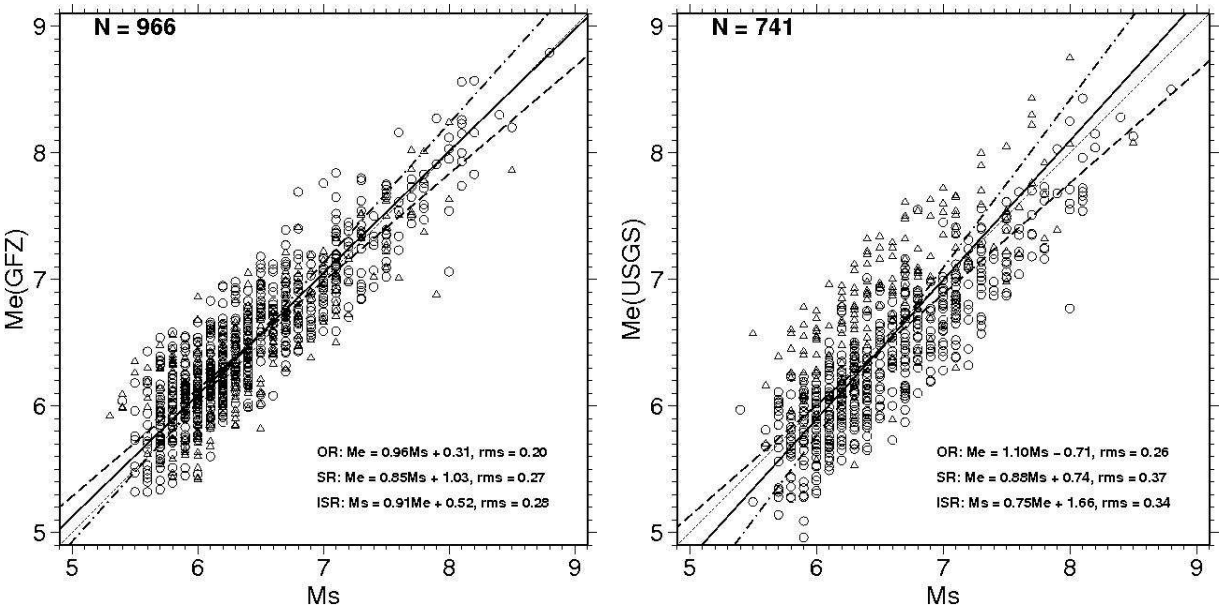

Fig. 3.77 Regression relationships for Me(GFZ) (left diagram) and Me(USGS) (right diagram) over USGS Ms, which is in fact an Ms_20. See inserted formulas for OSR, SR1 and ISR = SR2 with their related rms. Triangles represent strike slip earthquakes, circles all other types of mechanisms.

In view of the large difference between the two established Me procedures and results the question arises, how these two different approaches of Me measurement relate to Mw. Fig. 3.78 presents Mw(GCMT) over Me(GFZ) and Me(USGS), respectively. Again, Me(GFZ) correlates better than Me(USGS) with Mw(GCMT) at reduced scatter. While at Mw = 5.5 Me(GFZ) values are on average 0.16 m.u. smaller than MeUSGS), Me(GFZ) is on average 0.16 m.u. larger at Mw = 9. The OSR relationship Mw(GCMT) over Me(GFZ) is on average very close to 1:1, whereas the slope of the respective relationship with Me(USGS) is clearly

less than one. The scatter of Me with respect to Mw is mainly due to differences in the Mw-scaled release of radiated seismic energy, which is closely related to differences in seismic stress-drop and/or rupture velocity (see, e.g., Kanamori and Brodsky, 2004; Venkatamaran and Kanamori, 2004b; Bormann and Di Giacomo, 2011). It can not be excluded, however, that the much larger data scatter of Me(USGS) is at least partially due to a overcorrection for theoretically expected source-radiation effects (see section 3.2.7.2).

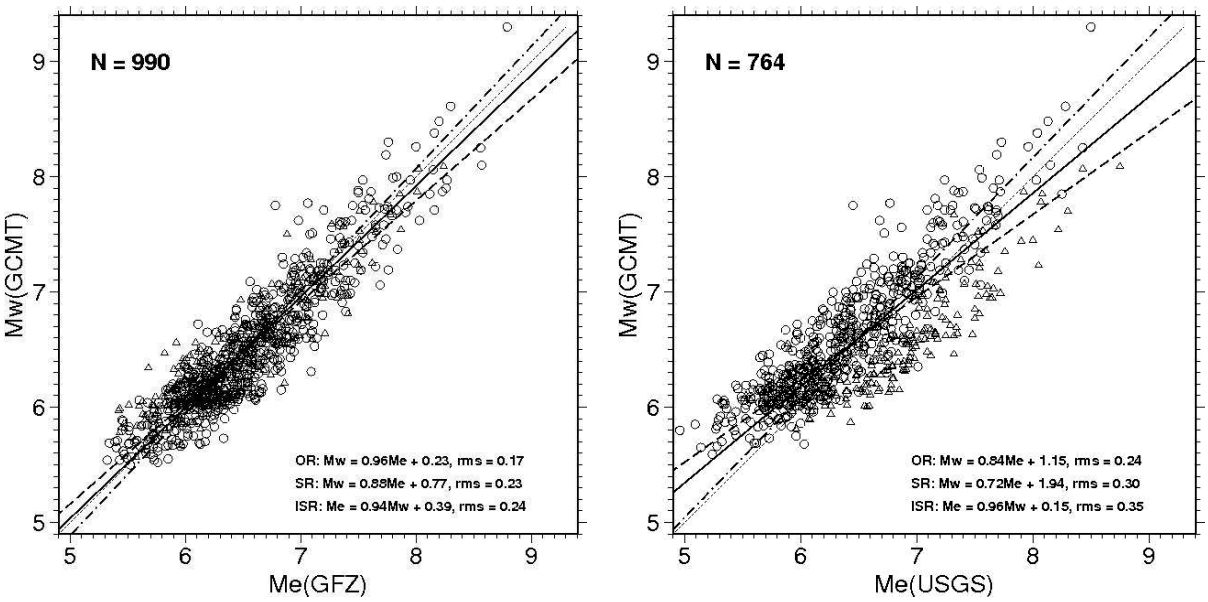

Fig. 3.78 Regression relationships of Mw(GCMT) over Me(GFZ) (left-hand diagram) and Me(USGS) (right-hand diagram), respectively. Triangles represent strike slip earthquakes, circles all other types of mechanisms.

Bormann at al. (2009) published regression relations between Mw(GCMT) and Me(USGS) with all 4 teleseismic IASPEI magnitude standards (see Figs. 3.79 and 3.80 and Tab. 3.4). One should recognize, however, that magnitude conversion relationship aimed at catalog homogenization are generally not used for converting Mw or Me to classical magnitudes but rather to use the latter, which are both more frequently and for much longer time-spans available than the more recent physically based magnitudes, into proxy estimates of Mw and Me. And since we give preference to the use of the OSR relationships we have highlighted in Tab. 3.4 those resolved for Mw and Me, respectively, in bold blue.

We realize that, with the exception of Ms_20 conversions for Ms < 6.8 and conversions of mB_BB into Mw with standard deviations SD ≈ ±0.2, proxy estimates of Mw from other classical magnitudes have generally an SD ≈ ±0.3 and for conversions of classical magnitudes into Me even values around SD ≈ ±0.4, with the exception of somewhat lower standard deviations when converting Ms data.

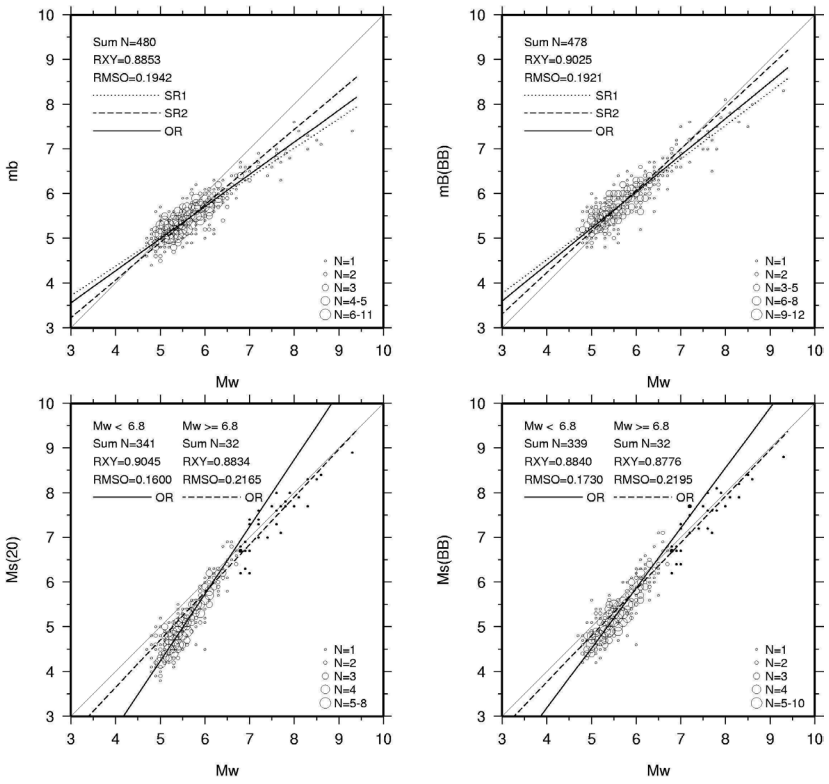

Fig. 3.79 SR1, SR2 and OR relationships between mb, mB_BB, Ms_20 and Ms_BB over Mw(GCMT). Legend as in Fig. 3.71. (Copy of Figure 13 in Bormann et al. (2009); © Seismological Society of America).

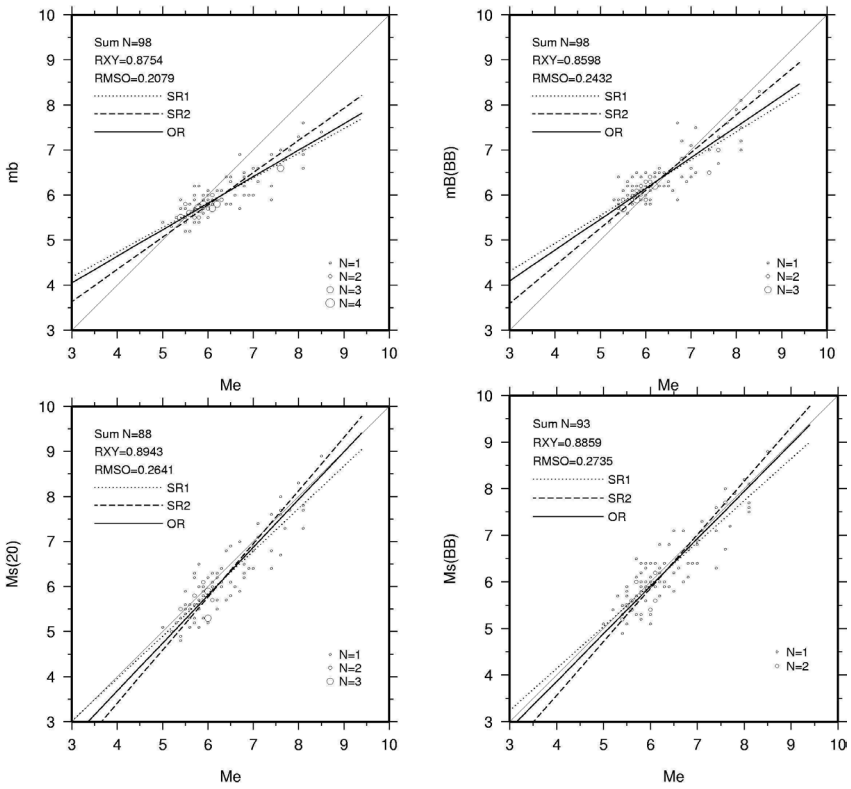

Fig. 3.80 SR1, SR2 and OR relationships between mb, mB_BB, Ms_20 and Ms_BB over Me(USGS). Legend as in Fig. 3.71. (Copy of Figure 14 in Bormann et al. (2009); © Seismological Society of America).

Tab. 3.4 Relationships of magnitudes determined from CNSN data according to the new IASPEI measurement standards with Mw(GCMT) and Me(USGS), respectively. Legend as in Tab. 3.3. (modified Table 3 in Bormann et al. (2009).

M_x-M_y N	Regression	Relationship	rms Error	Figure
Mw – mb 480	SR1 SR2 **OR**	mb ← 0.66Mw + 1.73 Mw ← 1.19mb - 0.83 **1.14 = -0.58Mw + 0.81mb** mb = 0.72Mw + 1.40 **Mw = 1.39mb - 1,94**	±0.24 ±0.32 **±0.19** ±0.24 **±0.33**	**Fig. 3.76** upper left
Mw – mB_BB 478	SR1 SR2 **OR**	mB_BB ← 0.75Mw + 1.52 Mw ← 1.08mB_BB - 0.59 **0.87= -0.63Mw + 0.77mB_BB** mB_BB = 0.82Mw + 1.15 **Mw = 1.22mB_BB - 1.40**	±0.24 ±0.29 **±0.19** ±0.24 **±0.30**	upper right
Mw – Ms_20 for Mw < 6.8 341	SR1 **OR**	Ms_20 ←1.31Mw - 2.19 **1.81 = 0.83Mw - 0.55Ms_20** Ms_20 = 1.50Mw - 3.27 **Mw = 0.667Ms_20 + 2.18**	±0.28 **±0.16** ±0.29 **±0.19**	lower left
Mw – Ms_20 for Mw ≥ 6.8 32	SR1 **OR**	Ms_20 ← 0.93Mw + 0.37 **0.42 = 0.73Mw - 0.68Ms_20** Ms_20 = 1.06Mw - 0.61 **Mw = 0.943 Ms_20 + 0.575**	±0.31 **±0.22** ±0.32 **±0.30**	lower left
Mw – Ms_BB for Mw < 6.8 339	SR1 **OR**	Ms_BB ←1.15Mw –1.10 **1.31 = 0.80Mw - 0.60Ms_BB** Ms_BB = 1.34Mw - 2.19 **Mw = 0.746Ms_BB + 1.634**	±0.28 **±0.17** ±0.28 **±0.21**	**Fig. 3.76** lower right
Mw – Ms_BB for Mw ≥ 6.8 32	SR1 **OR**	Ms_BB ←0.91Ms + 0.60 **0.27 = 0.72Mw - 0.69Ms_BB** Ms_BB = 1.04 Mw - 0.39 **Mw = 0.961 Ms_BB + 0.375**	±0.31 **±0.22** ±0.32 **±0.30**	lower right
Me – mb 98	SR1 SR2 **OR**	mb ← 0.55M_e + 2.54 Me ← 1.40mb - 2.08 **1.97 = -0.51Me + 0.86mb** mb = 0.59Me + 2.28 **Me = 1.70mb - 3.86**	±0.24 ±0.38 **±0.21** ±0.24 **±0.41**	**Fig. 3.77** upper left
Me – mB_BB 98	SR1 SR2 **OR**	mB_BB ← 0.62Me + 2.46 Me ← 1.20mB_BB - 1,30 **1.69 = -0.56Me + 0.83mB_BB** mB_BB = 0.68Me + 2.05 **Me = 1.47mB_BB - 3.42**	±0.29 ±0.40 **±0.24** ±0.29 **±0.43**	upper right

Me – Ms_20 93	SR1 SR2 **OR**	Ms_20 ← 0.94Me + 0.20 Me ← 0.85Ms_20 + 1,08 **0.38 = 0.73Me - 0.69Ms_20** Ms_20 = 1.06Me - 0.53 **Me = 0.943Ms_20 + 0.50**	±0.38 ±0.36 **±0.26** ±0.3 **±0.33**	lower left
Me – Ms_BB 93	SR1 SR2 **OR**	Ms_BB ← 0.90Me + 0.53 Me ← 0.87Ms_BB + 0.89 **0.15 = 0.71Me - 0.70Ms_BB** Ms_BB = 1.02Me - 0.21 **Me = 0.980Ms_BB + 0.196**	±0.38 ±0.37 **±0.27** ±0.38 **±0.36**	lower right

Other conclusions to be drawn from Figs. 3.79 and 3.80 as well as from Tab. 3.4 and formula (3.105) are:

- According to Fig. 3.79 (lower two diagrams) the relationship between Mw with Ms_BB and Ms_20, respectively, is better approximated by a bi-linear OSR.
- While both Ms_BB and Ms_20 correlate with **Mw > 6.5** with a **slope close to 1 (up to about 8.5) the slope is less than 1 for smaller Ms.**
- **At magnitudes < 6.5 Ms_BB deviates on average less (about half) from Mw than Ms_20** (for formulas see Tab.3. 4)

.

- The OSR between Mw and mB_BB according to the Chinese data in Tab. 3.4 has the same slope of 1.22 as in the formulas (3.104) and (3.105), yields, however, in the whole magnitude range on average Mw proxy estimates that are 0.33, respectively 0..28 m.u. larger than those derived with formula (3.105).

- The orthogonal regression between Ms_BB and Me in Fig. 3.79 and Tab. 3.4 has a slope near 1:

$$Ms\_BB = 1.02\ Me - 0.21 \quad \text{with SD} = \pm 0.38 \qquad (3.107)$$

  and is only somewhat larger (1.06) when plotting Ms_20 over Me.

- This good agreement between Me and Ms is understandable, because the magnitude formula Me = ($\log E_S$ – 4.4)/1,5 has been scaled by Choy and Boatwright (1995) to USGS surface-wave Ms in the wide range between 5.5 and 8.3 , adopting the slope of 1.5 in the Richter (1958) $\log E_S$-Ms relationship.
- This explains the almost perfect agreement of the SR1 regression mB_BB - Me in Tab. 3.4:

$$mB\_BB \leftarrow 0.62\ Me + 2.46 \quad (\text{with SD} = \pm\ 0.29). \qquad (3.108)$$

  with the classical Gutenberg-Richter (1956) relationship mB = 0.63Ms + 2.5, because when deriving the Me formula, Choy and Boatwright (1995) substituted Ms by Me.

These quantitative comparisons between classical and new relationships illustrate that by linking the physically well-defined size parameters M_0 and E_S with magnitude, both Mw and Me are completely tied to the classical empirical magnitudes of mB and Ms with all their possible biases that are, with the exception of saturation, not yet well known and documented.

The most recent GOR models have been derived by Di Giacomo et al. (2013) in the framework of the ISC-GEM project for creating a New Reference Global Instrumental Earthquake Catalogue (1900-2009) (see section 3.2.9.5). For the bi-linear Mw-Ms relationship they read:

$$Mw = 0.67\ Ms + 2.13 \quad \text{for } M_S \leq 6.47 \tag{3.109}$$

and

$$Mw = 1.10\ Ms - 0.67 \quad \text{for } M_S > 6.47 \tag{3.110}$$

and are comparable with bi-linear standard models obtained from more than 26.000 globally distributed earthquakes by Scordilis (2006):

$$Mw = 0.67(\pm 0.005)\ Ms + 2.07(\pm 0.03) \text{ with SD} = \pm 0.17 \text{ m.u for } 3.0 \leq Ms \leq 6.1 \tag{3.111}$$

and

$$Mw = 0.99(\pm 0.02)\ Ms + 0.08(\pm 0.13) \text{ with SD} = \pm 0.20 \text{ m.u for } 6.2 \leq Ms \leq 8.2 \tag{3.112}$$

or the GOR models by Das et al. (2011)

$$Mw = 0.67\ Mw + 2.12 \quad \text{for } 3.0 \leq M_S \leq 6.1 \tag{3.113}$$

and

$$Mw = 1.06\ Ms - 0.38 \quad \text{for } 6.2 < M_S \leq 8.4. \tag{3.114}$$

All these relationships (3.109) to (3.114), based on some 10.000 to 20.000 data points,.are almost identical with the OSR relationships in Tab. 3.4 derived by Bormann et al. (2009) based on only 373 proper Ms_20 event magnitudes determined from Chinese National Network data:

$$Mw = 0.667\ Ms\_20 + 2.18 \quad \text{for Ms between 4.0 and 6.5} \tag{3.115}$$

and

$$Mw = 0.943\ Ms\_20 + 0.575 \quad \text{for Ms} > 6.5 \text{ to } 8.8, \tag{3.116}$$

respectively. Mw proxies calculated with (3.115) differ from those derived by the currently most representative ISC-GEM relationship (3.109) in the magnitude range 4.0 to 6.5 by ≤+0.04 m.u., the respective Das et al. (2011) GOR relationship (3.113) by constant -0.01 m.u. and the Scordilis (2006) relationship (3.111) by constant -0.06 m.u. The differences are larger for magnituded Ms > 6.5 where all relationships are based on much less data. Yet still Mw proxy estimates according to Das et al. (2011) agree with the respective ISC-GEM estimates up to Ms = 8.5 within 0.05 m.u, and those by the Bormann et al. (2009) formula within 0.1 m.u.. With -0.18 m.u in Mw at Ms = 8.5 the Scordilis relationship The largest difference.

Although much inferior as compared to the Mw-mB_BB relationships published by Bormann et al. (2009) and above [see formulas (3.101), (3.104) and 3.105) as well as Figs. 3.74, 3.75 and 3.78], in common literature only regression relationship between Mw and mb have been published for converting body-wave magnitudes into Mw proxies. The reason is that globally operating seismological data centers such as the ISC, NEIC, and GCMT published so far, since the mid 1970s, only shortperiod mb body-wave magnitudes.

The most recent Mw-mb linear GOR relationship, based on more than 27.000 data points, has been derived by Di Giacomo et al (2013):

$$Mw = 1.38\ mb - 1.79 \quad \text{for} \quad 4.0 < mb < 7.5 \tag{3.117}$$

It is rather close to the Bormann et al.(2009) OSR relationship, based on just 480 data points:

$$Mw = 1.39\ mb - 1{,}94 \text{ with } SD = \pm 0.33 \quad \text{for} \quad 4.5 \leq mb \leq 7.5 \tag{3.118}$$

The Mw proxy estimates via (3.117) and 3.118) differ in the range $4.5 \leq mb \leq 7.5$ less than 0.1 m.u..

Both relationships, however, differ strongly from the GOR relationship between Mw(GCMT) and ISC mb values published by Wason et al. (2012) with a slope of only 1.13, and even more from the slope of the SR1 relationship by Scordilis (2006), based on more than 40.000 data points:

$$Mw = 0.85\ mb + 1.03 \quad \text{for } 3.5 \leq m_b \leq 6.2 \tag{3.119}$$

These large differences in slope are mainly due to the dataset truncation at mb = 6.2 by both Scordilis (2006) and Wason et al. (2012).

However, since the standard errors with which event Mw and mb are typically determined (≤ 0.1 m.u. and 0.2 to 0.3 m.u., respectively) are very different, ordinary OSR and GOR, based on the assumption that the ratio of initial errors of the two magnitudes is close to 1, are no longer optimal. Castellaro and Bormann (2007) showed that for standard error ratios <0.7 the inverse regression relationship, i.e., in our case mb over Mw, is closer to optimal. Bormann et al. (2011) give mb = 0.66Mw + 1.73 and Das et al. (2011) mb = 0.65 Mw + 1.65. When resolved for Mw these relationships read for the Bormann et al. (2009) data

$$Mw = 1.52\ mb - 2.62 \tag{3.120}$$

and for the Das et al. (2011) data

$$Mw = 1.54\ mb - 2.54. \tag{3.121}$$

For mb = 7.5, which is about the largest value so far measured for standard mb, (3.120) and (3.121) would yield Mw proxy values of 8.78 and 9.01, respectively. These are reasonably large values for such large mb values, more likely than those derived via (3.117; Mw = 8.56) and (3.118; Mw = 8.49). However, proxy Mw estimate via linear regression relationships with mb, which really cannot fit well a highly non-linear data cloud (see Fig. 3.82 in the next section), generally tend to underestimate Mw for both the strongest and the weakest earthquakes.

Therefore, we do not recommend the conversion of short-period mb into long-period Mw. If it has to be done, for what reason ever, then a non-linear relationship, as presented in the next section, should be used. Yet, in future such mb-Mw relationships should be based on new standard mb data only. They saturate later and thus reduce the strong non-linear distribution) of older mb data that have been measured on records with often different responses and within more or less fixed limited time windows after the first P-wave arrival. As one can see from Fig. 3.79, the relation between standard mb and Mw is reasonably linear in a rather large range of magnitudes.

Wason et al. (2012) also published a GOR relationship between Me and mb:

$$Me = 1.445\ mb - 2.33. \quad (3.122)$$

It differs strongly from the OSR relationship **Me = 1.70mb - 3.86** by Bormann et al. (2009), but is very close to the related standard regression (see Tab. 3.4):

$$Me \leftarrow 1.40\ mb - 2.08 \quad \text{with SD} = \pm 0.38\ \text{m.u.}. \quad (3.123)$$

In the range of applicability of (3.122), i.e., for input values of $5.0 < mb < 6.5$, the Me proxy estimates differ less than 0.04 m.u. from those derived via (3.123). The latter relationship, however, is applicable up to mb = 7.5.

3.2.9.5 Non-linear ISC-GEM relationships between Ms and mb with Mw

(D. DiGiacomo and P. Bormann)

The ISC-GEM project aimed at the establishment of a New Reference Global Instrumental Earthquake Catalogue (1900-2009) (see Storchak et al., 2013; Di Giacomo et al., 2013) made every effort to use uniform procedures of magnitude determination during the entire period of the catalogue. Both surface-wave magnitudes Ms and short-period body-wave mb were recalculated, benefitting from new hypocenters (Bondár et al., 2013), previously unavailable amplitude-period data digitized during this project (Di Giacomo et al., 2013) and a more reliable algorithm for magnitude computation based on 20% alpha-trimmed median network magnitude from several stations (Bondár and Storchak, 2011). For Ms up to 1970 several thousands of station magnitudes not available before were processed.

The re-computed M_S and mb values provided an ideal basis for deriving new conversion relationships to moment magnitude M_W. Therefore, rather than using already published regression models, new empirical relationships were derived using both Generalized Orthogonal Linear and exponential non-linear models to obtain M_W proxies from Ms and mb. The new models were tested against true values of Mw and the newly derived exponential models were found to be preferable to the linear GOR regressions in computing Mw proxies for the new ISC-GEM catalog. For more details see Di Giacomo et al. (2013).

The linear GOR relationships derived by Di Giacomo et al. (2013) for converting recalculated ISC Ms and mb values into Mw proxies have been given already in the previous section as formulas (3.109), (3.110) and (3.117), respectively. Below they are plotted together with the non-linear regressions and the median values polygons through the Ms-Mw and mb-Mw data clouds (Figs. 3.81 and 3.82).

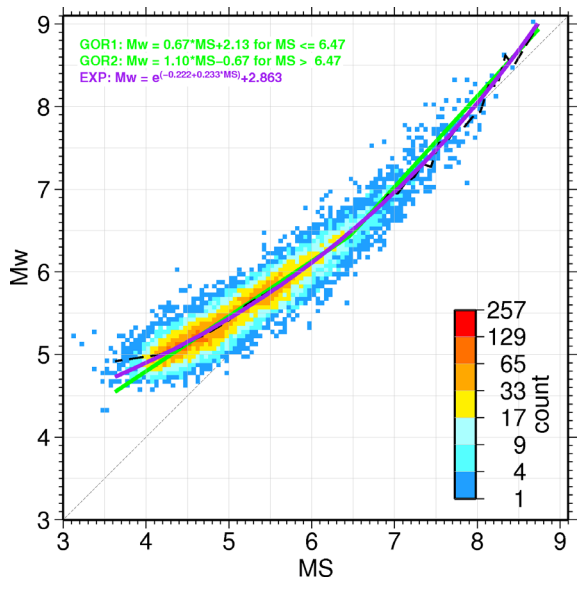

Fig. 3.81 Training dataset set Ms-Mw with regression models: the exponential model is drawn in purple; the bi-linear GOR model is shown in green. The dashed black polygon curve represents the median values for separated bins. Note the good fit between the exponential model and the median values. (Copy of Fig. ??? of Di Giacomo et al., 2013, © PEPI)

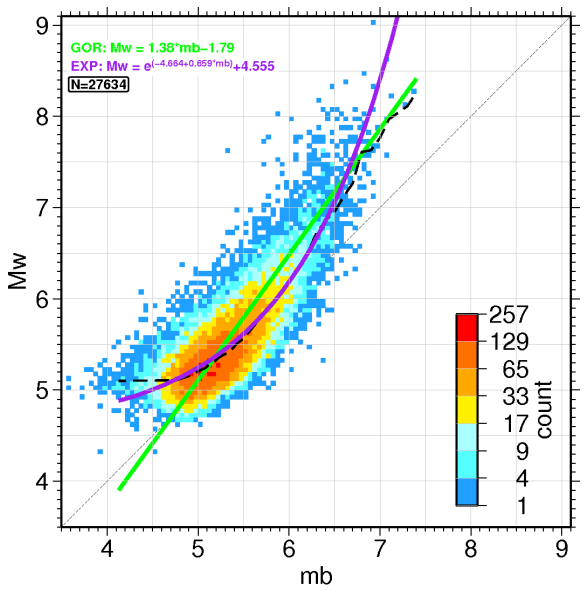

Fig. 3.82 Training dataset set mb-Mw with regression models: Purple - the exponential model; green - the linear GOR model. The dashed black polygon curve connects the median values for separated bins. Note the good fit between the exponential model and the median values between mb=4.7 and 6.5. (Copy of Fig. ??? of Di Giacomo et al., 2013, © PEPI)

Although it is obvious from Fig. 3.81 that fitting the Ms-Mw data cloud with a bi-linear orthogonal regression is good enough for obtaining sufficiently reliable Mw proxy estimates within realistic error limits, such an approach introduces some arbitrariness in the data set separation and also a discontinuity point in the relationships derived. The transition between slope ~0.7 and ~1 is not sharp at all and the separation, which had been adopted by Scordilis (2006) and Das et al. (2011) at Ms = 6.1, by Bormann et al. (2009) at 6.5 and by Ekström and Dziewonski (1988) even at 6.8, could in fact be moved anywhere in this range. Thus, data pairs in this M_S range may belong to one or another domain depending on the subjective choice of an author of how the data set was divided into the two domains. This also raises the question on how to consistently map the uncertainty in Ms to Mw proxies around the separation of the two linear trends. To approximate sufficiently well the highly non-linear trend in the mb-Mw data cloud of Fig. 3.82 one would even need at least three or even four linear GOR regression lines.

In order to avoid this problems Di Giacomo et al. (2013) fitted a single, continuous regression curve to the two training dataset of data points, using an exponential model of the form $My = e^{(a+b\times Mx)} + c$. As on can see from Figs. 3.81 and 3.82, these exponential curves fit rather well with the median values for separated bins. The regression is performed using the

non-linear least square algorithm (Bates and Watts, 1988; Bates and Chambers, 1992), which is freely available with the R-language.

The exponential model to convert Ms to proxy Mw reads as

$$M_W = e^{(-0.222+0.233\times M_S)} + 2.863 \tag{3.124}$$

and that for converting mb into proxy Mw as

$$M_W = \exp^{(-4.664+0.859\times m_b)} + 4.555\,. \tag{3.125}$$

After all the pros and cons of deriving and using conversion relationship as discussed above in section 3.2.9.4 and by Di Giacomo et al. (2013), including also verification tests, it is strongly recommended to use in future for converting Ms_20 type of surface waves from the global data centers only formula (3.125). However, one should refrain from converting mb into Mw proxies, if Ms event data are available. If not, the inferior mb derived Mw proxies should be used and interpreted only with caution. In any event, one should never mix and use with equal weight directly measured Mw and proxy values.

For now more and more up-coming IASPEI standard Ms_BB and mB_BB values, however, the preliminary conversion relationships into Mw, published by Bormann et al. (2009), respectively those for converting mB_BB into Mw according to the relationship (3.104) (see also Fig. 3.74) should be used until masses of these new standard data have become available. They may permit upgrading or revising these preliminary relationships. We could, however, repeatedly demonstrate in section 3.2.9.4 that just a few hundred carefully measured global event magnitude data, even when based on single station or regional network records only, can reproduce within the limits of general measurement error global relationships based on tens of thousands of event magnitudes determined from global network readings.

3.2.9.6 Relationships for converting local and regional magnitudes into Mw

(P. Bormann)

So far we have looked only into relationships between the most common types of instrumentelly measured magnitudes with emphasis on the recently approved new IASPEI standard magnitudes. They are mostly teleseismic ones. However, the great majority of events in national-regional catalogs are local or regional events associated with primarily local (Ml) or duration (Md) magnitude types, often not yet according to standardized rules. Because of this and the regionally highly varying attenuation laws, Ml formulas, even when calibrated to the ML standard, may differ significantly (see DS 3.1). The same applies to Md formulas (3.2.4.5). Yet, also such data are nowadays converted into "unified" moment magnitudes Mw, based on regression relationships not with Mw(GCMT), which is routinely available only for Mw $\geq$ 5.5, but to regional Mw estimates, down to much weaker events, via spectral parameter analysis (see EX 3.3) instead of fitting long-period waveforms.

A very detailed report about the derivation and use of local-regional event conversion relationships based on both local and teleseismic magnitudes as well as regional and GCMT Mw has been presented by Braunmiller et al. (2006) by way of example for Switzerland. These authors also give average uncertainties for the Mw proxy estimates via such relations. They range between ±0.2 for Ml and ±1.0 m.u. for the macroseismic magnitude estimates

Mms of the Swiss Earthquake Service (SED). This is clearly worse than for any proper direct Mw measure. Yet, Braunmiller et al. derived also average Mw conversion relationships for Ml and Md data published by agencies in neighboring countries, which are relevant for the seismic hazard assessment on the Swiss territory too. This concerns data of the Landeserdbebendienst Baden-Württemberg (LED) and of the University of Karlsruhe (KHE) in Germany, the Laboratoire de Detection Geophysique (LDG) in France, and the Istituto Nationale di Geofisica e Volcanlogia in Italy (INGV). Interestingly, the local magnitudes of all these institutions scale with a slope of 1 with Mw, however their constants as well as the average uncertainty of the Mw proxy estimates vary strongly, hinting to not standardized level scaling, different degree of reliability of the input Ml (see relationships 3.126), Md (see relationships 3.127), and Mm (relationship 3.128) and thus the incompatibility of the respective agency magnitudes and therefrom calculated Mw proxy estimates:

$$\begin{aligned} Mw &= Ml(SED) - 0.2 \pm 0.2 = Ml(KHE) - 0.2 \pm 0.4 = Ml(LED) - 0.3 \pm 0.4 \\ &= Ml(LDG) - 0.6 \pm 0.4 = Ml(INGV) - 0.3 \pm 0.7, \end{aligned} \tag{3.126}$$

$$Mw = Md(LDG) - 0.8 \pm 0.5 = Md(INGV) + 0.1 \pm 0.5, \tag{3.127}$$

$$Mw = Mms(SED) \pm 0.5 - 1.0. \tag{3.128}$$

Yet, often published relationships aim not at calculating Mw proxies but at estimating via Ml $\log M_0$. The latter we converted with the Mw standard formula (3.68) into Mw-Ml relationships and compiled them together with some other regional Mw-Ml relations in Tab. 3.5.

In summary, one realizes that in contrast to most relationships between teleseismic magnitudes with Mw there are no globally representative relationship for converting local magnitudes into Mw. Not only the slopes may differ strongly, between about 0.6 and 1.0, but even when the slopes are comparable, then the constants may differ strongly, up to half a magnitude unit or even more. Striking examples in Tab. 3.5 are the difference between the conversion formulas in Western Canada for events in the continental crust and those in the subducting slab (Ristau et al., 2005), or between NW Turkey and Italy. This highlights the need to base any such local-regional conversion formulas on own careful investigations in the respective area. There is no chance to find a priori well-fitting ones in publications related to other seismotectonic regions, although one might later find out a very close agreement with a formula for another region, as, e.g. Margaris and Papazachos (1999) for their logMo - Ml_{SM} (SM = strong motion) formula for Greece with that by Hanks and Kanamori (1979)(see Tab. 3.6).

Tab. 3.6 Linear regression formulas for converting local and regional Ml into Mw. Ml_{SM} = strong motion Ml

Mw =	Ml range	Region	Reference
0.61 Ml + 0.85	0 - < 4.5	NW Italy	Bindi et al. (2005)
0.78 Ml + 0.68	0.5 – 6.0	NW Turkey	Parolai et al. (2007)
0.79 Ml + 1.20	3.5 – 5.8	Italy	Castello et al. (2007)
0.80 Ml + 0.93	1.0 – 6.0	California	Chávez & Priestley (1975)
0.87 Ml + 0.60	2.2 – 5.3	Israel	Shapira & Hofstetter (1993)
1.00 Ml_{SM} – 0.02	3.9 – 6,6	Greece	Margaris & Papazachos (1999)
1.00 Ml – 0.05	≈3 - 7	Southern California	Thatcher & Hanks (1973)

1.00 Ml – 0.16	2.7 – 5.9	Switzerland	Braunmiller et al. (2005)
1.00 Mlcrust + 0.06	3.6 - < 5.5	Western Canada	Ristau et al. (2005)
1.00 Mlslab + 0.58	3.6 – 6.0	Western Canada	Ristau et al. (2005)

Besides dominatingly linear relationships between Mw and Ml one finds occasionally also non-linear ones, e.g., those published by Gusev (1991) and Gusev and Melnikova (1992) (see also Figure 9 in IS 3.7). Another logarithmic one has been published by Wu et al. (2001) for Taiwan:

$$Ml = 4.53 \times \ln(Mw) - 2.09 \pm 0.14, \tag{3.129}$$

and a non-orthogonal non-linear one with a quadratic term included by Parolei et al. (2007) for Northwestern Turkey:

$$Mw \leftarrow (0.95 \pm 0.03) + (0.58 \pm 0.02)Ml + (0.003 \pm 0.004)Ml^2. \tag{3.130}$$

3.2.10 Summary remarks about magnitudes and their perspective (P. Bormann)

According to Richter (1935), magnitude was intended to be a measure of earthquake size in terms of the seismic energy E_S released by the source. Yet, more than 40 years later, Kanamori (1977), in his effort to develop a non-saturating magnitude scale, proposed to relate magnitude to the scalar seismic moment M_0 and thus to the amount of "work" performed by rupturing and displacing the earthquake fault. For estimating energy via M_0 assumed an average stress drop and ratio between E_S/M_0.

E_S, being proportional to the squared velocity of ground motion, can theoretically be obtained by integrating spectral energy density over all frequencies contained in the transient waveform, e.g., of the P-, S-, or surface-wave train. This procedure could not be carried out efficiently with analog recordings. Therefore, Gutenberg (1945b and c) assumed that the maximum amplitude observed in a body-wave group was a good measure of the energy density in that arrival. As classical seismographs were relatively broadband displacement sensors, he estimated ground motion velocity by dividing the maximum ground displacement of body-wave phases by their associated periods in the range between some 2 to 20 s for calculating a medium-period broadband magnitude mB [see Eq. (3.43)]. But the largest displacement plateau amplitude occurs at somewhat longer periods than the maximum velocity amplitudes (see Fig. 3.5). None the less, according to the published formula, Gutenberg's intention was to measure $(A/T)_{max}$ and not (A_{max}/T). For estimating the magnitude Ms from surface waves, however, Gutenberg (1945a) proposed measuring just the maximum displacement amplitude in the surface-wave train around 20 s, although one finds in pre-1960s station bulletins plenty of surface-wave A_{max} data published at periods between some 10 and 30 s (Di Giacomo et al., 2013??). According to Fig. 3.5, the spectral amplitudes sampled around 20 s are reasonably good estimators of the maximum of the source velocity spectrum and thus of E_S for magnitudes between about 6 and 8.5 as well as of the maximum displacement amplitude plateau and thus of seismic moment for magnitudes < 7.5. Richter's ML also measures only the displacement amplitude maximum in local earthquake records, typically at frequencies < 1 s. Yet, according to Fig. 3.5, such amplitudes are on average both a reasonably good seismic moment estimator for magnitudes < 5 (see several Mw-Ml

relationships in section 3.2.9.6) and a good estimator of the maximum of high-frequency energy release for magnitudes < 6.

Further, one should note that all classical calibration functions for ML, mB and Ms, including also the IASPEI standard Ms formula since 1967 [see Eq. (3.36)], which accepts proper $(A/T)_{max}$ measurements in a wider range of periods (3 to 60 s) and distances (2° - 160°), do account only for distance- (and for body waves additionally depth-) dependent attenuation but neither for any source-mechanism correction nor for a frequency-dependence of the quality factor Q. The latter seems to be justified at least for periods ≥ 4 s, for which the frequency dependence of Q, if any, becomes negligible or not separable from other disturbing influences on the measured amplitudes (see Chapter 2, section 2.5.4.2).

Since the pioneering works of Richter (1935), Gutenberg (1945 a, b, and c) as well as Gutenberg and Richter (1956 a, b, and c) magnitudes have become, besides phase identification, onset time readings and source locations derived therefrom, the most important earthquake parameter data published in station bulletins and national as well as international earthquake catalogs. Admittedly, seismic moment tensor solutions, scalar seismic moment M_0, radiated seismic energy E_S and strong-motion maps may be of greater scientific interest, giving a more precise, complete and physically based description of the investigated seismic source processes and their static, kinematic and dynamic effects. Yet magnitude data will remain also in future an indispensable, most frequently asked for and practically used earthquake source parameter, for both long-term statistical assessment of seismicity and seismic hazard, as well as for public announcements on earthquakes and tsunami and for providing a first rapid event assessment to guide disaster management and relief operations. Neither the public, nor decision makers and disaster managers can comprehend and base meaningful actions on physical parameters given to them in the range of many orders of magnitude (in different physical units and with a precision of several decimals). What is relevant in the earthquake disaster context for practical actions are simple integer numbers, such as intensity degrees related to felt earthquake shaking strength and related damages, ranging from 1 to 7 degrees in Japan or 1 to 12 degrees in most other countries (see Chapter 12), or ground accelerations in decimal fractions of the earth gravity g, or just magnitudes, always being less than 10 and given with a precision not better than one decimal. Such scales are comprehensible and relate to each other sufficiently well. A higher precision is not required, neither for warning messages nor for decisions related to response, disaster preparedness and mitigation efforts.

Yet, three major issues hamper the usefulness of magnitude data:

a) The diversity and inhomogeneity of procedures;

b) Changes of procedures, made by agencies or stations, which have often not been well documented and/or analyzed for their effects, thus disrupting the necessary long-term stability and compatibility of magnitude data that have been published with identical symbols/names;

c) The current fashion of converting all types of magnitudes in catalogues just into Mw, often not even saying from which type of magnitudes such proxy estimates of Mw have been derived and what the different ranges of uncertainties for such proxy estimates are.

Examples for a)

With the establishment by the United States of the WWSSN in the 1960s and 70s no more medium-period broadband systems, required for the determination of mB, had been available in this global network of seismic stations. This global network aimed mainly at lowering the detection threshold for seismic events globally down to body-wave magnitudes of about magnitude 4 (instead of 5 to 5.5 achievable with mB for teleseismic events). A magnitude 4 corresponds approximately to that of a well contained underground nuclear explosion (UNE) of about 1 kt TNT equivalent. Yield estimates via such magnitudes as well as best possible discrimination between explosions and earthquakes were other original priority tasks for the WWSSN. These goals were hoped to be best achieved by two band-limited seismograph responses with maximum magnification at periods between about 0.5 to 1.0 s (termed WWSSN-SP) and between about 10 and 20 s (termed WWSSN-LP). For the body waves this necessitated the introduction of another, short-period, scale, termed mb, although the measured amplitudes were continued to be calibrated with the same Gutenberg-Richter (1956a) calibration function Q(Δ,h)PV for medium- to long-period vertical-component P-wave amplitude readings. Additionally, in the interest of best possible discrimination between UNE or other explosions from earthquakes, it was regulated to measure $(A/T)_{max}$ not within the whole P-wave train, as Gutenberg did, but within the first few seconds after the P arrival. These changes in both record responses and measurement-time window resulted in the much earlier saturation of mb, as compared to mB. And the USGS/NEIC Ms_20 values, based on WWSSN-LP records and the use of the IASPEI standard Ms formula, show a distinct distance dependence and are not fully compatible with broadband Ms measured in a wider period and distance range using the same calibration function.

Similarly, other requirement or concepts for classifying the size of seismic events resulted in the development of even more magnitude scales such as the Russian K-class, the duration magnitude Md or mbLg for near and regional events, or of m(P, 1Hz), m(PKP), the mantle magnitude Mm, the more physically based moment magnitude Mw and energy magnitude Me, the fast Mw proxy estimators Mwp, Mwpd and others for teleseismic events, or the assignment of macroseismic magnitude values Mms to historical earthquakes. The reasons for their development and the specific procedures of their measurement have been outlined in detail in the sections 3.2.4 to 3.2.8. These scales have different precision and are more or less reliable mutually scaled (see, e.g., 3.2.9.2 and 3.2.9.6). This notwithstanding, magnitudes of different kinds will still persist and be required in the foreseeable future to allow the size classifications of seismic events under very different instrumental and environmental conditions. Their proper use, however, requires an understanding of their potentials, limitations, original definitions and mutual relationships. Some of these scales are really important complements, such as the narrow-band magnitudes mb and Ms_20. Their difference permits to draw essentially the same inferences on kinematic-dynamic differences between seismic events as they can now be made, even better, by comparing Me and Mw (see section 3.2.7.2 and IS 3.5). However, for the ordinary user of magnitude data all these details and the reasons for differences and discrepancies between the different types of magnitude can just not be overlooked and reliably be assessed from the vast literature. The previous sections hopefully can help to alleviate this problem.

Examples for b)

Even more confusing and discouraging are inconsistent and even temporal changes of procedures for magnitude data of the same kind, published with the same magnitude symbol.

As outlined in section 3.2.4.1, it was found out only decades later that the ML data in California have not been measured consistently. Not properly documented and investigated changes in analog and digital amplitude reading practices resulted in baseline shifts that faked temporal changes in seismicity rates which were misinterpreted as being related to the Mw7.5 Kern County earthquake of 1952. This led Habermann (1995) to state that: "Such mistakes have the potential to undermine the relationship between the seismological community and the public we serve."

Less dramatic but still significant have been the changes made at the USGS/NEIC with respect to early years mb (see example a) when following IASPEI recommendations of 1976 to increase the measurement time window, for great earthquakes up to about one minute, and later by replacing the original WWSSN-SP response with the PDE response which has a somewhat broader relative bandwidth and steeper roll-off towards lower frequencies (see Figure 3 in IS 3.3). And the IDC of the CTBTO uses still another pre-processing filter before measuring its mb. It has an even higher frequency of peak amplification and still steeper flanks towards lower and higher frequencies. In the extreme case of the great Mw9.3 Sumatra Andaman earthquake of 2004 these different agencies reported mb values which differed up to 1.5 m.u.: mb(IDC) = 5.7; mb(CENC) = 6.4; mb(PDE) = 7.2.

Such discrepancies between magnitudes of the same type are alarming and unacceptable. The recently adopted IASPEI (2005, 2011, and 2013) standards for the most widely used common types of magnitudes: mb, mb_Lg, mB_BB, ML, Ms_20 and Ms_BB as well as for the calculation of Mw (see sections 3.2.3.2; 3.2.4.2; 3.2.5.1; 3.2.5.2 as well as IS 3.3) aim at eliminating or at least significantly reducing procedural differences between magnitudes of the same kind.

Magnitudes of the same type as these standard magnitudes but based on different measurement procedures which yield values that differ on average more than 0.1 m.u. from these standard magnitudes have to be published in future with a specifying nomenclature (see IS 3.2). Moreover, seismological agencies publishing magnitude data are requested to give full evidence of their procedures of magnitude determination by filling in the questionnaire in Annex 2 of IS 3.4 and by publishing this information on their related website and/or in their bulletins and deposit it at the main international seismological data centers, such as the ISC and the NEIC. With these measures it is expected to drastically reduce in the foreseeable future heterogeneity and the scatter of magnitude data and to assure improved long-term continuity and stability of magnitude data, thus increasing their value for application and research.

In the following section we summarize a selection of important so-called scaling relationships between magnitudes and a variety of geometric as well as kinematic and dynamic source parameters. In this context we will also look into the need (or not) of revising the currently used formulas for Mw and Me determination in the light of modern data on the relationships between mB_BB and Ms_20 with released seismic energy.

3.3 Similarity conditions and seismic scaling relations
(P. Bormann)

3.3.1 Similarity of seismic sources and the definition and use of seismic scaling relations

The *similarity* of seismic sources over a wide range of magnitude or other "size" parameters are the precondition for the derivation of scaling relationships, e.g., between the shape and level of radiated seismic spectra as a function of frequency, as in Fig. 3.5. Similarity of earthquake ruptures exists under certain conditions of static (geometric) and dynamic similarity. With the assumption of a constant stress drop, e.g., one gets

$$W/L = k_1 \qquad \text{i.e., a constant fault aspect ratio} \qquad \text{and} \tag{3.131}$$

$$\bar{D}/L = k_2 \qquad \text{i.e., constant strain } \alpha. \tag{3.132}$$

One can combine Eqs. (3.131) and (3.132) with the definition of the seismic moment $M_0 = \mu \bar{D} W L = \mu k_1 k_2 L^3$ and gets $M_0 \sim L^3$ which is valid for source dimensions smaller than the thickness of the *seismogenic layer*.

In addition there is a dynamic similarity, namely, the rise time t_r required for reaching the total displacement, i.e., the duration of the source-time function, is

$$t_r = k_3 \times L/v_{cr} \tag{3.133}$$

with v_{cr} the crack or rupture velocity (see Fig. 3.4). This is equivalent to the Eq. (3.132) of constant strain. Lay and Wallace (1995) showed that this results in period-dependent amplitudes of seismic waves which scale with the fault dimension. For periods $T >> t_r$ the amplitude does not depend on fault length L. This corresponds to the plateau of the "source displacement spectrum". But if $T << t_r$ then the amplitudes scale as $1/L^2$ or f^{-2} (see Fig. 3.5). This explains the saturation effect when analyzing frequencies much higher than the corner frequency of the source spectrum.

Both in earthquake and engineering seismology the term "scaling law" is widely used. According to Boore (1983) the Fourier spectrum of an earthquake record can be represented as the product of the source, propagation path and site terms. Then it would be very helpful if the entire source term could be represented by just one parameter, e.g., by assuming similarity of the spectra of all earthquakes. This was first done by Aki (1967) when investigating the dependence of the amplitude spectrum of seismic waves on source size on the basis of two different dislocation models of an earthquake source. One has been the Haskell (1966) ω^{-3} model, in which the spectral amplitudes decay well beyond the corner frequency f_c with the third power, and the other one an ω^{-2} model, as in Fig. 3.5. Aki considered the surface-wave magnitude Ms to be a most suitable parameter for scaling the source spectrum. Later this was commonly substituted by the scalar seismic moment M_0, as in the Geller (1976) scaling laws for body and surface waves and in Fig. 3.5, or by the moment magnitude Mw, which itself has been scaled to Ms (see section 3.2.7.1). According to Aki (1967) the theoretical ω^{-2} model agreed better with the observed spectra than the ω^{-3} model, which would also imply absolute saturation of spectral amplitudes for $f >> f_c$, as also in the Geller (1976) models, according to which mb would already completely saturate at 5.9 and Ms at 8.0. Yet, Ms has already been observed up to 8.9 (see, e.g., Bormann et al., 2009) and with respect to mb Geller had only pre-1976 values available which were based on amplitude measurements within the first few cycles only, as nowadays still the mb(IDC-CTBTO). The IASPEI standard mb, however, which always measures the largest amplitude in the whole P-wave train, measures values up to about 7.6.

Beresnev (2001 and 2008) rightly questions the assumption of a strict similarity of earthquake source processes and even Aki (1967) hints already in his pioneering paper to "…some indications of departure from similarity". It is rather obvious from wave physics that low-frequency measures such as the scalar seismic moment M_0, being according to equation (3.1) only a static measure of earthquake size, or the moment magnitude Mw derived therefrom, cannot provide direct information about the kinematics and dynamics of the rupture process. While the low-frequency asymptote of the displacement spectrum and thus M_0 are solely controlled by the final static offset of the fault rupture, the actual stress drop (see, e.g., Abe, 1982; Choy and Boatwright, 1995) and rupture velocity (Fig. 3.6 and Venkataraman and Kanamori, 2004a and b) may vary strongly for equal moment earthquakes. These latter source parameters, however, control the corner frequency and with it the relative high-frequency content of the source spectrum and thus the amount of radiated seismic energy per unit of M_0 (see Fig. 3.15). Therefore, the single source parameter scaling of seismic spectra is not a viable model and we will look into the scaling problem in a wider context.

We should always keep in mind that ANY earthquake model is a (usually gross) simplification of the complex earthquake rupture process. Models tend to reduce as much as possible the number of controlling parameters, for which usually no directly measured and sufficiently accurate empirical data available and in order to make the models tracktable. A good example may be the extensive debate by Scholz (1994 a and b), Romanowicz (1994), Romanovicz and Rundle (1994) and Sornette and Sornette (1994) about a paper by Scholz (1982) dealing with the scaling laws for large earthquakes. He interpreted the observation that the mean slip in large earthquakes is linearly proportional to fault length L and does not correlate with fault width W on the basis of two possible models for large earthquakes: a) models, in which stress drop and slip are determined by fault width Wand b) L models, in which these two parameters are fundamentally determined by L. But both models come to opposite conclusions with respect to mean particle motion and rise time of the source-time function. In a later paper Scholz (1997) could show, however, that such conflicts do not exists when the size distribution of faults is properly taken into account. Wang and Ou (1998), using the large data base by Wells and Coppersmith (1994), proved that W is independent of L for large earthquakes, that average displacement $\bar{D}$ relates to L as $\bar{D} \sim L$, seismic moment to L as $M_0 \sim L^2$ whereas $\bar{D}$ is independent of W. Accordingly, they concluded that the L-model proposed by Scholz (1992) is more appropriate than the W-model suggested by Romanowicz (1992) to describe the scaling of earthquake faults.

In any event, a rectangular fault plane is nothing but a rough approximation of a more or less irregularly shaped rupture area for medium to strong size earthquakes. According to Geller (1976), empirical data for earthquakes are agreeable with assuming an average aspect ratio L/W = 2 with a scatter of about 2. Purcaru and Berckhemer (1982), however, assume for great earthquakes aspect ratios even up to 30. The "true" L/W depends on the rupture dimensions with respect to the thickness h_{sg} of the seismogenic zone in the Earth crust, respectively lithosphere, which is capable of brittle fracturing. h_{sg}, however, depends on crustal thickness, age and heat flow conditions, which vary from region to region. In California, with its young crust and high heat flow, h_{sg} is only about 12 to 15 km. Deeper earthquakes hardly ever occur. The maximum width of an earthquake rupture is $W_{max} = h_{sg}/\sin\delta$, with δ the fault dip. Accordingly, the ratio L/W may vary between about 1 and about 10, or even more, e.g., for mega-events such as the great Mw 9.3 Sumatra-Andaman earthquake of December 2004 with a rupture length of about 1300 km.

If one defines, according to Scholz (1982), as small earthquakes those which have a source radius $r \leq W_{max}/2$, then they likely can be represented reasonably well by assuming even

circular fault planes with radius r in an elastic medium, whereas large earthquakes with r > W_{max} /2 are better treated as rectangular ruptures with one edge at the free surface and only L growing with magnitude.

Yet, even when using only circular source models for deriving some crucial source parameters from seismic spectra, such as source radius r, rupture area A, average displacement $\bar{D}$ and stress drop $\Delta\sigma$, then the calculated values may differ significantly even for identical input values of M_0 and f_c estimated from identical seismic spectra. E.g., the most common models by Brune (1970) and Madariaga (1976; models I and II) yield values for these inferred parameters that differ by factors between about 1.7 and 6 (see EX 3.4). Model inherent uncertainties in this range or even larger ones should therefore be kept in mind when using the scaling relationships. The main advantage of using quantifiable models is not that they tell us the absolute truths with respect to the derived parameters but that they reveal, in a consistent and reproducible manner, relative differences between these parameters for different events, provided that the model assumptions hold for all of them, and to assess their variability with magnitude, space and time.

In the following we present a selection of various relationships between magnitudes with physical or geometrical parameters of the seismic source, such as radiated seismic energy and seismic moment, stress drop, duration of rupture, area or length and width of rupture, fault dislocation, or between magnitudes and earthquake effects at some distance from the source, such as the area of felt shaking, or the intensity of shaking as a function of distance from the source (attenuation laws). If any of these parameters appears to be related in a systematic and predictable manner over a wide range of earthquake size, scaling "laws" based on similarity conditions may be inferred. Seismic scaling laws then allow to roughly estimate one parameter from another (e.g., E_S from magnitude, or M_0 from field evidence such as surface rupture length and/or displacement). Therefore, the knowledge of theoretically well founded scaling laws or empirical scaling relationships is of crucial importance for both probabilistic and deterministic seismic hazard analyses. They aim at assessing the future earthquake potential of a region on the basis of data from past events, dating back as far as possible.

Scaling laws are often the only way to estimate parameters of historical earthquakes for which no instrumental measurements of magnitude, seismic energy or scalar seismic moment are available. Specifically, one often has to make reasonable estimates of the size of the largest earthquake that might have occurred at or could be generated by a particular fault or fault segment and of the kind of seismic spectrum it might (have) radiate(d). However, as stated above, seismic sources differ not only in their geometrical size, shape, aspect ratio, rupture velocity and average slip. Ambient stress conditions and stress drop, the dominant modes of faulting and related seismic source spectra may also differ significantly from region to region. For instance, events of the same seismic moment may radiate seismic energies which differ by 2 to 3 orders (see sections 3.1.2.3 – 3.1.2.5, 3.2.7.2 and IS 3.5). Therefore, globally-derived scaling relations may not be appropriate for use in some areas or outside the magnitude/size ranges for which they have been derived. Regional scaling laws should be used, therefore, whenever available, particularly when inferences have to be drawn on regional seismic strain rates, and seismic hazard, the latter being mainly controlled by the frequency of occurrence and the potential of earthquakes to generate strong high-frequency motions.

3.3.2 Relationships between seismic energy, seismic moment and magnitudes (P. Bormann and D. Di Giacomo)

Gutenberg (1956) proposed the following relationship between seismic energy E_S (in units of Joule ; 1 J = 10^7 erg) and the so-called unified body-wave magnitude m, which he measured in a wide range of periods between about 2 and 20 s and later renamed mB:

$$\log E_S = 2.4\ m - 1.2. \tag{3.134}$$

Eq. (3.134) is based on a rather small data set (see Fig. 3.83). Gutenberg (1956) estimated the error in $\log E_S$ calculated via (3.134), which is in fact not a proper standard regression relation, to be *"probably less than one unit."* Together with mB = 2.5 + 0.63 Ms in Gutenberg and Richter (1956a), Eq. (3.134) yields

$$\log E_S = 1.5\ Ms + 4.8. \tag{3.135}$$

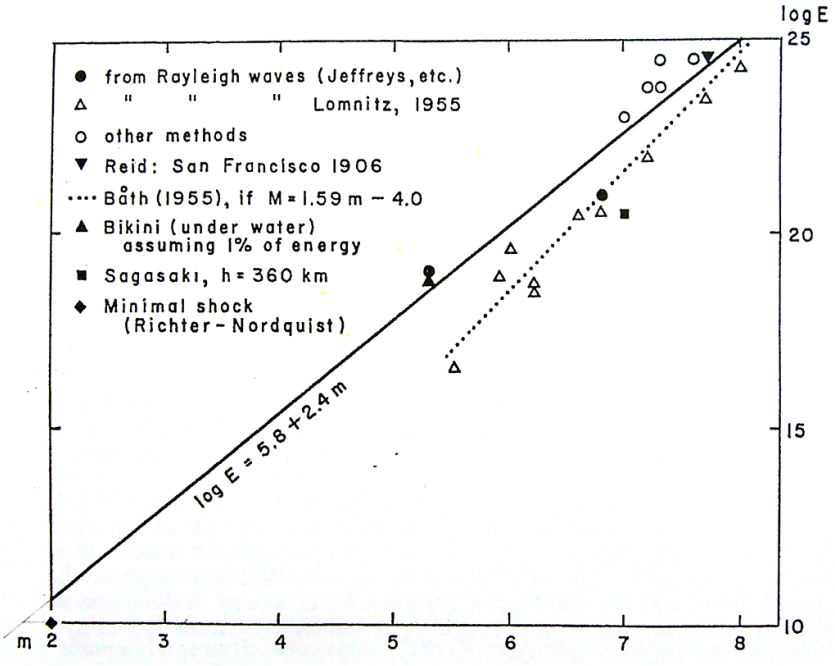

Fig. 3.83 Primary relation, between seismic energy E_S as a function of the "unified" magnitude m, as published first by Gutenberg (1956). m is an average weighted event mB.

Eq. (3.135) was first proposed by Richter (1958), however published with a printing error in the constant (4.4 instead of 4.8). Up to now it is the most widely applied relationship between seismic energy and magnitude and generally referred to as a Gutenberg-Richter relationship. One should be aware, however, that Gutenberg preferred and authorized with any of his own - or co-authored - publications only Eq. (3.134). In Gutenberg and Richter (1956b) he stated that *"Present studies are directed toward a scale based on the quotient (A/T) rather than on amplitudes. ...It is believed that magnitudes determined from body waves of teleseisms are more coherent with the original scale than those from surface waves, which have been in use as the general standard"*. The reason is that mB, determined by measuring A/T in a wide range of periods, is more directly related to ground motion velocity and thus to seismic energy released by earthquakes in a wider range of magnitude than Ms, which is measured around 20 s only. Kanamori (1977), however, when investigating the energy release in great earthquakes

and developing the concept of a non-saturating seismic moment magnitude Mw (see 3.2.5.3), considered only Eq. (3.135) because of the long corner periods of strong and great earthquakes.

Later, with more Ms(20) data of the NEIC in a wider magnitude range being available as well as direct E_S determinations from analyzing broadband velocity records (see IS 3.6) Choy and Boatwright (1995) found

$$\log E_S = 1.5\ Ms + 4.4. \qquad (3.136)$$

be a better approximation to the data, confirmed also by later compilations with many more data (Choy et al., 2006; see Fig. 3.84).

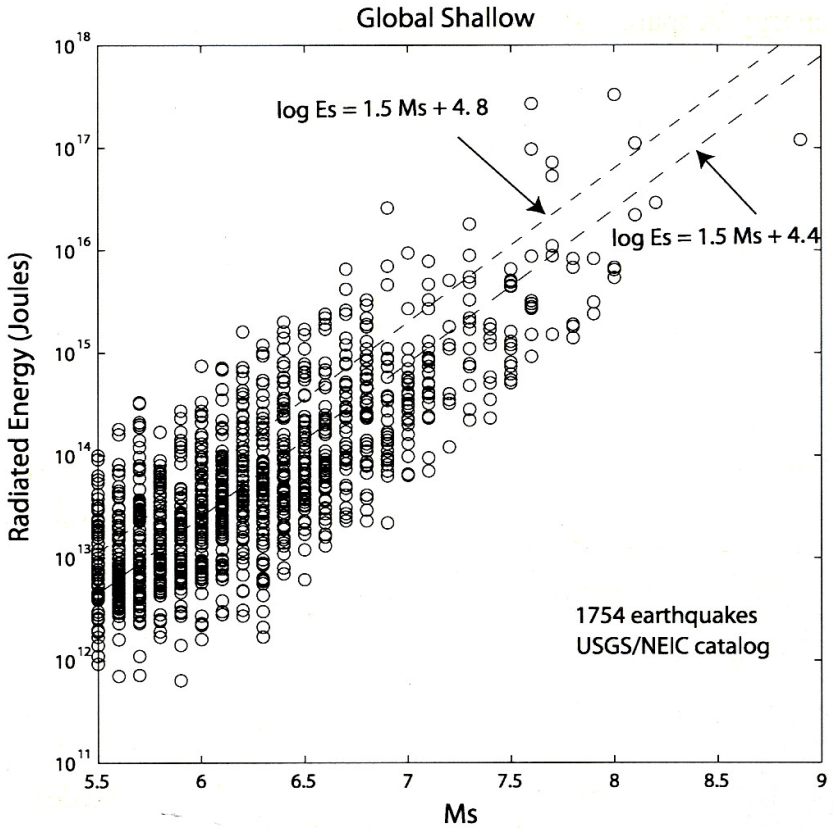

Fig. 3.84 Relationship between radiated energy E_S and Ms as calculated by the USGS. (Copy of Figure 1 by Choy et al. (2006) in Abercrombie R., McGarr, A., and Kanamori, H. (eds): Radiated energy and the physics of earthquake faulting, *AGU Geophys. Monogr. Ser.* **170**, p. 45; © American Geophysical Union).

However, Eq. (3.136) and the respective regression line in Fig. 3.84 did not result from an optimal least square fit through the data. Rather, in the interest of assuring widest possible continuity with Eq. (3.135) and the later definition of the Mw scale, on which decades of research results rest, these authors preferred to revise only the constant by looking for the best fitting 1.5-slope line through the E_S-Ms data cloud. Yet, when searching for best fitting orthogonal linear regressions through modern logE_S, mB(BB) and Ms(20) data, then rather different relationships were found [see Figs. 3.85 and 3.86 and relations (3.137) to (3.140)].

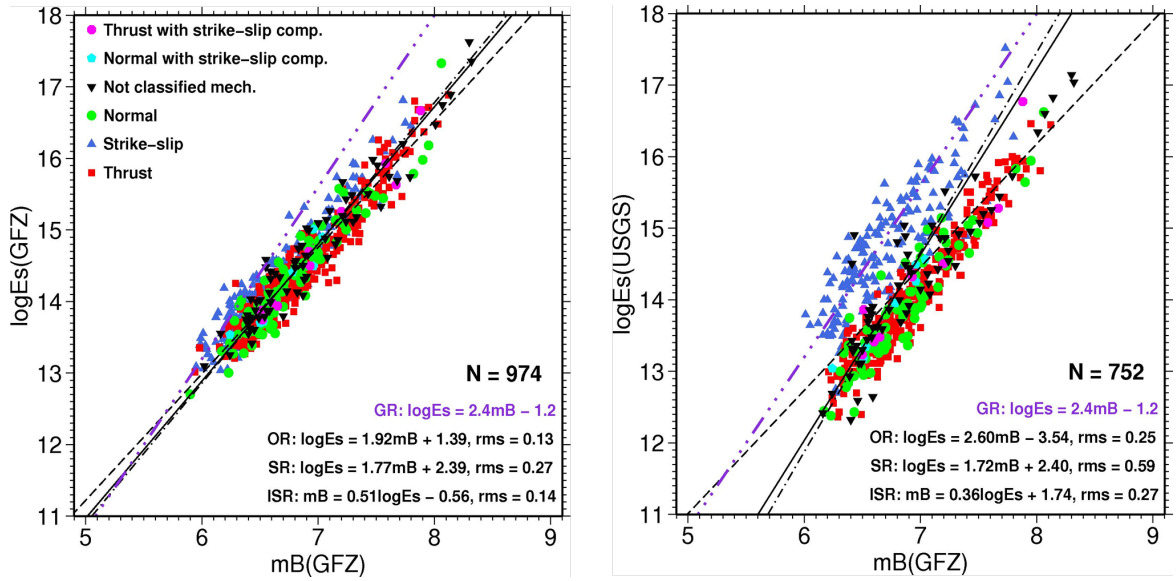

Fig. 3.85 Comparison of Gutenberg´s (1956) $logE_S$-mB relationship (blue hatched-3dot line) with standard (SR and ISR) and orthogonal (OR) regression relationships (black lines; hatched, hatch-dotted and full line, respectively) between $logE_S$ and automatically measured IASPEI standard mB_BB values according to the GFZ procedure described by Bormann and Saul (2008). The mB data were kindly provided by J. Saul in 2010. **Left:** $logE_S$(GFZ) is based on E_S determined by applying the automatic GFZ procedure for processing broadband velocity records as described by Di Giacomo et al. (2009 a and b); **Right:** $logE_S$(GS) is based on E_S values published by the US Geological Survey (USGS). They are determined interactively according to the procedure described by Choy and Boatwright (1995) as well as in IS 3.6. The colored data point symbols relate to different types of source mechanism, e.g., the blue upright triangles to strike-slip earthquakes. For formulas see lower right inserts.

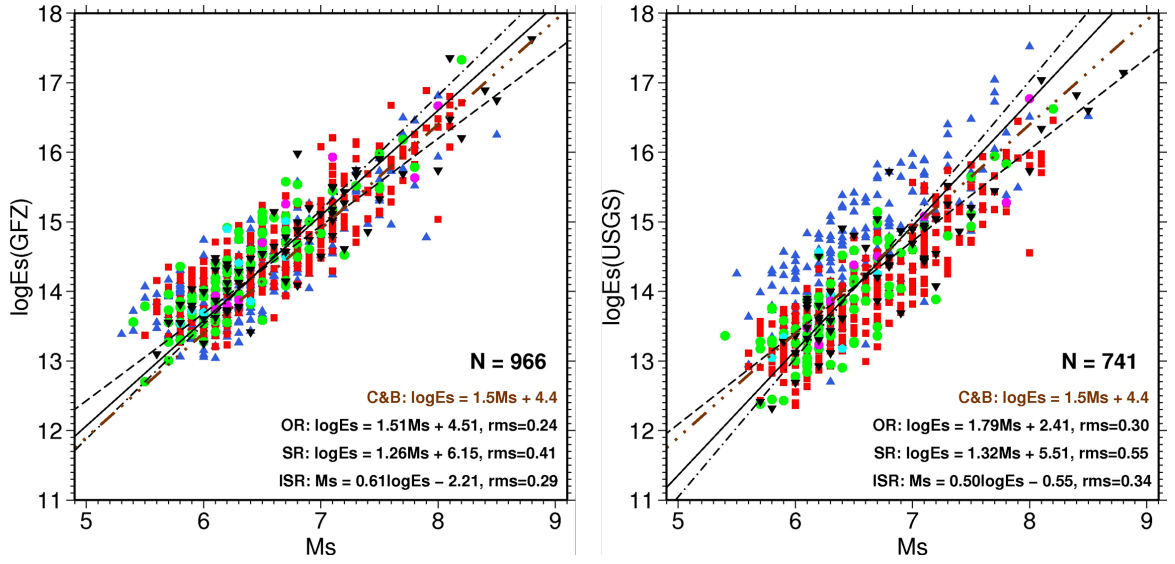

Fig. 3.86 Comparison of Choy and Boatwright's (1995) $logE_S$-Ms relationship (brown hatched-3dot line) with standard and orthogonal regression relationships (legend as in Fig. 3.87) between $logE_S$ values determined at the GFZ (left) and the US Geological Survey (USGS) (right), respectively, with USGS Ms_20 values. The Richter (1958) relationship logEs = 1.5 Ms + 4.8 would be parallel to the C&B line but 0.4 logEs units higher.

The following conclusions can be drawn from Figs. 3.85 and 3.86:

- $\log E_S$(GFZ) correlates much better than $\log E_S$(USGS) with both IASPEI standard mB(BB) and Ms(20). The reason is that the GFZ procedure, in contrast to that of the USGS, does not apply any source mechanism corrections, which are not common for all classical magnitude scales. Such corrections produce the large average off-set between the data points for strike-slip earthquakes and those related to other source mechanisms, which is interpreted in terms of exceptionally large apparent stress, respectively stress drop, in strike-slip environments.
- The slopes and constants of the standard OR regression relations through modern $\log E_S$ data differ significantly from the original Gutenberg and Richter (1956a) $\log E_S$-mB relationship in Eq. (3.135). Remarkably, however, the latter is a rather good average fit through the $\log E_S$(USGS) data for strike-slip earthquakes in Fig. 3.86 right. For other types of source mechanisms, however, it would overestimate $\log E_S$ on average by about 1 unit.
- The $\log E_S$(GFZ)-mB(GFZ) OR relationship has a very high correlation coefficient RXY and a small orthogonal rms (RMSO). It reads:

$$\log E_S(\text{GFZ}) = 1.92\ \text{mB(GFZ)} + 1.39 \quad \text{with RMSO} = 0.13. \tag{3.137}$$

  Values of $\log E_S$, calculated with (3.137) from mB, are at mB = 6.0 and 8.3 about -1.3 and -2.4 $\log E_S$ units smaller than those derived via the Gutenberg-Richter formula (3.135), which yields already constantly values that are 0.4 units larger than those derived by the Choy and Boatwright (1995) relation (3.136).
- The $\log E_S$(USGS)-mB(GFZ) OR relationship has a much larger RMSO:

$$\log E_S(\text{USGS}) = 2.60\ \text{mB(GFZ)} - 3.54 \quad \text{with RMSO} = 0.30. \tag{3.138}$$

- Values of $\log E_S$, calculated with (3.138) from mB, are at mB = 6.0 and 8.3 about -1.1 and -1.7 $\log E_S$ units smaller than those derived via the Gutenberg-Richter formula (3.135).
- The much larger and not random scatter of $\log E_S$(USGS) data explains the large slope offset between the orthogonal and SR1 standard regression relations (see Fig. 3.86 right). This offset is almost negligible for the $\log E_S$(GFZ)-mB relationship (see Fig. 3.86 left). For general discussion of the relationship between SR, ISR and OR see Bormann et al. (2007) and Castellaro and Bormann (2007).
- The large difference between the regression relationships based on apparently the same type of $\log E_S$ data highlights again the importance to specify with a unique nomenclature different procedures applied to calculate such data. Otherwise, procedural effects might be misinterpreted as being effects of real nature or the latter might be hidden due to procedural noise.
- The differences between the Richter (1958) $\log E_S$-Ms relationship and the regression relations between different versions of $\log E_S$ and Ms(20) are less pronounced yet still significant.
- The orthogonal regression between $\log E_S$(GFZ) and Ms(20) of the USGS confirms almost perfectly the Choy and Boatwright (1995) $\log E_S$-Ms relationship in Eq. (3.136). It reads:

$$\log E_S = 1.51\ \text{Ms} + 4.51 \quad \text{with RMSO} = 0.24 \tag{3.139}$$

  and yields in the whole considered magnitude range between Ms 5.2 and 8.8 values

of $\log E_S$ that are only between +0.16 and +0.20 units of $\log E_S$ larger than those calculated via the Choy and Boatwright (1995) formula (3.136). This is within the uncertainty range of energy calculations in general.

- In contrast, despite still reasonably good agreement between the orthogonal $\log E_S$(USGS)-Ms relationship

$$\log E_S = 1.79\ Ms + 2.41 \quad \text{with RMSO} = 0.30 \qquad (3.140)$$

and (3.136) for medium-size earthquakes, the differences for converting Ms into $\log E_S$ reach for Ms = 5.2 and 8.8 values of -0.42 and + 0.56 $\log E_S$ units, respectively, which is unacceptably large. Thus, the orthogonal regression between $\log E_S$(GFZ) and Ms(USGS) constrains the Choy and Boatwright (1995) formula (3.136) much better than the orthogonal regression between $\log E_S$(USGS) and Ms(USGS) or the conditional regression applied by these authors to their data (see Fig. 3.84 and related comments).

- When substituting in the relationships (3.139) and (3.140) Ms by Me, as done by Choy and Boatwright (1995) when deriving the currently applied Me standard formula (3.72) Me = (log E_S – 4.4)/1.5, then relationship (3.139) would yield

$$\text{Me} = (\log E_S - 4.51)/1.51 \qquad (3.141)$$

and (3.140)

$$\text{Me} = (\log E_S - 2.41)/1.79. \qquad (3.142)$$

- When calculating for $\log E_S$ values of 12 and 18, corresponding to Me values of approximately 5 and 9, via relationship (3.141) Me then the values are in this $\log E_S$ range only between 0.11 m.u. and 0.14 m.u. smaller then values calculated with the current Me formula (3.72). In contrast, relationship (3.142) yields values that differ in this range between +0.40 m.u. and -0.36 m.u.

- Moreover, the RMSO scatter of $\log E_S$(GFZ) over both USGS Ms(20) and mB(GFZ) is significantly smaller than that of $\log E_S$(USGS).This questions, within the unavoidable range of data scatter, the suitability of applying mechanism dependent corrections in the USGS procedure to the calculated E_S values, or at least the size of such corrections applied to strike-slip earthquakes and to more high-frequency data for smaller earthquakes in general.

The latter point has repeatedly been discussed, e.g., by Newman and Okal (1998), Pérez-Campos and Okal (2001), and Bormann and Di Giacomo (2011). Also Okal and Talandier (1989) pointed out that a *"..magnitude concept, which ignores the exact focal geometry, could be a more robust measure of the true size of the event than one correcting for an expected small source excitation, but failing to account for non-geometrical effects"* such as scattering or multi-pathing of energy in inhomogeneous media. Moreover, calculated average point-source fault-plane solutions are afflicted with unavoidable uncertainties in the order of several degrees (up to about 10°) . Also, the orientation and radiation pattern of sub-segments of rough non-planar faults and rupture irregularities may significantly differ from those calculated for planar point source fault-plane solutions. Such non-accountable details in real Earth and earthquake ruptures, however, effect especially higher frequencies that largely contribute to the E_S estimates, the more the smaller the earthquakes and the radiated wavelength are. This may also explain why Schweitzer and Kværna (1999) could not prove any significant influence of source radiation patterns on globally observed short-period mb estimates.

Finally, we again make the point that it is rather arbitrary to scale the energy magnitude Me, based on E_S estimates resulting from the integration of squared velocity broadband P-wave records in a wide range of periods between about 1 and 100 s, to narrow-band long-period surface-wave magnitude Ms_20. This was surely not the intention of Gutenberg (1956) when he proposed (3.134) based on body-wave magnitude measurements in a wide range of period. This inappropriate scaling can only be understood by the fact that during the decades of WWSSN dominated seismology no more medium-period broadband records were available in the "Western World" and measuring "old-fashioned" broadband mB was just out of debate. Yet, with mB_BB, based on velocity-broadband P-wave records, being now again a IASPEI recommended body-wave magnitude standard that "saturates" much later than short-period mb, it is strongly recommended to reconsider the scaling of Me to mB_BB instead to long-period Ms_20. Also Abe (1982) came to the conclusion that the size of earthquakes, both deep and shallow, is consistently quantified by the amount of seismic energy expressed by the broadband body-wave magnitude mB.

When following the practice of Kanamori (1977) and Choy and Boatwright (1995) of substituting Ms by Mw, respectively Me, when deriving (3.68) and (3.72), then the respective logE_S-mB relationships (3.138) and (3.139) would yield the following alternative Me relationships:

$$Me = (\log E_S - 1.39)/1.92 \qquad (3.143)$$

and

$$Me = (\log E_S + 3.54)/2.60. \qquad (3.144)$$

Considering the same range of log E_S between 12 and 18 as above, then, when compared with Me values calculated by the current Me formula (3.72), (3.143) would yield values that differ between +0.46 m.u. und -0.42 m.u., and (3.144) values that differ even more, namely up to +0.91m.u. and -0.79 m.u., respectively. At values around 7.6, however, the current Ms-scaled and new mB-scaled Me values would agree well. This makes sense, because according to the scaling law in Fig. 3.5, right panel, the average seismic source velocity spectra have their maximum velocity amplitudes at this magnitude on average around 20 s periods.

The general conclusion to be drawn from such a reasonable rescaling of the broadband body-wave Me to broadband mB is, however, that the current Ms-scaled Me formula may significantly underestimate Me at magnitudes less than 7.6 and overestimate Me for stronger earthquakes. Yet, such a physically logical and even demanding rescaling of Me would question many of the conclusions derived since the 1990s from log E_S and Me data calculated on the basis of their current scaling to Ms.

We will now refer to some earlier results and considerations on other logE_S-magnitude relationships. From theoretical considerations Randall (1973) derived a relationship between E_S and the local magnitude Ml which was later confirmed empirically by Seidl and Berckhemer (1982) as well as by Berckhemer and Lindenfeld (1986). On the basis of direct energy calculations for earthquakes from the Friuli region, Italy, using digital broadband records of the Gräfenberg array in Germany, the latter obtained:

$$\log E_S \sim 2.0\ Ml. \qquad (3.145)$$

This is close to the empirical findings by Gutenberg and Richter (1956a) (log E_S ~ 1.92 Ml) for southern California and the more recent one by Kanamori et al. (1993). The latter found

$$\log E_S = 1.96\ Ml + 2.05 \qquad (3.146)$$

in the magnitude range $1.5 < Ml < 6.0$. For $Ml > 6.5$ Ml saturates.

For short-period body-wave magnitudes mb, Sadovsky et al. (1986) derived the relationship

$$\log E_S = 1.7\ mb + 2.3 \qquad (3.147)$$

that is applicable for both earthquakes and underground explosions. **Note:** According to the slopes in the above equations one unit of magnitude increase in Ms, mb, Ml or mB, respectively, corresponds to an increase of E_S by a factor of about 32, 50, 100 and 250 times, respectively!

In this context one should mention that in the countries of the former USSR the energy scale after Rautian (1960), $K = \log E_S$ (with E_S in J), is widely used and given in the catalogs. It is based on the same elements as any other magnitude scale such as an empirical calibration function and a reference distance (here 10 km). K relates on average to magnitude M approximately via

$$K = 1.8\ M + 4. \qquad (3.148)$$

Riznichenko (1992) summarized data and relationships published by many authors (see Fig. 3.87) between magnitude M and K on the one hand and $\log M_0$ on the other hand. Depending on the range of distance and size, M stands here for Ml, mb, mB or Ms. For more details on $K = \log E_S$ and other types of magnitude see section 3.2.4.6 and IS 3.7.

3.3.3 Relationship between M_0, E_S and magnitude
(P. Bormann and D. DiGiacomo)

Kanamori (1983) published linear relationships between $\log E_S$ and $\log M_0$ for both shallow and intermediate to deep events (see Fig. 3.88). These two relationships are rather similar and correspond, on average, to a ratio of moment scaled energy of $E_S/M_0 = 5 \times 10^{-5}$, or, according to Okal and Talandier (1989), to a so-called "slowness parameter" $\Theta = \log (E_S/M_0)$ of -4.3. Kanamori (1977) assumed this value to be representative for global earthquake sets and used it for developing the moment magnitude scale Mw. However, as previously mentioned in the sub-sections 3.2.7.1 and 3.2.7.2 on moment and energy magnitudes, scaling laws based on a constant ratio E_S/M_0 must be used with great caution. Later investigations revealed sometimes significant deviations from the Kanamori ratio of E_S/M_0 (e.g., Kikuchi and Fukao, 1988; Choy and Boatwright, 1995; Bormann and Di Giacomo, 2011). Variations in E_S/M_0, respectively Θ, are mainly due to local and regional differences in source mechanism, related stress drop, rupture velocity and time history of the rupture process.

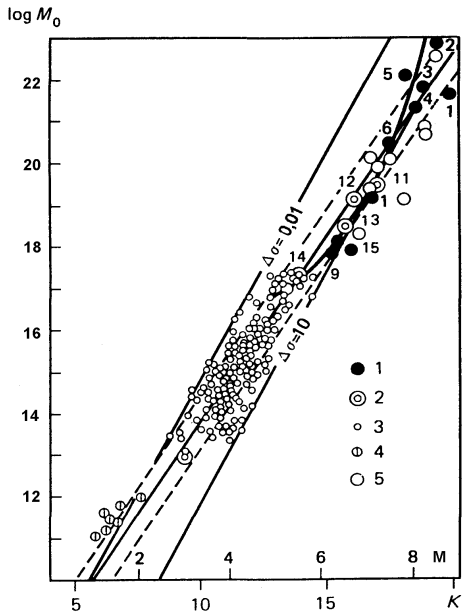

Fig. 3.87 Correlation between seismic moment M_0 (in Nm = J), magnitude M and Rautian´s (1960) energetic class K according to a compilation of data from many authors. Related stress drop $\Delta\sigma$ has been given in MPa (full straight lines). Broken lines mark the 68% confidence interval. 1 - large global earthquakes; 2 - average values for individual regions; 3 - earthquakes in the western USA; 4 - micro-earthquakes in Nevada; 5 - M_0 determinations from field data; 6 to 15 - individual values from different regions (modified from Riznichenko, 1992, Fig. 1; with permission from Springer-Verlag).

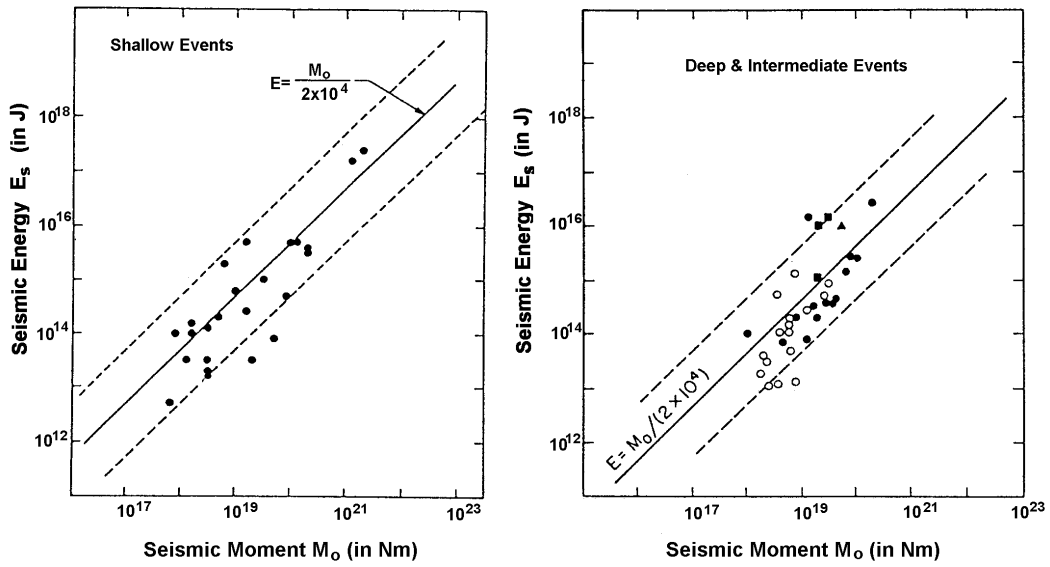

Fig. 3.88 Relations between seismic moment M_0 and energy E_S for shallow events (left) and intermediate to deep events (right) according to Vassiliou and Kanamori (1982). The solid line indicates the relation $E_S = M_0 /(2\times10^4)$, which had been suggested by Kanamori (1977) on the basis of elastostatic considerations (modified from Kanamori, 1983 in Tectonophysics, Vol. 93, p. 191 and 192, with permission from Elsevier Science).

Fig. 3.89 depicts the Θ values for a large global event data set, plotted over Mw and calculated as the difference between $\log E_S$(USGS=GS) (upper panel), respectively $\log E_S$(GFZ) (lower panel), and $\log M_0$(GCMT). Note the difference in data scatter and in

average Θ values: Θ(Kanamori, 1977) = -4.3, Θ(GFZ) = -4.6, and Θ(USGS) = -4.8. For individual earthquakes, Θ may vary between about -3.0 > Θ > 7.0 (see also Weinstein and Okal, 2005, and Lomax and Michelini, 2009a). The latter authors identified values below -5.7 to be a reliable indicator for very slow tsunami earthquakes.

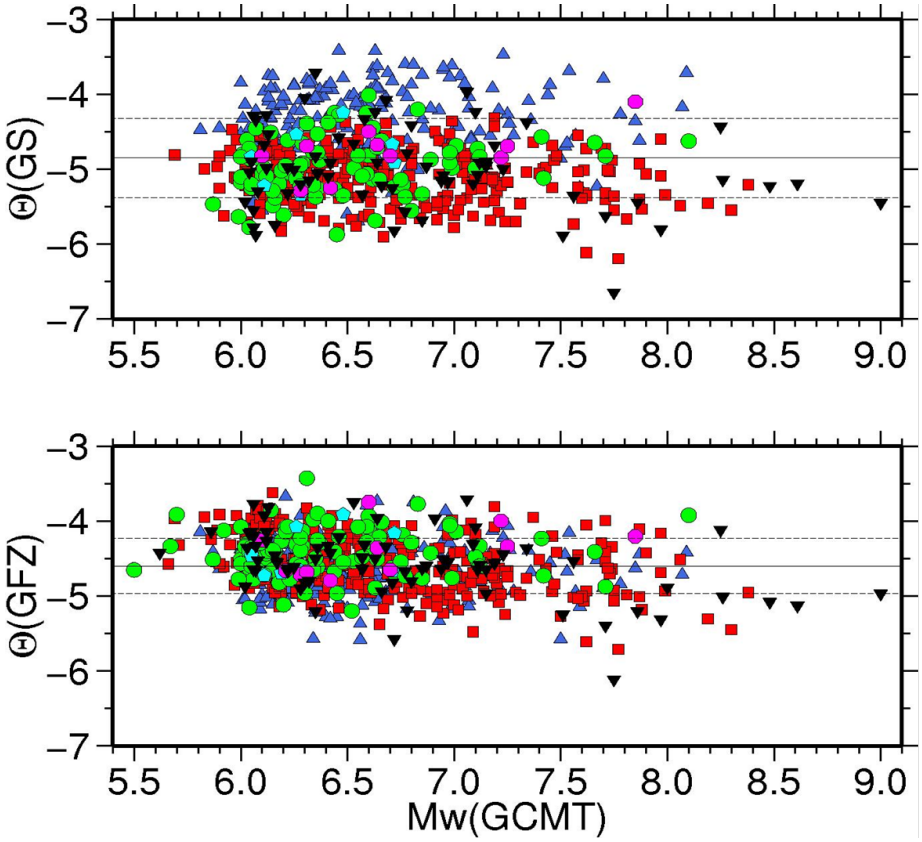

Fig. 3.89 Comparison between the Θ = log(E_S/M_0) values calculated as the difference between logE_S(USGS=GS) (upper panel), respectively logE_S(GFZ) (lower panel), and Mw(GCMT) in the magnitude range between 5.5 and 9.0. There is a tendency of decreasing Θ with the magnitude of strong and great, mainly subduction zone earthquakes. The different color symbol relate to different types of source mechanism, e.g., upright blue triangles to strike-slip (SS) earthquakes. Note again, as in Figs. 3.85 and 3.86, the much larger data scatter of the USGS data set with its distinct separation of SS earthquakes, which have been corrected for theoretically expected reduced radiation coefficients according to Boatwright and Choy (1986).

Mw has been defined via the logE_S-Ms relationship. Following the discussions in Bormann and Di Giacomo (2011), the definition formula for Mw can be decomposed as follows:

$$Mw = (\log M_0 - \mathbf{A}_{\text{const. in the log}E_S\text{-Ms relation}} + \mathrm{B}_{\text{average }\Theta}) / \mathbf{C}_{\text{slope of the log}E_S\text{-Ms relation.}} \quad (3.149)$$

Since Kanamori (1977) and Hanks and Kanamori (1979) based their Mw formula on the Richter (1958) logEs-Ms relations with a constant of 4.8 and slope 1.5, and on an assumed average Θ = -4.3, they got the Mw relation, which reads in its standard form of writing

$$Mw = (\log M_0 - 4.8 - 4.3)/1{,}5 = (\log M_0 - 9.1)/1.5. \quad (3.150)$$

Yet, modern direct $\log E_S$ determinations and their **orthogonal** regression with the respective event Ms(USGS) = Ms_20 data (see Fig. 3.87) as well as the average values of Θ derived from Fig. 3.89, could not, or only partially, reproduce the constants A to C on which the current Mw formula is based. For $\log E_S$(GFZ) we got according to formula (3.139) and Fig. 3.89 for A = 4.51, for B = -4.6 and for C = 1.51. When inserting these constants into the relationship (3.149) we get on the basis of $\log E_S$(GFZ) data the new Mw formula

$$Mw = (\log M_0 - 9.11)/1.51. \qquad (3.151)$$

This is very similar with the current standard formula, yielding Mw values that differ for $\log M_0$ between about 17 and 23 (i.e., Mw ≈ 5.3 to 9.3) only within -0.04 and -0.07 m.u.

In contrast, the constants based on the orthogonally regressed $\log E_S$(USGS) data according to (3.140) and on the Θ values in Fig. 3.89 are A = 2.41, B = -4.8, and C = 1.79, yielding

$$Mw = (\log M_0 - 7.21)/1.79. \qquad (3.152)$$

Mw values calculated via (3.152) with $\log M_0$ (respectively Mw) values as above would differ from those derived with the current Mw standard formula between +0.2 und -0.45 m.u. Thus, the correctness of the current Mw formula is essentially confirmed by statistically correct treated GFZ E_S data, not, however, the respective USGS E_S data. Interestingly, however, the more heuristically derived relationship $\log E_S = 1.5\ Ms + 4.4$ by Choy and Boatwright (1995) would lead with an average $\Theta_{USGS} = -4.8$ from Fig. 3.89, upper diagram, to

$$Mw = (\log M_0 - 9.2)/1.5. \qquad (3.153)$$

This is very close to (3.150) and yields Mw values that are constantly smaller than those derived with the standard formula by only 0.07 m.u., i.e., it matches with the latter almost as good as the Mw formula (3.151) based on regressing $\log E_S$(GFZ) over Ms(USGS). Thus, we can state, that the current Mw standard formula is well supported also by modern $\log E_S$ data, better than the currently used Me formula (see the discussion above following the Figs. 3.86 and 3.87.

One should be aware, however, that the large scatter of Θ makes global relationships between $\log E_S$ and $\log M_0$ often unsuitable for drawing inferences on regional differences in tectonic deformation, stress accumulation and release rates. Furthermore, scaling laws for source parameters derived from low-frequency data, such as Mw or M_0, may - with the exception for assessing the tsunami hazard - not be suitable for a realistic assessment of the risk of shaking damage. The latter is mainly caused by frequencies above 0.3 Hz, which are, therefore, of greatest interest for earthquake engineers.

Global relations for calculating M_0 via Ms were published by Ekström and Dziewonski (1988). They plotted more than 2.300 global NEIC PDE Ms values over Harvard CMT $\log M_0$ values and calculated for three ranges of $\log M_0$ the regression relations for Ms vs. $\log M_0$. They read, with M_0 in Nm (**1 Nm = 1 J = 10^7 dyn cm = 10^7 ergs**) also in all other relations below):

$Ms = \log M_0 - 12.24$ for $M_0 < 3.2\times10^{24}$

$Ms = -12.24 + \log M_0 - 0.088(\log M_0 - 17.5)^2$ for $3.2\times10^{24} \le M_0 \le 2.5\times10^{26}$

$Ms = 0.667 \log M_0 - 6.06$ for $M_0 \geq 2.5 \times 10^{26}$

However, Ekström and Dziewonski (1988) resolved these SR1 relations for $\log M_0$, which read with M_0 in Nm

$\log M_0 = Ms + 12.24$ for $Ms < 5.3$, (3.148a)

$\log M_0 = 23.20 - (92.45 - 11.40\ Ms)^{1/2}$ for $5.3 \leq Ms \leq 6.8$, (3.148b)

$\log M_0 = 1.5\ Ms + 9.14$ for $Ms > 6.8$. (3.148c)

These inverse relations, however, are strictly speaking, not fully correct since the data scatter is significant. Therefore, Ambrasey (1990a) did not recommend their application for moment prediction from Ms values. Solving (3.148a-c) for M_0 may systematically overestimate moments for larger events and underestimate M_0 for small events. However, Purcaru and Berckhemer (1978 and 1982) derived already earlier for constant strain drop practically the same relationship as in (3.148c), namely $\log M_0 = 16.1 + 1.5Ms = 16.1 + 1.5\ M_E$, with M_E = strain energy magnitude. According to their data plot of $\log M_0$ over Ms and M_E, respectively, M_0 varies for fixed values of Ms or M_E within a factor of 6.

Chen and Chen (1989) published detailed global relations of M_0 with Ms, mb and Ml in different ranges of magnitudes, respectively seismic moment. These relationships are based on data from about 800 earthquakes in the magnitude range $0 < M < 8.6$. These authors also showed that their empirical data are well fit by theoretical scaling relations derived from a modified Haskell model of a rectangular fault which produces displacement spectra with three corner frequencies. Similar global scaling relations had been derived earlier by Geller (1976), also based on the Haskell (1964 and 1966) ω^{-3} model. In both papers these relations show saturation, in our opinion too early, for Ml at about 6.3, for mb between about 6.0 and 6.5, and for Ms between about 8.2 and 8.5 (see introductory discussion in section 3.3.1).

Chen and Chen (1989) derived the following $\log M_0$-Ms relationships with a standard deviation of individual values $\log M_0$ of about ± 0.4:

$\log M_0 = 1.0\ Ms + 12.2$ for $Ms \leq 6.4$, (3.149a)

$\log M_0 = 1.5\ Ms + 9.0$ for $6.4 < Ms \leq 7.8$, (3.149b)

$\log M_0 = 3.0\ Ms - 2.7$ for $7.8 < Ms \leq 8.5$, and (3.149c)

with $Ms = 8.5 = \text{const.}$ for $\log M_0 > 22.8$ Nm. (3.149d)

However, Ms-M_0 relations (and vice versa) vary regionally. According to Ambraseys (1990) the global relations (3.148a-c) systematically underestimate Ms for events in the Alpine region of Europe and adjacent areas by 0.2 magnitude units on average. And Abercrombie (1994) discussed possible reasons for the anomalous high surface-wave magnitudes of continental earthquakes relative to their seismic moment. This illustrates the need for regional scaling of moment-magnitude relationships even in the relatively long-period range.

For M_0 and body-wave magnitudes mb (when measured at 1s period) Chen and Chen (1989) give the following global scaling relations (with saturation at mb = 6.5 for $\log M_0 > 20.7$).

Note, however, that this applies only to old mb data with amplitude measurement within the first few seconds. IASPEI (2005, 2011 and 2013) standard mb saturates in fact only around near 7.5 (see Fig. 3.51 and IS 3.3):

$$\log M_0 = 1.5\ mb + 9.0 \qquad \text{for} \qquad 3.8 < mb \leq 5.2, \qquad (3.150a)$$

$$\log M_0 = 3\ mb + 1.2 \qquad \text{for} \qquad 5.2 < mb \leq 6.5, \qquad (3.150b)$$

For the M_0-Ml relationship for California the same authors assume saturation at Ml = 6.3 at $\log M_0 > 20.1$ and they approximate the in fact non-linear relationship by three linear relationships in limited magnitude ranges:

$$\log M_0 = Ml + 10.5 \qquad \text{for} \qquad Ml \leq 3.6, \qquad (3.151a)$$

$$\log M_0 = 1.5\ Ml + 8.7 \qquad \text{for} \qquad 3.6 < Ml \leq 5.0, \qquad (3.151b)$$

$$\log M_0 = 3\ Ml + 1.2 \qquad \text{for} \qquad 5.0 < Ml \leq 6.3. \qquad (3.151c)$$

Average scaling relations among mb, Ms and M_0 for plate-margin earthquakes have been derived by Nuttli (1985). They yield practically identical values as the equations (3.149a-c) for M_0 when Ms is known while the deviations are not larger than about a factor of 2 when using mb and Eqs. (3.150a and b)) instead.

The need for regional relationships between M_0 and magnitudes is particularly evident for Ml. When calculating M_0 according to Eqs. (3.150b) and (3.151c) for California and comparing them with the values calculated for a relationship given by Kim et al. (1989) for the Baltic Shield

$$\log M_0 = 1.01\ Ml + 9.93 \qquad \text{for} \qquad 2.0 \leq Ml \leq 5.2 \qquad (3.152)$$

we get for Ml = 2.0, 4.0 and 5.0, respectively, values for M_0 which are 3.5, 5.4 and 16.6 times larger for California than for the Baltic Shield. Using instead an even more local relationship for travel paths within the Great Basin of California (Chávez and Priestley, 1985), namely

$$\log M_0 = 1.2\ Ml + 10.49 \qquad \text{for} \qquad 1 \leq Ml \leq 6 \qquad (3.153)$$

we get for the same magnitudes even 9, 21 and 32 times larger values for M_0 than for the Baltic Shield according to Eq. (3.152).

Other M_0-Ml relationships are:

for Southern California (Thatcher & Hanks, 1973):

$$\log M_0 = 1.5\ Ml + 9.05 \qquad \text{in the range } 3 \leq Ml \leq 7, \qquad (3.154)$$

for Ml from strong-motion records in Greece (Margris & Papazachos):

$$\log M_0 = 1.5\ Ml + 9.07 \qquad \text{in the range } 3.9 \leq Ml \leq 6.6, \qquad (3.155)$$

for Israel (Shapira & Hofstetter, 1993):

$$\log M_0 = 1.3\ Ml + 10.0 \qquad \text{in the range } 2.2 \leq Ml \leq 5.3, \tag{3.156}$$

for Northwestern Turkey (Parolai et al., 2007):

$$\log M_0 = 1{,}17\ Ml + 10.12 \qquad \text{in the range } 0.5 < Ml < 6, \tag{3.157}$$

for the Italian earthquake catalog (Castello et al., 2007):

$$\log M_0 = 1.18\ Ml + 10.92 \qquad \text{in the range } 3.5 \leq Ml \leq 5.8, \tag{3.158}$$

and for Northwestern Italy (Bindi et al., 2005):

$$\log M_0 = 0.95\ Ml + 10.36 \qquad \text{in the range } 0 < Ml < 4.5. \tag{3.159}$$

When comparing these various $\log M_0$-Ml relationships we realize that the slope for data in the range $0 < Ml < 7$ tends to increase with Ml from about 1 to 1.5. Accordingly, the slope for the respective Mw-Ml relationship varies in this range from about 2/3 to 1 (see Tab. 3.6). The very step slope in (3.151c), however, is mainly due to the assumption in the related scaling law calculations of a too early saturation of Ml at 6.3 already.

The slope change, which is in fact a gradual one, is mainly related to the magnitude and stress-drop dependent variability of the seismic source spectra and their corner frequencies in the range of magnitudes considered with respect to the passband of the Wood-Anderson seismometer, whereas the different constants are mainly controlled by regional differences in the attenuation laws (see, e.g., the difference in Tab. 3.6 between the slop 1 Mw-Ml relationships (or slope 1.5 $\log M_0$-Ml relationships) by Ristau et al. (2005) for crustal and slab earthquakes, respectively, with $Ml \geq 3.6$ but < 6 in Western Canada). Therefore, in order to avoid physically or regionally wrong conclusions to be drawn from slope differences of various $\log M_0$ (or Mw)-Ml relationships it is absolutely necessary to take the magnitude-range of their applicability into account.

While there are plenty relationships for converting Ml, mb(old) and Ms(20) data into $\log M_0$ (or Mw), relationships between $\log M_0$ (respectively Mw) and mB are very rare. Exceptions are the data plots by Abe (1982) of $\log M_0$ over classical mB for both shallow and deep earthquakes (see Fig. 3.90).

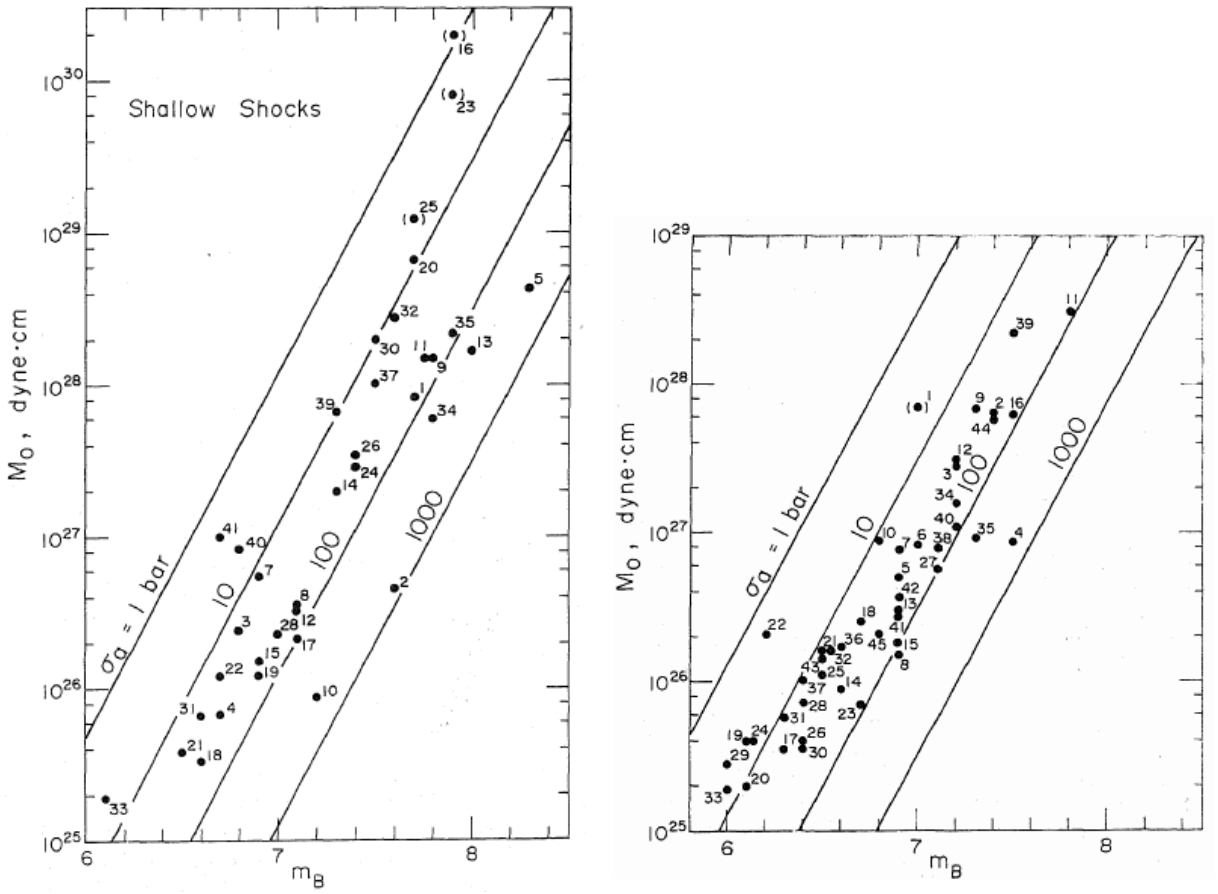

Fig. 3.90 log M_0 (in units of dyne cm = 10^{-7} N m) versus mB for shallow (left diagram) and for intermediate-depth to deep earthquakes (right diagram) according to Figures 1 and 3 of Abe (1982). The apparent stress $\sigma_a = \mu(E_S/M_0)$ is given in units of bar = 0.1 MPa. Note that for calculating M_0 and C for intermediate-depth to deep earthquakes a three times higher rigidity (shear modulus) μ of the source medium ($\mu = 9 \times 10^{11}$ dyn/cm^2) than for shallow earthquakes has been assumed by Abe.

The lines in Fig. 3.90 have been calculated for increment values of σ_a with the relationship

$$\log M_0 = 2.4\ mB - 1.2 - \log(\sigma_a/\mu), \text{ with } M_0 \text{ in N m.} \qquad (3.160)$$

This relation results from inserting into the Gutenberg-Richter logE_S-mB relationship (3.134) $E_S = M_0 \times (\sigma_a/\mu)$ and resolving it for logM_0. A line for $\sigma_a \approx 40$ bar = 4 MPa, and thus for a stress drop $\Delta\sigma \approx 8$ MPa, would be a reasonably good average fit of the data in Fig. 3.90 and correspond for shallow earthquakes with $\mu = 3 \times 10^{11}$ dyn/cm^2 = 3×10^4 N m to a relationship

$$\log M_0 = 2.4\ mB + 2.68 \qquad (3.161)$$

However, when calculating for shallow earthquakes the linear OSR standard regression through some 974 data pair of GCMT logM_0 vs. mB(GFZ) = mB_BB, with the latter measured according to the procedure described by Bormann and Saul (2008), one gets

$$\log M_0 = 1.90\ mB\_BB + 6.09, \qquad (3.162)$$

and when fitting the same data with a non-linear regression relationship

$$\log M_0 = e^{(-1{,}103 + 0.375\ mB\_BB)} + 14.659. \qquad (3.163)$$

All three relationships have been plotted together with the GCMT-GFZ data in Fig. 3.91. One realizes that within the range of the definition by data

- Eq. (3.163) approximates best the relationship between IASPEI standard mB_BB and GCMT log M_0;
- all three relationships yield identical average log M_0 proxy estimates at mB = 6.7;
- other logM_0 proxy estimates via mB differ not more than about 0.5 units from directly measured logM_0.

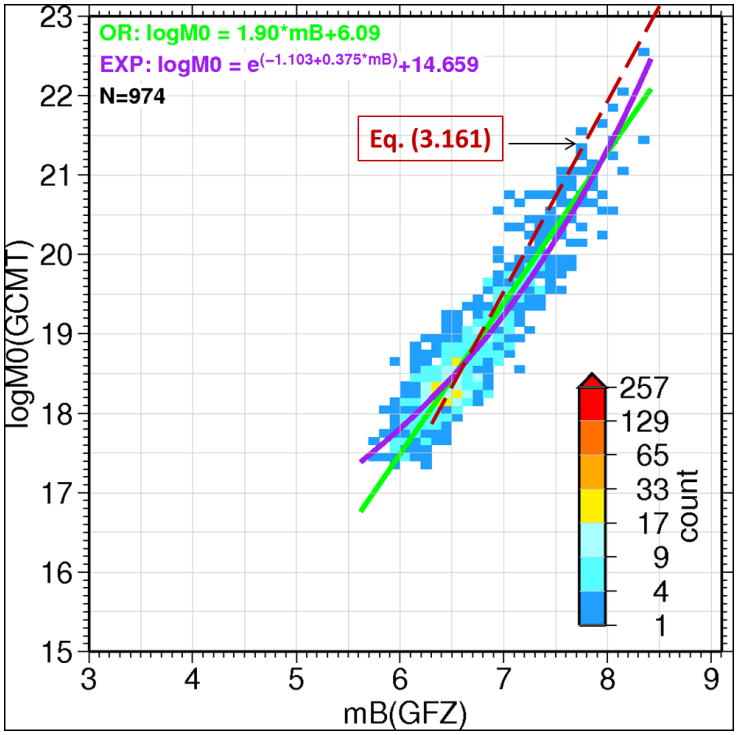

Fig. 3.91 mB (GFZ) - logM_0 (GCMT) regression models: The exponential model [(Eq. (3.163)] is drawn in purple, the linear OSR model [(Eq. (3.162)] in green and Eq. (3.161), derived by us on the basis of early log M_0 and classical mB data by Abe (1982), as red broken line. The data distribution is shown as color-coded count cells, 0.1 × 0.1 units wide.

Finally, we present in Figs. 3.92 a and b the most recent non-linear regression relationships based on 30,709 logM_0-mb as well as 17,472 logM_0-Ms data of the ISC-GEM Global Instrumental Earthquake Catalog (1900 – 2009). According to Di Giacomo et al. (2013) the respective OSR relationships are

$$\log M_0 = 1.95\ mb + 7.03, \qquad (3.164)$$

$$\log M_0 = 1.00\ Ms + 12.30 \quad \text{for } Ms < 6.47, \qquad (3.165)$$

and

$$\log M_0 = 1.66\ Ms + 7.97 \quad \text{for } Ms > 6.47, \qquad (3.166)$$

and the corresponding exponential relationships read

$$\log M_0 = e^{(-4{,}261 + 0.859\ mb)} + 15.922, \tag{3.167}$$

and

$$\log M_0 = e^{(0{,}213 + 0.230\ Ms)} + 13.28. \tag{3.168}$$

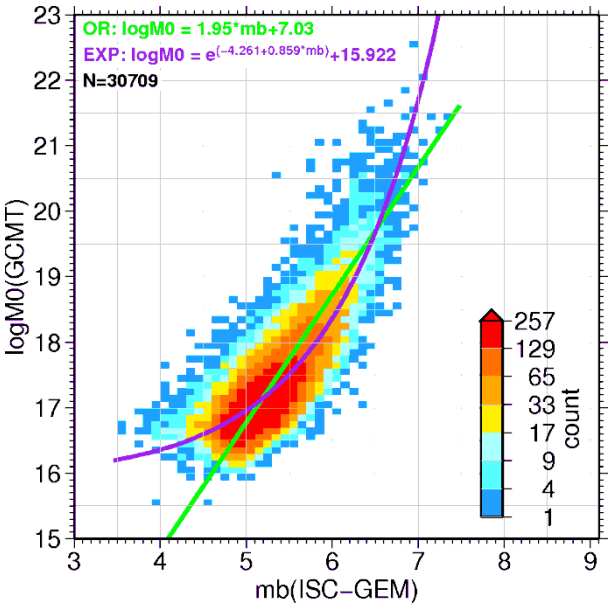

Fig. 3.92a mb (ISC - GEM) – log M_0 (GCMT) regression models: The exponential model is drawn in purple and the linear OSR model in green. The data distribution is shown as color-coded count cells 0.1 × 0.1 wide.

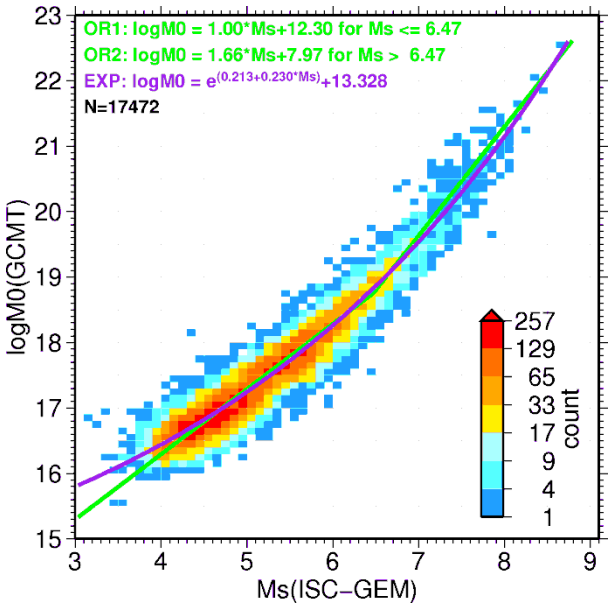

Fig. 3.92b Ms (ISC - GEM) – log M_0 (GCMT) regression models: the exponential model is drawn in purple and the bi-linear OSR model in green. The data distribution is shown as color-coded count cells 0.1 × 0.1 wide.

The OSR relationships between log M_0 and Ms, based on the newest and most homogeneous ISC-GEM Global Instrumental Earthquake Catalogue data set (1900 – 2009) almost perfectly confirms the respective relationships published earlier by Chen and Chen (1989) for Ms < 6.4 [see Eqs. (3.149a)] and of Ekström and Dziewonski (1988) for Ms < 5.3 [Eq. (3.148a)]. The slope of 1.66 in (3.166), however, is larger than the slope of 1.5 in both the Ekström and Dziewonski relationship (3.148c) for Ms > 6.8 and in the Chen and Chen relationship (3.149b) for 6.4 ≤ Ms < 7.8. Remember that Kanamori (1977), in his effort to estimate the seismic energy released by strong earthquakes and to develop a non-saturating magnitude scale, calibrated M_0 to Ms via the Richter (1958) logE_S-Ms relationship, knowing about the close relationship between log M_0 and Ms in the range 6.5 < Ms < 8 and assuming a constant average E_S/M_0 ratio (see section 3.2.7.1). Having now plenty of direct M_0 measurements available one could scale them directly to Ms without the detour over an assumed average E_S/M_0 ratio. This was done by Choy and Boatwright (1995) when developing the energy magnitude scale Me by relating directly measured E_S to Ms (see section 3.2.7.2). Accordingly, by substituting in (3.166) Ms by Mw and resolving it for Mw one gets

$$Mw = (\log M_0 - 7.97)/1.66. \tag{3.169}$$

When compared with the Kanamori (1977) based IASPEI standard Mw scale formula (3.68), Mw = (log Mo – 9.1)/1.5, (3.169) would yield for $\log M_0 = 16$ Mw = 4.84 and for $\log M_0 = 23$ Mw = 9.05, instead of Mw = 4.60 and 9.27, respectively, when using (3.68). Thus the difference between Mw values calculated with the established and the new formula would be within this range of log M_0, approximately corresponding to $4.5 < Mw < 9.3$, generally less than 0.25 m.u. This is still a reasonably good agreement but none the less worth considering a change to an Mw scale that is directly scaled to Ms and not via a log E_S-Ms relationship and an assumed constant E_S/M_0 ratio. What is more bothering, however, is the fact that the current Mw scaling to Ms for magnitudes larger than about 6.5 with the slope of 1.5 is nowadays even applied down to Mw = -4.4 (Kwiatek et al., 2010).

3.3.4 Scaling relations of magnitudes, M_0 and E_S with fault parameters (P. Bormann)

Scaling relations of magnitude, seismic moment and energy with fault parameters are used in two ways:

1) to get a rough estimate of relevant fault parameter when M, M_0 or E_S of the event are known from the evaluation of instrumental recordings; or
2) in order to get a magnitude, moment and/or energy estimates for historic or even prehistoric events for which no recordings are available but for which some fault parameters such as the length of surface rupture and/or amount of surface displacement can still be determined from field evidence.

The latter is particularly important for improved assessment of seismic hazard and for estimating the maximum possible earthquake, especially in areas with long mean recurrence times for strong seismic events. Of particular importance for hazard assessment are also relationships between macroseismic intensity, I, and magnitude, M, on the one hand (see Eqs. in 3.2.6.6) and between ground acceleration and I or M, on the other hand. Unfortunately, the measured maximum accelerations for equal values of intensity I scatter in the whole range of I = III to IX by about two orders of magnitude (Ambraseys, 1975). The reason for this scatter is many-fold, e.g., human perception is strongest for frequencies around 3 Hz while acceleration and damage might be strongest for more high frequent ground motions. Also, damage depends not only on the peak value of acceleration (PGA) but also depends on its frequency with respect to the natural period of the shaken structures and on the duration of strong ground shaking. Moreover, especially in real-time applications for damage prediction and assessment, peak ground velocity (PGV) data have proven to be much more important than PGA data, especially for mid-rise and high-rise buildings that are typical of modern societies (e.g., Wu et al., 2003). And some structures are particularly vulnerable to large ground displacements and not so much to high accelerations, e.g., pipelines or very long free-spanning bridges.

Relationships between M_0, Ms, and E_S with various fault parameters are mostly based on model assumptions on the fault geometry, rupture velocity and time history, ambient stress or stress drop, etc. But sometimes these fault parameters can, at least partially, be confirmed or constrained by field evidence or by petrophysical laboratory experiments. As for other scaling relations discussed above, global relationships can give only a rough orientation since the scatter of data is considerable due to regional variability. Whenever possible, regional relationships should be developed.

Sadovsky et al. (1986) found that for both crustal earthquakes and underground explosions the following relationship holds between seismic energy E_S (in erg) and the seismic source volume V_{source} (in cm^3):

$$\log E_S = 3 + \log V_{source} \tag{3.170}$$

with V_{source} for earthquakes being estimated from the linear dimensions of the aftershock zone. This means that the critical energy density for both natural and artificial crustal seismic sources is about equal, roughly10^3 erg/cm^3 or 100 J/m^3. It does not depend on the energy released by the event. E_S increases only because of the volume increase of the source. Accordingly, it is not the type of seismic source but the properties of the medium that play the decisive role in the formation of the seismic wave field. However, local and regional differences in ambient stress and related stress drop $\Delta\sigma \approx 2\mu\ E_S/M_0$ may modify this conclusion.

Fig. 3.93 shows the relation between seismic moment M_0 and the area A_r of fault rupture as published by Kanamori and Anderson (1975). A_r is controlled by the stress drop $\Delta\sigma$; as $\Delta\sigma$ increases for a given rupture area, M_0 becomes larger. One recognizes that intraplate earthquakes have on average a higher stress drop (around 10 MPa = 100 bars) than interplate events (around 3 MPa). The data in Fig. 3.93 are also well fit by the average relationship suggested by Abe (1975), namely:

$$M_0 = 1.33 \times 10^{15}\ A_r^{3/2} \tag{3.171}$$

which is nearly identical with the relation by Purcaru and Berckhemer (1982):

$$\log M_0 = (1.5 \pm 0.02) \log A_r + (15.25 \pm 0.05) \tag{3.172}$$

with M_0 in Nm and A_r in km^2. Eq. (3.172) corresponds to the theoretical scaling relation derived by Chen and Chen (1989) for a modified Haskell model with the assumption L = 2W (L - length and W- width of fault rupture, $A_r = LW = 0.5\ L^2$) and an average displacement $\bar{D} = 4.0 \times 10^{-5}$ L. Note that empirical data indicate also other aspect ratios L/W up to about 30 (e.g., Purcaru and Berckhemer, 1982).

Wells and Coppersmith (1994) gave another relation between moment magnitude and A_r, derived from a very comprehensive data base of source parameters for historical shallow-focus earthquakes (h < 40 km) in continental interplate or intraplate environments:

$$Mw = (0.98 \pm 0.03) \log A_r + (4.07 \pm 0.06) \tag{3.173}$$

For the related data see Fig. 3.95b.

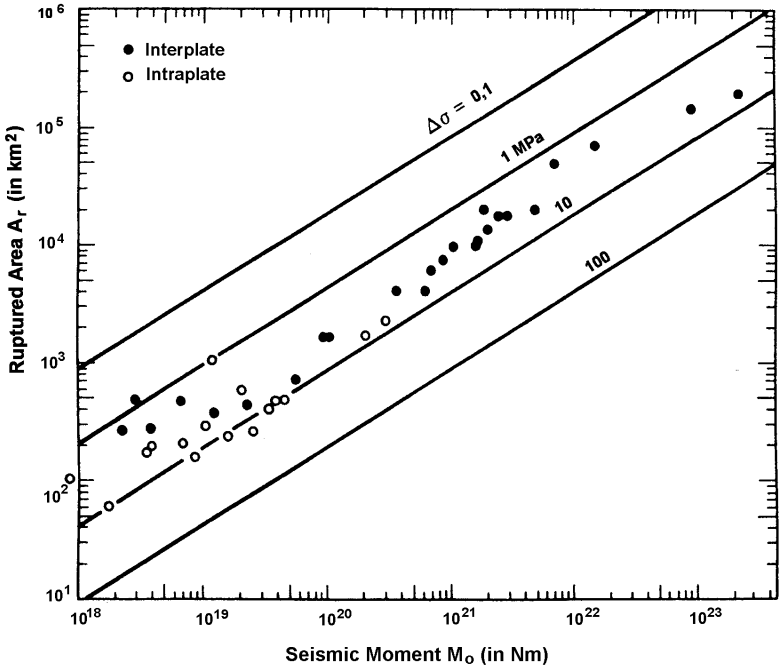

Fig. 3.94 Relation between area of fault rupture A_r and seismic moment M_0 for inter- and intraplate earthquakes. The solid lines give the respective relationships for different stress drop $\Delta\sigma$ (in MPa; 1 Pa = 10^{-5} bars) (modified from Kanamori and Anderson, Theoretical basis of some empirical relations in seismology, Bull. Seism. Soc. Am., Vol. 65, p. 1077, Fig. 2, 1975; © Seismological Society of America).

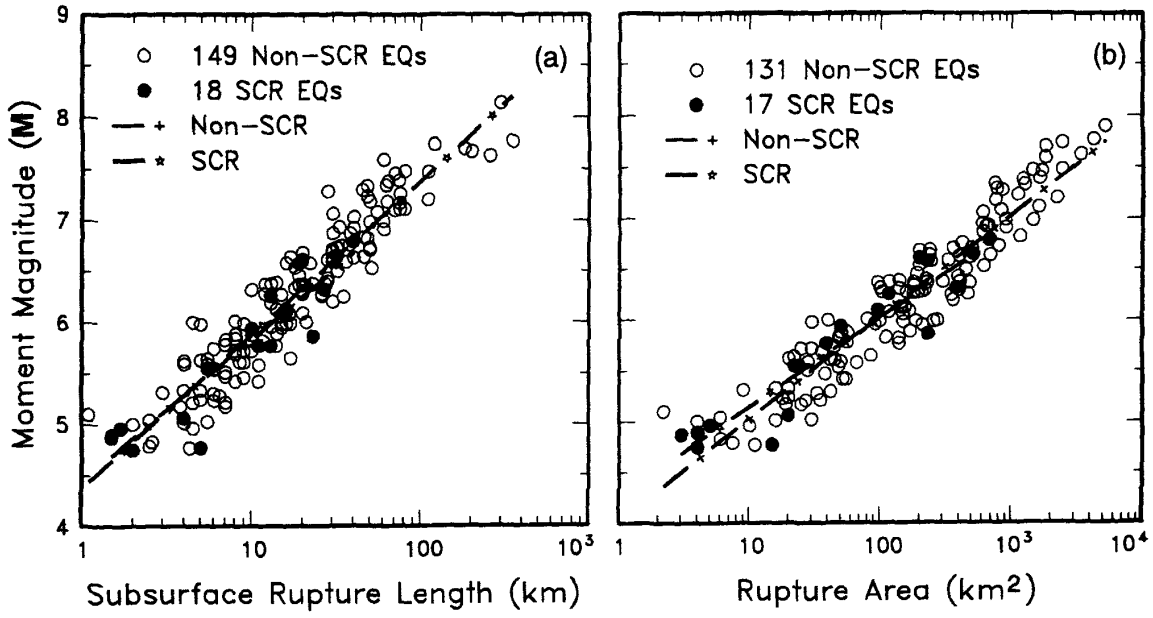

Fig. 3.95 Data plots and regression lines for the relationship between moment magnitude and surface rupture length (left panel), respectively rupture area (right panel), for earthquakes in stable continental regions (SCR) and non-SCR according to Wells and Coppersmith (1994), Bull. Seism. Soc. Am., 54(4), Fig. 17. © Seismological Society of America.

There also exist linear log-log relationships between L and M_0. One of such relations, published by Wells and Coppersmith (1994), has been plotted in the left diagram of Fig. 3.95 for earthquakes in stable continental regions (SCR) and non-stable ones. For another average relationship between Mw and the surface rupture length SRL of strike slip, reverse and normal faulting earthquakes (77 events) these authors give:

$$Mw = 1.16 \log SRL(km) + 5.08. \qquad (3.174)$$

According to Scholz et al. (1986), L is for a given seismic moment on average about 6 times larger for interplate (strike-slip) events than for intraplate ones (see Fig. 3.96) and the ratio α between average fault displacement (slip) $\bar{D}$ and fault length L, $\alpha \approx 1 \times 10^{-5}$ for interplate and $\alpha \approx 6 \times 10^{-5}$ for intraplate events. Since this result is independent of the type of fault mechanism, it implies that intraplate faults have a higher frictional strength (and thus stress drop) than plate boundary faults but smaller length for the same seismic moment.

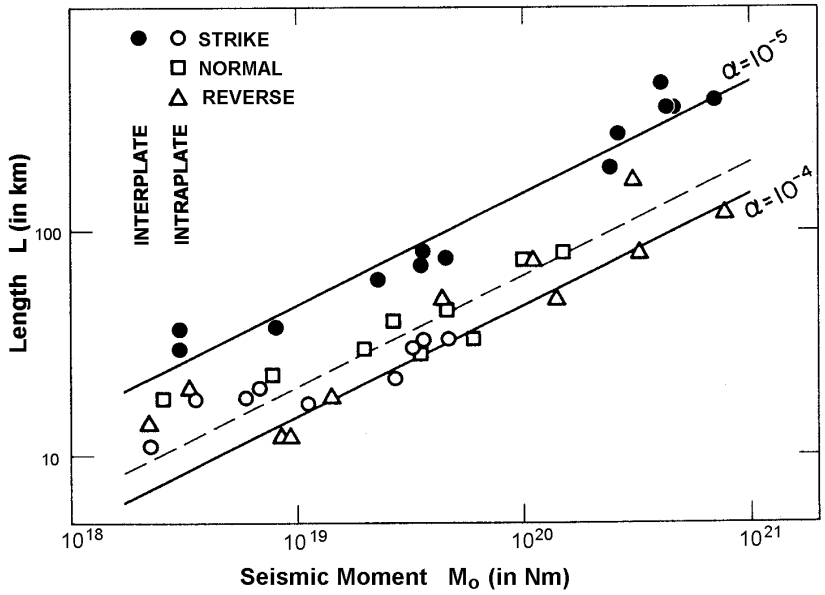

Fig. 3.96 Fault length L versus seismic moment M_0 for large inter- and intraplate earthquakes. The solid lines give the respective relationship for the ratio $\alpha = \bar{D}/L$ (modified from Scholz et al. (1986), Scaling differences between large interplate and intraplate earthquakes, Bull. Seism. Soc. Am., Vol. 76, No. 1, p. 68, Fig. 1; © Seismological Society of America).

The slope of the curves in Fig. 3.96 is 0.5. This corresponds to a relation $M_0 \sim L^2$ (Scholz 1982; Pegeler and Das, 1996) which is only valid for large earthquakes (M > about 6.5 to 7). Then the width W of the fault is already saturated, i.e., has reached its largest extension within the seismogenic zone of brittle fracturing in the crust, respectively lithosphere. Depending on heat flow and composition, the seismogenic zone in the crust is about 10 to 30 km thick. Accordingly, for larger earthquakes, the growth of the fault area with increasing M_0 is in the length direction only.

Recently, there has been some serious debate on the scaling of large earthquakes and their ratio α (Scholz, 1994a and b and 1997; Romanowicz 1994; Romanowicz and Rundle, 1993 and 1994; Sornette and Sornette, 1994; Wang and Ou, 1998). Romanowicz (1992), who prefers to scale slip not with length but with width, even gives a relationship of $M_0 \sim L$ in case

of very large earthquakes. In contrast, Hanks (1977) showed that earthquakes with rupture dimensions smaller than the thickness of the seismogenic layer scale according to $M_0 \sim L^3$ which is equivalent to Eq. (3.170).

Accordingly, in agreement also with a data compilation by Riznichenko (1992), shown in Fig. 3.97, often rather different correlation relationships between source length L, magnitude M and energetic class K have been published by various authors for events in different seismotectonic environments.

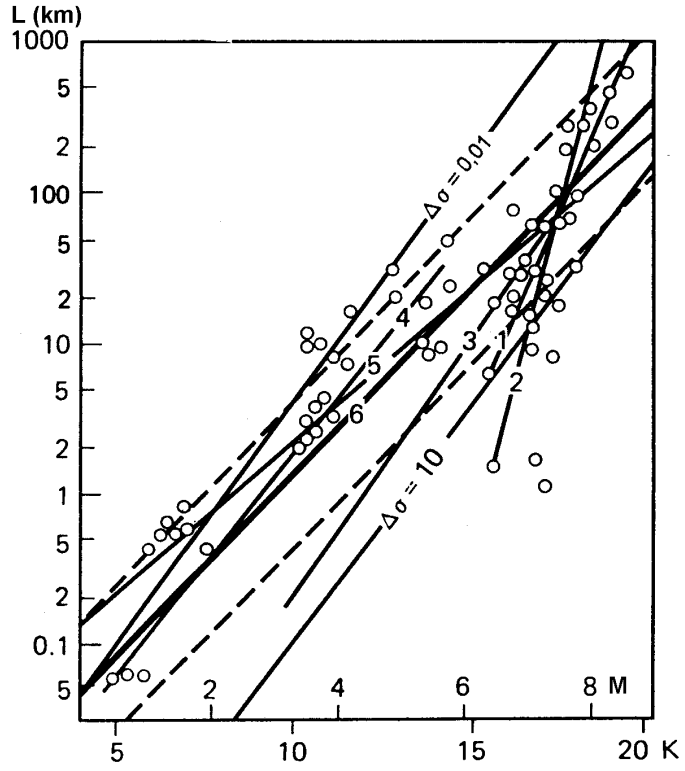

Fig. 3.97 Correlation of source length L with magnitude M and energetic class K according to data from various sources (e.g., curve 1 by Tocher, 1958, curve 2 by Iida, 1959; curve 6 average by Riznichenko, 1992; Russian original 1985). Thin straight lines: related stress drops $\Delta\sigma$ are given in MPa; broken lines mark the limits of the 68% confidence interval with respect to the average curve 6 (modified from Riznichenko, 1992, Fig. 3; with permission of Springer-Verlag).

Ambraseys (1988) published relationships derived from the dimensions of fault surface ruptures for Eastern Mediterranean and Middle Eastern earthquakes (with L - observed surface rupture length in km, $\bar{D}$ - relative fault displacement in cm, M_{SC} - predicted surface-wave magnitudes):

$$M_{SC} = 1.43 \log L + 4.63 \tag{3.175}$$

and

$$M_{SC} = 0.4 \log (L^{1.58} \bar{D}^2) + 1.1. \tag{3.176}$$

They yield results which are in good agreement with those by Nowroozi (1985) for Iran but they differ significantly from the respective relations given by Tocher (1958) for Western USA and from Iida (1959) for Japan (see curves 1 and 2 in Fig. 3.97).

Khromovskikh (1989) analyzed available data for more than 100 events of different faulting types from different seismotectonic regions of the Earth. He derived 7 different relationships between magnitude M and the length L of the rupture zone, amongst them those for the following regions:

a) the Circum-Pacific belt: $M = (0.96 \pm 0.25) \log L + (5.70 \pm 0.34)$ (3.177)
b) the Alpine fold belt: $M = (1.09 \pm 0.28) \log L + (5.39 \pm 0.42)$ (3.178)
c) rejuvenated platforms: $M = (1.25 \pm 0.19) \log L + (5.45 \pm 0.28)$ (3.179)

and compared them with respective relationships of other authors for similar areas.

Other relationships for estimating L (in km), when Ms is known, were derived by Chen and Chen (1989) on the basis of their general scaling law using a modified Haskell model for a rectangular fault. These relationships clearly show the effect of width saturation:

$$\log L = Ms/3 - 0.873 \quad \text{for} \quad Ms \leq 6.4 \tag{3.180}$$

$$\log L = Ms/2 - 1.94 \quad \text{for} \quad 6.4 < Ms \leq 7.8 \tag{3.181}$$

$$\log L = Ms - 5.84 \quad \text{for} \quad 7.8 < Ms \leq 8.5. \tag{3.182}$$

The same authors also gave similar relations between the average dislocation $\bar{D}$ (in m) and Ms, namely:

$$\log \bar{D} = Ms/3 - 2.271 \quad \text{for} \quad Ms \leq 6.4 \tag{3.183}$$

$$\log \bar{D} = Ms/2 - 3.34 \quad \text{for} \quad 6.4 < Ms \leq 7.8 \quad \text{and} \tag{3.184}$$

$$\log \bar{D} = Ms - 7.24 \quad \text{for} \quad 7.8 < Ms \leq 8.5 \tag{3.185}$$

while Chinnery (1969) derived from still sparse empirical data a linear relation between magnitude M and $\log \bar{D}$ (with $\bar{D}$ in m) for the whole range $3 < M < 8.5$

$$M = 1.32 \log \bar{D} + 6.27 \tag{3.186}$$

which changes to

$$M = 1.04 \log \bar{D} + 6.96 \tag{3.187}$$

when only large magnitude events are considered.

Probably best established are the relations which Wells and Coppersmith (1994) have determined for shallow-focus (crustal) continental interplate or intraplate earthquakes on the basis of a rather comprehensive data base of historical events. Since most of these relations for strike-slip, reverse and normal faulting events were not statistically different (at a 95% level of significance) their average relations for all slip types are considered to be appropriate

for most applications. Best established are the relationships between moment magnitude Mw and rupture area [see Eq. (3.167 and Fig. 3.95 right)], surface rupture length (SRL) (see Fig. 3.95 left) and subsurface rupture length (RLD) (both in km). They have the strongest correlations (RXY = 0.89 to 0.95) and the least data scatter:

$$Mw = (1.16 \pm 0.07) \log (SRL) + (5.08 \pm 0.10) \tag{3.188}$$

$$Mw = (1.49 \pm 0.04) \log (RLD) + (4.38 \pm 0.06) \tag{3.189}$$

$$\log (SLR) = (0.69 \pm 0.04)\, Mw - (3.22 \pm 0.27) \tag{3.190}$$

$$\log (RLD) = (0.59 \pm 0.02)\, Mw - (2.44 \pm 0.11) \tag{3.191}$$

When comparing Eqs. (3.190) and (3.191) it follows that in general the observed surface rupture length is only about 75% of the subsurface rupture length inferred from modeling.

The correlations between Mw and $\bar{D}$ as well as $\bar{D}$ and SLR are somewhat smaller (RXY = 0.71 to 0.78):

$$Mw = (0.82 \pm 0.10) \log \bar{D} + (6.693 \pm 0.05) \tag{3.192}$$

$$\log \bar{D} = (0.69 \pm 0.08)\, M_w - (4.80 \pm 0.57) \tag{3.193}$$

$$\log \bar{D} = (0.88 \pm 0.11) \log (SLR) - (1.43 \pm 0.18) \tag{3.194}$$

$$\log (SLR) = (0.57 \pm 0.07) \log \bar{D} + (1.61 \pm 0.04). \tag{3.195}$$

Wells and Coppersmith (1994) reasoned that the weaker correlation may reflect the wide range of displacement values for a given rupture length (differences up to a factor 50 in their data set!). These authors also give relations between SLR and the maximum surface displacement which is, on average, twice the observed average surface displacement while the average subsurface slip ranges between the maximum and average surface displacement.

Chen and Chen (1989) also derived from their scaling law the following average values:

- rupture velocity $v_r = 2.65$ km/s;
- total rupture time T_r (in s) = 0.35 (s/km) × L (km); (3.196)
- slip velocity dD/dt varying between 2.87 and 11.43 m/s.

However, v_r and dD/dt usually vary along the fault during the fracture process. From teleseismic studies we obtain usually only spatially and temporally averaged point source values of fault motion but the actual co-seismic slip is largely controlled by spatial heterogeneities along the fault rupture (see Figs. 3.9-3.12). Large slip velocities over 10 m/s suggest very high local stress drop of more than 10 MPa (Yomogida and Nakata, 1994). On the other hand, sometimes very slow earthquakes may occur with very large seismic moment but low seismic energy radiation (e.g., "tsunami earthquakes"; Kanamori, 1972; Polet and

Kanamori, 2009). This has special relevance when deriving scaling relations suitable for the prediction of strong ground motions (e.g., Fukushima, 1996).

Scaling relationships between fault parameters, especially between D and L, are also controlled by the fault growth history, by age and by whether the event can be considered to be single and rare or composite and frequent (e.g., Dawers et al., 1993; Tumarkin et al., 1994). There exist also scaling relations between fault length and recurrence interval which are of particular relevance for seismic hazard assessment (e.g., Marrett, 1994).

Using Eqs. (3.175), (3.177)-(3.179) and (3.188), one gets for a surface rupture length of 100 km magnitudes M = 7.5, 7.7, 7.6, 7.95 and 7.4, respectively. When knowing the Ms or Mw and calculating L and $\bar{D}$ according to Eqs. (3.180-3.181), (3.182-3.183), (3.190) and (3.193), one gets for magnitude 7.0 L = 36 km and 41 km, $\bar{D}$ = 1.4 m and 1.1 m and for magnitude 8.0 L = 145 km and 200 km, $\bar{D}$ = 3.8 m and 5.2 m. The good agreement of the calculated values for magnitudes 7 and the stronger disagreement for magnitudes 8 are obviously due to the growing difference between Ms (used in the relations by Chen and Chen, 1989) and Mw (used in the relations by Wells and Coppersmith, 1994) for Ms > 7 (saturation effect). For the rupture duration we get according to Eq. (3.196) for Ms = 7 and 8 and the respective rupture lengths (3.181) and (3.182) approximately 13 s and 51 s, respectively. If we use, however, the empirically derived average rupture duration relation (3.3) according to Bormann and Saul (2009a) the average rupture duration of earthquakes with M = 7 and 8 would be about 25 s and 100 s, respectively.

3.4 Determination of fault-plane solutions (P. Bormann and S. Wendt)

3.4.1 Introduction

The direction (polarity) and amplitude of motion of a seismic wave arriving at a distant station depends both on the wave type considered and the position of the station relative to the motion in the earthquake source. This is illustrated by Figs. 3.98a and b.

Fig. 3.98a represents a linear displacement of a point source **S** while Fig. 3.98b depicts a right lateral (dextral) shear dislocation along a fault plane **F**. Shear dislocations are the most common model to explain earthquake fault ruptures. Note that in the discussion below we consider the source to be a point source with rupture dimension much smaller than the distance to the stations and also much smaller than the wave length considered. First we look into the situation depicted in Fig. 3.98a. When S moves towards Δ1 then this station will observe a *compressional* (+) P-wave arrival (i.e., the first motion is *away* from **S**), Δ4 will record a P wave of opposite sign (-), a *dilatation* (i.e., first motion *towards* **S**), and station Δ2 will receive no P wave at all. On the other hand, S waves, which are polarized parallel to the displacement of **S** and perpendicular to the direction of wave propagation, will be recorded at Δ2 but not at Δ1 and Δ4 while station Δ3 will receive both P and S waves.

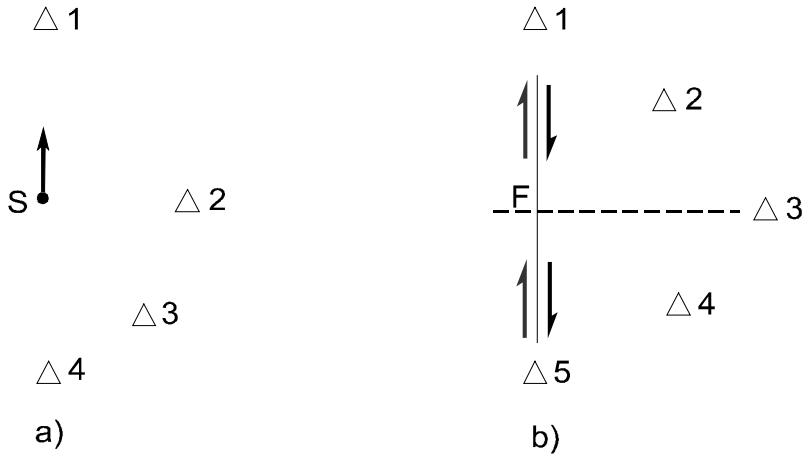

Fig. 3.98 Direction of source displacement with respect to seismic stations Δi for a) a single force at point S and b) a fault rupture F. Note that in the discussion below we consider the source to be a point source with a rupture dimension much smaller than the distance to the stations (Figure by courtesy of M. Baumbach †, 2001).

Somewhat different is the case of a fault rupture (Fig. 3.98b). At stations Δ1 and Δ5, which are positioned in the strike direction of the fault, the opposite signs of P motion on both side of the fault will cancel, i.e., no P waves will be observed. The latter also applies for station Δ3 which is sited perpendicular to the fault. On the other hand, stations Δ2 and Δ4, which are positioned at an angle of 45° with respect to the fault, will record the P-wave motions with maximum amplitudes but opposite sign. This becomes clear also from Fig. 3.100a. It shows the different polarities and the amplitude "lobes" in the four quadrants. The length of the displacement arrows is proportional to the P-wave amplitudes observed in different directions from the fault. Accordingly, by observing the sense of first motions of P waves at many stations at different azimuths with respect to the source it will be possible to deduce a "fault-plane solution". But because of the symmetry of the first-motion patterns, two potential rupture planes, perpendicular to each other, can be constructed. Thus, on the basis of polarity data alone, an ambiguity will remain as to which one was the acting fault plane. This can only be decided either by field evidence on the orientation and nature of seismotectonic faults (see, e.g., Figure 7 and discussion in EX 3.3) or by taking into account additional data on azimuthal amplitude and frequency, respectively wave-form patterns (see Glossary: *directivity, directivity focusing, directivity pulse*). The latter are due to *Doppler* and constructive wave interference *effect*s caused by the moving and waves radiating source.

In accordance with the above, the amplitude distribution of P waves, A_P, for a point source with pure double-couple shear mechanism is described in a spherical co-ordinate system (θ, ϕ) (Aki and Richards, 1980; see Fig. 3.99) by

$$A_P(\theta, \phi) = \cos\phi \sin 2\theta. \qquad (3.197)$$

This expression divides the focal sphere into four quadrants. The focal sphere for a seismic point source is conceived of as a sphere of arbitrarily small radius centered on the source. Within each quadrant the sign of the P-wave first motion (polarity) does not change but amplitudes are large in the center of the quadrant and small (or zero) near to (or at) the fault plane and the auxiliary plane, which is perpendicular to the fault plane. The nodal lines for P waves, on which $A_P(\theta, \phi) = \cos\phi \sin 2\theta = 0$, separate the quadrants. They coincide with the

horizontal projection of the two orthogonal fault planes traces through the focal sphere. Opposite quadrants have the same polarity, neighboring quadrants different polarities. Note that *compressional first-motion* signals are observed at stations falling into the azimuth and take-off angle range of the *tension quadrant* of the source (with tension force directed away from the point source) while *dilatational first-motion signals* are observed at stations falling into the respective *compression quadrant* (with pressure force directed towards the point source).

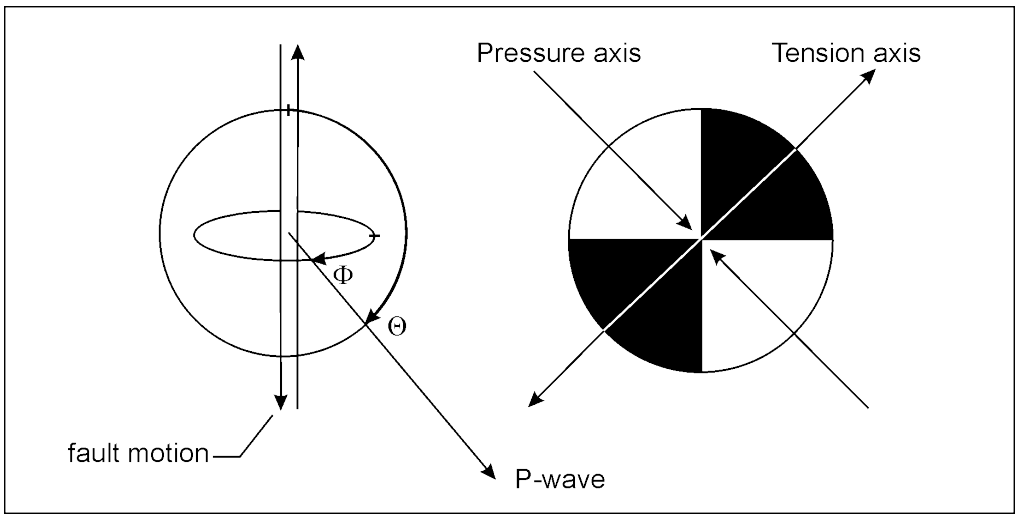

Fig. 3.99 Map view of P-wave radiation pattern for a shear fault. θ is the azimuth in the plane while ϕ is in fact three-dimensional. See also Fig. 3.98b. Black areas: polarity +, i.e., **upward** P-wave first motion in vertical component records; white areas: - , i.e., **downward** P-wave first motion in vertical component records (modified according to a Figure kindly provided by M. Baumbach †, 2001).

The position of the quadrants on the focal sphere depends on the orientation of the active fault and of the slip direction in space. This is illustrated by Fig. 3.100, which shows the P-wave radiation pattern for a thrust event with some strike-slip component. Thus, the estimation of the P-wave first motion polarities and their back-projection onto the focal sphere allows us to identify the type of focal mechanism of a shear event (termed fault-plane solution). The only problem is that the hypocenter and the seismic ray path from the source to the individual stations must be known. This may be difficult for rays propagating in a heterogeneous Earth with 2-D or even 3-D velocity structure.

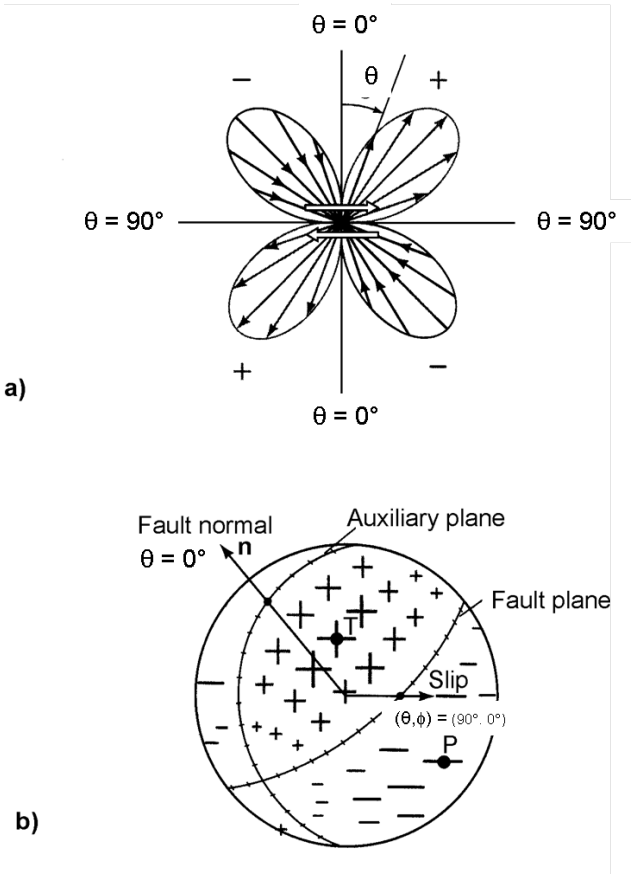

Fig. 3.100 Radiation pattern of the radial displacement component (P wave) due to a double-couple source: a) for a plane of constant azimuth (with lobe amplitudes proportional to sin2θ) and b) over a sphere centered on the origin. Plus and minus signs of various sizes denote the alternating amplitude variations (with the spherical coordinates θ and ϕ) of outward (+; extensional quadrant) and inward (-; compressional quadrant) directed motions of the source. The fault plane and auxiliary plane are nodal lines on which cosϕ sin2θ = 0. The pair of open arrows in a) at the center denotes the shear dislocation and **P** and **T** in b) mark the penetration points of the pressure and tension axes, respectively, through the focal sphere. (modified from Aki and Richards 1980; with kind permission of the authors).

Fault-plane solutions based on P-wave first motion polarities will be better constrained if additionally the different radiation pattern of S-waves displacement amplitudes is taken into account. In the case of a double-couple mechanism, the S-wave amplitude pattern follows the relationship (see Aki and Richards, 1980)

$$\boldsymbol{A_S} = \cos2\theta \cos\phi\boldsymbol{\theta} - \cos\theta \sin\phi\boldsymbol{\phi} \qquad (3.198)$$

with $\boldsymbol{\theta}$ and $\boldsymbol{\phi}$ - unit vectors in θ and ϕ direction, $\boldsymbol{A_S}$ - shear-wave displacement vector.

An example is given in Fig. 3.101 for the same fault-plane solution as shown in Fig. 3.100 for P waves. Fig. 3.102 shows the calculated azimuth-dependent vertical component PV, as well as vertically polarized SV and horizontally polarized SH amplitude lobe patterns for two different combinations of **strike, dip and rake** angles of a seismic fault as well as different incidence angles *Incd* of the seismic rays at the station. *Incid* corresponds in the case of a shallow source in a homogeneous 1-D Earth model to the take-off angles of the considered

seismic ray from the source. And Fig. 3.103 shows the P- and S-wave radiation pattern lobes for a local earthquake with respect to the azimuth towards two seismic stations of a local network in Germany and their related records, which show striking differences in their P/S amplitude ratios. For a more general introduction into source directivity and the radiation patterns of earthquake fault mechanisms see section 2.4 in IS 1.1. It provides additional figures plus animations that illustrate the great variability of amplitude radiation and directivity patterns, depending on the controlling fault and rupture parameter combinations.

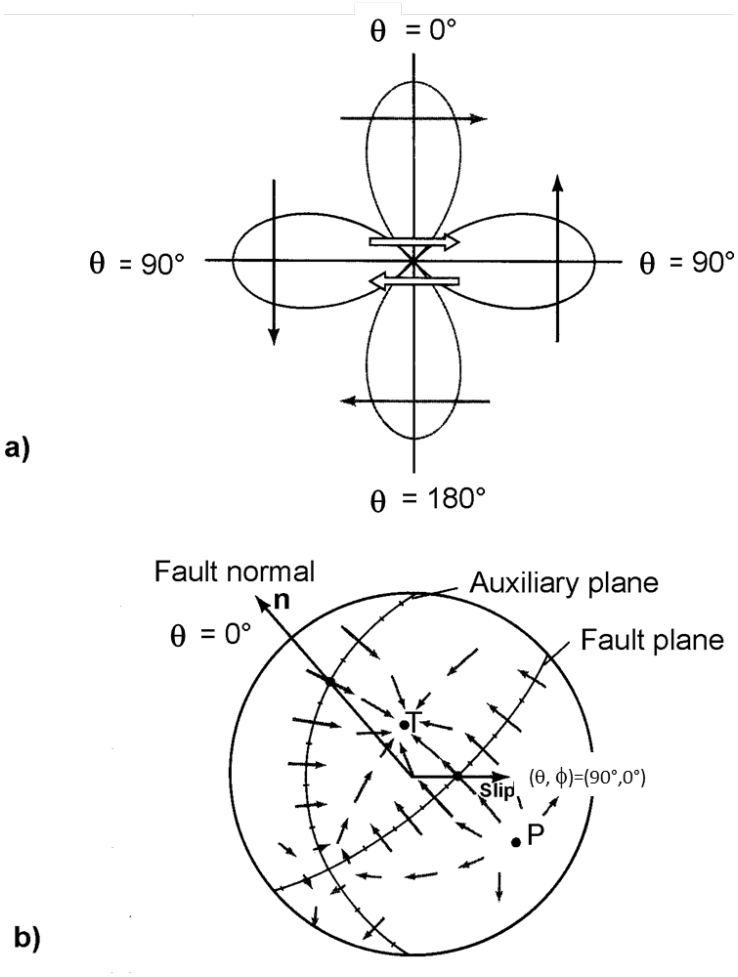

Fig. 3.101 Radiation pattern of the transverse displacement component (S wave) due to a double-couple source. a) in the plane $\{\phi = 0, \phi = \pi\}$ and b) over a sphere centered on the origin. Arrows imposed on each lobe in a) show the direction of particle displacement associated with the lobe while the arrows with varying size and direction in the spherical surface in b) indicate the variation of the transverse motions with θ and ϕ. P and T mark the penetration points of the pressure and tension axes, respectively, through the focal sphere. There are no nodal lines as in Fig. 3.100 but only nodal points where there is zero motion. The nodal point for transverse motion at $(\theta, \phi) = (45°, 0°)$ at T is a maximum in the pattern for longitudinal motion (see Fig.3.100) while the maximum transverse motion (e.g., at $\theta = 0$) occurs on a nodal line for the longitudinal motion. The pair of arrows in a) at the center denotes the shear dislocation (modified from Aki and Richards 1980; with kind permission of the authors).

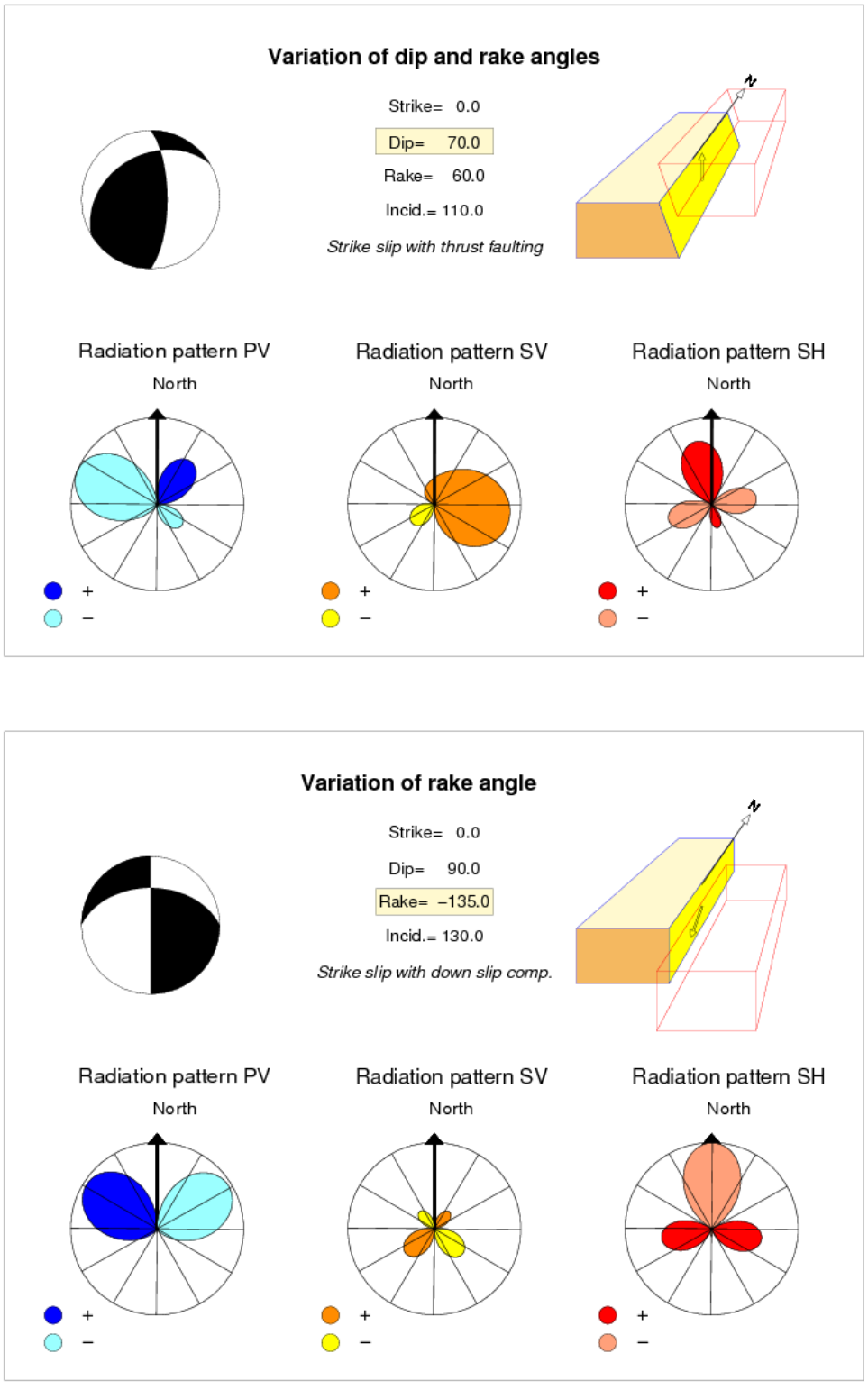

Fig. 3.102 Radiation patterns of PV, SV and SH amplitudes for two earthquake ruptures with different fault **dip**, **rake** (= slip direction) **and take-off angle** of the seismic rays at the source (which is in the case of a shallow seismic source in a homogeneous 1-D Earth model equal with the incidence angle **Incid** at the receiving seismic station).

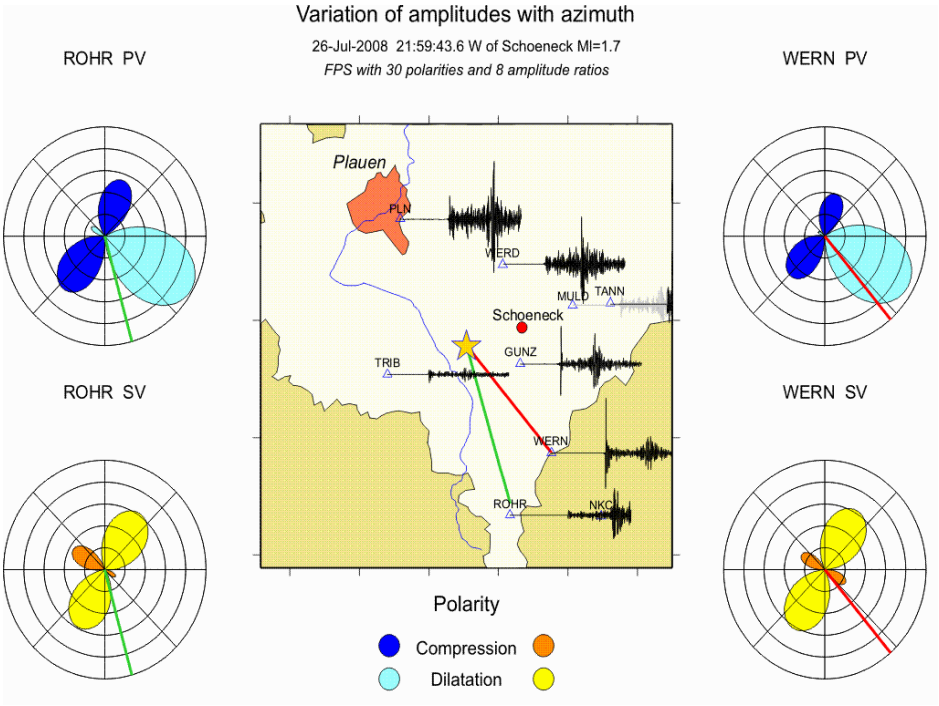

Fig. 3.103 Comparison of theoretically calculated radiation patterns for an earthquake with well constrained fault plane solution and slip direction with the really observed amplitude ratios between vertical component P and S amplitudes at stations of a local seismic network in Germany. The source depth of the earthquake has been 12.1 km and the epicenter (respectively hypocenter) distances of stations WERN and ROHR were 13.5 km (18.1 km) and 17.5 km (21.3 km).

3.4.2 Determination of fault-plane solutions from P-wave polarities

Most fault-plane solutions are still based on P-wave polarity readings only, especially for smaller earthquakes, although a steadily growing number results nowadays from moment tensor solutions via waveform fitting (see Figs. 3.66 and 3.67 as well as IS 3.8, 3.10 and 3.11). Advanced event location and seismogram analysis programs allow plotting of measured polarities on either an equal-angle Wulff net or a Lambert-Schmidt equal area projection (Figs. 3.104; see also Aki and Richards, 1980, Vol. 1, p. 109-110), yet without showing the net grids itself. Then they search for the optimal separation of the quadrants with plus and minus polarities. The quadrants are separated by the two potential fault planes which are, in the assumed idealized rupture model in a homogeneous full-space, perpendicular to each other. As the final result, usually only the black-and-white, or in different colors shaded quadrants of the horizontal 2-D focal-sphere representations, nick-named also as “beach-ball” solutions, are then plotted and presented together with the respective numbers for the strike, dip and rake of the two fault planes. For the basic types of strike-slip, normal and thrust faulting this is shown in Fig. 3.105 and for mixed types of faulting in Fig. 3.106, In the latter figure additionally the poles of the axes of maximum pressure P and maximum tension T have been marked. In this idealized rupture model they are assumed to be situated in the center of the negative and positive polarity quadrants, respectively.

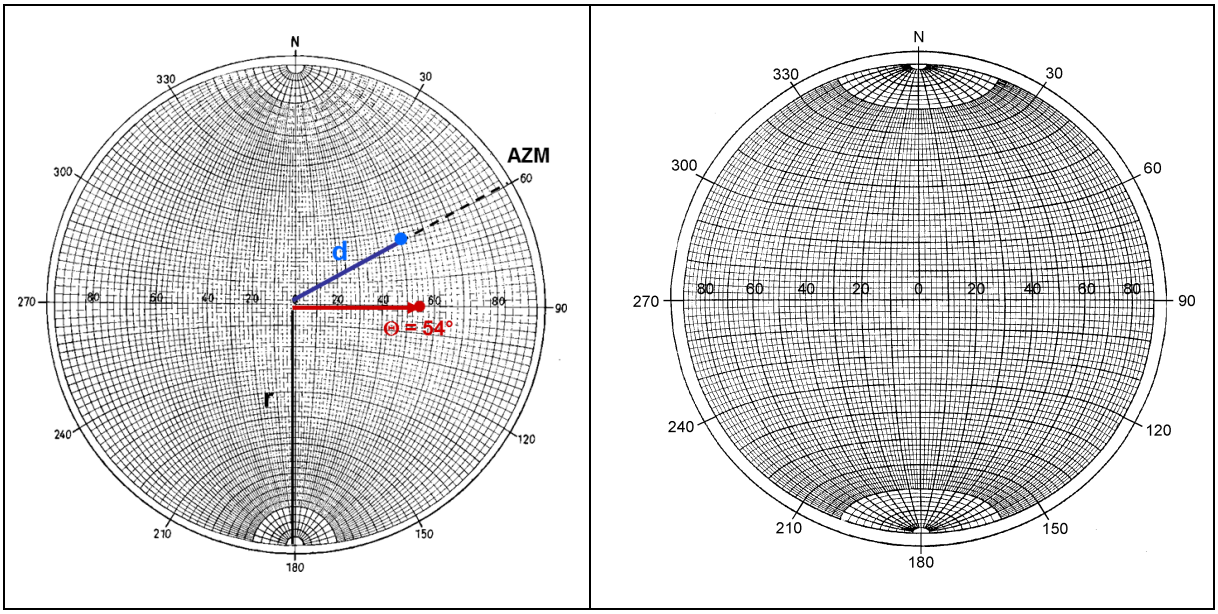

Fig. 3.104 Left: Equal angle Wulff net, for which holds **d = r · tan(Θ/2)** with r – radius of the net and d – distance from the network center of a data point with a given azimuth AZM and take-off angle **Θ**. **Right:** equal area Lambert-Schmidt net with **d = r · sin(Θ/2)**.

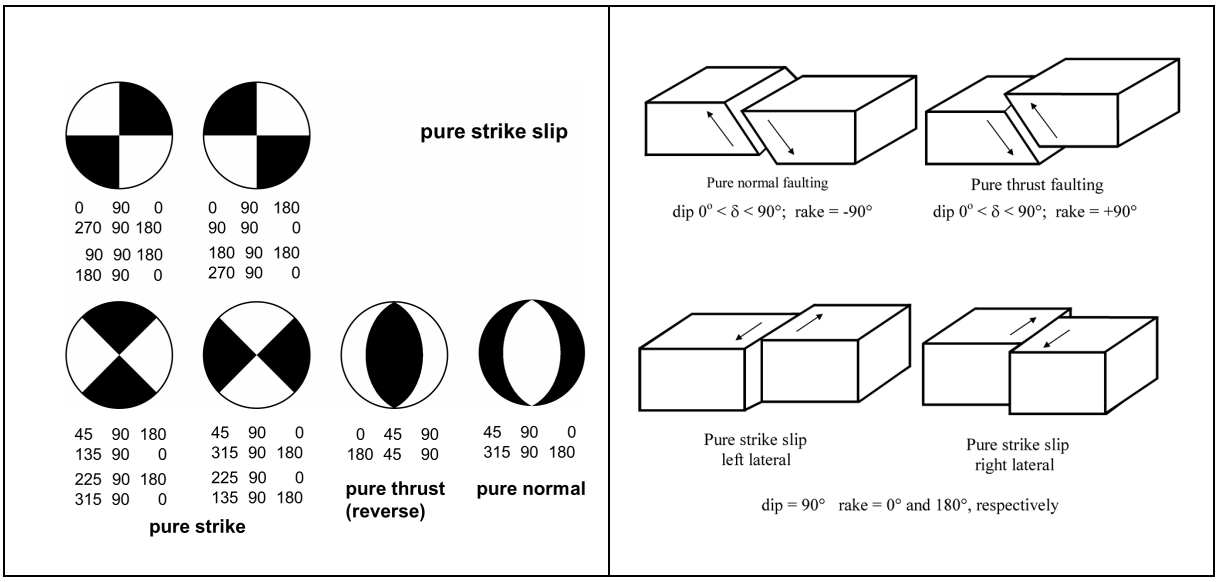

Fig. 3.105 Left: "Beach-ball" representations of basic types of faulting together with the respective numbers of strike, dip and rake angle for the respective fault plane and auxiliary plane, which is a potential fault plane as well. **Right:** Cartoons of the related motions of crustal blocks.

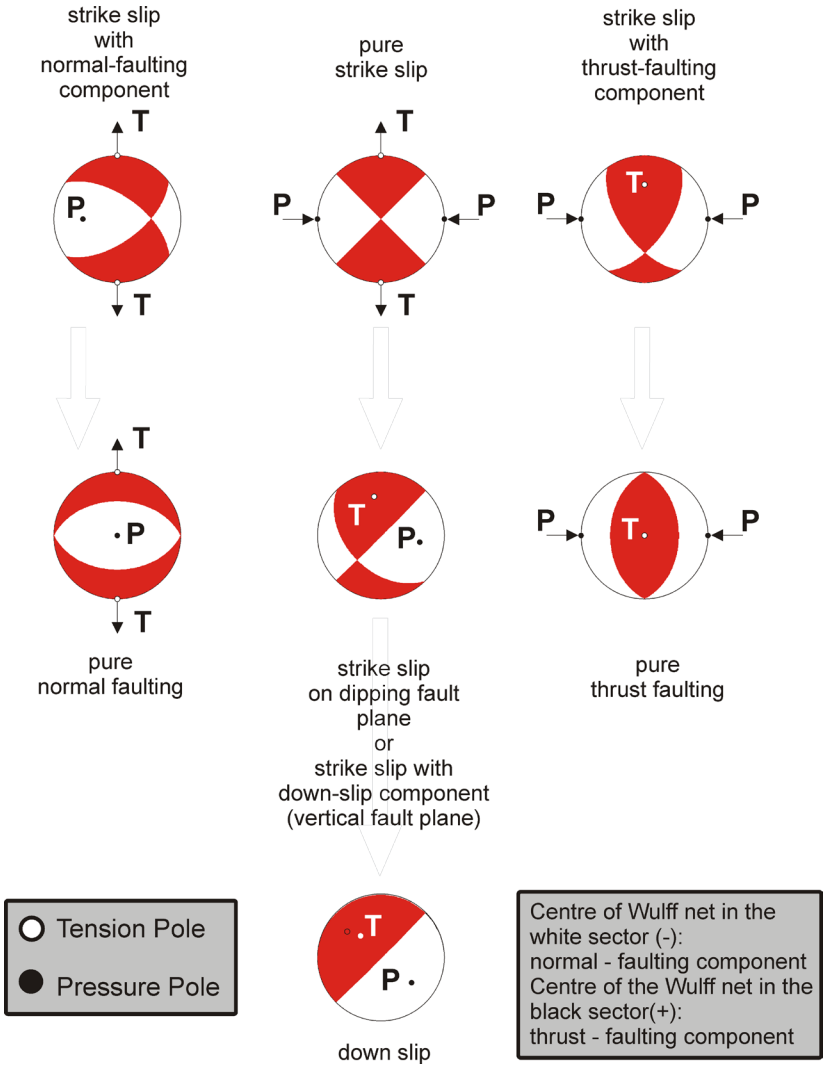

Fig. 3.106 "Beach-ball" presentation of the net projections of the fault plane **cut-traces**, the quadrants of different polarities, and of the penetration points (poles) of the P- and T-axes through the **lower focal hemisphere** for different faulting mechanisms. White sectors correspond to negative and black sectors to positive P-wave first-motion polarities. Note that mixed types of faulting occur when the rake angle $\lambda \neq 0$, 180^o or $\pm 90^o$, e.g., in the case of normal faulting with a strike-slip component or strike-slip with a thrust component. Also, dip angles δ may vary between $0^o < \delta \leq 90^o$ (modified Figure after M. Baumbach †, 2001).

Two important terms, printed in bold letters in Fig. 3.106, have to be explained, namely the notions *cut-trace* and lower *focal hemisphere*. Our problem is that the fault plane cuts through a conceived 3-D "*focal sphere*", which can be separated into an upper and a lower one. All cut traces of the fault through the focal sphere are great circles. In order to reconstruct the orientation of the fault plane in space and to measure its strike, dip and rake angles in a 2-D stereoscopic net we have to project the great circle cut trace of the fault through the focal sphere onto the horizontally placed net. The degree of bending of the projected cut traces depends on the fault dip. Vertically dipping faults are represented by straight lines running through the center of the net, whereas half-circles along the perimeter of the net represent a horizontal fault. However, from Fig. 3.107 we realize that a single fault would yield two such

cut-trace projections, one resulting from the cut through the upper hemisphere and the other from the cut through the lower hemisphere. These two traces are mirrored on the strike direction of the fault, resulting in an 180° ambiguity. To avoid this, one has first to make up one's mind which data should be projected to the horizontal diagram, those related to the lower hemisphere or to the upper hemisphere. This, however, depends on the distance range of observation. In the local range, the P-wave first motion will usually be related to Pg, which has left the source upward through the upper focal hemisphere. However, stations at distances larger than about 150 to 250 km will record Pn as the first P-wave, which has left the source through the lower focal hemisphere. The same applies to all teleseismic P-wave rays. However, with EX 3.2 we demonstrate that even in the local distance range, considering only records at distances less than 50 km, the first arriving P-wave first may already be a critically refracted P at a pronounced velocity discontinuity in the upper crust and thus of a head-wave type as Pn which has left the lower focal hemisphere. If one then wishes to make use of the data of both upper and lower hemisphere rays in order to have a better azimuth and take-off angle distribution of data in the diagram then one has to correct the data from the non-priority hemisphere accordingly. How the corrections of the take-off angles and azimuths of the "wrong" hemisphere rays have to be calculated is illustrated with Figures 1 and 2 of EX 3.2.

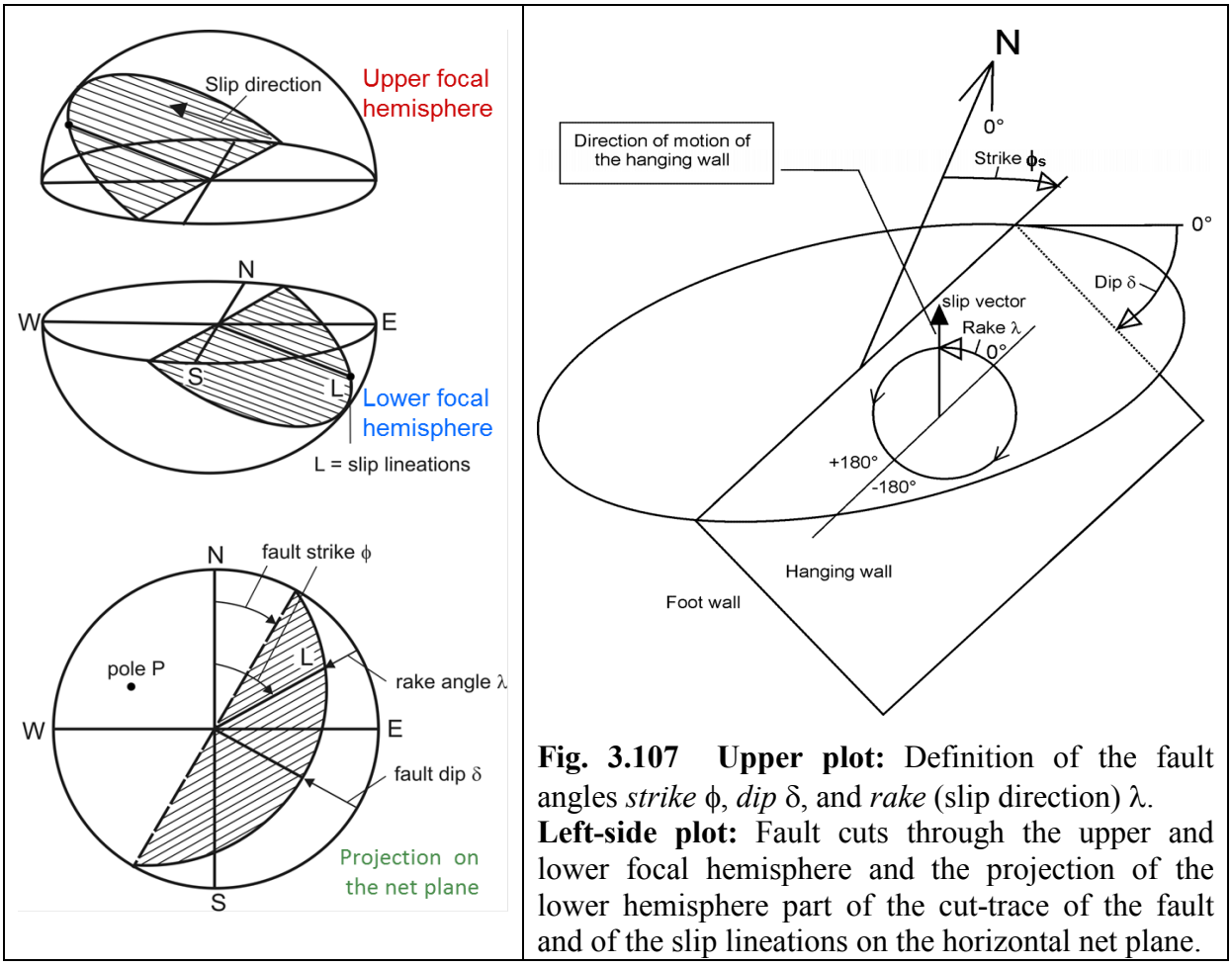

Fig. 3.107 Upper plot: Definition of the fault angles *strike* ϕ, *dip* δ, and *rake* (slip direction) λ. **Left-side plot:** Fault cuts through the upper and lower focal hemisphere and the projection of the lower hemisphere part of the cut-trace of the fault and of the slip lineations on the horizontal net plane.

Although black-box computed fault-plane solutions are very comfortable, they are educationally not very much revealing, how the procedure really works, on which assumptions it is based and how accurate the fault-plane solutions are. In ordertTo get at least a feeling for it as well as an appreciation for the cumbersome tedious work accomplished by

the early "fathers" of systematic investigations of fault-plane solutions and their relationships to seismotectonics, one should have done oneself at least once a few fault-plane solutions manually. We outline in the following the basic principles and provide with EX 3.2 an exercise with detailed step-by-step guidance, solutions and discussions.

A good seismogram analysis software, used for phase onset and polarity picking as well as the event location, can produce as a spin-off output also a file with the following data (see, e.g., Table 1 in EX 3.2): Station code, epicenter distance, azimuth AZM of the station with respect to the source, take-off angle Θ of the seismic ray from the source, and the P-wave first motion polarities + (or U = upward motion in the record) or – (or D = downward motion in the record). These polarities have to be plotted on either the Wulff or the Lambert net at the correct position for the given AZM and Θ of seismic ray towards the station (as shown in Fig. 3.104, left side, for one observation in the Wulff net). Principally, both the Wulff net and the Lambert net projections yield quantitatively the same results. The latter, however, has the advantage that it provides visually a less cluttered plot of data with take-off angles less than 45°.

As a first step we should pin a transparent sheet with a needle to the net center and mark the N, E, S, and W direction as well as the network perimeter on the transparent sheet. Next we transfer all data points according to their AZM and Θ values on the transparent sheet (shown in gray on Fig. 3.108a) and mark them there with their respective polarities in an unambiguous signature. Then the transparent sheet should be rotated over the net center until one finds on the underlying net a great circle meridian which separates best the + and – signs (or related symbols as in Fig. 3.108). By clockwise rotation, we find in our demonstration example a meridian on the left side which separates well the compressional first motions from the dilatational ones. This great circle trace should be drawn with a marker pen on the transparent sheet and termed fault plane one = FP1 (red in Fig. 3.108b).

Next we search for the complementary second (or auxiliary) fault plane trace FP2, remembering that it should be situated 90° apart from FP1 in the case of rupture in a homogeneous full-space. Therefore, we should mark on the transparent sheet the pole P1 of FP1, through which FP2 has to go. P1 is perpendicular from the middle of FP1, 90° away towards the right (red dot in Fig. 3.108b). By counter clockwise back rotation of the transparent sheet we find then indeed another great circle, marked in blue in Fig. 3.108c, which goes through P1 and separates at least the majority of black dots from the majority of the open circles on the right side. FP1 and FP2 cross each other in the lower part of the net at an angle of 90°. Accordingly, the pole P2 of FP2 would be placed on FP1, 90° upwards from this crossing point of the two fault planes. Note that all angles have to be measured on great circles.

You will realize that sometimes polarities + and – are rather close to each other, respectively very close to the fault plane trace which is supposed to separate them. As in Fig. 3.108c, we might even find some polarities to be on apparently the wrong side of the fault, in the wrong quadrant. This, however, is unavoidable. We should remember that a fault plane is a nodal line for P waves (see Fig. 3.100), along which P-wave amplitudes vanish or are very small. Accordingly, if recorded at all, they have a very low signal-to-noise ratio. This may result in wrong reading of the polarity of the usually weaker first half swing. Therefore, nearby placed opposite polarities in the data plot are even "strategic points" to look for, because they are likely to be situated close to the nodal lines. This is also illustrated below by one example from EX 3.2 (Fig. 3.109). In fact, computer programs for finding the optimal fault-plane cut

traces through polarity plots aim at minimizing both their distance from conflicting polarity clusters as well as of the number of wrong polarities in the respective quadrants.

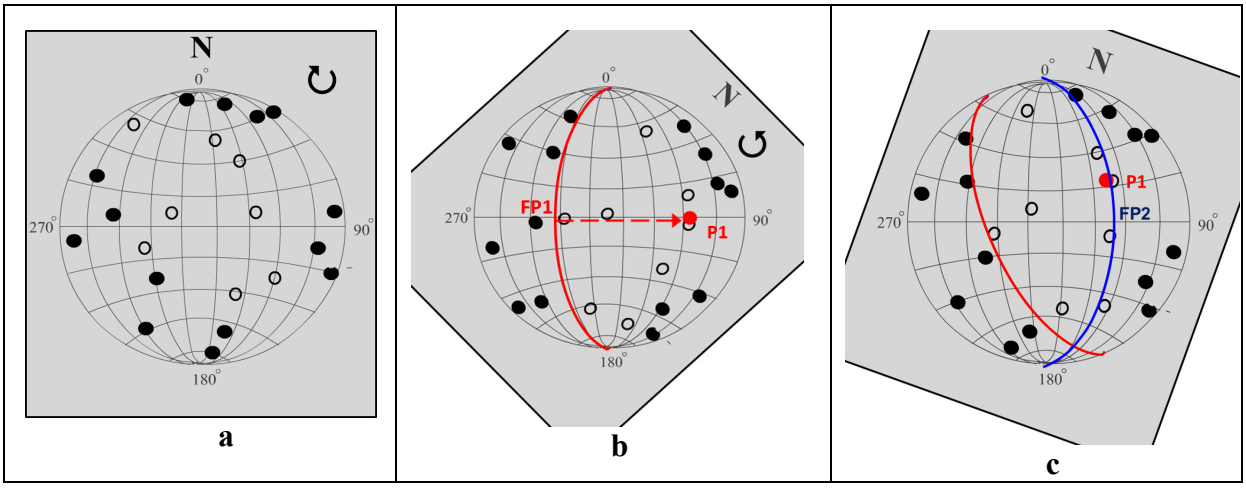

Fig. 3.108 Illustration of the first essential steps when manually searching for the two fault plane traces that associate at least the majority of read polarities correctly with compressional and dilatational quadrants. FP1 = fault plane 1, FP2 = auxiliary second fault plane, P1= pole of FP1. Modified and amended from http://www.learninggeoscience.net/free/00071.

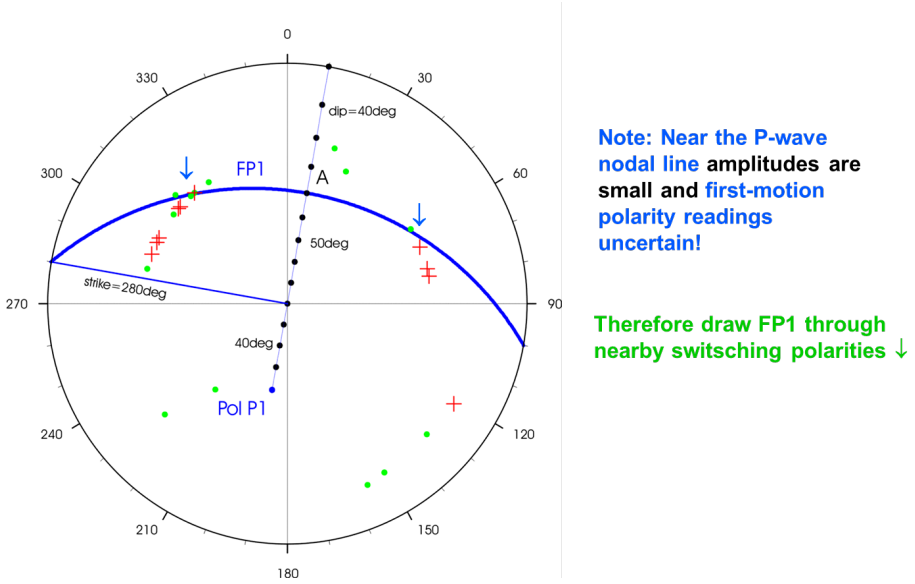

Fig. 3.109 Example for another data set from EX 3.2 to illustrate how FP1 has been found as an appropriate great circle which passes through two clusters of nearby switching polarities, (see blue arrows) and at the same time separating well the majority of + and – (green dots) first motions in the upper part of the data plot. Shown is also how to find the pole P1 and how to measure the dip and the strike of FP1.

In summary, for obtaining a fault-plane solution, basically three steps are required:

(1) Calculating the positions of the penetration points of the seismic rays through the focal sphere which are defined by the ray azimuth AZM and the take-off (incidence) angle Θ of the ray from the source.

(2) Marking these penetration points through the upper or lower hemisphere in a horizontal projection of that sphere using different symbols for compressional and dilatational first arrivals. Usually, lower hemisphere projections are used. Rays which have left the upper hemisphere have then to be transformed into their equivalent lower hemisphere ray. This is possible because of spherical symmetry of the radiation pattern (see Fig. 3.100).
(3) Partitioning the projection of the lower focal sphere by two perpendicular great circles which separate all (or at least most) of the + and - arrivals in different quadrants.

When moving back the marked N direction on the transparent overlay sheet in Fig. 3.108c to the north direction of the stereographic net then we get the beach-ball fault-plan solution depicted in Fig. 3.110. And Fig. 3.111 shows, how the strike, dip, and rake (slip) angles of the two potentially acting faults FP1 and FP2 as well as the azimuth and plunge angles of the pressure and tension axes P and T can then be read on the net diagram. P and T are situated on the equatorial plane EP midway between FP1 and FP2. For more details and how one can decide by way of field evidence, which of the two calculated fault planes has likely be the acting one, see EX 3.2.

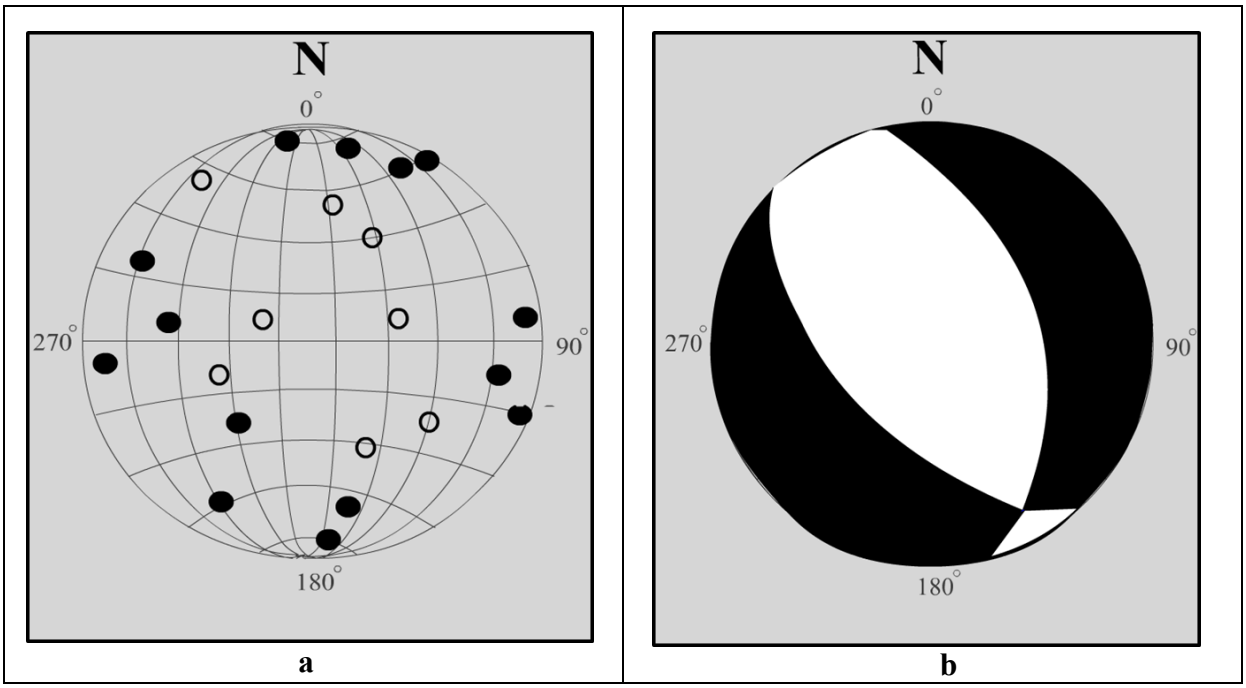

Fig. 3.110 Left: Polarity data plot in in a Lambert-Schmidt net with black dots representing compressional P-wave first arrivals and open circles dilatational signals, respectively; **Right:** the "beach-ball" fault-plane solution deduced from this polarity pattern. It represents a normal faulting with a small strike-slip component along a NNW, respectively SSE striking fault.

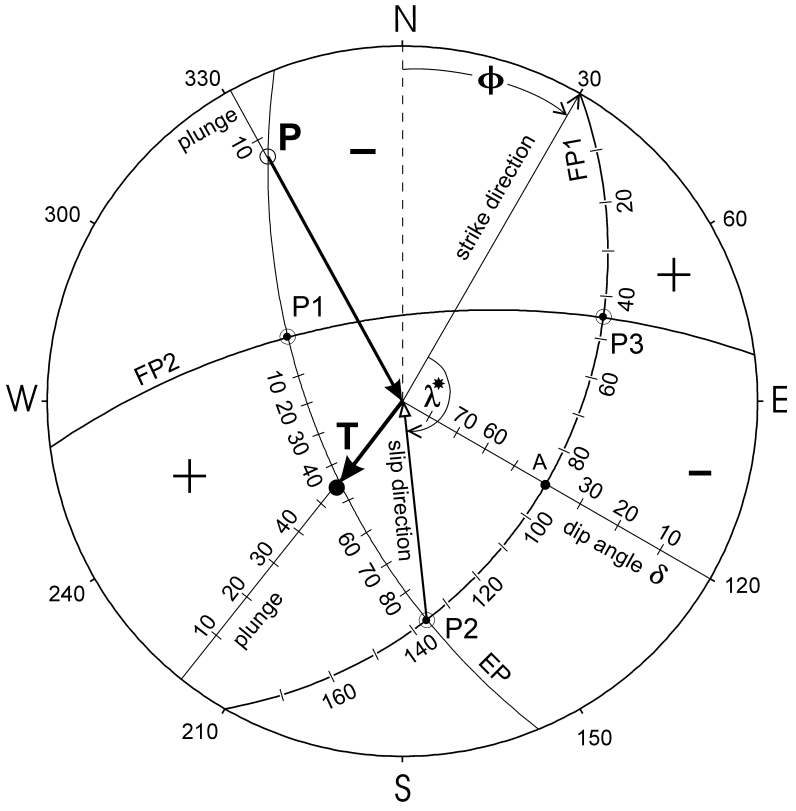

Fig. 3.111 Determination of the fault plane parameters ϕ, δ and λ in the net diagram. The polarity distribution, slip direction and projection of FP1 in this diagram corresponds qualitatively to the faulting case depicted in Fig. 3.107 upper right, namely to a thrust earthquake with a strike-slip component. For abbreviations used see text. **Note:** $\lambda^* = 180° - \lambda$ when the center of the net lies in the tension (+) quadrant (i.e., event with thrust component) or $\lambda^* = -\lambda$ when the center of the net lies in the pressure quadrant (i.e., event with normal faulting component. P1, P2 and P3 mark the positions of the poles of the planes FP1 (fault plane), FP2 (auxiliary plane) and EP (equatorial plane) in their net projections. All three planes are perpendicular to each other and intersect in the poles of the respective third plane, i.e., FP1 and FP2 in P3, FP1 and EP in P2 etc. **P** and **T** are the penetration points (poles) of the pressure and tension axes, respectively, through the focal sphere. + and – signs mark the quadrants with compressional and dilatational P-wave first motions.

For quick proper understanding of published beach-ball solutions, one should just remember a few "rules of thumb", which are well documented by Fig. 3.106:
Note that on the basis of polarity readings alone it cannot be decided whether FP1 or FP2 was the active fault.

- If the two potential fault planes cross each other within the beach ball or net, then there is some strike-slip component involved;
- In the case of pure strike-slip the two fault traces cross as straight lines in the center of the net, respectively the beach-ball;
- If this center is situated in a dilatation or in a compression quadrant then there is a normal faulting, respectively a thrust faulting component involved;

- In the case of pure normal or thrust faulting, either the P axis or the T axis is placed in the net or beach-ball center and the two fault planes do not cross each other within the perimeter (see Fig. 3.106);
- For proper determination of the strike directions of the two faults think yourself standing in the net center with the FP1 fault trace towards your right-hand side. Then look forward along the fault trace until it meets the perimeter. The strike direction of FP1 is then the angle clockwise from north which you read on the perimeter of the net. For finding ϕ(FP2) you have to turn around at the net center so as to place now FP2 at your right-hand side, and then look again towards the end point of FP2 on the perimeter. For the fault-plane solution in Fig. 3.111 you thus get ϕ(FP1) = 30° and ϕ(FP2) = 157°;
- On the basis of polarity readings alone it cannot be decided whether FP1 or FP2 was the active fault.

However, discrimination from seismological data alone is still possible but requires additional study of the *directivity effects* such as azimuthal variation of frequency (*Doppler* effect), amplitudes and/or waveforms (see, e.g., Fig. 3.112 and related discussions and figures in Lay and Wallace, 1995, and in section 2.4 in IS 1.1). For sufficiently large shocks these effects can more easily be studied in low-frequency teleseismic recordings while in the local distance range, high-frequency waveforms and amplitudes may be strongly influenced by resonance effects due to near-surface low-velocity layers (see Chapter 14).

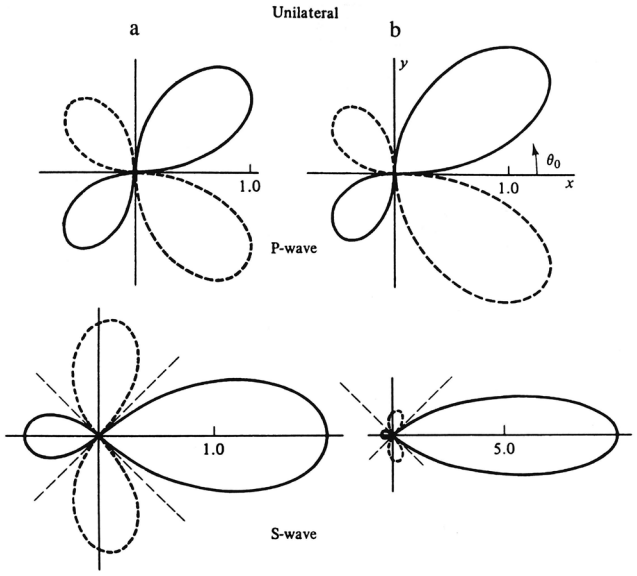

Fig. 3.112 Example for an amplitude directivity effects: Variability of P- and SH-wave amplitude for a fault rupture propagating unilaterally from left to right with a ratio between rupture and shear wave velocity v_r/v_S = 0.5 (left column) and v_r/v_S = 0.9 (right column), respectively. (From Kasahara, 1981; © Cambridge University Press).

Moreover, seismotectonic considerations or field evidence from surface rupture in the case of strong shallow earthquakes may also allow to resolve this ambiguity (see EX 3.2, Figure 7 and related discussion).

Finally, we present a with Fig. 3.113 an example for the fault-plane solution derived for a local earthquake in the Vogtland swarm earthquake region in Germany by means of polarity readings. One can nicely associate the positive first-motion polarity traces (in red) and the respective negative record traces (in blue and turquoise) with the related + and – quadrants of the fault-plane solution plotted over the epicenter of this earthquake.

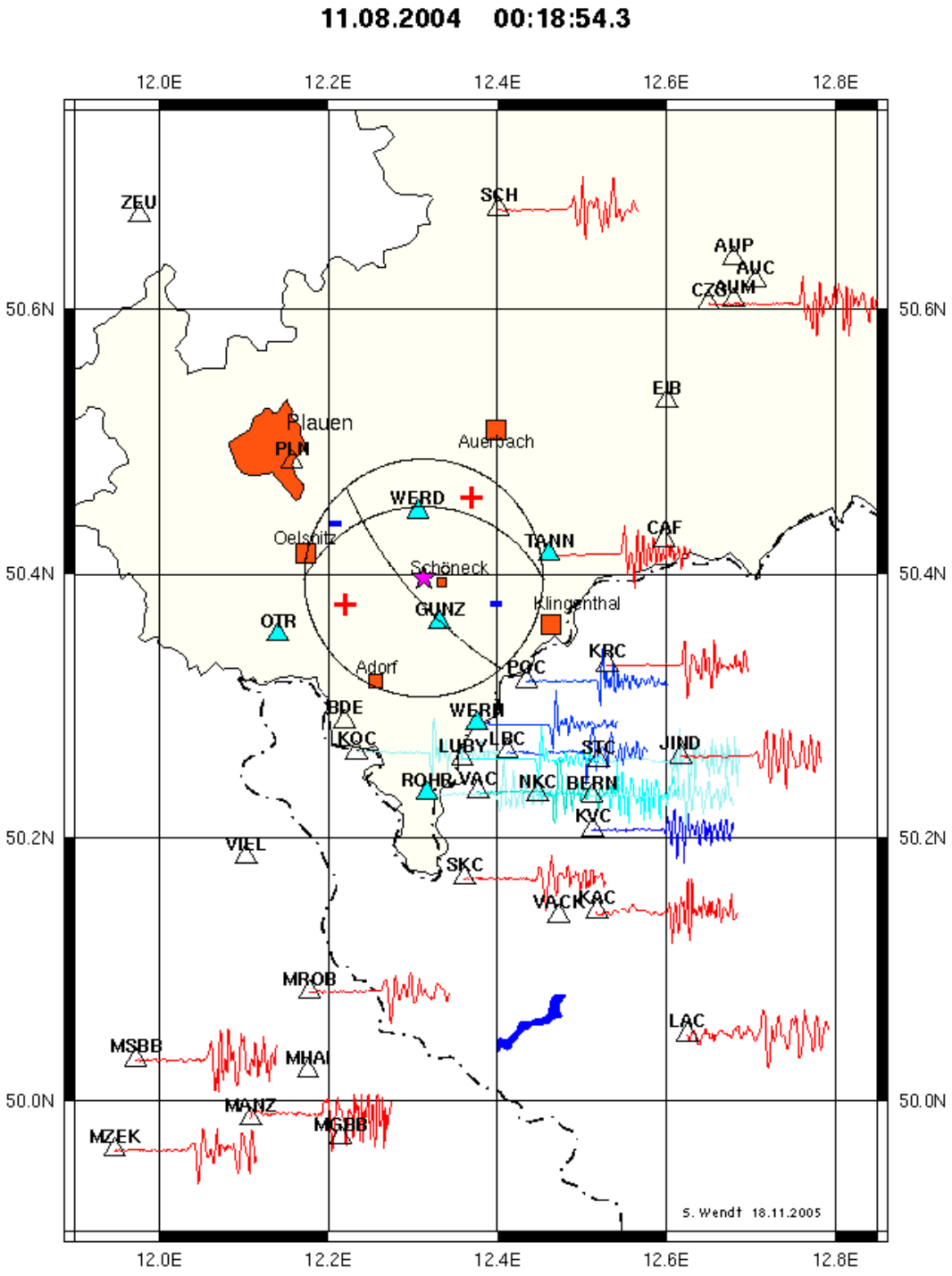

Fig. 3.113 Vertical component recordings of Pg first arrivals at seismic stations in Germany from a local earthquake at epicentre distances between 10 km and 55 km in different azimuths and the „beach ball“ fault-plane solution derived from first motion polarities plotted over the epicenter. The acting fault plane had a strike of about 150° north. It was a normal faulting rupture with a left-lateral strike-slip component.

3.4.3 Accuracy of fault-plane solutions

Fault planes determined by eye-fit to the polarity data may be uncertain by about ± 10°. This is acceptable. Even computer assisted best fits to the data will produce different acceptable solutions within about the same error range with only slightly different standard deviations (e.g., Figure 3.114 with NEIC and HRVD solutions, respectively).

NEIC Moment-tensor solution: s23, scale 10^{17} Nm; M_{rr}-3.05; $M_{\theta\theta}$-0.97; $M_{\phi\phi}$4.03; $M_{r\theta}$-2.51; $M_{r\phi}$-1.95; $M_{\theta\phi}$2.71. Depth 272km; Principal axes: T 6.09, Plg17°, Azm117°; N -136, Plg27°, Azm216°; P -4.73, Plg57°, Azm358°; Best double couple: M_o5.4x10^{17}Nm; NP1:ϕ_s172°, δ36°, λ-140°. NP2: ϕ_s48°, δ68°, λ-60°.

*HRVD 05^d 13^h 24^m 15^s.7±0^s.2, 39°.10N±°.02x15°.39E±°.02, h295^{km}±8^{km}, Centroid moment-tensor solution. Data used: GDSN; LP body waves: s50, c**; Half duration: 1^s.9. Moment tensor: Scale 10^{17}Nm; M_{rr}-2.17±.06; $M_{\theta\theta}$-1.97±.10; $M_{\phi\phi}$4.14±.09; $M_{r\theta}$-3.51±.09; $M_{r\phi}$--3.29±.09; $M_{\theta\phi}$0.01±.09. Principal Axes: T 5.83, Plg27°, Azm103°; N 0.32, Plg30°, Azm210°; P -6.15, Plg48°, Azm339°. Best Double couple: M_o6.0x10^{17}Nm, NP1:ϕ_s146°, δ33°, λ-157°. NP2: ϕ_s37°, δ78°, λ-60°.*

ISC $05^d13^h24^m11^s.4$±0^s.13, **39.16**±0^s.16x**15°.18E**±°.014, **h290^{km}**±1.3^{km}, **(h286km**±2.7^{km}**:pP-P), n757, σ1^s.04**/729, **Mb5.7**/107, **119C-155D, Southern Italy.**

OVO	Vesuviano	1.77	340	↑*i*P	13 24 57.2	+1.5
MCT	Mte Cammarata	1.95	219	P	13 24 57.7	+0.6
FG4	Candela	1.99	8	P	13 24 58.2	+0.9
MEU	Monte Lauro	2.07	186	dP	13 24 56.8	-1.3
PZI	Palazzolo	2.14	186	eP	13 24 57	-1.7
FAI	Favara	2.21	213	dP	13 24 59.5	+0.1
MSC	Monte Massico	2.23	336	↑*i*P	13 25 01.1	+1.6
SGG	Gregorio Matese	2.30	345	↑*i*P	13 25 01.9	+1.8

Figure 3.114 Typical section of an ISC bulletin (left) with NEIC (USGS National Earthquake Information Center) and Harvard University (HRVD) moment-tensor fault-plane solutions (right) for the Italy deep earthquake (h = 286 km) of Jan. 05, 1994. Columns 3 to 5 of the bulletin give the following data: 3 - epicentral distance in degrees, 4 - azimuth AZM in degrees, 5 - phase code and polarity.

In addition, one has to be aware that different fitting algorithm or error-minimization procedures may produce different results within this range of uncertainty for the same data. A poor distribution of seismograph stations (resulting in insufficient polarity data for the net diagram), erroneous polarity readings and differences in model assumptions (e.g., in the velocity models used) may result in still larger deviations between the model solutions and the actual fault planes. One should also be aware that the assumed constant angular (45°) relationship between the fault plane on the one hand and the pressure and tension axis on the other hand is true in fact only in the case of a fresh rupture in a homogeneous isotropic full-space. It may not be correct in the stress environment of real tectonic situations (i.e., **P** and **T** $\neq \sigma_1$ and $-\sigma_3$, respectively; see discussion in section 3.1.2.6: *Parameters which describe and control the source mechanism*).

3.4.4 Computer-assisted fault-plane solutions (P. Bormann)

There exist quite a number of computer programs for the determination of both single and joint fault-plane solutions from first-motion data (e.g., Brillinger et al., 1980; Buforn and Udías, 1984; Udías and Buforn, 1988, and others referred to below). In most applications for local earthquakes homogeneous flat-layered velocity models are acceptable, i.e., layers with constant velocities and velocity discontinuities at the boundaries. The majority of location programs (e.g., HYPO71 by Lee and Lahr, 1975; HYPOELLIPSE by Lahr, 1989 and 2003; HYPOINVERS by Klein, 1978, 1985 and 2002) are based on this type of velocity model. However, HYPOINVERS and HYPOELLIPSE do also accept layers with linear velocity gradients. Moreover, HYPOELLIPSE may locate local events with predefined travel-time tables, too. During the location procedure the ray paths to the stations are calculated. The azimuth AZM and the take-off angle Θ at which the P wave, arriving at a given station, leaves the focal sphere are listed in the output files. The remaining problem to be solved is to find the distribution of P-polarities on the focal sphere and to estimate the angles describing the focal mechanism.

The computer program FPFIT (Reasenberger and Oppenheimer, 1985) calculates double-couple fault-plane solutions based on P-wave polarity readings. It accepts as input the output files of the localization programs HYPO71, HYPOELLIPSE and HYPOINVERSE. The inversion is accomplished through a grid-search procedure that finds the source model by *minimizing a normalized weighted sum of first-motion polarity discrepancies*. Two weighting factors are incorporated in the minimization. One of them reflects the estimated variance of the data while the other one is based on the absolute value of the P-wave radiation amplitude. In addition to the minimum-misfit solution, FPFIT finds alternative solutions corresponding to significant relative misfit minima. The existence of several minima may be due to insufficient number of polarity readings, localization errors, polarity misreadings or an inadequate velocity model (e.g., not modeled refractions) resulting in an incorrect position of the P-wave first-motion polarities on the focal sphere. One has also to be aware that it sometimes may happen that the seismometer component outputs have been wrongly plugged at a given station, resulting in systematically wrong polarity readings by such a station. In the case of models which perfectly fit the data, FPFIT applies an additional constraint. Its effect is to maximize the distance sum between the observation points and the nodal planes on the focal sphere. The display program FPPLOT shows the final fault-plane solution and the estimated uncertainty in terms of the range of possible orientations of the pressure and tension axes which is consistent with the data. This USGS software for Unix and Linux platforms is also available from the ORFEUS Software Library.

While the above programs accept only the output files of the hypocenter localization programs for local events, another widely used program package for seismogram analysis, SEISAN (Havskov, 1996; Havskov and Ottemöller, 1999) uses a modified version of the program HYPOCENTER (Lienert et al., 1988; Lienert, 1991; Lienert and Havskov, 1995. Its version 9.2 can be downloaded via the link *Download programs and files* on the front page or directly via http://folk.uib.no/lot081/seisan.html. The main modifications are that it can also accept secondary phases and locate teleseismic events. The output files are used in conjunction with the programs FOCMEC (Snoke et al., 1984; meanwhile version 2008), FPFIT and HASH (see below) for the determination of the fault plane parameters by using both P-wave first-motion polarities and P/S amplitude ratios, both in the local, regional and teleseismic distance range.

In the case of sparse networks or weak events, the number of polarity data may be too small and/or their distribution in distance and azimuth not appropriate for reliable estimation of fault-plane solutions on the basis of P-wave polarity readings alone. In this case P-, SV- and SH-amplitudes can be used in addition to polarities in order to get more stable and better constrained, i.e., less ambiguous fault-plane solutions. This is due to the difference in the azinuth and take-off angle dependent P-wave and S-wave polarity andamplitude patterns for a given source mechanism (see Figs, 3.100 – 3.103). Fig. 3.115 illustrates this for a teleseismic deep earthquake.

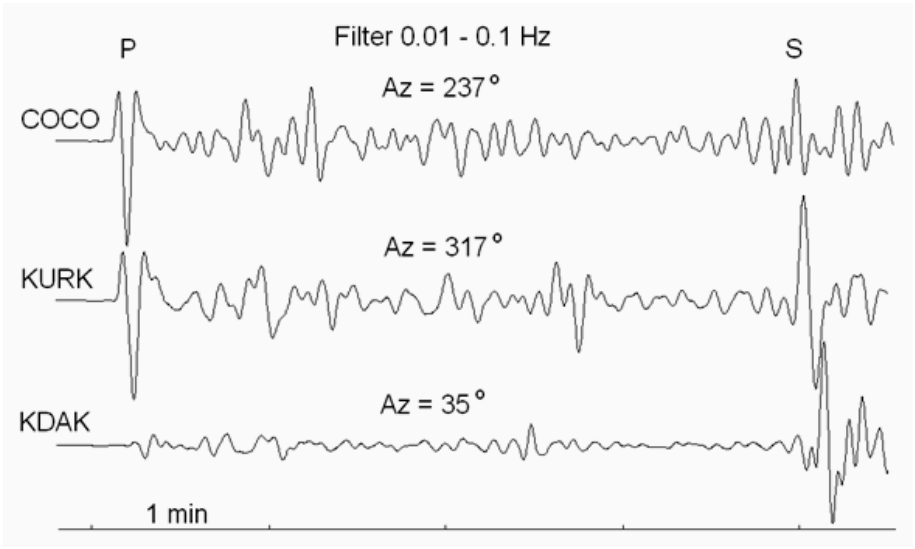

a)

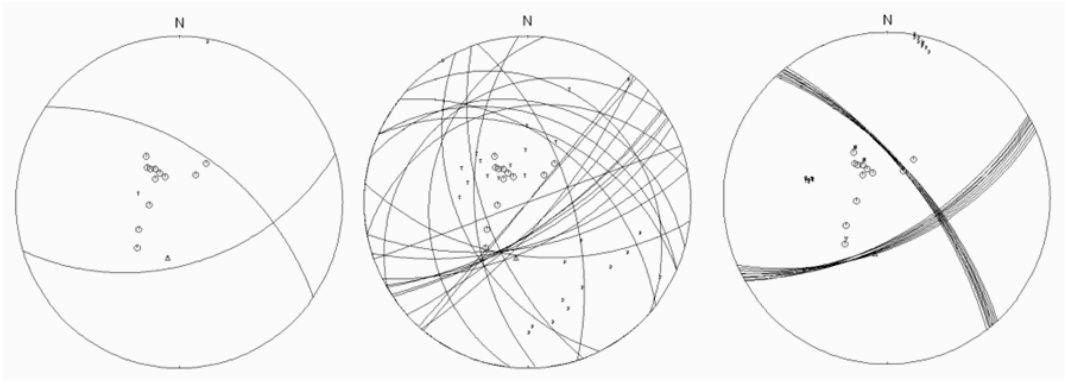

b)

Fig. 3.115 a) Vertical component P and S-wave records from a deep earthquake near Japan (28 Sept. 2007, mb(PDE) = 6.7, h = 260 km). The three stations have similar epicentral distances (Δ = 54 - 58˚) and all recorded a compressional P-wave first motion. This does not tell much about the soure mechanism, in contrast to the S/P amplitude ratio which strongly differs with azimuth Az.

b) The fault-pane solutions FPS obtained for this earthquake. **Left:** The FPS derived from the Harvard moment tensor inversion, here plotted together with 13 available P-wave polarity readings which all fall within one quadrant. **Middle:** Completely inconsistent possible FPSs obtained by a grid search for the 13 polarity readings, all but one being compressional. P and T are the related possible pressure and tension axes **Right:** FPSs obtained by using the 13 polarities and 5 amplitude ratios from 3 stations. Triangle is dilation, hexagon compression and H and V indicate horizontal and vertical component amplitude ratios,. Copied with kind agreement of the authors from Havskov and Ottemöller (2010); © Springer Publishers.

The program FOCMEC (Snoke, 1984, and version 2008) from the IRIS software library allows to calculate best fitting double-couple fault-plane solutions from P, SH and SV polarities and/or SV/P, SH/P or SV/SH amplitude ratios provided that the ratios are corrected to the focal sphere by taking into account geometrical spreading, attenuation and free-surface effects. For surface correction the program FREESURF, which is supplied together with FOCMEC, can be used. The applied Q-model has to be specified according to the regional attenuation conditions or related corrections. When adopting a constant V_P/V_S velocity ratio, the geometrical spreading is the same for P and S waves and absolute changes in amplitude cancel each other in the above amplitude ratios. Head waves and amplitude changes at velocity boundaries require special treatment. The solution is obtained by grid search over strike, dip and slip of the double-couple source. The program FOCPLT, also provided together with FOCMEC, allows to plot upper or lower hemisphere projections of the focal sphere and to show the data, i.e., the fault planes, together with the poles of the pressure (P) and tension (T) axes for SH and SV waves. Note that S-wave amplitudes are zero in the direction of P and T.

A more recent USGS program is HASH 1.0 for Unix platforms. It also computes double-couple earthquake focal mechanisms from both P-wave first motion polarities and, optionally S/P amplitude ratios.

FMSI is a program developed by Gephart (1990). It is a focal mechanism stress inversion package using earthquake focal mechanisms and fault/slickenside data. Kikuchi and Kanamori (1982 and 1986) developed a program for teleseismic body-wave inversion aimed at deriving information about the fault kinematics and/or fault mechanics, and Another program for interactive moment tensor retrieval, termed ISOLA-GUI (Authors: Jiri Zahradnik and Efthimios Sokos) can be downloaded via seismo.geology.**upatras.gr**/isola/.

Other important software tools are presented in the IASPEI (2002) Handbook (TDMT_INVC, Time Domain Seismic Moment Tensor Inversion Code by Douglas Dreger; ftp://www.orfeus-eu.org/pub/software/iaspei2003/8511.html) and in "Computer Programs in Seismology" (Charles J. Ammon and George Randall; regional moment tensor inversion set of programs; http://www.eas.slu.edu/eqc/eqccps.html). For more information and links to programs consult the ORFEUS Software Library (http://www.orfeus-eu.org/Softwarelib.html) and IRIS (http://www.iris.washington.edu).

3.4.5 Estimating M_0, the size of rupture area, average slip and stress-drop from measured seismic spectra (P. Bormann)

Besides deriving some rough estimates of the point source type of rupture, i.e., of the fault-plane solution and average slip direction by analyzing the azimuthal direction of P-wave first motion polarities and/or S/P amplitude ratios additional information about the seismic moment, the size of the rupture area, the average slip and stress drop can be derived by analyzing the seismic spectra of the recorded P and/or S waves. However, with reference to the discussions in section 3.3.1 on seismic scaling laws one should be aware that all these inferences on not directly measurable source parameters are model-based and none of the available models can correctly account for all the parameter and rupture complexities in the real inhomogeneous Earth lithosphere. Therefore, all calculations aimed at deriving these additional parameter informations, have to make assumptions. We shortly demonstrate this here by way of example, also with reference to the related exercise EX 3.4 and the conclusions drawn from it.

With reference to Fig. 3.5 and to formulas (3.1) and (3.2) the scalar seismic moment is written

$$M_0 = \mu \bar{D} A = 4\pi d \rho v^3_{p,s} u_0 / R^{p,s}_{\theta,\varphi} \quad (3.199)$$

and thus be calculated when measuring the spectral displacement plateau amplitude u_0 of the radiated seismic source spectrum. However, this is not directly available, but is available only via the spectra recorded at some distance and specific azimuth away from the source. Therefore, in order to get a reasonable realistic estimate of the primary source spectrum one has to correct it for wave propagation and source radiation effects. This, however, requires either reliable knowledge or good average model assumptions about the

- hypocenter distance d of the source;
- distribution of density ρ and of the P- or S-wave velocity v_p or v_s in the more or less inhomogenous Earth;
- frequency-dependent intrinsic and scattering attenuation of the recorded wave amplitudes for correcting the measured spectral amplitudes;
- surface amplification factor that depends on the incidence angle of the considered seismic wave at the recording station and which is in fact again frequency dependent (see Fig. 2.7 in Chapter 2);
- source radiation coefficient R with respect to the seismic ray recorded at the given seismic station, which is different for P and S waves and depends on the take-off angle and azimuth under which considered seismic ray has left the source.

It is obvious, that most of these factors are only roughly known and that some of the errors, e.g. in the velocity model, propagate even with the third power (Eq. (3.193).

Additionally, the recorded waveforms of well defined non-dispersive seismic body phases have a limited duration of only a few seconds for near earthquakes, up to a few minutes at best for very strong teleseismic events. This limits the spectral range that can be analyzed and makes the recorded spectra rather noisy (see Fig. 3.116). This limits in turn also the accuracy with which u_0 and the corner frequency f_c can be measured on real spectra. f_c is related to the geometric size of the rupture and instrumental for calculating either the radius of assumed circular ruptures (usually for smaller sources) or via even more vaguely estimated additional corner frequencies in the sloping part of the spectrum also of the width W and length L of the rupture plane of larger earthquakes. Knowing either R or L plus W, one may roughly estimate the rupture area via the relationship

$$f_c = c_{m1} v_{p,s}/\pi R = c_{m2} v_{p,s}/(LxW)^{1/2} \quad (3.200)$$

with c_{m1} and c_{m2} being model-dependent constants. Via (3.194) one can relate f_c to a critical wavelength λ_c which is in the order of the source diameter or the sqr of the product L × W:

$$\lambda_c = v_{p,s}/ f_c = c_{m3} \pi R = c_{m4} (LxW)^{1/2}. \quad (3.201)$$

Again, c_{m3} and c_{m4} are other model-dependent parameters.

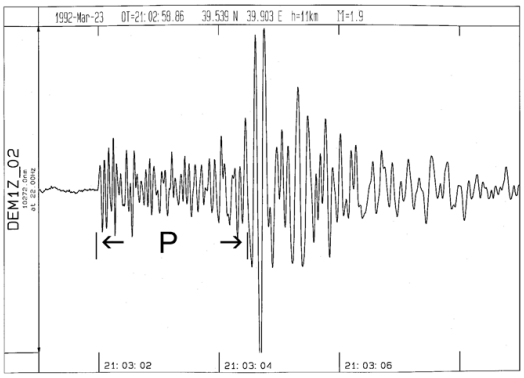

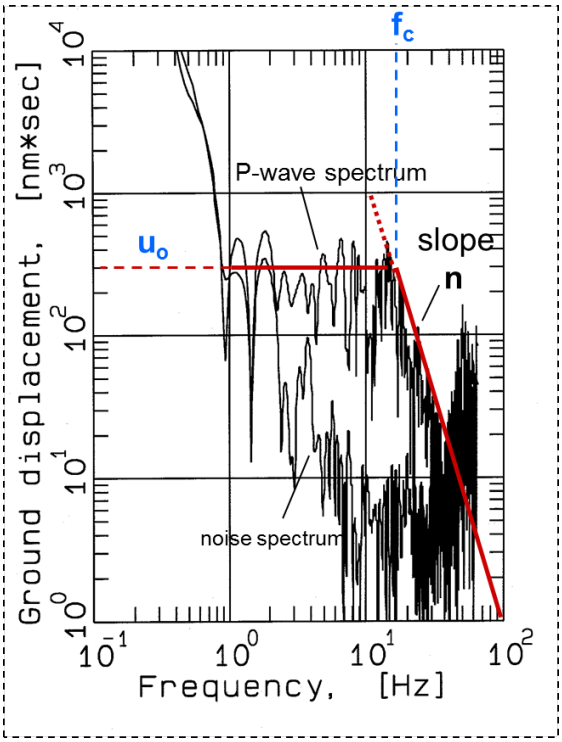

Fig. 3.116 Vertical component record of an Erzincan, Turkey, earthquake aftershock. For the indicated P-wave window the source spectrum on the right side, corrected for instrument response, source distance and attenuation, has been calculated. **Note:** The apparent strong increase of noise amplitudes for f > 30 Hz is sampling noise due to the steep anti-alias filter roll-off for higher frequencies.

With EX 3.4 we show that even for identical measurement input parameters u_0 and f_c, which are both already afflicted with model and reading errors, the calculated values for R, A, average displacement $\bar{D}$ via Eq. (3.193), and stress drop via the formula $\Delta\sigma = 7\ M_o /(16\ R^3)$ according to Keilis-Borok (1959), may already differ by a factor of about 1.8, 3, 4 and 6, respectively, depending one whether one calculates them either according to the Brune (1970) or to the two Madariaga (1976) models, which all assume a circular rupture. This means, however, that one has to use all such model-derived parameters with great caution and accept that they cannot be accurate in absolute terms. Nevertheless, they may be useful, especially when comparing relative parameter changes in space and time in certain seismotectonic areas, or, e.g., for specific aftershock sequences or earthquake swarms. And if in future for the given area better models are available then one may have a chance also to re-calibrate earlier data with the hope to improve also their accuracy in absolute terms.

Acknowledgments and comments

The new Chapter 3 is a strongly revised and largely expanded version of the Chapter 3 in the NMSOP-1 editions of 2002 and 2009. Two of the former co-authors (M. Baumbach and G. Bock) have regrettably passed away already at much too young an age. We have kept and acknowledged some of the figures by M. Baumbach in the current Chapter and moved others in the related exercise EX 3.2 by Bormann, Baumbach and Wendt. The former sub-chapter of G. Bock has now the status of an independent Information Sheet (IS 3.8), thus being a lasting memory to Günther's major contribution to NMSOP-1. Also, the original sub-chapter on seismic energy determinations by G. Choy has become an independent IS 3.6, complemented already by IS 3.5 and awaiting another committed IS 3.9 on seismic energy determination from local and regional seismic events, in collaboration with J. L. Boatwright. Thus, the upgrading and complementation of these important and rapidly developing modern topics have been made independent on the future availability of the editor and main author of Chapter 3. In concordance with this, also the complementation and upgrading of G. Bock's IS

3.8 will be taken up by F. Krueger and co-authors in two new related information sheets IS 3.10 on seismic moment tensor solutions in the local, regional and teleseismic range and IS 3.11, which will become a tutorial on seismic moment tensor solutions. All these new or still forthcoming complementary IS should be considered as being integral parts of Chapter 3.

The current Chapter 3 describes in detail the new IASPEI recommendations for magnitude measurement standards as well the relationship between these new and the common classical magnitudes. These important new pieces of information should be available as early as possibly for the seismological community world-wide. Therefore we opted for an earlier, pre-review publication of Chapter 3 on the Internet. It will be replaced by the finally reviewed and revised version during 2013. However, major parts, especially those relating to the new IASPEI standards as well as several topical sub-sections, have already been reviewed in the current pre-review version. For these careful partial reviews, editorial changes and additional contributions, some made in terms of complementary figures, the editor ows great thanks to J. Dewey, G. Choy, J. Havskov, G. Nolet, A. Lomax and A. Michelini and L. Ottemöller. Quite many figures have also been contributed by J. Saul of the GFZ German Research Centre for Geosciences. They are based on a collaborative work and a joint presentation with P. Bormann and S. Wendt at the 2012 General Assembly of the European Seismological Commission. All contributed figures have been separately acknowledged in the respective captions and J. Saul has been invited to co-author section 3.2.3.2. (acceptance still pending).

Recommended overview readings

Aki and Richards (1980 and 2002)
Båth (1981)
Ben Menahem and Singh (1981 and 2000)
Bormann (2011)
Bormann and Saul (2009a)
Das and Kostrov (1988)
Di Giacomo and Bormann (2011)
Di Giacomo et al. (2013)
Grünthal (2011)
Kanamori and Brodsky (2004)
Lay and Wallace (1995)
Richter (1958)
Scholz (1990 and 2002)
Udias (1999 and 2002)

References

Abe, K. (1975). Reliable estimation of the seismic moment of large earthquakes. *J. Phys. Earth*, **23**, 381-390.

Abe, K. (1979). Size of great earthquakes of 1837-1974 inferred from tsunami data. *J. Geophys. Res.*, 84, 1561-1568.

Abe, K. (1981a). Magnitudes of large shallow earthquakes from 1904 to 1980. *Phys. Earth Planet. Interiors*, **27**, 72-92.

Abe, K. (1981b). Physical size of tsunamigenic earthquakes of the northwestern Pacific. *Phys. Earth Planet. Inter.*, **27**, 194-205.

Abe, K. (1982). Magnitude, seismic moment and apparent stress for major deep earthquakes. *J. Phys. Earth,* **30**, 321-330.

Abe, K. (1984). Complements to "Magnitudes of large shallow earthquakes from 1904 to 1980". *Phys. Earth Planet. Interiors*, **34**, 17-23.

Abe, K., and Kanamori, H. (1979). Temporal variation of the activity of intermediate and deep focus earthquakes. *J. Geophys. Res.*, 84, B7, 3589-3595.

Abe, K., and Kanamori, H. (1980). Magnitudes of great shallow earthquakes from 1953 to 1977. *Tectonophys.*, **62**, 191-203.

Abe, K. (1989). Quantification of tsunamigenic earthquakes by the M_t scale. *Tectonophysics*, **166**, **27-34.**

Abercrombie, R. E. (1994). Regional bias in estimates of earthquake M_s due to surface-wave path effects. *Bull. Seism. Soc. Am.*, **84**, 2, 377-382.

Abercrombie, R. E. (1995). Earthquake source scaling relationships from -1 to 5 M_L using seismograms recorded at 22.5 km depth. *J. Geophys Res.*, **100**, 24,015-24,036.

Adams, W. M., and Allen, D. W. (1961). Seismic decoupling for explosions in spherical underground cavities. *Geophysics*, **26**(6), 772-799.

Adams, W. M., and Swift, L. W. (1961). The effect of shotpoint medium on seismic coupling. *Geophysics*, **26**(6), 765-771.

Aki, K. (1966). Generation and propagation of *G* waves from the Niigata earthquake of June 16, 1964, part 2: Estimation of earthquake moment, released energy, and stress-strain drop from the *G* wave spectrum. *Bull. Earthq. Res. Inst. Toyo Univ.*, **44**, 73-88.

Aki, K. (1967). Scaling law of seismic spectrum. *J. Geophys. Res*., **72**, 1217-1231.

Aki, K., and Chouet, B. (1975). Origin of coda waves: Source, attenuation and scattering effects. *J. Geophys. Res*., **80**, 3322.

Aki, K., and Patton, H. (1978). Determination of seismic moment tensor using surface waves. *Tectonophysics,* **49,** 213−222.

Albarello, D., Berardi, A., Margottini, C., and Mucciarelli, M. (1995). Macroseismic estimates of magnitude in Italy. *Pure Appl. Geophys*., **145**, 2, 297-312.

Allen, R.V., and Kanamori, H. (2003). The potential for earthquake early warning in Southern California. *Science*, 300, 786-789.

Alsaker, A., Kvamme, L. B., Hansen, R. A., Dahle, A., and Bungum, H. (1991). The M_L scale in Norway. *Bull. Seism. Soc. Am*., **81**, 2, 379-389.

Ambraseys, N. N. (1985). Magnitude assessment of northwestern European earthquakes. *Earthq. Eng. Struct. Dynam*., **13**, 307-320.

Ambraseys, N. N. (1988). Magnitude-fault length relationships for earthquakes in the middle east. In: W. H. K. Lee (ed.). Historical seismograms and earthquakes of the world. *Academic Press*, 309-310.

Ambraseys, N. N. (1990a). Uniform magnitude re-evaluation of European earthquakes associated with strong-motion records. *Earthq. Eng. Struct. Dynam*, **19**, 1-20.

Ambraseys, N. N. (1990b). Uniform magnitude re-evaluationg-motion data base of Europe and adjacent areas. *Europ. Earthq. Eng*., **2,** 3-16.

Ammon, C. J. (2001). Moment tensor inversion overview. http://eqseis.geosc.psu.edu/ ~cammon/ (last accessed January 2005).

Anderson, E. M. (1951). The dynamics of faulting and dyke formation with applications to Britain. 2nd ed. rev., *Oliver & Boyd Publishers*, Edinburgh.

Anderson, D. L., Kanamori, H., Hart, R.S., and Liu, H. (1976). The Earth as a seismic absorption band. *Science*, **196**,1104-1106.

Anderson, D. L., and Given, J.W. (1982). Absobtion band Q model for the Earth. J. Geophys. Res., **87**, 3893-3904.

Atkinson, G. M., and Hanks, Th. (1995). A high-frequency magnitude scale. *Bull. Seism. Soc. Am.*, **85**, 3, 825-833.

Atkinson, G. M., and Beresnev, I. A. (1997). Don't call it stress drop. *Seism. Res. Lett.*, **68**, 3-4.

Bakun, W. H., and Joyner, W. (1984). The M_L scale in Central California. *Bull. Seism. Soc. Am.*, **74**, 5,1827-1843.

Bakun, W. H., and Lindh, A. G. (1977). Local magnitudes, seismic moments, and coda durations for earthquakes near Oroville, California. *Bull. Seism. Soc. Am.*, **67**, 615 -629.

Bakun, W. H., and Wentworth, C. M. (1997). Estimating earthquake location and magnitude from seismic intensity data. *Bull. Seism. Soc. Am.,* **87**, 1502-1521.

Bates, D. M., and Watts, D. G. (1988). *Nonlinear regression analysis and its applications* Wiley, New York.

Bates, D. M., and Chambers, J. M. (1992). Nonlinear models. In Chambers, J. M. and Hastie, T. J. (Eds). *Statistical Models in S*, Wadsworth, Pacific Grove, CA, 421-454,

Båth, M. (1962). Seismic records of explosions – especially nuclear explosions. *Part III FOA 4 Rapport.*

Båth, M. (1981). Earthquake magnitude - recent research and current trends. *Earth Science Reviews*, **17**, 315-398.

Båth, M. (1985). Surface-wave magnitude corrections for intermediate and deep earthquakes. *Physics Earth Planet. Interiors*, **37**, 228-234.

Båth, M, Kulhánek, O., van Eck, T., and Wahlstroem, R. (1976). Engineering analysis of ground motion in Sweden. *Seismological Institute of Uppsala, University Report no. 5-76.*

Bates, D. M., and Watts, D. G. (1988). *Nonlinear regression analysis and its applications*. Wiley, New York.

Bates, D. M., and Chambers, J. M. (1992). Nonlinear models. In: Chambers, J. M. and Hastie, T. J. (eds), *Statistical Models in S*, 421-454, Wadsworth, Pacific Grove, CA.

Ben-Menahem, A., and Singh, S. J. (1981). *Seismic waves and sources*. Springer Verlag, New York, Heidelberg, Berlin, 1108 pp.

Ben-Menahem, A., and Singh, S. J. (2000). *Seismic waves and sources*." 2nd edition, Dover Publications, New York.

Benz, H. M., Frankel, A., and Boore, D. M. (1997). Regional Lg attenuation for the continental United States. *Bull. Seism. Soc. Am*., **87**(3), 606-619.

Ben-Zion, Y. (1989). The response of two joined quarter spaces to SH line sources located at the material discontinuity interface. *Geophys. J. Int.,* **98**, 213-222.

Ben-Zion, Y. (2001). On quantification of earthquake source. *Seism. Res. Lett*., **72** (2), 151-152.

Ben-Zion, Y., and Zhu, L. (2002). Potency-magnitude scaling relations for southern California earthquakes with $1.0 < M_L < 7.0$. Geophys. J. Int., **148**, F1-F5

Berckhemer, H., Kampfmann, W., Aulbach, E., and Schmeling, H. (1982). Shear modulus and Q of forsterite and dunite near partial melting from forced-oscillation experiments. *Phys. Earth Planet. Inter*., **29,** 30-41.

Berckhemer, H., and Lindenfeld, M. (1986). Determination of source energy from broadband seismograms. In: Buttkus, B. (Ed.)(1986). Ten years of the Gräfenberg Array: Defining the frontiers of broadband seismology. *Geologisches Jahrbuch* Reihe E, Heft 35, 79-83.

Beresnev, I. A. (2001). What we can and cannot learn about earthquake. *Bull. Seism. Soc. Am*., **91**, 397-400.

Beresnev, I. A. (2008). The reality of the scaling law of earthquake-source spectra? J. Seismol.; DOI: 10.1007/s10950-008-9136-9.

Beyreuther, M., Barsch, R., Krischer, L., Megies, T., Behr, Y., and Wassermann, J. (2010). ObsPy: A Python Toolbox for Seismology. *Seism. Res. Lett*., **81**(3), 530-533; doi: 10.1785/gssrl.81.3.530.

Bindi, D., Spallarossa, D., Eva, C., and Cattaneo, M. (2005). Local and duration magnitudes in Northwestern Italy, and seismic moment versus magnitude relationships. *Bull. Seism. Soc. Am*., **95**, 2, 592- 604.

Boatwright, J., and Choy, G. (1986). Teleseismic estimates of the energy radiated by shallow earthquakes. *J. Geophys. Res*., **91**, B2, 2095-2112.

Boatwright, J., and G. L. Choy (1989). Acceleration spectra for subduction zone earthquakes. *J. Geophys. Res.*, **94**, B11, 15,541-15,553.

Bondár, I. and D. Storchak. (2011). Improved location procedures at the International Seismological Centre. *Geophys. J. Int.,* **186**, 1220-1244, doi:10.1111/j.1365-246X2011.05107.x

Bonner, J. L., Russel, D. R., Harkrider, D. G., Reiter, D. T., and Herrmann, R. B. (2006). Development of a time-domain, variable-period surface-wave magnitude measurement procedure for application at regional and teleseismic distances, part II: Application and Ms-mb performance. *Bull. Seism. Soc. Am.* **96**, 2, 678-696, doi: 10.1785/0120050056.

Boore, D. M. (1977). The motion of the ground in earthquakes. *Scientific American*, December 1977, W. H. Freeman and Company, San Francisco, 1-19.

Boore, D. M. (1983). Stochastic simulation of high-frequency ground motions based on seismological models of the radiated spectra. *Bull. Seism. Soc. Am*., **83**, 1865-1894.

Boore, D. M. (1989). The Richter scale: its development and use for determining earthquake source parameter. *Tectonophysics*, **166**, 1-14.

Bormann, P. (1966). *Recording and interpretation of seismic events (principles, present state and tendencies of development)* (in German: Registrierung und Auswertung seismischer Ereignisse – Grundlagen, Stand und Entwicklungstendenzhen). Publications of the Institut für Geodynamik, Jena, Akademie Verlag, Berlin, Vol. 1, 158 pp.

Bormann, P. (2011). Earthquake magnitude. In: Harsh Gupta (ed.). *Encyclopedia of Solid Earth Geophysics,* Springer, 207-218; doi: 10.1007/978-90-481-8702-7.

Bormann, P., and Khalturin, V. I. (1975). Relations between different kinds of magnitude determinations and their regional variations. *Proceed. XIVth General Assembly of the European Seismological Commission*, Trieste, 16-22 September 1974. Published by the Nationalkomitee Geod. Geophys., AdW der DDR, Berlin, 27-39.

Bormann, P., and Wylegalla, K. (1975). Investigation of the correlation relationships between various kinds of magnitude determination at station Moxa depending on the type of

instrument and on the source area (in German). *Public. Inst. Geophys. Polish Acad. Sci*., **93**, 160-175.

Bormann, P., Wylegalla, K., and Grosser, H. (1992) The strong mining event of March 13, 1989: Analysis of the multiple event. *Proced. XXII. General Assembly of the European Seismological Commission (ESC), Barcelona, 17-22 Sept. 1990*, Proceedings and Activity Report 1988-1990, Servei Geològic de Catlunya, 153-158.

Bormann, P., and Wendt, S. (1999). Identification and analysis of longitudinal core phases: Requirements and guidelines. In: Bormann (1999), Regional International Training Course 1999 on Seismology, Seismic Hazard Assessment and Risk Mitigation. Lecture and exercise notes. Vol. I and II, GeoForschungsZentrum Potsdam, *Scientific Technical Report* **STR99/13**, 346-366.

Bormann, P., and K. Wylegalla (2005). Quick estimator of the size of great earthquakes. *EOS, Transactions, American Geophysical Union*, **86** (46), 464.

Bormann, P., and J. Saul (2008). The new IASPEI standard broadband magnitude m_B, *Seismol. Res. Lett.* **79** (5), 699-706.

Bormann, P., and Saul, J. (2009a). Earthquake magnitude. In: *Encyclopedia of Complexity and Systems Science*, edited by A. Meyers, Springer, Heidelberg, Vol. 3, 2473-2496.

Bormann, P., and Saul, J. (2009b). A fast, non-saturating magnitude estimator for great earthquakes, *Seism. Res. Lett.* **80** (5), 808-816; doi: 10.1785/gssrl.80.5.808.

Bormann, P., Liu, R., Ren, X., Gutdeutsch, R., Kaiser, D., Castellaro, S. (2007). Chinese national network magnitudes, their relation to NEIC magnitudes, and recommendations for new IASPEI magnitude standards. *Bull. Seism. Soc. Am.*, **97**, 114-127.

Bormann, P., Liu, R., Xu, Z., Ren, K., Zhang, L., Wendt S. (2009). First application of the new IASPEI teleseismic magnitude standards to data of the China National Seismographic Network, *Bull. Seism. Soc. Am.*, **99** (3), 1868-1891; doi: 10.1785/0120080010

Bormann, P., and D. Di Giacomo (2011). The moment magnitude M_w and the energy magnitude M_e: common roots and differences. *J. Seismology*, **15**, 411-427; doi: 10.1007/s10950-010-9219-2.

Bouchon, M. (1982). The complete synthesis of seismic crustal phases at regional distances, *J. Geophys. Res.* 78, 1735-1741.

Bouchon, M., and Vallée, M. (2003). Observation of long supershear rupture during the magnitude 8.1 Kunlunshan earthquake. *Science*, **301**, 824-826.

Braunmiller, J., Deichmann, N., Giardini, D., Wiemer, St., and the SED Magnitude Working Group (2005). Homogeneous moment-magnitude calibration in Switzerland. *Bull. Seism. Soc. Am*., **95**, 1, 58-74.

Brillinger, D. R., Udias, A., and Bolt, B. A. (1980). A probability model for regional focal mechanism solutions. *Bull. Seism. Soc. Am*., **70**, 149-170.

Brune, J. N. (1970). Tectonic stress and the spectra of shear waves from earthquakes. *J. Geophy. Res.*, **75**, 4997-5009.

Brune, J. N., and Engen, G. R. (1969). Excitation of mantle Love waves and definition of mantle wave magnitude. *Bull. Seism. Soc. Am*., **59**, 923-933.

Buforn, E., and Udias, A. (1984). An algorithm for focal mechanism determination using signs of first motion of P, SV, SH waves. *Rev. Geofisica*, **40**, 11-26.

Bullen, K. E., and Bolt, B. A. (1985). An introduction to the theory of seismology. Fourth Edition, *Cambridge University Press*, 4th revised ed., xvii+499 pp., ISBN: 0-521-28389-2, 451-454, 499 pp..

Castellaro, S., Mulargia, F., and Kagan, Y. Y. (2006). Regression problems for magnitudes. *Geophys. J. Int.*, **165,** 913-930.

Castello, B., Olivieri, M., and Selvaggi, G. (2007). Local and duration magnitudes determination for the Italian earthquake catalog, 1981-2002. *Bull. Seism. Soc. Am.*, **97**, 128-139.

Chávez, D. E., and Priestley, K. F. (1985). ML observations in the Great Basin and Ms versus ML relationships for the 1980 Mammoth Lakes, California, earthquake sequence. *Bull. Seism. Soc. Am.*, **75**, 6, |1583-1598.

Chen, P., and Chen, H. (1989). Scaling law and its applications to earthquake statistical relations. *Tectonophysics*, **166**, 53-72.

Chinnery, M. A. (1969). Earthquake magnitude and source parameters. *Bull. Seism. Soc. Am.*, **59**, 5, 1969-1982.

Choy, G. L. (2012). IS 3.5: Stress conditions inferable from modern magnitudes: development of a model of fault maturity, 10 pp., DOI: 10.2312/GFZ.NMSOP-2_IS_3.5; In: Bormann, P. (Ed.) (2012). *New Manual of Seismological Observatory Practice (NMSOP-2)*, *IASPEI,* GFZ German Research Centre for Geosciences, Potsdam; http://nmsop.gfz-potsdam.de; DOI: 10.2312/GFZ.NMSOP-2.

Choy, G. L., and Boatwright, J. L. (1995). Global patterns of readiated seismic energy and apparent stress. *J. Geophys. Res.*, **100**, B9, 18,205-18,228.

Choy, G. L., and Kirby, S. H. (2004). Apparent stress, fault maturity and seismic hazard for normal-fault earthquakes at subduction zones, *Geophys. J. Int.*, **159**, 991-1012.

Choy, G. L., and Boatwright, J. (2007). The energy radiated by the 26 December 2004 Sumatra-Andaman earthquake estimated from 10.minute P-wave windows. *Bull. Seism. Soc. Am*., **97**, 1A, S18-S24; doi: 10.1785/0120050623.

Choy, G. L., McGarr, A., Kirby, S. H., and Boatwirght, J. (2006). An overview of the global variability in radiated energy and apparent stress; in: Abercrombie R. , McGarr, A., and Kanamori, H. (eds): Radiated energy and the physics of earthquake faulting, *AGU Geophys. Monogr. Ser.* **170**, 43-57.

Christoskov, L., Kondorskaya, N. V., and Vaněk, J. (1978). Homogeneous magnitude system of the Eurasian continent. *Tectonophysics*, **49**, 131-138.

Christoskov, L., Kondorskaya, N. V., and Vaněk, J. (1983). Homogeneous magnitude system of the Eurasian continent: S and L waves. *World Data Center A for Solid Earth*, Boulder Report SE-34.

Christoskov, L., Kondorskaya, N. V., and Vaněk, J. (1985). Magnitude calibration functions for a multidimensional homogeneous system of reference stations. *Tectonophysics*, **118**, 213-226.

Christoskov, L., Kondorskaya, N. V., and Vaněk, J. (1991). Homogeneous magnitude system with unified level for usage in seismological practice. *Studia geoph. ett geod*., **35**, 221-233.

Cifuentes, I. L., and Silvers, P. G. (1989). Low-frequency source characteristics of the great 1960 Chilean earthquake. *J. Geophys. Res.*, **94**, No. B1, 643-663.

Das, S., and Kostrov, B. V. (1988). Principles of earthquake source mechanics. *Cambridge University Press.*

Das, R., Wason, H. R., and Sharma, M. L. (2011). Global regression relations for conversion of surface wave and body wave magnitudes to moment magnitude. *Nat. Hazards*, **59**, 801-810.

Das, R., Wason, H. R., and Sharma, M. L. (2013).General orthogonal regression relations between body-wave and moment magnitudes. *Seism. Res. Lett.*, **84**(2), 219-224; doi: 10.1785/0220120125.

Dawers, N. H., Anders, M. H., and Scholz, C. H. (1993). Growth of normal faults: Displacement-length scaling. *Geology*, **21**, 1107-1110.

Der, Z. A., McElfresh, Th. W., and O´Donnell, A. (1982). An investigation of the regional variations and frequency-dependence of anelastic attenuation in the mantle under the United States in the 0.5-4 Hz band. *Geophys. J. R. astr. Soc.*, **69**, 68-99.

Dewey, J. W., Cantavella Nathal, J.V., and Wendt, S. (2011). Testing of USGS/NEIC automatic procedures for computing IASPEI standard magnitudes. Poster presented at the IUGG Meeting 2011 in Melbourne.

Di Giacomo, D., and Bormann, P. (2011). Earthquake energy. In: Harsh Gupta (ed.). *Encyclopedia of Solid Earth Geophysics,* Springer, 233-236; doi: 10.1007/978-90-481-8702-7.

Di Giacomo, D., Grosser, H., Parolai, S., Bormann P., and Wang, R. (2008). Rapid determination of Me for strong to great shallow earthquakes. *Geophys. Res. Lett.*, **35**, L10308; doi:10.1929/2008GL033505.

Di Giacomo, D., Parolai, S., Bormann P., Grosser, H., Saul, J., Wang, R., and Zschau, J. (2010a). Suitability of rapid Energy magnitude estimations for emergency response purposes. *Geophys. J. Int.*, **180**, 361-374; doi: 10.1111/j.1365-246X.2009.04416.x.

Di Giacomo, D., Parolai, S., Bormann P., Grosser, H., Saul, J., Wang, R., and Zschau, J. (2010b). Erratum to "Suitability of rapid Energy magnitude estimations for emergency response purposes." *Geophys. J. Int.*, **181**, 1725-1726; doi: 10.1111/j.1365-246X.2010.04610.x.

Di Giacomo, D., Bondár, I., Storchak, D. A., Engdahl, E., R., Bormann, P., and Harris, J. (2013). ISC-GEM: Global Instrumental Earthquake Catalogue (1900-2009), III. Re-computed M_S and m_b, proxy M_W, final magnitude composition and completeness assessment. *Phys. Earth Planet. Int.* (submitted).

Dindi, E. J., Havskov, J., Iranga, M., Jonathan, E., Lombe, D. K., Mamo, A., and Tutyomurugyendo, G. (1995). *Bull. Seism. Soc. Am.*, **85**,354-360.

Doornbos, D. J. (Ed.) (1988). Seismological algorithms, Computational methods and computer programs. *Academic Press*, New York, xvii + 469 pp.

Duda, S. J. (1986). The spectra and magnitudes of earthquakes. In: Buttkus, B. (Ed.). Ten years of the Gräfenberg Array: Defining the frontiers of broadband seismology. *Geologisches Jahrbuch* Reihe E, Heft **35**, 71-79.

Duda, S. J., and Kaiser, D. (1989). Spectral magnitudes, magnitude spectra, and earthquake quantification: the stability issue of the corner period and of the maximum magnitude for a given earthquake. *Tectonophysics*, **166**, 205-219.

Duda, S. J., and Yanovskaya, T. B. (1993). Spectral amplitude-distance curves for P-waves: effects of velocity and Q-distribution. *Tectonophysics*, **217**, 255-265.

Dziewonski, A. M., and Anderson, D. L. (1981). Preliminary reference Earth model. *Phys. Earth Planet. Inter.,* **25**, 297-356.

Dziewonski, A. M., Chou, T. A., and Woodhouse, J.H. (1981). Determination of earthquake source parameters from waveform data for studies of global and regional seismicity. *J. Geophys. Res*., 86, 2825-2852.

Eaton, J. P. (1992). Determination of amplitude and duration magnitudes and site residuals from short-period seismographs in Northern California. *Bull. Seism. Soc. Am*., **82**, 2, 533-579.

Ebel, J. E. (1982). M_L measurements for northeastern United States earthquakes. *Bull. Seism. Soc. Am.*, **72**, 1367-1378.

Ebel, J. E. (1994). The $M_{Lg}(f)$ magnitude scale: A proposal for its use for northeastern North America. *Seism. Res. Lett*., **65**, 2, 157-166.

Ekström, G., and Dziewonski, A. M. (1988). Evidence of bias in estimations of earthquake size. *Nature*, **332**, 319-323.

Ekström, G., Nettles, M., and Dziewonski, A.M. (2012). The global CMT project 2004–2010: Centroid-for 13,017 earthquakes, *Phys. Earth Planet. Inter.*, 200-201, 1-9.

Engdahl, E. R., and Gunst, R. H. (1966). Use of a high speed computer for the preliminary determination of earthquake hypocenters. *Bull. Seism. Soc. Am.,* **56**, 325-336.

Eshelby, J. D. (1969). The elastic field of a crack extending non-uniformly under general anti-plane loading. *J. Mech. Phys. Solids*, **8**, 100-104.

Espinoza-Aranda, H. M., Jiminez, A., Ibarrola, G., Alcantar, F., Aguilar, A. et al. (1995): Mexico City seismic alert system. Seism. Res. Lett., 66, 42-53.

Espinoza-Aranda, H. M., and Rodriguez, F. H. (2003). The seismic Alert System of Mexico City. In: Lee, W. H. K., Kanamori, H., Jennings, P. C., and Kisslinger, C. (Eds.) (2002). *International Handbook of Earthquake and Engineering Seismology*, Part B. Academic Press, Amsterdam, 1253-1259.

Ewing, M., Jardetzky, W. S., and Press, F. (1957). *Elastic Waves in Layered Media*. McGraw-Hill, New York, 358 pp..

Fukao, Y. (1979). Tsunami earthquakes and subduction processes near deep-sea trenches. J. Geophys. Res., **84**, 2303–2314.

Frankel, A. (1994). Implications of felt area-magnitude relations for earthquake scaling and the average frequency of perceptible ground motion. *Bull. Seism. Soc. Am*., **84**, 2, 462-465.

Galanopolous, A. G. (1961). On magnitude determination by using macroseismic data. *Ann. Geofis.*, **14**, 225-253.

Gasperini, P., Bernardini, F., Valensise, G., and Boschi, E. (1999). Defining seismogenic sources from historical earthquakes felt reports. *Bull. Seism. Soc.Am*., **89**, 94-110.

Geller, R. J. (1976). Scaling relations for earthquake source parameters and magnitudes. *Bull. Seism. Soc. Am.,* **66**, 1501-1523.

Geller, R. J., and Kanamori, H. (1977). Magnitudes of great shallow earthquakes from 1904 to 1952. *Bull. Seism. Soc. Am*., **67** (3),587–598.

Geller, R. J., and Mueller, C. S. (1980). Four similar earthquakes in central California. *Geophys. Res. Lett.*, **7**, 821-824.

Gephart, J. W. (1990). FMSI: Focal mechanism stress inversion package using earthquake fault mechanisms and faul/slickenside data. *Computer and Geosiences*, **16**(7), 953-989.

Gephart, J. W., and Forsyth, D. W. (1984). An improved method for determining the regional stress tensor using earthquake focal mechanism data: application to the San Fernando earthquake sequence. *J. Geophys. Res*., **89**, 9305-9320.

Giardini, D. (1988). Frequency distribution and quantification of deep Earthquakes. *J. Gophys. Res.*, 93, 2095-2105.

Goldstein, P., and Archuleta, R. I. (1991). Deterministic frequency-wavenumber methods and direct measurement of rupture during earthquakes using a dense array-data analysis. *J. Geophys. Res.*, **96**, 6187-6198.

Gordon, D. W. (1971). Surface-wave versus body-wave magnitude. *Earthquake Notes*, **42**, 3-4, 20-28.

Granville, J. P., Kim, W.-Y., and Richards, P. G. (2002). An assessment of seismic body-wave magnitudes published by the Prototype International Data Centre. *Seism. Res. Lett*., **73**(6), 893-906.

Granville, J. P., Richards, . G., Kim, W.-Y., and Sykes, L. R. (2005). Understanding the differences between three teleseismic m_b scales. *Bull. Seism. Soc. Am.*, **95**(5), 1809-1824.

Grecksch, G., and Kümpel, H.-J. (1997). Statistical analysis of strong-motion accelerograms and its application to earthquake early-warning systems. *Geophys. J. Int.*, **129**, 113-123.

Greenhalgh, S. A., and Singh, R. (1986). A revised magnitude scale for South Australian earthquakes. *Bull. Seism. Soc. Am*., **76**, 3, 757-769.

Greenhalgh, S. A., Denham, D., McDougall, R., and Rynn, J. M. (1989). Intensity relations for Australian earthquakes. Tectonophysics, **166**, 255-267.

Griggs, D., and Press, F. (1961). Probing the earth with nuclear explosions. *J. Geophys. Res.*, **66**(1) 237-258.

Gross, S. (1996). Magnitude distributions and slip scaling of heterogeneous seismic sources. *Bull. Seism. Soc. Am*., **86** (2), 498-504.

Grünthal, G. (Ed.) (1998). European Macroseismic Scale 1998, *Cahiers du Centre Europèen de Gèodynamique et de Seismologie*, **15**, Conseil de l'Europe, Luxembourg, 99 pp.

Grünthal, G. (2011). Earthquake intensity. In: Harsh Gupta (ed.). *Encyclopedia of Solid Earth Geophysics,* Springer, 237-242; doi: 10.1007/978-90-481-8702-7.,

Grünthal, G., and Wahlström, R. (2003). An Mw based earthquake catalogue for central, northern and northwestern Europe using a hierarchy of magnitude conversions. *J. Seismol.*, **7** (4), 507-531.

Grünthal, G., Wahlström, R., and Stromeyer, D. (2009). Harmonization check of Mw within the central, northern, and nortwestern European earthquake catalogue (CENEC). *J. Seismology*, **13**(4), 613-623.

Gusev, A. A. (1989). Multiasperity fault model and the nature of short-period subsources. *Pure Appl. Geophys.*, **130**, 635-660.

Gusev, A. A. (1991). Intermagnitude relationships and asperity statistics. *Pure Appl. Geophys*., **136**, 515-527.

Gusev, A. A., and Melnikova, V. N. (1992). Relationships between magnitude scales for global and Kamchatkan earthquakes. *Volc. Seism*.,,**12**, 723-733. (English translation of the original Russian publication: Гусев А. А., Мельникова, В. Н. (1990). Связи между магнитудами - среднемировые и для Камчатки. *Вулканология и сейсмология***, №6**, 55-63.

Gusev, A. A., Guseva, E. M., and Panza, G. F. (2007). Size and duration of the high-frequency radiator in the source of the 2004 December 26 Sumatra earthquake. *Geophys. J. Int.*, **170**, 1119-1128; doi: 10.1111/j.1365-246X.2007.03368.x.

Gutdeutsch, R., Kaiser, D., and Jentzsch, G. (2002). Estimation of earthquake magnitudes from epicentral intensities and other focal parameters in central and southern Europe. *Geophys. J. Int.,* **151** (3), 824-834.

Gutdeutsch, R., Castellaro, S., and Kaiser, D. (2011). The magnitude conversion problem: Further insights. *Bull. Seism. Soc*. Am., **101**, 379-384; doi: 10.1785/0120090365..

Gutenberg, B. (1945a). Amplitudes of surface waves and magnitudes of shallow earthquakes. *Bull. Seism. Soc. Am*., **35**, 3-12.

Gutenberg, B. (1945b). Amplitudes of P, PP, and S and magnitude of shallow earthquakes. *Bull. Seism. Soc*. Am., **35**, 57-69.

Gutenberg, B. (1945c). Magnitude determination of deep-focus earthquakes. *Bull. Seism. Soc. Am.*, **35**, 117-130.

Gutenberg, B. (1956). The energy of earthquakes. *Q. J. Geol. Soc*. London, **112**, 1-14.

Gutenberg, B., and Richter, C. F. (1934). On seismic waves (first paper). *Gerl. Beitr. Geophysik*, **43**, 56 – 133.

Gutenberg, B., and Richter, C. F. (1936). On seismic waves (third paper). *Gerl. Beitr. Geophysik*, **47**, 73-131.

Gutenberg, B., and Richter, C. F. (1942). Earthquake magnitude, intensity, energy and acceleration. *Bull. Seism. Soc. Am*., **32**, 163-191.

Gutenberg, B., and Richter, C. F. (1954). Seismicity of the Earth and asscociated Phenomena. 2nd edition, Princeton University Press, 310 pp.

Gutenberg, B., and Richter, C. F. (1956a). Magnitude and energy of earthquakes. *Annali di Geofisica*, **9**, 1-15.

Gutenberg, B., and Richter, C. F. (1956b). Earthquake magnitude, intensity, energy and acceleration. *Bull. Seism. Soc. Am*., **46**, 105-145.

Habermann, R. E. (1995). Opinion. *Seism. Res. Lett*., **66**, 5, 3.

Hanks, T. C. (1977). Earthquake stress drops, ambient tectonic stress, and the stresses that drive plate motion. *Pure Appl. Geophys*., **115**, 441-458.

Hanks, T. C. and Kanamori, H. (1979). Moment magnitude. *J. Geophys. Res*., **84,** 2348-2350.

Hanks, T. C., and Johnston, A. C. (1992). Common features of the excitation and propagation of strong ground motion for North American earthquakes. Bull. Seism. Soc. Am., **82**, 1-23.

Hanks, T. C., Hileman, J. A., and Thatcher, W. (1975). Seismic moments of the larger earthquakes of the southern California region. *Soc. Bull. Geol*., **86**, 1131-1139.

Hansen, R. A., Ringdal, F., and Richards, P. G. (1990). The stability of RMS Lg measurements and their potential for accurate estimation of the yields of Soviet underground nuclear explosions. *Bull. Seism. Soc. Am*., **80**(6), 2006-2126.

Hara, T. (2007a). Measurement of the duration of high-frequency energy radiation and its application to determination of the magnitudes of large shallow earthquakes. *Earth Planets Space* **59**, 227-231.

Hara, T. (2007b). Magnitude determination using duration of high frequency radiation and displacement amplitude: application to tsunami earthquakes. *Earth. Planet Space* **59**, 561-565.

Hartzel, S. H., and Heaton, T. (1985). Teleseismic time functions for large, shallow subduction zone earthquakes. *Bull. Seism. Soc. Am.*, **75**(4), 965-1004.

Haskell, N. A. (1964). Total energy and energy spectral density of elastic wave radiation from propagating faults. *Bull. Seism. Soc. Am*., **54**, 1811-1841.

Haskell, N. A. (1966). Total energy and energy spectral density of elastic wave radiation from propagating faults. Part II. A statistical fault model. *Bull. Seism. Soc. Am*., **56**, 125-140.

Hayes, G. P., Rivera, L., and Kanamori, H. (2009). Source inversion of the W-phase: Real-time implementation and extension to low magnitudes. *Seism. Res. Lett.*, 80, 5, 817-822; doi: 10.1/85/gssrl.80.5.817.

Havskov, J. (Ed.) (1996). The SEISAN earthquake analysis software for the IBM PC and SUN, Version 5.2. *Institute of Solid Earth Physics, Univ. of Bergen*, August 1996.

Havskov, J., and Ottemöller, L. (1999). Electronic Seismologist - SeisAn Earthquake Analysis Software. *Seism. Res. Lett*., **70**, 532-534.

Havskov, J., and Sorensen, M. B. (2006). New coda magnitude scales for mainland Norway and the Jan Mayen region. Norwegian National Seismic Network, *Technical Report No. 19, University of Bergen.*

Havskov, J., and Ottemöller, L. (2010). *Routine data processing in earthquake seismology*. Springer, 347 pp.

Herak, M., and Herak. D. (1993). Distance dependence of M_S and calibrating function for 20 s Rayleigh waves. *Bull. Seism. Soc. Am*., **83**, 6, 1881-1892.

Herak, M., Panza, G., and Costa, G. (2001). Theoretical and observed depth corrections for Ms. *Pure Appl. Geophys*., **158**, 1517-1530.

Herrmann, R. B. (1975). The use of duration as a measure of seismic moment and magnitude. *Bull. Seism. Soc. Am*., **65**, 899-913.

Herrmann, R. B., and Nuttli, O. W. (1982). Magnitude: The relation between M_L and m_{bLg}. *Bull. Seism. Soc. Am*., **72**, 389-397.

Herrmann, R. B., and Kijko, A. (1983). Modeling some empirical Lg relations. *Bull. Seism. Soc. Am.*,**73**, 1835-1850.

Hirshorn, B., and Weinstein, S. (2009). Earthquake source parameters, rapid estimates for tsunami warning. In *Encyclopedia of Complexity and Systems Science*, ed. R. Meyers, *Springer,* Heidelberg-New York: vol. **3**, 2657-2675.

Houston, H. (1999). Slow ruptures, roaring tsunamis, *Nature* **400**, 409-410

Houston, H., and Kanamori, H. (1986). Source spectra of great earthquakes: teleseismic constraints on rupture process and strong motion. *Bull. Seism. Soc., Am*., **76**, 1, 19-42.

Hunter, R. N. (1972). Use of LPZ for magnitude. In: *NOAA Technical Report ERL 236-ESL21*, J. Taggart, Editor, U.S. Dept. Commerce, Boulder, Colorado.

Husseini, M. I. (1977). Energy balance for formation along a fault. *Geophys. J. Roy. Astron. Soc.*, **49**, 699-714.

Hutton, L. K., and Boore, D. M. (1987). The M_L scale in Southern California. Bull. Seism. Soc. Am., **77**, 6, 2074-2094.

Hutton, L. K., and Jones, L. M. (1993). Local magnitudes and apparent variations in seismicity rates in Southern California. *Bull. Seism. Soc. Am*., **83**, 2, 313-329.

Hwang, L. J., and Kanamori, H. (1989). Teleseismic and strong-motion source spectra from two earthquakes in western Taiwan. *Bull. Seism. Soc. Am.,* **79**, 935-944.

Hyvernaud, O., Reymond, D., Talandier, J., and Okal, E. A. (1993). Four years of automated measurement of seismic moments at Papeete using the mantle magnitude M_m: 1987-1991. Tectonophysics, **217**, 175-193.

IASPEI (2005) Summary of Magnitude Working Group recommendations on standard procedures for determining earthquake magnitudes from digital data. http://www.iaspei.org/commissions/CSOI/summary_of_WG_recommendations_2005.pdf

IASPEI (2013) Summary of Magnitude Working Group recommendations on standard procedures for determining earthquake magnitudes from digital data.

http://www.iaspei.org/commissions/CSOI/Summary_WG-Recommendations_20130327.pdf

Iida, K. (1959). Earthquake energy and earthquake fault length. *J. Earth Sci*., Nagoya Univ., **7**, 98-107.

Janský, J., Ruprechtova, L., and Tittel, B. (1977). Magnitude determination based on short-period core phases. *Studia geophys. et geod.,* **21**, 267-273.

Janský, J., and Kvasnicka, M. (1992). Theoretical PKIKP magnitude determination. *Studia geophys. et geod.,* **36,** 20-25.

Johnston, A. C. (1996). Seismic moment assessment of earthquakes in stable continental regions – II. Historical seismicity. *Geophys. J. Intern.*, **125**(3), 639-678.

Kanamori, H. (1972). Mechanism of tsunami earthquakes. *Phys. Planet. Earth Inter.*, **6**, 346-359.

Kanamori, H. (1977). The energy release in great earthquakes. *J. Geophys. Res*., **82**, 2981-2987.

Kanamori, H. (1983). Magnitude scale and quantification of earthquakes. *Tectonophysics*, **93**, 185-199.

Kanamori, H. (1988). The importance of historical seismograms for geophysical research. In: W. H. K. Lee (ed), *Historical seismograms and earthquakes of the world*, Academic Press, New York, 16-33.

Kanamori, H. (2005). Real-time seismology and earthquake damage mitigation. *Annu. Rev. Earth Planet. Sci,*, **33**, 195-214; doi: 10.1146/annurev.earth.33.092203.122626.

Kanamori, H. (2006). The radiated energy of the 2004 Sumatra-Andaman earthquake; In: Abercrombie R, McGarr A, Kanamori H (eds): Radiated energy and the physics of earthquake faulting, *AGU Geophys. Monogr. Ser*., **170**, 59-68.

Kanamori, H., and Cipar, J. J. (1974). Focal process of the great Chilean earthquake May 22, 1960. *Phys. Earth Planet. Inter*., **9**, 128-136.

Kanamori, H., and Anderson, D. L. (1975). Theoretical basis of some empirical relations in seismology. *Bull. Seism. Soc. Am*., **65**, 1073-1095.

Kanamori, H., and Jennings, P. C. (1978). Determination of local magnitude, M_L, from strong motion accelerograms. *Bull. Seism. Soc. Am*., **68**, 471-485.

Kanamori, H., and Given, J. (1981).Use of long-period surface waves for rapid determination of earthquake-source parameters. *Phys. Earth Planet. Inter.*, **27**, 8-31.

Kanamori, H., and Kikuchi, M. (1993). The 1992 Nicaragua earthquake: a slow tsunami earthquake associated with subducted sediments. *Nature*, **361**, 714-716.

Kanamori, H., and Kikuchi, M. (1995). Source characteristics of the 1992 Nicaragua tsunami earthquake inferred from teleseismic body waves. *Pure Appl. Geophys*., **144**, 441-453.

Kanamori, H., and Brodsky, E. E. (2004). The physics of earthquakes. *Rep. Prog. Phys*., **67**, 1429-1496; doi: 10.1088/0034-4885/67/8/R03.

Kanamori, H., and Helmberber, D. (2005). Energy radiation from the Sumatra earthquake. *Nature*, **434**, p. 582.

Kanamori, H., and Rivera, L. (2008). Source inversion of W phase: speeding up seismic tsunami warning. *Geophys. J. Int.*, **175**, 222-238.

Kanamori, H., Mori, J., Hauksson, E., Heaton, Th. H., Hutton, L. K., and Jones, L. M. (1993). Determination of earthquake energy release and M_L using TERRASCOPE. *Bull. Seism. Soc. Am.*, **83**, 2, 330-346.

Kanamori, H., Hauksson, E., and Heaton, T. (1997) Real-time seismology and earthquake hazard mitigation. Nature 390: 461-464

Karnik, V. (1956). Magnitudenbestimmung europäischer Nahbeben. (In German).Travaux Inst. Géophys. Acad. Tchecosl. Sci., No. **64**.

Karnik, V. (1969). Seismicity of the European area. Part I. *Reidel Publishing Company*, Dordrecht, 364 pp.

Karnik, V. (1972). Differences in magnitudes. Vorträge des Soproner Symposiums der 4. Subkommission von KAPG 1970, Budapest, 69-80.

Karnik, V., Kondorskaya, N. V., Riznichenko, Yu. V., Savarensky, Ye. F., Soloviev, S. L., Shebalin, N. V., Vaněk, J., and Zatopek, A. (1962). Standardisation of the earthquake magnitude scales. *Studia Geophysica et Geodaetica*, **6**, 41-48.

Katsumata, A. (1964). A method to determine the magnitude of deep focus earthquakes in and near Japan. (in Japanese), *Zisin*, II, vol. 17, 158-165.

Katsumata, A. (1996). Comparison of magnitudes estimated by the Japan Meteorological Agency with moment magnitudes for intermediate and deep earthquakes. *Bull, Seism. Soc. Am.*, **86**(3), 832-842.

Kaverina, A. N., Lander, A. V., and Prozorov, A. G. (1996). Global creepex distribution and its relation to earthquake–source geometry and tectonic origin. *Geophys. J. Int.*, **135**, 249-265

Kawasumi, H. (1951). Measures of earthquake danger and expectancy of maximum intensity throughout Japan as inferred from the seismic activity in historical times. *Bull. Earthq. Res. Inst.*, **29**, 469-482.

Kennett, B. L. N. (1985). On regional S*, Bull. Seism. Soc. Am.*, **75**, 1077-1086.

Khromovskikh, V. S. (1989). Determination of magnitudes of ancient earthquakes from dimensions of observed seismodislocations. *Tectonophysics*, **166**, 269-280.

Kikuchi, M., and Kanamori, H. (1982). Inversion of complex body waves. *Bull. Seism. Soc. Am*., **72**, 491-506.

Kikuchi, M., and Kanamori, H. (1986). Inversion of complex body waves – II. *Phys. Earth Planet. Int.*, **43**, 205-222.

Kikuchi, M., and Fukao, Y. (1987). Inversion of long-period P-waves from great earthquakes along subduction zones. *Tectonophysics*, **144**, 231-247.

Kikuchi, M., and Ishida, M. (1993). Source retrieval for deep local earthquakes with broadband records. *Bull. Seism. Soc. Am*., **83**, 6, 1855-1870.

Kim, W.-Y. (1998). The M_L scale in Eastern North America. *Bull. Seism. Soc. Am*., **88**, 4, 935-951.

King, G. C. P. (1978). Geological faults, fractures, creep and strain. *Phil. Trans. R. Soc. London*, **A., 288**, 197-212.

Kiratzi, A. A., and Papazachos, B. C. (1985). Local Richter magnitude and total signal duration in Greece. *Ann. Geophys*., **3**, 4, 531-537.

Klein, F. W. (1978). Hypocenter location program HYPOINVERSE. *U.S. Geol. Surv. Open-File Report.* **78-694**.

Klein, F. W. (1985). HYPOINVERSE, a program for VAX and professional 350 computers to solve the earthquake locations. *U.S. Geological Survey Open-File Report* **85-515**, 53 pp.

Klein, F. W. (2002). User's guide to HYPOINVERSE-2000, a Fortran program to solve for earthquake locations and magnitudes. *Open File Report 02-171, U.S. Geological Survey*.

Klinge, K. (1989). Duration magnitudes. In: Bormann, P. (ed.). *Monitoring and analysis of the earthquake swarm 1985/86 in the retion Vogtland/Western Bohemia.* Akademie der Wissenschaften der DDR, ZIPE Veröffentlichung Nr. 110, 109-114.

Knopoff, L., Schwab, F., and Kansel, E. (1973). Interpretation of Lg. *Geophys. J. R. Astr. Soc.*, **33**, 389-404.

Kostrov, B.V. (1966). Unsteady propagation of longitudinal shear cracks. *J. Appl. Math. Mech*., **30**, 1241-1248.

Kostrov, B. (1974). Seismic moment and energy of earthquakes, and seismic flow of rock. *Izv. Acad. Sci., USSR, Phys. Solid Earth* (Engl. Transl.), **1**, 23-40.

Kowalle, G., Tittel, B., and Bormann, P. (1983). Determination of a magnitude function using short-period readings of PKP. *Tectonophysics*, 93, 289-294.

Koyama, J. (1985): Earthquake source time-function from coherent and incoherent rupture.. Tectonophysics, **118**(3–4), 227–242.

Koyama, J., and Zheng, S.-H. (1985). Excitation of short-period body-waves by great earthquakes. *Physics Earth Planet. Int*., **37**, 108-123.

Koyama, J., and Shimada, N. (1985). Physical basis of earthquake magnitudes: an extreme value of seismic amplitudes from incoherent fracture of random fault patches. *Phys. Earth Planet. Int.*, **40**, 301-308.

Krüger, F., and M. Ohrnberger (2005b). Spatio-temporal source characteristics of the 26 December 2004 Sumatra earthquake as imaged by teleseismic broadband arrays. *Geoph. Res. Lett.*, **32**, L24312, doi:10.1029/2005GL023939.

Krüger, F., and Ohrnberger, M. (2005a). Tracking the rupture of the M_w = 9.3 Sumatra earthquake over 1,150 km at teleseismic distances. *Nature*, **435**, 937-939; doi: 10.1038/nature03696.

Lahr, J. C. (1989). HYPOELLIPSE/Version 2.0: A computer program for determining local earthquakes hypocentral parameters, magnitude, and first motion pattern. *U.S. Geological Survey Open-File Report* **89-116**, 92 pp.

Lahr, J. C. (2003). The HYPOELLIPSE earthquake location program. In: Lee, W. H. K., Kanamori, H., Jennings, P. C., and Kisslinger, C. (Eds.) (2003). International Handbook of Earthquake and Engineering Seismology, Part B. *Academic Press, Amsterdam*, 1617-1618.

Langston, C. A. (1981). Source inversion of seismic waveforms: The Koyna, India, earthquakes of 13 September 1967. *Bull. Seism. Soc. Am.,* **71,** 1−24.

Langston, C. A., Brazier, R., Nyblade, A. A., and Owens, T. J. (1998). Local magnitude scale and seismicity rate for Tanzania, East Africa. *Bull. Seism. Soc. Am*., **88**, 3, 712-721.

Latter, A. L., Le Levier, R. E., Martinelli, E. A., and McMillan, W. C. (1961a). Method of concealing underground nuclear explosions. *J. Geophys. Res.*, **66**, 943-946.

Latter, A. L., Martinelli, E. A., Mathews, J., and McMillan, W. C. (1961b). The effect of plasticity on decoupling of underground explosions. *J. Geophys. Res.*, **66**, 2929-2937.

Lay, T., and Wallace, T. C. (1995). Modern global seismology. ISBN 0-12-732870-X, *Academic Press*, 521 pp.

Lay, T., and Bilek, S. (2007). Anomalous earthquake ruptures at shallow depths on subduction zone megathrusts. In: T. H. Dixon and C. Moore (Eds.),*The seismogenic Zone of subduction thrust faults*, Columbia Univ. Press, New York, 692 pp ISBN:978-0-231-13866-6.

Lazareva, A. P., and Yanovskaya, T. B. (1975). The effect of the lateral velocity on the surface wave amplitudes. Proc. Intern. Symp. Seismology and Solid-Earth Physics, Jena, April 1-6, 1974. *Veröff. Zentralinstitut für Physik d. Erde*, **No. 31**, Vol. 2, 433-440.

Lee, W. H. K. (1995). Realtime seismic data acquisition and processing. *IASPEI Software Vol.1*, 2nd Edition.

Lee, W. H. K., and Lahr, J. C. (1975). HYPO71 (revised): A computer program for determining hypocenter, magnitude and first motion pattern of local earthquakes. U.S. Geological Survey Open-File Report 75-311, 116 pp.

Lee, W. H. K., Bennet, R., and Meagher, K. (1972). A method of estimating magnitude of local earthquakes from signal duration. *U.S. Geol. Surv. Open-File Rep*., 28 pp.

Lee, V., Trifunac, M., Herak, M., Živčić, M., and Herak, D. (1990). M_L^{SM} computed from strong motion accelerograms recorded in Yugoslavia. *Earthq. Engin. Structur. Dyn*., **19**, 1167-1179.

Lee, W. H. K., and Espinoza-Aranda, J. M. (2002). Earthquake earlywarning systems: current status and perspectives. In: Zschau, J., and Küppers, A. N. (Eds.), *Early Warning Systems for Natural Disaster Reduction,* Springer, Berlin, 409-423.

Lee, W. H. K., Kanamori, H., Jennings, P. C., and Kisslinger, C. (Eds.) (2002). *International Handbook of Earthquake and Engineering Seismology*, Part A. Academic Press, Amsterdam, section with articles on earthquake geology and mechanics, 455-661.

Lemzikov, V. K., and A. A. Gusev (1991). Coda-based energy classification of near Kamchatka earthquakes. *Volc. Seis.*, **11**,**.** 558-578. Englisch translation of the original publication in Russian: Лемзиков В.К., Гусев А.А.(1989). Энергетическая классификация близких камчатских землетрясений по уровню кода-волн. *Вулканология и сейсмология*, №4., 83-97.

Lienert, B. R. E. (1991). Report on modifications made to Hypocenter. *Institute of Solid Earth Physics, University of Bergen*.

Lienert, B. R. E., Berg, E., and Frazer, L. N. (1988). HYPOCENTER: An earthquake location method using centered, scaled, and adaptively least squares. *Bull. Seism. Soc. Am*., **76**, 771-783.

Lienert, B. R. E., and Havskov, J. (1995). A computer program for locating earthquakes both locally and globally. *Seism. Res. Lett*., **66**, 26-36.

Lienkaemper, J. J. (1984). Comparison of two surface-wave magnitude scales: M of Gutenberg and Richter (1954) and Ms of "Preliminary Determination of Epicenters". *Bull. Seism. Soc. Am.*, **74**(6), 2357-2378.

Liu, H.-P., Anderson, D.L., and Kanamori, H. (1976). Velocity dispersion due to anelastisity; implications for seismology and mantle composition. *Geophys. J. R. Astron. Soc*., **47**, 41-58.

Lolli, B., and Gasperini, P. (2012). A comparison among general orthogonal regression methods applied to earthquake magnitude conversions. *Geophys. J. Int.*, **190,** 1135–1151 doi: 10.1111/j.1365-246X.2012.05530.x

Lomax, A. (2005). Rapid determination of earthquake size for hazard warning. *EOS*, **86**, 21, p. 202.

Lomax, A., Michelini, A., and Piatanesi, A. (2007). An energy-duration procedure for rapid and accurate determination of earthquake magnitude and tsunamigenic potential, *Geophys.l J. Int.*, **170**, 1195-1209; doi: 10.1111/j.1365-246X.2007.03469.x.

Lomax, A., and A. Michelini (2009a). M_{wpd}: A duration-amplitude procedure for rapid determination of earthquake magnitude and tsunamigenic potential from *P* waveforms, *Geophys.l J. Int.*, **176**, 200-214; doi: 10.1111/j.1365-246X.2008.03974.x.

Lomax, A., and Michelini, A. (2009b). Tsunami early warning using earthquake rupture duration. *Geophys. Res. Lett.*, **36**, L09306; doi: 10.1029/2009GL037223.

Lomax, A., and Michelini, A. (2011a). Tsunami early warning using earthquake rupture duration and P-wave dominant period: the importance of length and depth of faulting. *Geophys. J. Int.*, **185**(1), 283-291; doi: 10.1111/j.1365-246X.2010.04916.x.

Lomax, A., and Michelini, A. (2011b). Erratum. Geophys. J. Int., **186,** 1454, doi:10.1111/j.1365-246X.2011.05128.x.

Lomax, A., and Michelini, A. (2012). Tsunami early warning within five minues. *Pure Appl. Geophys.*, **169**, nnn-nnn; doi: 10.1007/s00024-012-0512-6

Madariaga, R. (1976). Dynamics of an expanding circular fault. *Bull. Seism. Soc. Am.*, **66**, 639-666.

Madariaga, R. (2011). Earthquakes, source theory. In: Harsh Gupta (ed.). *Encyclopedia of Solid Earth Geophysics,* Springer, Vol. 1, 248-252; doi: 10.1007/978-90-481-8702-7.

Madariaga, R., and Olsen, K. B. (2002). Earthquake dynamics. In: Lee, W. H. K., Kanamori, H., Jennings, P. C., and Kisslinger, C. (Eds.) (2002). *International Handbook of Earthquake and Engineering Seismology*, Part A. Academic Press, Amsterdam, 175-194.

McGarr, A., and Fletcher; J. B. (2002). Mapping apparent stress and energy radiation over fault zones of major earthquakes. *Bull. Seism. Soc. Am.*, **92**, 1633-1646.

Mackey, K. G., Fujita, K., Hartse, H. E., Stead, R. J., Steck, L. K., Gunbina, L. V., Leyshuk, N., Shibaev, S. V., Koz'min, B. M., Imaev, V. S., Gordeev, E. I., Chebrov, V. N., Masal'ski, O. K., Gileva, N. A., Bormatov, V. A., Voitenok, A. A., Levin, Y. N., and Fokina, T. A. (2010). Seismicity Map of Eastern Russia, 1960–2010. *Seism. Res. Lett.*, **81**(5), 761-768; doi: 10.1785/gssrl.81.5.

Margaris, B. N., and Papazachos, C. B. (1999). Moment-magnitude relations based on strong-motion records in Greece. *Bull. Seism. Soc. Am.*, **89**, 442-455.

Marshall, P.D., and Basham, P.W. (1972). Discrimination between earthquakes and underground explosions employing an improved M_S scale, *Geophys. J. R. astr. Soc.* **28**, 431-458.

Marrett, R. (1994). Scaling of intraplate earthquake recurrence interval with fault length and implications for seismic hazard assessment. *Geophys. Res. Lett.*, **21**, 24, 2637-2640.

Mason, D. B. (1996). Earthquake magnitude potential of the intermountain seismic belt, USA, from surface-parameter scaling of Late Quaternary faults. *Bull. Seism. Soc. Am.*, **86**, 5, 1487-1506.

Masuda, K. (1992). P-coda amplitudes as a measure of earthquake magnitude of local microearthquake. *J. Phys. Earth*, **40**, 565-572.

Mayeda, K. (1993). Mb(LgCoda): A stable single station estimator of magnitude. *Bull. Seism. Soc. Am.*, **83**, 851-861.

Medvedev, S. V. (1962). Engineering seismology (in Russian). *Academy of Sciences, Inst. of Physics of the Earth*, Publ. house for literature on Civil Engineering, Architecture and Building Materials, Moscow.

Meissner, R., and Wever, Th. (1988). Lithosphere rheology: Continental versus oceanic unit. J. Petrology, *Oxford Univerity Press*, Special Lithosphere Issue, 53-61.

Mendez, A. J., and Anderson, J. G. (1991). The temporal and spatial evolution of the 19 September 1985 Michoacan earthquake as inferred from near-source ground-motion records. Bull. Seism. Soc. Am., **81**, 3, 1655-1673.

Miyamura, S. (1974). Determination of body-wave magnitudes for shallow earthquakes in the New Zealand and Macquarie Loop regions using PKP phases. *Phys. Earth Planet. Int.*, **8**, 167-176.

Mizone, M. (1977). On the magnitude calibration function for core phases with special reference to the PKP1-PKP2 caustic. *J. Phys. Earth.*, **25**, 143-162.

Moore, G. F., Bangs, N. L., Taira, A., Kuramoto, S., Pangborn, E., Tobin, H. J. (2007). Three-dimensional splay fault geometry and implications for tsunami generation. *Science*, **318**, 1128, doi:10.1126/science.1147195.

Muir-Wood, R. (1993). From global seismotectonics to global seismic hazard. Annali di Geofisica, **36**, 3-4, 153-168.

Musson, R. M. W. (1996). Determination of parameters for historical British earthquakes, *Annali di Geofisica*, **39**(5), 1041-1048.

Musson, R. M. W., and Cecić, I. (2002). Macroseismology. In: Lee, W. H. K., Kanamori, H., Jennings, P. C., and Kisslinger, C. (Eds.) (2002). *International Handbook of Earthquake and Engineering Seismology, Part A*. Academic Press, Amsterdam, 807-822.

Musson, R. M. W., and Jiménez, M.-J. (2008). Macroseismic estimation of earthquake parameters. *NERIES project report*, Module NA4, Deliverable D3, Edinburgh.

Nabelek, J.(1984). Determination of earthquake source parameters from inversion of body waves. *Ph.D. Thesis,* Mass. Inst. Tech., Cambridge.

Nakamura, Y. (1988). On the urgent earthquake detections and alarm system (UrEDAS). *9th World Conference on Earthquake Engineering, Vol. VII*, 673-678.

Nakamura, Y., and Saita, J. (2007). UrEDAS: The earthquake warning system today and tomorrow. In: Gasparini, P., Manfredi, G., and Zschau, J. (2007). *Earthquake Early Warning Systens*. Springer, Berlin-Heidelberg, 249-281.

Newman, A. V., and Okal, E. A. (1998). Teleseismic estimates of radiated seismic energy: The E/M_o discriminant for tsunami earthquakes. *J. Geophys. Res.*, **103**, 26,885-26,897.

Neuman, A.V., Hayes, G., Wei, Y., and Convers, J. (2011). The 25 October 2010 Mentawai tsunami earthquake, from real-time discriminants, finite-fault rupture, and tsunami excitation, *Geophys. Res. Lett.,* **38**, L05302 ; doi:10.1029/2010GL046498.

Ni, S., Kanamori, H., and Helmberger, D. (2005). Seismology – Energy radiation from the Sumatra earthquake. *Nature*, **434**, 582-582.

Nolet, G., Krueger, S., and Clouser, R. M. (1998a). Empirical determination of depth-distance corrections for m_b and M_w from Global Seismograph Network stations. *Geophys. Res. Lett.*, **25**(9), 1451-1454.

Nolet, G., Krueger, S., and Clouser, R. M. (1998b). Comment on "Empirical determination of depth-distance corrections for mb and Mw from global seismograph network stations". *Geophys. Res. Lett.*, **25**, 22, 4271-4272.

Nowroozi, A. (1985). Empirical relations between magnitudes and fault parameters for earthquakes in Iran. Bull. Seism. Soc. Am., **75**, 1327-1338.

Nuttli, O. W. (1973). Seismic wave attenuation and magnitude relations for eastern North America. *J. Geophys. Res*., **78**, 876-885.

Nuttli, O. W. (1985). Average seismic source-parameter relations for plate-margin earthquakes. *Tectonophysics*, **118**, 161-174.

Nuttli, O .W. (1986). Yield estimates of Nevada Test Site explosions obtained from seismic Lg waves, *J. Geophys. Res*., **91**, 2137-2151.

Nuttli, O. W. (1988). Lg magnitudes and yield estimates for underground Novaya Zemlya nuclear explosions, *Bull. Seism. Soc. Am.* 78, 873-884.

Nuttli, O. W., and Zollweg, J. E. (1974). Relation between felt area and magnitude for central United States earthquakes. *Bull. Seism. Soc. Am*., **64**, 1, 73-85.

Nuttli, O. W., Bollinger, G. A., and Griffith, D. W. (1979). On the relation between modified Mercalli intensity and body-wave magnitude. *Bull. Seism. Soc. Am.***, 69**, 3, 893-909.

Ochozimskaya, M. V. (1974). Relationship between m_{PV} and M_{LH} depending on the source depth of earthquakes. In: Magnitude and energetic classification of earthquakes (II), (in Russian), *Institut Fiziki Zemli, Akademii Nauk*, Moskva, 203-207.

Okal, E. A. (1992a). Use of the mantle magnitude M_m for the reassessment of the moment of historical earthquakes. I: Shallow events. *Pageoph*, **139**, 1, 17-57.

Okal, E. A. (1992b). Use of the mantle magnitude M_m for the reassessment of the moment of historical earthquakes. II: Intermediate and deep events. *Pageoph*, **139**, 1, 59-85.

Okal, E. A., and Talandier, J. (1989). M_m: A variable-period mantle magnitude. J. *Geophys. Res*., **94**, 4169-4193.

Okal, E. A., and Talandier, J. (1990). M_m: Extension to Love waves of the concept of a variable-period mantle magnitude. *Pure Appl. Geophys*., **134**, 355-384.

Okal, E. A., Alsset, P.-J., Hyvernaud, O., and Schindelé, F. (2003). The deficient T waves of tsunami earthquakes. *Geophys. J. Int.*, **152**, 416-432.

Olson, E. L., and Allen, R. (2005). The deterministic nature of earthquake rupture. *Nature*, **438**, 212-215.

Oth, A., Bindi, D., Parolai, S., and DiGiacomo, D. (2010). Earthquake scaling characteristics and the scale-(in)dependence of seismic energy-to-moment ratio: Insights from KiK-net data in Japan. *Geophys. Res. Lett.*, **37**, L19304;,doi:10.1029/2010GL044572.

Panza, J. F., Duda, S. J., Cernobori, L., and Herak, M. (1989). Gutenberg´s surface-wave magnitude calibrating function: theoretical basis from synthetic seismograms. *Tectonophysics*, **166**, 35-43.

Panza, J. F., Prozorov, A. G., and Pazzi, G. (1993). Extension of global creepex definition (Ms-mb) to local studies (Md-ML): The case of the Italian region. *Terra Nova*, **5**, 2, 150-156.

Parolai, S., Bindi, D., Durukal, E., Grosser, H., and Milkereit, C. (2007). Source parameter and seismic moment-magnitude scaling for northwestern Turkey, *Bull. Seism. Soc. Am.* **97**(2), 655-660.

Pasečnik, J. P., Kogan, S. D., Sultanov, D. D., and Cibulskij, V. I. (1960). Rezul´taty sejmičeskij nabljudenij pri podzemnych jadernych vzryvach. *Akad. Nauk SSSR, Trudy Inst. Fiz. Zemli, Ser. Geofiz*., **6**, 3-52.

Patton, H. J. (1998). Bias in the centroid moment tensor for central Asian earthquakes: Evidence from regional surface wave data. *J. Geophys. Res.*, **103**, 26,885-26,898.

Patton, H. J. (2001). Regional magnitude scaling, transportability, and M_S:m_b discrimination at small magnitudes, Pure and Applied Geophysics, **158**, 1951-2015.

Patton, H.J., and J. Schlittenhardt (2005). A transportable mb(Lg) scale for central Europe and implications for low-magnitude Ms-mb discrimination. *Geophys. J. Int*., **163**, 126-140.

Pegeler, G., and Das, S. (1996). Analysis of the relationship between seismic moment and fault length for large crustal strike-slip earthquakes between 1977-92. *Geophys. Res. Lett*., **23**, 905-908.

Pérez-Campos, X., and Beroza, G. C. (2001). An apparent mechanism dependence of radiated seismic energy. *J. Geoöphys. Res.*, **106**, B6, 11,127-11,136.

Phillips, W.S., and Stead, R.J. (2008). Attenuation of Lg in the western US using the USArray (2008). *Geopys. Res. Lett*., **35**, L07307, doi:10.1029/2007GL032926, 5p.

Plešinger, A., Zmeškal, M., and Zednik, J. (1995). PREPROC - Software for automated preprocessing of digital data. Ver.2.1, Ed. Bergman, E., NEIC Golden/FI, Prague.

Plešinger, A., Zmeškal, M., and Zednik, J. (1996). Automated preprocessing of digital seismograms: Principles and software. Version 2.2, Bergman, E. (Ed.), *Prague & Golden*.

Polet, J., and Kanamori, H. (2000). Shallow subduction zone earthquakes and their tsunamigenic potential. *Geophys. J. Int.*, **142**, 684-702.

Polet, J., and Kanamori, H. (2009). Tsunami earthquakes; in: Meyers, R. (ed), Encyclopedia of complexity and systems science, Vol. 10, 9577-9592.

Pomeroy, P. W., and Oliver, J. (1960). Seismic waves from high altitudes nuclear explosions. *J. Geophys. Res.*, **53**, 549-562.

Prozorov, A. G., and Hudson, J. A. (1974). A study of the magnitude difference Ms – mb for earthquakes. *Geophys. J. R. ast. Soc.,* **39,** 551-554.

Prozorov, A. G., Hudson, J. A., and Shimshoni, M. (1983). The behaviour of earthquake magnitudes in space and time. *Geophys. J. R. astr. Soc.*, **73**, 1-16.

Prozorov, A. G., and Shabina, F. J. (1984). Study of properties of seismicity of the Mexico region. *Geophys. J. R. ast. Soc.,* **76,** 317-336.

Purcaru, G., and Berckhemer, H. (1978). A magnitude scale for very large earthquakes. *Tectonophysics*, **49**, 189-198.

Purcaru, G., and Berckhemer, H. (1982). Quantitative relations of seismic source parameters and a classification of earthquakes. *Tectonophysics*, **84**, 57-128.

Ranalli, G., and Murphy, D. C. (1987). Rheological stratification of the lithosphere. *Tectono-physics*, **132**, 281-295.

Randall, M. J. (1973). The spectral theory of seismic sources. *Bull. Seism. Soc. Am.*, **63**, 1133-1144.

Rautian, T. G. (1960). Energy of earthquakes, in Y. V. Riznichenko (editor), *Methods for the Detailed Study of Seismicity*, Moscow: Izdatel'stvo Akademii Nauk SSSR, 75-114. (in Russian)

Rautian, T. G., and Khalturin, V. I. (1978). The use of the coda for determination of earthquake source spectrum. *Bull. Seism. Soc. Am.*, **68**, 923-948.

Rautian, T. G., Khalturin, V. I., and Shebalin, I. S. (1979). Ogibajuschtschie seismitscheskoy kody i ozenka magnitude zemletrjazenij kavkaza (The envelop of seismic coda and magnitude estimate of earthquakes in the Caucasus). Fiziki Zemli, 6, 22-31.

Rautian, T. G., Khalturin, V. I., and Zakirov, M. S. (1981). Experimental studies of seismic coda (in Russian). *Nauka*, Moscow, 144 pp.

Rautian, T. G., Khalturin, V. I., Dotsev, N. T., and Sarkisyan, N. M. (1989). Macroseismic magnitude. In: *Voprosy inzhenneroy seismologigii*, iss. **30**, 98-109.

Rautian, T., Khalturin, V., Fujita, K., Mackey, K., and Kendall, A. (2007). Origins and methodology of the Russian energy K-class system and its relationship to magnitude scales: *Seis. Res. Lett.*,**78**, 579-590.

Reches, Z. (1987). Determination of the tectonic stress tensor from slip along faults that obey the Coulomb yield condition. *Tectonics*, **6**, 849-861.

Rezapour, M., and Pearce, R. G. (1998). Bias in surface-wave magnitude M_S due to inadequate distance corrections. *Bull. Seism. Soc. Am.*, **88**, 1, 43-61.

Richard, P. (2002). Seismological methods of monitoring compliance with the Comprehensive Nuclear Test Ban Treaty. In: Lee, W. H. K., Kanamori, H., Jennings, P. C., and Kisslinger, C. (Eds.) (2002).. *International Handbook of Earthquake and Engineering Seismology*, Part A. Academic Press, Amsterdam, 369-382.

Richard, P. G., and Wu, Z. (2011). Seismic monitoring of nuclear explosions. In: Harsh Gupta (ed.). *Encyclopedia of Solid Earth Geophysics,* Springer, Vol. 2, 1144-1156; doi: 10.1007/978-90-481-8702-7.

Richter, C. F. (1935). An instrumental earthquake magnitude scale. *Bull. Seism. Soc. Am.*, **25**, 1-32.

Richter, C. F. (1958). Elementary seismology. *W. H. Freeman and Company*, San Francisco and London, viii + 768 pp.

Ristau, J. (2009). Comparison of magnitude estimates for New Zealand earthquakes : moment magnitude, local magnitude, and teleseismic body-wave magnitude. *Bull. Seism. Soc. Am.*, **99**, 1841-1852.

Ristau, J., Rogers, G. C., and Cassidy, J. F. (2005). Moment magnitude-local magnitude calibration for earthquakes in Western Canada. *Bull. Seism. Soc. Am.*, **95**, 5, 1994-2000.

Rivera, L. (1989). Inversion du tenseur des contraintes et des mécanismes au foyer à partir des données de polarité pour une population de séismes. *Thèse de doctorat, Université Louis.Pasteur de Stasbourg.*

Riznichenko, Yu. V. (1992). Problems of seismology. *Mir and Springer Publishers*, Moscow and Berlin-Heidelberg-New York, 445 pp. (English translation of the original Russian publication of 1985).

Romanowicz, B. (1992). Strike-slip earthquakes on quasi-vertical transcurrent faults: inferences for general scaling relations. *Geophys. Res. Lett.*, **19**, 481-484.

Romanovicz, B. (1994). Comment on "A repraisal of large earthquake scaling" by C. Scholz. *Bull. Seism. Soc. Am.*, **84**, 5, 1675-1676.

Romanowicz, B., and Rundle, J. B. (1993). On scaling relations for large earthquakes. *Bull. Seism. Soc. Am.*, **83**, 1294-1297.

Romanovicz, B., and Rundle, J. (1994). Reply to comments on "On scaling relations for large earthquakes" by B. Romanovicz and J. Rundle from the perspective of a recent nonlinear diffusion equation linking short term deformation to long term tectonics. *Bull. Seism. Soc. Am*., **84**, 5, 1684-1685.

Rydelek, P., and Horiuchi, S. (2006). Is earthquake rupture deterministic? *Nature*, **444**, E5-E6.

Sadovsky, M. A., Kedrov, O. K., and Pasechnik, I. P. (1986). On the question of energetic classification of earthquakes (in Russian). *Fizika Zemli*, Moscow, **2**, 3-10.

Satake, K. (2002). Tsunamis. In: W.H.K. Lee, H. Kanamori, P.C. Jennings and C. Kisslinger (Eds.). International Handbook of Earthquake and Engineering Seismology, Academic Press, Amsterdam, Vol. 1, 437–451.

Saul, J., and Bormann, P. (2007). Rapid estimation of earthquake size using the broadband P-wave magnitude mB. *Eos, Transactions, American Geophysical Union, AGU 2007 fall meeting*, **88**, no. 52, Suppl., Abstract S53A-1035.

Savage, M. K., and Anderson, J. G. (1995). A local-magnitude scale for the Western Great Basin-Eastern Sierra Nevada from Wood-Anderson seismograms. *Bull. Seism. Soc. Am.*, **85**, 4, 1236-1243.

Scholz, C. H. (1982). Scaling laws for large earthquakes: consequences for physical models. *Bull. Seism. Soc. Am*., **72**, 1-14.

Scholz, C. H. (1990). *The mechanics of earthquakes and faulting*. Cambridge University Press, Cambridge, 439 pp.

Scholz, C. H. (1994a). A repraisal of large earthquake scaling. *Bull. Seism. Soc. Am*., **84**, 215-218.

Scholz, C. H. (1994b). Reply to comments on "A repraisal of large earthquake scaling" by C. Scholz. *Bull. Seism. Soc. Am*., **84**, 5, 1677-1678.

Scholz, C. H. (1997). Size distributions for large and small earthquakes. *Bull. Seism. Soc. Am.*, **87**, 4, 1074-1077.

Scholz, C. H. (2002). *The Mechanics of Earthquakes and Faulting*. 2nd edition, Cambridge University Press, Cambridge, 496 pp.

Schweitzer, J., and T. Kværna (1999). Influence of source radiation patterns on globally observed short-period magnitude estimates (mb), *Bull. Seism. Soc. Am.* **89**(2), 342-347.

Seidl, D. (1980). The simulation problem for broad-band seismograms. *J. Geophys*., **48**, 84-93.

Seidl, D., and Berckhemer, H. (1982). Determination of source moment and radiated seismic energy from broadband recordings. *Phys. Earth Planet. Inter*., **30**, 209-213.

Seidl, D., and Stammler, W. (1984). Restoration of broad-band seismograms (part I). *J. Geophys.*, **54**, 114-122.

Seidl, D., and Hellweg, M. (1988). Restoration of broad-band seismograms (part II): Signal moment determination. *J. Geophysics*, **62**, 158-162.

Shapira, A., and Hofstetter, A. (1993). Source parameters and scaling relationships of earthquakes in Israel. *Tectonoophys.*, **217**, 217-226.

Sieberg, A. (1912). Über die makroseismische Bestimmung der Erdbebenstärke. *Gerl. Beitr. Geophys.*, **11**, 227-239.

Simons, F. J., Dando, B. D., Allen, R. M. (2006). *Earth Planet. Sc. Lett.*, **250**, 214-223.

Sipkin, S. A. (1982). Estimation of earthquake source parameters by the inversion of waveform data: synthetic waveforms. *Phys. Earth Planet. Inter.,* **30**, 242-259.

Sipkin, S. A. (1986). Estimation of earthquake source parameters by the inversion of waveform data: global seismicity. *Bull. Seism. Soc. Am*., **76**, 1515-1541.

Soloviev, S. L. (1955). Classification of earthquakes in order of energy (in Russian). *Trudy Geofiz. Inst. AN SSSR*, **30**, 157, 3-31.

Soloviev, S. L., and Shebalin, N. V. (1957). Determination of the strength of earthquakes by means of the ground displacements of surface waves (in Russian: Opredelenie intensivnosti zemletrjasenij po smeschtscheniju potschvy v poverchnostinych volnach). *Izv. AN SSSR, Ser. Geofiz*., no. 7, 926.

Sornette, D., and Sornette, A. (1994). Comments on "On scaling relations for large earthquakes" by B. Romanovicz and J. Rundle from the perspective of a recent nonlinear diffusion equation linking short term deformation to long term tectonics. *Bull. Seism. Soc. Am*., **84**, 5, 1679-1683.

Spence, W. (1977). Measuring the size of an earthquake. *Earthq. Inform. Bull.*, **9**, 4, 21-23.

Sponheuer, W. (1960). Methoden zur Herdtiefenbestimmung in der Makroseismik, *Freiberger Forschungshefte* **C88**, Akademie Verlag, Berlin.

Spudich, P., and Cranswick, E. (1984). Direct observation of rupture propagation during the 1979 Imperial Valley, California, earthquake using a short baseline accelerometer array. *Bull. Seism. Soc. Am.*, **74**, 2083-2114.

Stein, S., and Okal, E. (2005). Speed and size of the Sumatra earthquake. Nature 434: 581-582

Stover, C. W., and Coffman, J. L. (1993). *Seismicity of the United States, 1568-1989* (Revised). United States Government Printing Office, Washington.

Street, R. L., and Turcotte, F. T. (1977). A study of northeastern North American spectral moments, magnitudes, and intensities. *Bull. Seism., Soc. Am.*, **67**, 2, 599-614.

Stromeyer, D., Grünthal, G., and Wahlström, R. (2004). Chi-square regression for seismic strength parameter relations, and their uncertainties, with application to an Mw based earthquake catalogue for central and northwestern Europe. *J. Seismol.*, **8** (1), 143-153.

Talandier, J., and Okal, E. A. (1992). One-station estimates of seismic moments from the mantle magnitude Mm: The case of the regional field ($1.5° \leq \Delta \leq 15°$). *Pure Appl. Geophys.*, **138**, 43-60.

Teisseiyre, R., and Majewski, E. (2002). Physics of earthquakes. In: Lee, W. H. K., Kanamori, H., Jennings, P. C., and Kisslinger, C. (Eds.) (2002). *International Handbook of Earthquake and Engineering Seismology*, Part A. Academic Press, Amsterdam, 229-235.

Teng. T. L., Wu, L., Shin, T. C., Tsai, Y. B., and Lee, W. H. K. (1997). One minute after – strong motion map, effective epicentre, and effective magnitude. *Bull. Seism. Soc. Am.*, **87**, 1209-1219.

Thatcher, W., and Hanks, T. C. (1973). Source parameters of southern California earthquakes. *J. Geophys. Res.*, **78**, 8547-8576.

Tinti, S., Vittori, T., and Mulargia, F. (1987). On the macroseismic magnitudes of the largest Italian earthquakes. *Tectonophysics*, **138**, 159-178.

Tittel, B. (1977). Zur Bestimmung von Erdbebenmagnituden aus longitudinalen Kernwellen. *Gerlands Beitr. Geophys.,* **86** (1), 79-85.

Tocher, D. (1958). Earthquake energy and ground breakage. *Bull. Seism. Soc. Am*., **48**, 147-153.

Toperczer, M. (1975). Zur Definition der Seismizität. *Arch. Meteorol. Geophys. Geoklimatol.*, **5**, 377-385.,

Toppozada, T. R. (1975). Earthquake magnitude as a function of intensity data in California and Western Nevada. *Bull. Seism. Soc. Am*., **65**, 5, 1223-1238.

Tsai, V. C., Nettles, M., Ekström, G., and Dziewonski, A. (2005). Multiple CMT source analysis of the 2004 Sumatra earthquake. *Geophysical Research Letters*, **32**; L17304, doi: 10.1029/2005GL023813.

Tsuboi, C. (1954). Determination of the Gutenberg-Richter´s magnitude of earthquakes occuring in and near Japan. *Zisin.* (*J. Seism. Soc. Japan*), Ser. II, **7**, 185-193.

Tsuboi, S., Abe, K., Takano, K., and Yamanaka, Y. (1995). Rapid determination of M_w from broadband P waveforms. *Bull. Seism. Soc. Am*., **85**, 2, 606-613.

Tumarkin, A. G., Archuleta, R. J., and Madariaga, R. (1994). Scaling relations for composite earthquake models. *Bull. Seism. Soc. Am.*, **84**, 4, 1279-1283.

Turcotte, D. L. (1997). *Fractals and chaos in geology and geophysics*. 2nd edition, Cambridge University Press, Cambridge.

Turcotte, R., and Malamud, E. (2002). Earthquakes as a complex system. In: Lee, W. H. K., Kanamori, H., Jennings, P. C., and Kisslinger, C. (Eds.) (2002). *International Handbook of Earthquake and Engineering Seismology*, Part A. Academic Press, Amsterdam, 209-227.

Udías, A., and Buforn, E. (1988). Single and joint fault-plane solutions from first-motion data. In: Doornbos (1988a).

Udías, A. (1999). *Principles of Seismology*. Cambridge University Press, United Kingdom, 475 pp.

Udias, A. (2002). Theoretical seismology: An introduction. In: Lee, W. H. K., Kanamori, H., Jennings, P. C., and Kisslinger, C. (Eds.) (2002). International Handbook of Earthquake and Engineering Seismology, Part A. *Academic Press, Amsterdam*, 81-102.

Uhrhammer, R. A., and Collins, E. R. (1990). Synthesis of Wood-Anderson seismograms from broadband digital records. *Bull. Seism. Soc. Am*., **80**, 702-716.

Uhrhammer, R. A., Loper, S. J., and Romanovicz, B. (1996). Determination of local magnitude using BDSN broadband records. *Bull. Seism. Soc. Am*., **86**, 1314-1330.

Uhrhammer, R. A., Hellweg, M., Hutton, K., Lombard, P., Walters, A. W., Hauksson, E., and Oppenheimer, D. (2011). California Integrated Seismic Network (CISN) local magnitude determination in California and vicinity. *Bull. Seism. Soc. Am.,* **101**, 2685-2693.

Ulug, A. and Berckhemer, H. (1984). Frequency dependence of Q for seismic body waves in the Earth's mantle. *J. Geophys.*, **56**, 9-19.

Utsu, T. (2002). Relationships between magnitude scales. In: *International Handbook of Earthquake and Engineering Seismology*, *Part A*, edited by W.H.K. Lee, H. Kanamori, P.C. Jennings, and C. Kisslinger, Academic Press, Amsterdam, 733–746.

van Seggern, D. (1977). Amplitude-distance relation for 20-second Rayleigh waves. *Bull. Seism. Soc. Am.,* **67**, 405-411.

Vaněk, J., Zapotek, A., Karnik, V., Kondorskaya, N.V., Riznichenko, Yu.V., Savarensky, E.F., Solov'yov, S.L., and Shebalin, N.V. (1962). Standarizaciya shkaly magnitude (in Russian), *Izvestiya Akad. SSSR., Ser. Geofiz.*, **2,** 153-158 (with English translation in 1962 by D. G. Frey, published in Izv. Geophys, Ser.).

Veith, K. F. (1998). Comment on "Empirical determination of depth-distance corrections for mb and Mw from global seismograph network stations". *Geophys. Res. Lett.*, **25**, 22, 4241-4242.

Veith, K. F. (2001). Magnitude estimation from short-period body waves. Paper circulated on Oct. 9, 2002, amongst the members of the IASPEI WG on Magnitude Measurements, 7 pp.

Veith, K. F., and Clawson, G. E. (1972). Magnitude from short-period P-wave data. *Bull. Seism. Soc. Am.*, **62**, 435-452.

Venkataraman, A., and Kanamori, H. (2004a). Effect of directivity on estimates of radiated seismic energy. *J. Geophys. Res.*, **109**, B04301; doi:10.1029/2003JB002548.

Venkataraman, A, and Kanamori, H. (2004b). Observational constraints on the fracture energy of subduction zone earthquakes. *J. Geophys. Res.*, **109**, B04301, doi: 0431.01029JB002549.

Viret, M. (1980). Determination of duration magnitude relationship for the Virginia Tech Seismic Network. In: Bollinger, G. A. (ed.): *Central Virginia Regional Seismic Report*, *December 1, 1980*, US Nuclear Regulatory Eommission Contract No. NRC-04-077-034, 1-8.

Wahlström, L. (1979). Duration magnitudes for Swedish earthquakes. Seismological Institute, Uppsala, Sweden, Report No. 5-79, 22 pp.

Wahlström, R., and Strauch, W. (1984). A regional magnitude scale for Central Europe based on crustal wave attenuation. *Seismological Dep. Univ. of Uppsala, Report* No. 3-84, 16 pp.

Wang, J.-H., and Ou, S.-S. (1998). On scaling of earthquake faults. *Bull. Seism. Soc. Am.*, **88**, 3, 738-766.

Wang, R., Xia, Y., Grosser, H., Wetzel, H.-U., Kaufmann, H., and Zschau, J. (2004). The 2003 Bam (SE Iran) earthquake: precise source parameters from satellite radar interferometry. *Geophys. J. Int.,* **159**, 917-922; doi: 10.1111/j.1365-246X.2004.02476.x

Wason, H. R., Das, R., and Sharma, M. L. (2012). Magnitude conversion problem using general orthogonal regression. *Geophys. J. Int.,* **190**, 1091-1096; doi: 10.1111/j.1365-246X.2012.05520.x.

Weinstein, S. A., and Okal, E. A. (2005). The mantle wave magnitude M_m and the slowness parameter Θ: Five years of real-time use in the context of tsunami warning. *Bull. Seism. Soc. Am.*, **95**, 779-799; doi: 10.1785/0120040112

Wells, D. L., and Coppersmith, K. J. (1994). New empirical relationships among magnitude, rupture length, rupture width, rupture area, and surface displacement. *Bull. Seism. Soc. Am.*, **84**, 4, 974-1002.

Weston, D. E. (1960). The low-frequency scaling laws and source levels for underground explosions and other disturbances. *Geophys. J.*, **3**, 191-210.

Wever, Th., Trappe, H., and Meissner, R. (1987). Possible relations between crustal reflectivity, crustal age, heat flow, and viscosity of the continents. *Annales Geophysicae*, **87**, 03 B, 255-266.

Willis, D. E. (1963). Seismic measurements of large underwater shots. *Bull. Seism. Soc. Am.*, **53**(4), 789-809.

Willis, D. E., and Wilson, J. T. (1962). Effects of decoupling spectra of seismic waves. . *Seism. Soc. Am.*, **52**(1), 123-131.

Willmore, P. L. (Ed.) (1979). Manual of Seismological Observatory Practice. *World Data Center A for Solid Earth Geophysics*, Report **SE-20**, September 1979, Boulder, Colorado, 165 pp.

Wood, H. O., and Neumann, F. (1931). Modified Mercalli intensity scale of 1931. *Bull. Seism. Soc. Am.*, **21**, 277-283.

Wu, Y.-M., and Teng, T. L. (2004). Near real-time magnitude determination for large crustal earthquakes. *Tectonophysic*, **390**, 205-216.

Wu, K..M., and Kanamori, H. (2005). Experiment on an onsite early warning method for the Taiwan early warning system. *Bull. Seism. Soc. Am.*, **95**, 1, 347-353

Wu., Y. M., and Zhao, L. (2006). Magnitude estimation using the first three seconds P-wave amplitude in earthquake early warning. *Geophy. Res. Lett.,* **33,** 4pp.,L16312; doi: 10.1029/2006GL026871.

Wu, Y. M., ,Chen, C. C., Shin, Y. B., Tsai, Y. B., Lee, W. H. K., and Teng, T. L. (1997). Taiwan Rapid Earthquake Information Release System. *Seism. Res. Lett.*, **68**, 931-943.

Wu, Y. M., Shin, T.-C., and Tsai, Y.-B. (1998). Quick and reliable determination of magnitude for seismic early warning. *Bull. Seism. Soc. Am.*, **88**, 5, 1254-1259.

Wu, Y. M., Shin, T.-C., and Chang, C. H. (2001). Near real-time mapping of peak ground acceleration and peak ground velocity following a strong earthquake. *Bull. Seism. Soc. Am.*, **91**, 5, 1218-1228.

Wu, Y. M., Teng, T. L., Shin, T. C., and Hsiao, N. C. (2003). Relationship between peak ground acceleration, peak ground velocitz, and intensity in Taiwan. *Bull. Seism. Soc. Am.*, **93**, 1, 386-396.

Wu, Y. M., Yen, H., Zhao, L., Huang, B., and Liang, W. (2006). Magnitude determination using initial P waves: A single-station approach. *Goephys. Res. Lett.*, **33**, L05306; doi: 10.1029/2005GL025395.

Xie, X. B. and T. Lay (1994). The excitation of *Lg* waves by explosions: a finite-difference investigation. *Bull Seism. Soc. Am.*, **84**, 324-342.

Xie, X.B., and Lay, Th. (1995). The log (rms *Lg)-mb* scaling law slope. *Bull. Seism. Soc. Am.*, **85**(3), 834-844.

Yacoub, N. K. (1998). Maximum spectral energy for seismic magnitude estimation. Part I: Rayleigh-wave magnitude. *Bull. Seism. Soc. Am*., **88**, 4, 952-962.

Yanovskaya, T. B. (2012). Surface-wave tomography for upper mantle studies: methods and results. Keynote lecture at the 33rd General Assembly of the European Seismological Commission, Moscow, 19-24 Aug. 2012.

Yomogida, K., and Nakata, T. (1994). Large slip velocity of the surface rupture associated with the 1990 Luzon earthquake. *Geophys. Res. Lett*., **21**, 1799-1802.

Zhao, L.-F., Xie, X.-B., Wang, W.-M., and Yao, Z.-X. (2008). Regional seismic characteristics of the 9 October 2006 North Korean nuclear test. *Bull. Seism. Soc. Am.*, **98**(6), 2571-2589.

Zoback, M. L. (1992). First- and second-order patterns of stress in the lithosphere: The World Stress Map Project. *J. Geophys. Res*., **97**, 11703-11728.

Zoback, M. D., and Zoback, M. L. (2002). State of stress in the Earth's lithosphere. In: Lee, W. H. K., Kanamori, H., Jennings, P. C., and Kisslinger, C. (Eds.) (2002). International Handbook of Earthquake and Engineering Seismology, Part A. *Academic Press, Amsterdam*, 559-568.

Zollo, A., Lancieri, M., and Nielsen, S. (2006). Earthquake magnitude estimation from peak amplitudes of very early seismic signals on strong motion records. *Geophys. Res. Lett.*, **33,** L23312; doi: 10.1029/2006GL027795.